Modelling of intersubband absorption in modulation doped deep quantum wells

Wong, KuanMeng

Award date:
2007

Awarding institution:
University of Bath

Modelling of Intersubband Absorption in Modulation Doped Deep Quantum Wells

KuanMeng Wong

A thesis submitted for the degree of Doctor of Philosophy

University of Bath

Department of Electronic and Electrical Engineering

April 2007

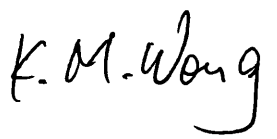

ProQuest LLC
789 East Eisenhower Parkway
P.O. Box 1346
Ann Arbor, MI 48106-1346

Abstract

An aim of this work was to investigate by detailed simulation the electric field dependence of intersubband optical absorption (ISBA) in deep quantum wells and its application to electro-optical modulation. ISBA is an attractive mechanism for high speed optical modulation, owing to the sub-picosecond relaxation time of an electron often undergoing upwards transition on the absorption a photon. Compared with optical modulators operating by band-to-band optical absorption, ultra-fast carrier relaxation will overcome the build-up of photogenerated carriers, removing a fundamental limitation on the electrical bandwidth of such devices.

The concept of an optical modulator based on ISBA is novel. To the best of the author's knowledge, this is the first systematic study of the prospects of creating an optical modulator based on ISBA. To this end, the simulation of ISBA involved the self-consistent solution of the coupled Poisson and Schrödinger equations including the band nonparabolicity. The quantum wells were designed to produce transition energies near 0.8 eV (1.55 μm wavelength) in $In_{0.53}GaAs_{0.47}$/AlAs quantum wells on InP substrate. The electric field dependence of absorption spectra associated with different doping conditions were simulated for single quantum well (SQW), double quantum well (DQW) and triple quantum well (TQW) structures. For DQW and TQW, two types of structures, strongly coupled and negligibly coupled, were designed and compared to the SQW structure.

The analysis shows that the well and barrier width are the essential factors for determining the absorption spectrum whilst the doping location and density are the main influences on the strength of the absorption. Simulation results also indicate that the density and the location of modulation doped regions have significant effects on the device operating conditions but only a small effect on any shift in the energy

position of the absorption peak. Larger differential absorption spectra can be achieved by a small field change under suitable doping conditions. Moreover, the limitation of the selection rules in ISBA was revealed. The results demonstrate not only the feasibility of using ISBA as a basis for electro-optical modulation, but also provide a basis for optimizing the design of such a novel photonic device. The thesis ends with suggestions for further research in the field.

Declaration

Some of the work in this thesis has been submitted for publication in the following papers:

K.-M. Wong and D. W. E. Allsopp, "Modelling Intersubband Electroabsorption Modulation", accepted for Conference on Lasers and Electro-Optics and Quantum Electronic and Laser Science Conference (CLEO/QELS) 2007, Baltimore, Maryland, 6-11 May, 2007

K.-M. Wong and D. W. E. Allsopp, "Electroabsorption Modulation Based on Intersubband Transitions", accepted for Conference on Laser and Electro-Optics and International Quantum Electronic Conference (CLEO/Europe-IQEC) 2007, Munich, Germany, 17-22 June, 2007

Acknowledgements

I am grateful to my supervisor, Dr. D. W. E. Allsopp for introducing me to the field of semiconductor quantum well structures. I wish to convey my sincere thanks to him for his valuable suggestions and guidance for the entire duration of this work.

Special thanks to Dr. J.-Z. Zhang, Dr. S. Banerjee and Mr. R. Taylor for helpful advice and stimulating discussions. Thanks are also due to Mr. Z. Ke for his valuable suggestions in programming and mathematic solutions. I wish to thank and appreciate the experience that I have acquired from Mr. T. Ryan in the clean room process and the field of device fabrication.

I am also grateful to my family for their love, financial support and encouragement.

Contents

CHAPTER 1

Introduction

1.1 Background

For the secure and satisfactory use of the next generation of information and telecommunication networks, network nodes with data transmitted and processed in the 100 Tb/s range are forecast for around 2015 [1]. Such systems are unlikely to be achieved without introducing novel devices, since signal processing in the present scheme based on electronic circuits fails because of the RC time constant limit of transition speeds. Therefore, ultrafast optoelectronic devices that can operate in the femtosecond time scale are greatly needed for fulfilling this future requirement. One of the key devices for practical applications of the systems is the femtosecond (1 fs = 1×10^{-15} s) laser source for generation and transmission [2]. The essential characteristics of such lasers are ultrashort pulse duration, high output power, and high repetition rate. Other key devices, such as all-optical switches and modulators for control and distribution, in which optical signals are directly processed without converting to electronic signals, are additional primary devices needing further development. An ultrafast response time, a high extinction ratio, a low insertion loss and a low switching energy are required of these devices [3].

1.2 Intersubband Transitions: a solution to the speed problem?

In the event of using a conventional optical device working on electrons and holes between conduction and valence bands, as illustrated in Fig. 1.1 (a) and (b) for band-to-band and conduction subband to valence subband transitions, respectively, the operational speed or response time is restricted to the range between a few picoseconds (1 ps = 1×10^{-12} s) and nanoseconds (1 ns = 1×10^{-9} s) [4,5] owing to the relatively slow interband recombination lifetimes. For instance, the fastest response time reported for a quantum well based electroabsorption modulator (EAM) for all-optical signal processing is ~5 ps [5]. This limitation of speed is due to the absorption saturation recovery time, which is limited by the sweep-out time of the

photogenerated carriers. The carrier lifetime (τ) in a quantum well mainly involves three independent physical mechanisms: recombination, thermionic emission and tunnelling. It can be expressed as $\frac{1}{\tau}=\frac{1}{\tau_R}+\frac{1}{\tau_E}+\frac{1}{\tau_T}$ where τ_R^{-1}, τ_R^{-1} and τ_R^{-1} are the recombination, thermionic emission and tunnelling rates, respectively [6]. Although a shorter sweep-out time can be achieved by reducing the barrier width, increasing the applied field or selecting a lower potential barrier material [6], the saturation intensity will become higher and therefore impracticable for achieving such ultrafast all-optical switches that operate by absorption saturation [7].

It has been suggested that this difficulty can be avoided by confining electrons in a quantum well, then utilising the optical transition between permissible electron energy levels quantised in the well, i.e. between the subbands of the same generic band. The absorption recovery time of such process is extremely short due to the particularly fast carrier relaxation process [8-13]. This phenomenon is known as an intersubband transition (ISBT) as shown in Fig. 1.1 (c).

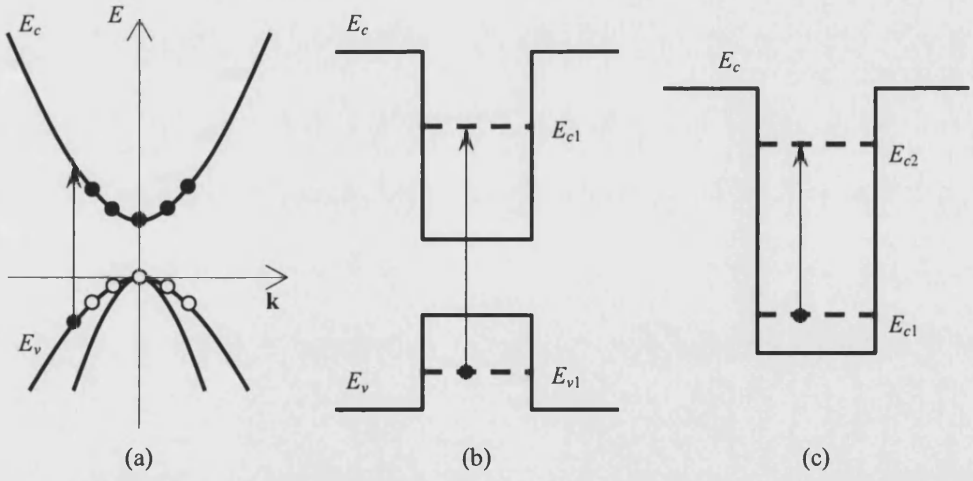

Figure 1.1: Diagram of (a) band-to-band electronic transitions in bulk semiconductors, (b) valence subband to conduction subband transitions (interband transition) in a quantum well, and (c) transitions between conduction subbands (intersubband transition) in a quantum well.

For developing semiconductor high-speed devices, the relaxation mechanism of ISBTs has been studied theoretically [8,9] and experimentally [11-13]. If the comparatively slow radiative recombination process is neglected, excited carriers are scattered first with finite wavevector ($\mathbf{k}_{//}$) to the ground subband, then cooling within the lower subband can occur, as shown in Fig. 1.2. This overall relaxation time can be estimated by a simple equation: $\tau = \tau_{inter} + E_{inter} / \eta\omega_{LO} \times \tau_{intra}$ where τ_{inter} is the intersubband scattering time and τ_{intra} average intrasubband LO-phonon emission time [10]. Intersubband scattering occurs on a sub-picosecond timescale while intrasubband relaxation is a much faster process [8]. Akiyama *et al* have reported on an ISBT from the InGaAs/AlAs/AlAsSb quantum well system, which is lattice-matched to the InP substrate, with an ultrafast absorption response of 685 fs at 1.55 μm wavelength [11]. A faster optical response is expected in GaN/AlGaN quantum wells because of strong coupling between electrons and LO-phonons enhancing the energy loss rate [12]. The recovery times at 1.55 ~ 1.73 μm wavelength have been measured to be 160 ~ 310 fs [13]. More details will be presented in Chapter 2. These results clearly demonstrate the potential of ISBTs for ultrafast devices.

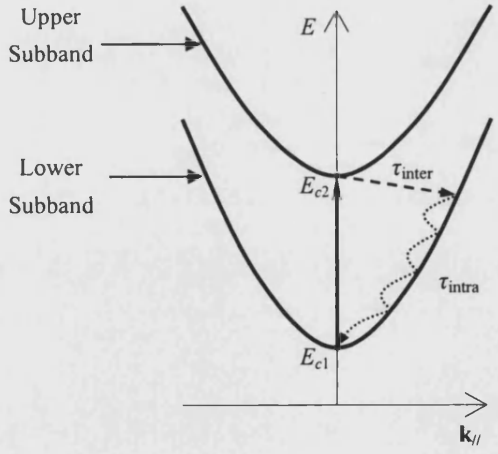

Figure 1.2: The model of the intersubband absorption and relaxation dynamics. The carrier is excited into the upper subband (solid up arrow). The relaxation occurs via the electron-LO-phonon scattering (dashed arrow) first in the time of τ_{inter} and then the intrasubband thermalisation (wavy dotted) in the time of τ_{intra}.

Besides the ultrafast response time, there are some other unique characteristics of ISBTs which offer many advantages as well as novel functionalities if applied in optical devices. In contrast to the conventional semiconductor laser, the wavelength of lasers based on ISBT is essentially determined by the quantum confinement of carriers. As such, the wavelength can be tailored over a wide spectral range using the same active material by artificially engineering the thickness of the quantum well layers [14]. As far as intersubband lasers are concerned, they inherently produce high optical power because of the unipolar nature of their operation involving only a single type of carrier [15]. Furthermore, with a large transition dipole moment, strong nonlinear optical effects are achievable [16].

In addition to the desirable characteristics mentioned above, ISBTs in doped quantum wells have opened the possibility of high-speed photonic switches, modulators and lasers for use in future optical communication systems [17,18]. In order to establish the necessary technologies for these novel devices, it is important to understand the fundamentals and the underlying physics of the ISBT in greater depth. Once the technological requirements of these concept devices are established, the novel optical networks become possible.

1.3 Project Aims and Objectives

In order to insure the fast response time, structures based on ISBTs are considered. To date, research has focused on ultrafast devices that operate by ISBT such as all-optical switching and lasers. Little work has been done on the scope for using ISBTs as a basis for EAMs in which a high absorption saturation intensity is advantageous, contrary to the requirements of all-optical switching. Therefore, a systematic study of the feasibility of their applications on voltage-controlled optical intensity modulation is necessary.

The need to develop and optimise suitable structures for EAMs provides strong technological motivation for an accurate modelling of semiconductor heterostructures. The intersubband absorption coefficient needs to be derived because it underpins the electronic and optical properties. Theoretical calculations of intersubband optical transitions in quantum well structures have been discussed in the literature [19-21]. In these calculations, the subband energies and the envelope wavefunction in a quantum well were calculated by solving the Schrödinger equation only. However, those approximations were applicable solely when the applied electric field and the spatial distribution of carriers were negligible. The main target of this thesis is to investigate theoretically the electroabsorption properties of ISBTs, where a small change in the applied voltage could cause a large change in the absorption.

On the one hand, the influence of an external electric field on subband energies and corresponding wavefunctions, can dominate the variation of intersubband absorption (ISBA) [22]. Accurately assessing the absorption coefficient as a function of wavelength and electric field can provide data which can be used not only in device design and optimisation, but also for optical modulator operation. The differential absorption spectra caused by modifying electric field strength can also be used to calculate the real part of the refractive index through the Kramers-Kronig relations. In principle, such modulators can operate by the direct influence of electroabsorption on a lightwave, or by phase shift arising from electrorefraction effects. As a consequence, effects of electric field on ISBA must be considered and form the main core of this work.

On the other hand, the effects of doping, notably modulation doping [23], leading to band bending in the potential energy profile, must also be considered. This is because viable operation of any device by ISBT implies that carriers, e.g. electrons, must be present in the structure. In the case of ISBA, the carriers will occupy a lower energy subband to be excited to a higher energy subband. Strong ISBA requires a high

occupancy of the ground state energy levels of a quantum well or system of coupled quantum wells. This can be achieved by modulation doping. As a consequence, the variation in the occupancy of the subbands with electric field is critical to device operation. Further, the presence of free carriers in the structure also implies the presence of ionised impurities (donors or acceptors). The location and concentration of ionised impurities will affect the electric field distribution through the structure. In the case of modulation doping, the spatial separation between the charged dopant atoms and the free electrical carriers creates another contribution to the local electrical potential in the structures. This induced electrical potential will modify the original potential profile which includes the built-in and externally applied potentials. The modification of the overall potential profile leads to changes in the electron energy levels and envelope wavefunctions and thus changes in the electronic and optical properties of the quantum well.

Overall the presence of impurities and free carriers and their likely spatial separation give rise to a need for self-consistent solution of the coupled Schrödinger and Poisson equations. This work has been carried out in order to develop an understanding of the contributions of charge control and field-induced distortion of the wavefunctions to ISBA from detailed self-consistent modelling. Based on this understanding, the research extends to a study of the influence of these effects on the characteristics of prospective optical modulator structures.

In keeping with the emphasis on a realistic simulation for device design and optimisation in the preceding sections, this thesis is further aimed at investigating the influence of coupling strength of quantum wells, i.e. the probability of electrons tunnelling through to the adjacent wells, on the peak detection wavelength and the shape of the absorption spectrum. These factors can be controlled by varying the structural parameters of the quantum well, i.e. well width and barrier width. To achieve the intersubband transition energy required for useful, fine-tuned, communication wavelengths, the well width should be very narrow, usually from 6 to

9 monolayer (MLs) [24-26], meaning that even one ML fluctuation in the well width will cause a significant shift in transition energies. Therefore, such parameters could have vital effects on ISBTs and will be studied in detail in this thesis.

This work also systematically extends the theoretical study of ISBA in single quantum wells (SQWs) to double quantum well (DQW) and triple quantum well (TQW) structures. This is because the coupled quantum well structure has been shown to be effective for achieving a faster optical response and a shorter transition wavelength [17]. Moreover, the variations of optical matrix elements in DQW and TQW are expected to be stronger than SQW under applied bias, which provides another way to modify ISBA. By comparing these three types of structures, which have the same quantum well width, barrier thickness and doping density in each well, one can deduce the properties in multiple quantum well (MQW) and superlattice (SL) structures with corresponding parameters in every single well. Furthermore, the comparison of doping at different concentrations and varied positions causing the ISBA change is presented. Such a theoretical investigation elucidates the trends in the ISBA behaviour among these structures, of which little is known.

1.4 Outline of Methods

In order to reveal the effects of the electric field, ionised impurities in the quantum well structures, a Poisson solver is needed, while a Schrödinger solver is required for considering the quantum mechanical system. However, the Poisson and Schrödinger solvers are interactive: the distribution of two-dimensional electrons in quantum wells is required in the Poisson solver for the accurate calculation of potential profile, while the potential profile is essential for the Schrödinger solver for calculating accurate subbands and wavefunctions. Under these circumstances, the potential profile, the electric field distribution and the carrier concentration of the quantum well structures are first simulated by solving the Poisson equation. Then, the electron

energy levels and envelope wavefunctions are calculated by solving the Schrödinger equation using the electrostatic potential profile previously obtained by solving the Poisson equation. The influence of quantum-size effects on the charge distribution and the potential profile is then recalculated followed by a correction of the energy levels and wavefunctions. The procedure is followed iteratively until the system is self-consistent as illustrated in Fig. 1.3. As a consequence, a self-consistent evaluation of the intersubband absorption coefficient can be achieved.

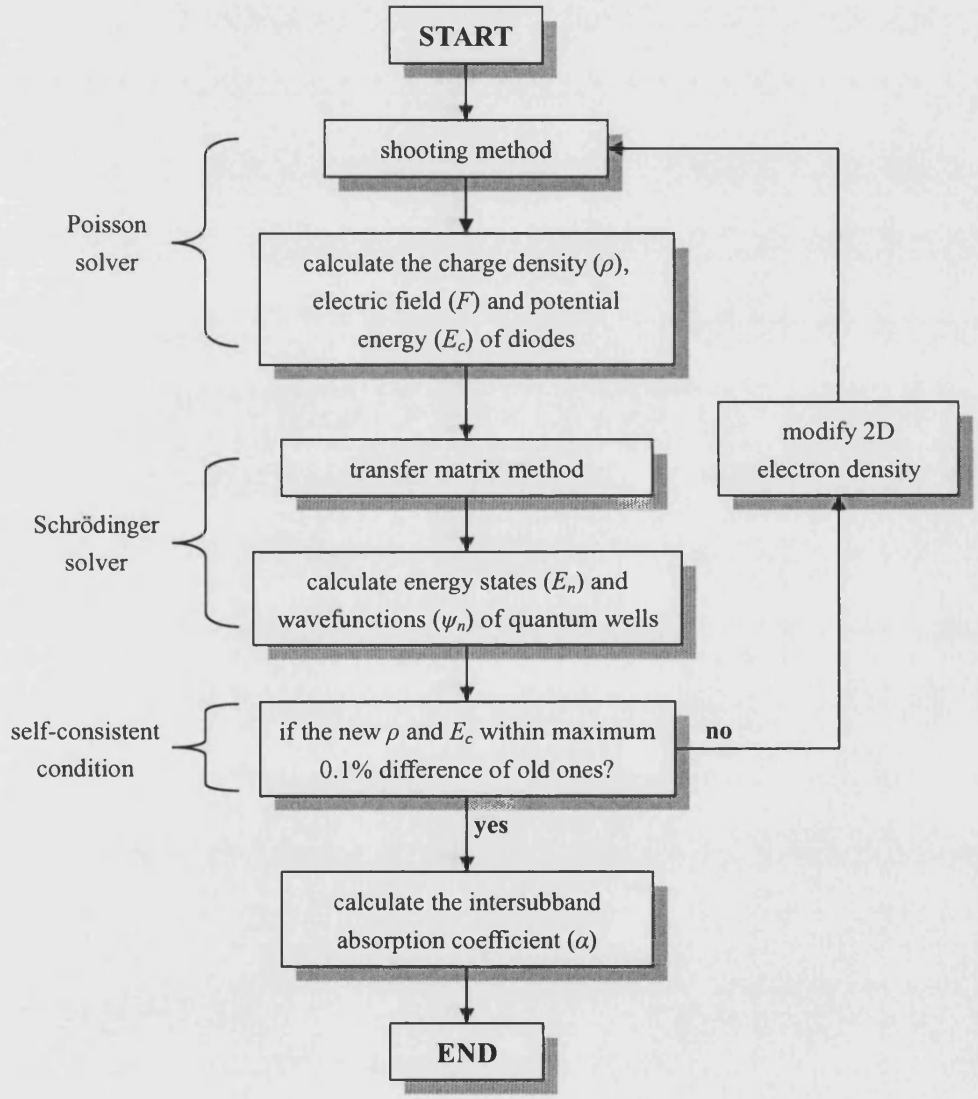

Figure 1.3: Flow chart of the iterative methods of self-consistent Schrödinger-Poisson approach in this thesis.

Accordingly, a numerical Poisson solver based on the "shooting method" is developed to simulate field and potential distributions in III-V semiconductor diodes, where quantum wells are fabricated in the middle of the intrinsic region. In addition, the transfer matrix method [27] is used to solve the single band Schrödinger equation for quantum well structures in the single band envelope approximation [28,29]. This self-consistent Schrödinger-Poisson approach is developed using the MATLAB software and is simple to use in application. The software can be used to calculate the intersubband optical transition energies and their absorption coefficient for quantum wells under external electric fields and different doping conditions. Additional information about the characteristics of ISBT can be extracted by understanding the wavefunction behaviour with varying field strength and charge density.

Therefore, by taking account of the different mechanisms mentioned above, i.e. the interaction of quantum effects, the electric field distribution and carrier density modulation, a model of greater validity is considered in this work. The design of optoelectronic devices relies on the precise simulation of the electronic band structure. Thus an accurate modelling of quantum well structure ensures a precise and versatile way of determining the electroabsorption between different electron eigenstates. It is intended that the numerical simulations presented here will stimulate new experimental efforts to develop novel ISBT based devices.

1.5 Layout of Thesis

This thesis investigates theoretically the electric field induced modulation of ISBA including the effects of doping in various quantum well structures and is organised as follows: the background of this research and the advantageous properties of ISBT are reviewed in this chapter. The targets of this work and its motivation are then introduced. Subsequently, a brief introduction of the method for the modelling of ISBT is presented.

In Chapter 2, a brief overview of heterostructures and a detailed review of ISBTs are presented. First, the properties and the applications of semiconductor heterostructures are given. The physical concepts and selection rules of ISBTs are then underlined. A review of the literature is presented mainly concerning the ultrafast dynamics and the large tunability of wavelength (transition energy) of ISBTs. Two significant devices based on ISBTs, quantum cascade lasers and quantum well infrared photodetector are reviewed, to provide background to the novel application of ISBTs to optical modulators described in this thesis. Next, some new material systems capable of the range of application of ISBTs, such as highly strained InGaAs/AlAs material system and the group III-V nitride semiconductors, are described in detail.

In chapter 3, a detailed derivation of the self-consistent Schrödinger-Poisson scheme including band nonparabolicity is presented. The basic physics of quantum confined structures is reviewed and an investigation and comparison between one-electron and many-electron Schrödinger equations follow. By developing the theory, the numerical solver based on transfer matrix method and effective mass equation for the arbitrary shaped quantum well structures is presented. For taking into account the ionised impurities and band bending caused by the modulation doping, a numerical Poisson solver based on the "shooting method" is introduced. The correction for band nonparabolicity in subband energies, not predicted in single band solutions of the Schrödinger equation, is also considered. In order to model optical spectra, the theoretical calculation of absorption coefficient is presented. Lastly, the accuracy and the validity of the model developed in this chapter are investigated.

Chapter 4 contains a detailed description of the calculations of the effect of an electrical field on ISBA performed for the SQW, DQW and TQW structures with different coupling strength between the wells. The influences of modulation doping are also included in assuming the use of the InGaAs/AlAs material system. This chapter is especially dedicated to establishing theoretically different ways of achieving strong differential absorption spectra in the spectral range of the

communication wavelength of 1.55 μm. The well-width dependence on the transition energies of ISBT in SQW is first revealed to establish the feasibility of 1.55 μm wavelength ISBT. Then, a detailed study in SQW of various doping conditions, namely changing doping location and density, is performed.

Coupled quantum well structures, which have been shown to be effective for achieving faster optical response and shorter transition wavelength, are potential device configurations to achieve strong modulation effect. The effect of the coupling strength in DQW is underlined by changing the barrier width. The dimensions of quantum wells are decided after examining the wavefunction behaviour of bound particle states under external electric field. Two types of DQW structures, strongly coupled and weakly coupled DQW, are simulated and detailed analysis of the data are followed. Similar simulations to the DQW cases are performed for the modulation doped TQW structures with applications in telecommunication in mind. Lastly, the comparisons of SQW, DQW and TQW are followed by a detailed qualitative and quantitative analysis of the data in order to assess both the feasibility of their application to optical modulation and as a basis for device optimisation.

Finally, in Chapter 5, a summary of the original results obtained and principal conclusions drawn from the simulation are consolidated and discussed. Suggestions regarding scope for further research are also presented.

Properties and Applications of Quantum Heterostructures

CHAPTER 2

2.1 Review of Quantum Well Structures

Before looking into the unique features and attractive applications of intersubband transitions, it is important to have a brief overview of the physics and properties of general quantum well structures. The development and the progress of modern crystal growth techniques such as molecular-beam epitaxy (MBE) [30-33] and metal organic chemical vapour deposition (MOCVD) [34-37] have demonstrated that it is possible to grow semiconductors of different atomic compositions on top of another semiconductor with monolayer (ML) precision. This enables the production of structures exhibiting quantum confinement of carriers caused by the difference of energy band gaps between the materials grown [38,39]. As a consequence, a wide variety of novel devices based on quantum heterostructures has become possible.

When a semiconductor thin film is clad on top and bottom by a thick layer of a second semiconductor whose conduction band edge is larger in energy than that of the intervening film, confining the electronic wavefunctions and quantising the energy levels, a single quantum well (SQW) is formed. This is shown in Fig. 2.1 (a). Quantum confined structures commonly used in practical devices include multiple quantum wells (MQWs) and superlattices (SLs). By fabricating many such quantum wells on top of each other, separated by thick layers of the barrier material, so that the electrons wavefunctions in adjacent quantum wells do not overlap, results in an MQW structure, as shown in Fig. 2.1 (b). The properties of an MQW are similar to those found in an isolated SQW of the same materials and well width, owing to the negligible coupling between adjacent wells. If the barrier layers are grown sufficiently thin that the probability of tunnelling between wells is significant, the result is a SL as illustrated in Fig. 2.1 (c) and first proposed by Esaki and Tsu in 1970 [40]. SLs are endowed with properties which are determined by the artificial periodicity of the multilayer configuration.

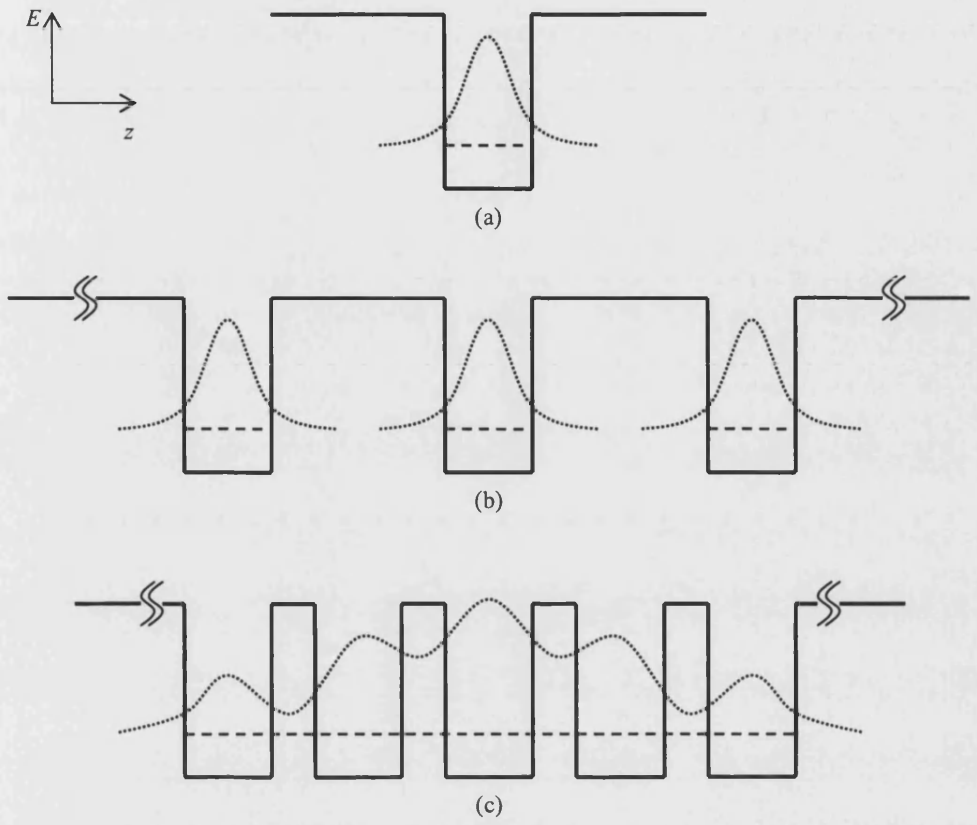

Figure 2.1: Sketch of conduction band (solid lines), subbands (dash lines) and corresponding wavefunctions (dotted lines) in a (a) SQW, (b) MQW and (c) SL structure.

Optical measurements provide direct evidence for the low-dimensional behaviour of electrons and holes in a quantum well. In a semiconductor, when the photon energy exceeds the energy gap between the valence and conduction band, known as the threshold, optical absorption increases rapidly with increasing energy. However, due to the quantum confinement in heterostructures, discrete states are then created in conduction and valence bands, so that the optical absorption consists of steps corresponding to the two-dimensional joint density of states for the both bands. Experiments of quantum confinement in semiconductor material were first performed by Dingle *et al*, who showed the steps in the absorption spectra and confirmed the formation of quantum states in wells [41].

2.1.1 Properties of Quantum Structures

(1) Density of states

To gain an understanding of the properties of quantum structures, a comparison with bulk semiconductors is necessary. The principal characteristic of quantum hetero-structures is the restriction on dimensionality. The density of states in the energy bands [$n(E)$] is three-dimensional in a bulk semiconductor as in Fig. 2.2 (a) [42]. In contrast, in a compositionally modulated semiconductor, the energy barriers caused by the heterojunction band offset confine the freedom of movement of electrons (and holes in the case of the valence) in the perpendicular direction of the interfaces. As mentioned, if the narrow band gap regions are thin enough (less than the de Broglie wavelength of an electron), this transverse confinement creates discrete bound energy states between barriers, e.g. E_{c1} and E_{c2} in the Fig. 2.3 (a). In essence, electrons of energy outside these energy states, i.e. $E \neq E_{c1}$, E_{c2} are no longer free to propagate in a direction perpendicular to the interface between these layers.

Although, the presence of two such barriers introduces an additional quantisation condition in that direction, it leaves an electron wave free to propagate in the other two dimensions defined by the plane parallel to the interfaces, as shown in Fig. 2.3 (b). Therefore, the corresponding density of states becomes step like in quantum wells, reflecting the reduced degree of freedom of motion. In SLs the density of states is quasi-two-dimensional. These two situations can be achieved simply by varying the configuration of the thickness of wells and barriers when growing semiconductors and their density states are shown in Fig. 2.2 (b).

If the freedom of movement is further confined by additional potential barriers, first quantum wires are formed in which carriers have one degree of freedom [Fig. 2.2 (c)] and then quantum dots in which carriers have zero degree of freedom of motion [Fig. 2.2 (d)]. The impact of the successive reductions in the degrees of freedom of motion on the density of state is also shown in Fig.s 2.2 (c) and (d) [42].

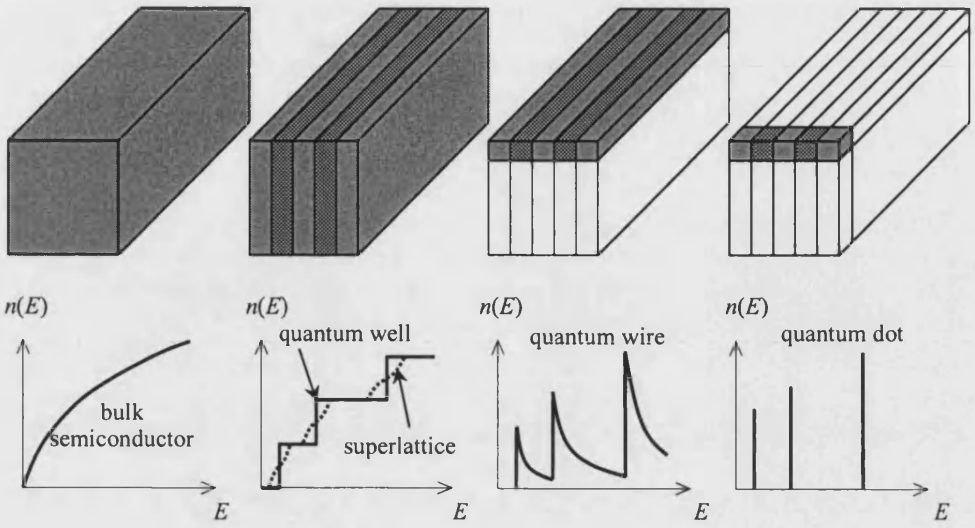

(a) 3D (b) 2D and quasi-2D (c) 1D (d) 0D

Figure 2.2: Density of states in (a) bulk semiconductor material (3D), (b) superlattice (quasi-2D) and quantum well (2D), (c) quantum wire (1D) and (d) quantum dot (0D).

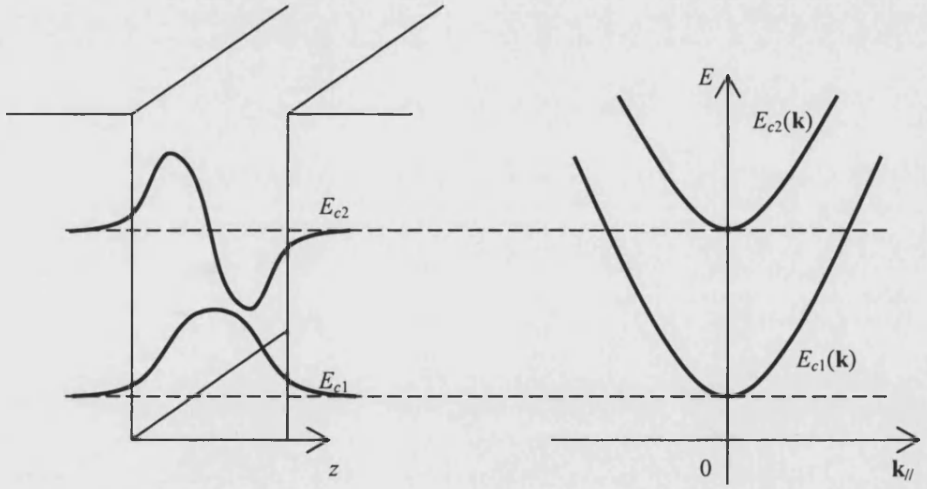

(a) (b)

Figure 2.3: Schematic of (a) potential well with two confined energy levels, (b) total energy including the bound state energy and the transverse kinetic energy versus electron wave vector in the plane of the interfaces for each subband.

(2) Tunnelling

Tunnelling is another fundamental but significant quantum mechanical concept in the field of low dimensional structures. Classically, a particle with its kinetic energy lower than the top of an energy barrier would not be able to pass over such barrier, but in quantum mechanics the particle has a finite probability to tunnel through the barrier. The probability for an electron to tunnel through a potential barrier decreases exponentially with the barrier width [43]. When the energy of the electron outside a quantum well is the same as any of the quantised energies of the well confined by two consecutive barriers, then there is a resonance between the two energies and the tunnelling probability is dramatically enhanced [43], an effect known as resonant tunnelling. If the barriers of a quantum well on either side are thin, an electron in a state between the barriers can tunnel through the barrier, giving a quasi-bound or resonant state rather than a true bound state.

Additionally, the role of tunnelling provides the means of coupling between quantum wells. In the double quantum well (DQW) structure, for example, the electron wavefunction in one well can tunnel through the barrier region into the other well. This tunnelling phenomenon then brings a shift of bound energy levels compared to those in identical but isolated wells, and also produces a splitting of the degenerate states in the DQW. For the electron states n localised in coupled quantum wells, the energies take the form $E_n^{\pm} = E_n - s_n \pm t_n$ [44]. The first term E_n is the energy of the confined state n in an isolated well without tunnelling, s_n and t_n are called a shift integral and a transfer integral, respectively, which represent two integrals that characterise electron tunnelling in a double-well structure. The diagram in Fig. 2.4 illustrates the modification of the energy levels and clarifies the meaning of the shift and the transfer integrals. The former indicates the energy shifting down from the initial energy levels in the single well, reflecting the increase in the overall width of the structure (effectively equivalent to two wells). The latter determines the splitting of the twofold degenerate level. Both shifting and splitting are caused by the overlap

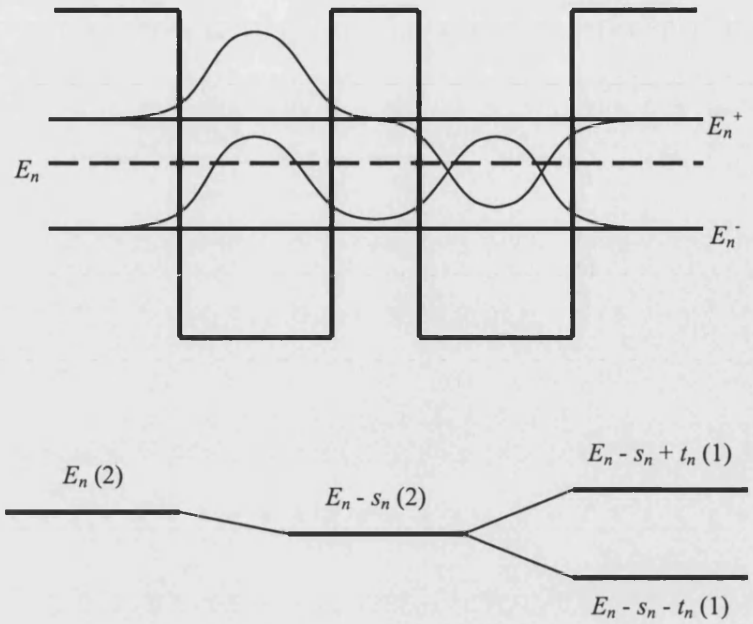

Figure 2.4: Diagram of an energy-level modification in a double-well heterostructure when shift and transfer integrals (s_n and t_n) are taken into account. The degeneracy of levels is indicated in parentheses.

of wavefunctions due to tunnelling phenomenon. A logical step beyond the DQW structure is to increase the number of quantum wells, which forms a SL and in this case the tunnelling effect on the confined energies results in a miniband. The concept and features of a miniband can be given by the tight binding approach or the Kronig-Penney model [4].

(3) Electron transport

For layered structures, such as heterojunction structures, MQWs and SLs, as well as quantum wire-containing structures, two types of electron transport, referring to the motion direction of motion, can be distinguished. The first type of transport is related to a motion of electrons in the direction along the layers or the wire axis, as shown schematically in Fig. 2.5(a). One refers to this type of electron motion as parallel transport. Modulation doped field effect transistors operate by this type of carrier motion [45,46]. The second type is related to the electron transfer in the directions

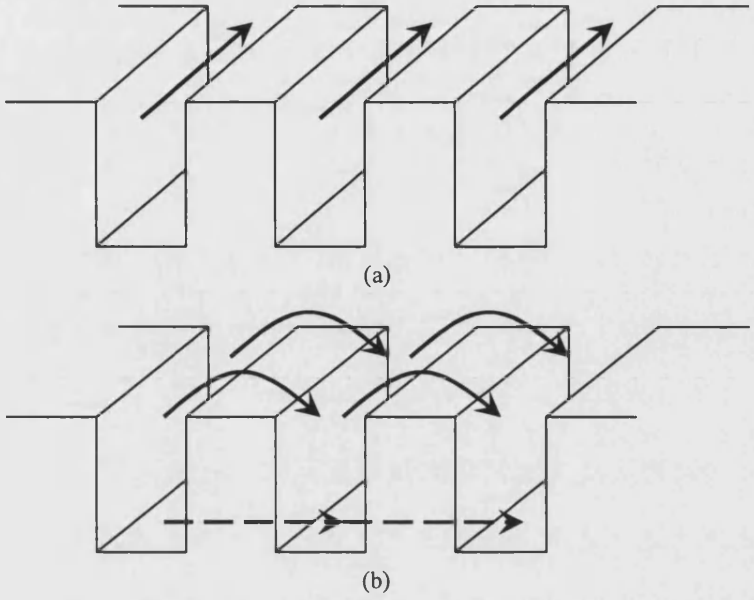

Figure 2.5: (a) Parallel electron motion along the layers of a multiple quantum well (solid arrows), (b) perpendicular transport over barrier (solid curved arrows) and quantum tunnelling (dashed arrows).

perpendicular to the layers or to the wire axis. This is called perpendicular transport, as depicted in Fig. 2.5 (b). An important example of perpendicular quantum transport is provided by resonant tunnelling, in which the double-barrier resonant-tunnelling structure are the most promising in this class [47].

Devices based on real-space transfer operate by both parallel and perpendicular motion [48]. In these devices electrons in a narrow semiconductor layer are accelerated by an electric field parallel to the layer, i.e. acquiring higher energy, known as heating, prior to transfer over the barrier. Such devices have been extensively investigated and show promise as logic devices, microwave sources, memory elements and electroluminescent devices [49,50]. Another example of the perpendicular transport is given by transport through superlattices and provides a new type of oscillations under applied electric field, known as Bloch oscillations. It has shown promise as a source of microwave emission up to a few terahertz [51,52].

(4) Field effects

Much as in atomic physics, the eigenstates of quantum wells can be modified by an external electric field. In 1982 Mendez *et al* proposed and demonstrated the use of a field perpendicular to the well planes to change both the energy and wavefunction of the ground state of the quantum well [53]. The effect, called the quantum-confined Stark effect (QCSE) [54,55], has been extensively studied since then and is the basis for electrooptical modulators [56] and self electro-optic effect devices (SEED) [57,58]. A related effect is that of an electric field on a semiconductor SL, by which the quasi-continuum of states that constitutes the SL's minibands is split into a series of discrete states. This is called the Wannier-Stark ladder, effectively inducing a transition from a quasi-three-dimensional to a two-dimensional density of states [59]. Although predicted long ago for solids in general, the Wannier-Stark ladder was not observed until 1988 when semiconductor SLs with a periodicity ten times larger than that of atomic planes in bulk semiconductors were used [60]. The demonstration of the Wannier-Stark ladder is at the core of extensive reports on the observation of Bloch oscillations [51,52].

2.1.2 Modulation Doping in Heterostructures

Many devices, especially electronic devices based on parallel transport in quantum structures, rely on electrons or holes for conduction and these must be introduced by doping. Unlike conventional semiconductor devices doped in the regions where electrons or holes are desired, modulation doping, or selective doping, is often used in heterostructures where doping is grown in one region but the carriers subsequently migrate to another [61,62]. This is illustrated by a heterojunction between *n*-AlGaAs and undoped GaAs in Fig. 2.6. The step like profile of the bands is unstable. Electrons are removed from the doped region and transferred to undoped region until an electrostatic field, which is produced by the charge redistribution, results in band bending, lining up the Fermi level across the structure and forming an electron channel at the interface. Instead of having an energy step as in Fig. 2.6 (a), one obtains the situation shown in Fig. 2.6 (b) which the band edges bend with distance.

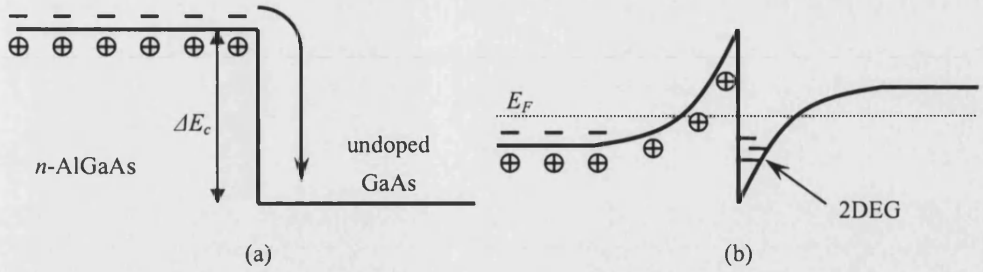

Figure 2.6: Conduction band around a heterojunction between *n*-AlGaAs and undoped GaAs showing how electrons are separated from their donors to form a 2DEG.

Ionised impurities exist in the doped region and there are free electrons inside the potential well, known as the two-dimensional electron gas (2DEG). The 2DEG trapped at a modulation doped heterojunction is the most important low-dimensional system for electronic transport. However, in such single heterojunction, the conducting channel at the interface only has a constant and uncontrollable electron concentration. In order to change the conductivity by modulating the electron concentration to realize useful devices, a metal contact would normally be placed on top of the n^+ layer of the AlGaAs barrier material, known as a gate and the structure so-called gated heterostructure. One also refers to the metal layer as Schottky contact. Such structure forms the core of heterostructure field-effect transistors (HFET) [62], also known as the modulation-doped field-effect transistor (MODFET) or high electron mobility transistor (HEMT) [45,46].

The principle of modulation doping can be applied to heterostructures with single or multiple quantum wells. The advantages of these types of selectively doped systems are a combination of electron transport in quantised states and in an undoped region where scattering is low, hence the mobility high [44,61]. When the thickness of the lower energy band gap material in a double heterojunction is sufficiently wide and the electrostatic potential inside the well exceeds the lowest confined state, two spatial regions exist in which electron wavefunction localisation arises, as shown in

Fig. 2.7 (a). If the well is rather narrow, normally a few nanometres, a quantum well is formed as illustrated in Fig. 2.7 (b). Such structures form the central point of this work. The additional electrostatic potential inside the quantum well, which changes as the electron concentration increases, affects the subbands and their wavefunctions. To describe the behaviour of the energy levels and the corresponding wavefunctions, self-consistent modelling has been widely used and proved to be effective in the theoretical studies of modulation-doped quantum structures [63-66]. It is also the central scheme used in Chapter 3.

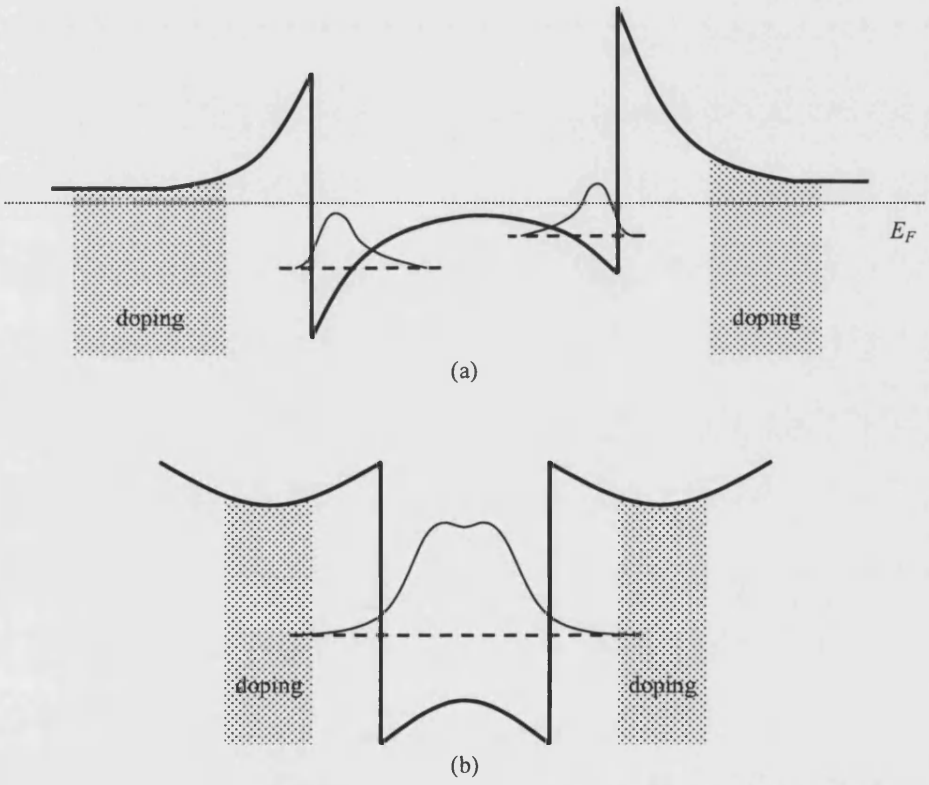

Figure 2.7: The energy-band edge for a heterostructure with two AlGaAs/GaAs junctions. The resultant double heterostructure is asymmetric in (a) because of an asymmetric doping and the wavefunctions are shown in the limit of a thick well in which two electron channels appear. With a narrower well width and symmetric doping in (b), a non-rectangular quantum well is formed.

2.1.3 Applications of Quantum Structures

Semiconductor quantum structures with these new electronic and optical properties can be custom designed for various applications. The quantum well laser is probably among the best examples of the numerous applications of the semiconductor quantum well in electronic and optoelectronic devices. The quantum well structures provide tunable wavelengths by varying the well width and the barrier height. The concept of quantum well structures for semiconductor lasers was proposed and realized experimentally in the late 1970s [41,67,68]. Strained quantum well lasers were proposed to improve the laser performance resulting in remarkable progress in high-performance diode lasers [69,70]. The ability to epitaxially grow a large array of layers of alternating and controlled alloy composition has also made possible the realisation of vertical quantum well lasers, in which the optical cavity is created by the region between two 'dielectric' mirrors, grown epitaxially under and above the active region that contains the quantum well [71]. Novel structures such as surface-emitting laser [71,72] and microdisk lasers have also been realized [73].

Semiconductor heterostructures have also been advantageous for devices operating by parallel-transport, in which electronic transport is in the plane of the heterostructure. Since the first report of a working MODFET in 1980s [74,75], technological development has continued to this day to improve its properties. In the most basic MODFET construction, a high bandgap material with a high doping concentration is grown above a low bandgap intrinsic material. It utilises a 2DEG, the concentration of which is modulated by the gate potential. The fundamental principle of the outstanding performance of MODFETs is the dopant-free nature of the electron channel achieved by bandgap engineering, resulting in high carrier mobility via reduced impurity scattering. High linearity at high efficiency is an attractive feature that makes MODFETs especially useful for high power applications [76]. Nowadays MODFETs are in commercial use as high-frequency, low-noise amplifiers and are actively researched for specialised digital applications.

Quantum well electroabsorption modulators (EAMs) at room temperature have been the subject of intensive research subject for many years. Research in semiconductor quantum well structures has shown that optical absorption in quantum wells exhibits a dramatic change due to QCSE caused by the applied electric field [54,55]. The key development in these structures is the strong exciton binding energy so that ionisation of excitons at room temperature can be avoided. It is because the quantum well barriers confine both the electrons and holes within the wells. The sharp excitonic absorption spectrum with a small scattering line width shows the significant possibility of achieving a significant change in the absorption coefficient by an applied voltage bias [55,77]. EAMs have become an enabling technology for high speed optical modulation and practical applications in photonic switching, information processing and high data rate optical communication systems [78,79].

2.2 Intersubband Transitions in Quantum Wells

2.2.1 Optical Transitions in Quantum Wells

Optical transitions in a quantum confined semiconductor structure such as a quantum well can occur either between conduction and valence band, known as interband transition, or within the conduction or valence band only, known as intersubband transition (ISBT). This is illustrated in Fig. 2.8. Since ISBTs were first observed [16], there have been many reports on this topic related to large oscillator strength of this process, its large optical nonlinearity and the fast carrier relaxation time [11-16].

Compared to the conventional interband structures, ISBTs based devices have some inherent characteristics such as high attainable material absorption due to the large dipole moment and insensitivity to saturation due to the fast carrier relaxation time. These properties are optimal for EAMs. For instance, the dipole matrix element of ISBTs is normally as large as tens e·Å (electron angstrom, 1 e·Å = 1.6×10^{-29} C·m), which is around the order of quantum well width, while the one of interband

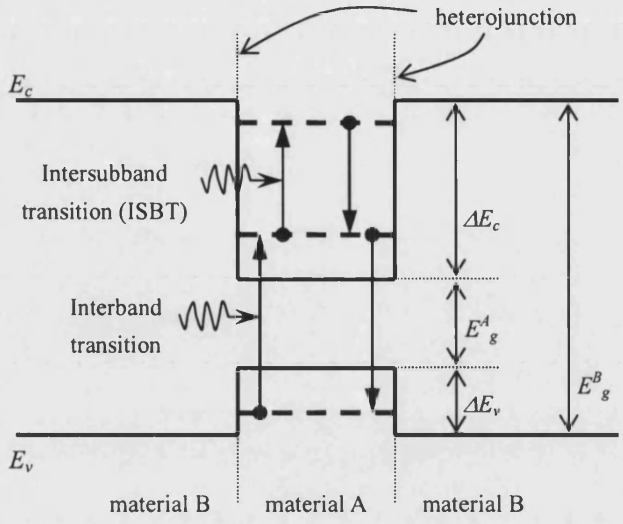

Figure 2.8: Interband and intersubband transitions in a quantum well. The maximum transition energy is mainly determined by the bandgap E_g and the conduction band offset ΔE_c, respectively.

transitions is only a few e·Å (of the order of a lattice width) [80]. The 10~50 times larger dipole matrix element in ISBTs can result in a stronger optical nonlinearity [80,81]. Moreover, unlike the recombination time of interband transitions at nanoseconds, ISBTs have very short nonradiative relaxation time, which makes them very attractive for possible ultra-high speed of elements in high bandwidth fibre optical networks [82]. More details about the advantage of ISBTs will be discussed in Section 2.3.

2.2.2 Various Intersubband Transitions

Different types of ISBT have been utilised to construct novel devices covering a wide range of wavelengths from near-infrared to far-infrared. The different schemes are shown in Fig. 2.9. Transitions between the ground and first excited subband in the conduction band of a quantum well, known as inter-conduction subband transition, are shown in Fig. 2.9 (a). When a very thin well is fabricated, only one subband in the conduction band occurs. The transitions from this subband to the continuum states above the barriers, as shown in Fig. 2.9 (b), are also utilised in

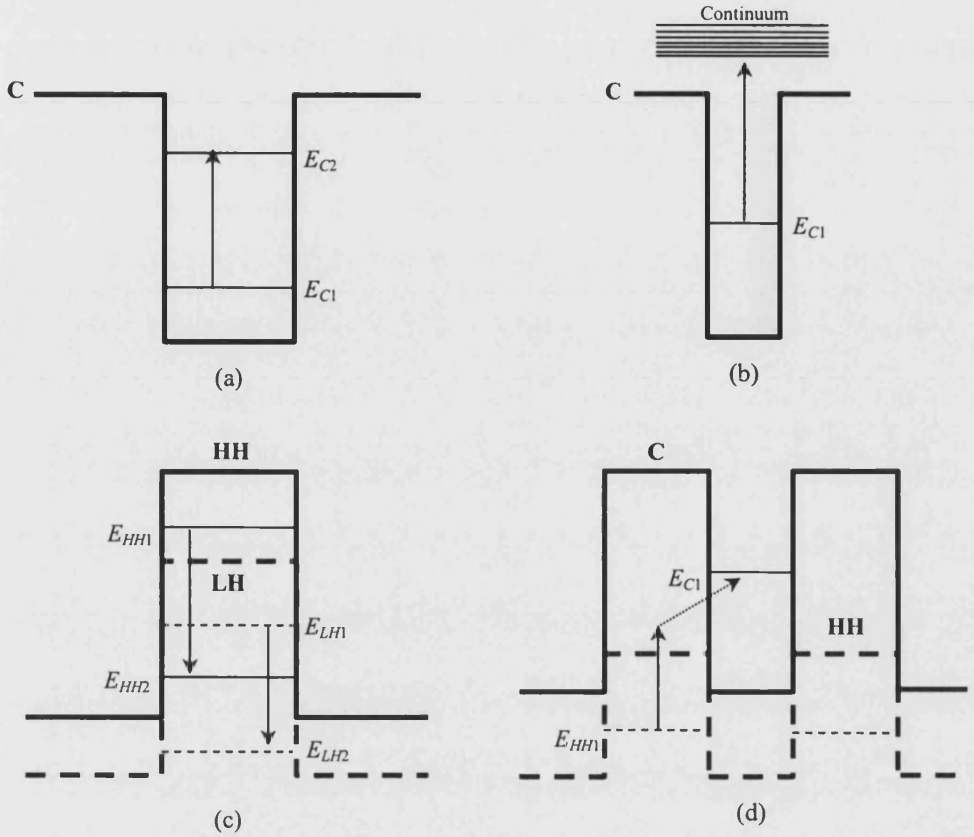

Figure 2.9: Various intersubband transitions: (a) from subband 1 to subband 2 in the conduction band; (b) from subband 1 to continuum states; (c) between hole subbands and (d) indirect transition in real space from hole subband to electron subband in type II quantum wells.

some devices as a means of achieving better collection of photogenerated carriers via the application of an electric field perpendicular to the heterojunction interfaces. In addition, ISBTs between valence bands including heavy hole (HH), light hole (LH) and split-off (SO) bands, such as HH-HH, LH-LH, HH-LH and HH-SO inter-valence subband transitions, are utilised in some laser devices based upon the band-mixing effects and the large effective mass of holes. Two such transitions are illustrated in Fig. 2.9 (c). Indirect transitions from a subband in the valence band to a subband in conduction band may occur in type II quantum wells. Several transitions in type II quantum wells may give rise to absorption and emission. This is illustrated in Fig. 2.9 (d). In this case, the transition is interband rather than intersubband, as it occurs between subbands belonging to the different bands.

Of all these different kinds of intersubband absorption (ISBA), the inter-conduction band absorption process, i.e. the one depicted in Fig. 2.9 (a), which may be alternatively called bound-to-bound transitions, is central to the study in this thesis. In the next chapter, an efficient method of calculation of the absorption coefficient for this process will be presented.

2.2.3 Selection Rules for Intersubband Transitions

As a foregoing statement, optical absorption only occurs between different subbands and therefore at energies given by the differences between the bound states in the well. However, there are limitations of absorption energies and the direction of the incident light in inter-conduction subband absorption, especially in symmetric quantum well structures [16,83]. In a theoretical study, Ahn and Chuang have suggested that ISBTs only occur when the polarisation vector of the incident light has a component perpendicular to heterojunction interfaces [84]. When the incident light is along the epitaxy growth axis, that is along the z-axis for the coordinate system indicated in Fig. 2.10, the polarisation unit vector ($\hat{\varepsilon}_z$) parallel to the heterointerface of the quantum well layer, i.e. $\hat{\varepsilon}_z = 0$, does not interact with electrons in the heterostructure. When light propagates along the layer, the light polarisation can lie either in the x-y plane (TE polarisation), i.e. $\hat{\varepsilon}_z = 0$, so that the light does not interact with the heterostructure, or perpendicular to this plane (TM polarisation), $\hat{\varepsilon}_z = 1$, so that the light is absorbed. Sung *et at* have reported that ISBA only occurred for TM polarisation but not for TE polarised light in their experiment [85]. This gives an explicit polarisation dependence of the ISBT, which is considered as the polarisation selection rule [83].

Another important selection rule follows from the symmetry of the quantum well. The wavefunctions in a symmetric potential well are either symmetric or antisymmetric functions in the direction of the z-axis, corresponding to the parity (the

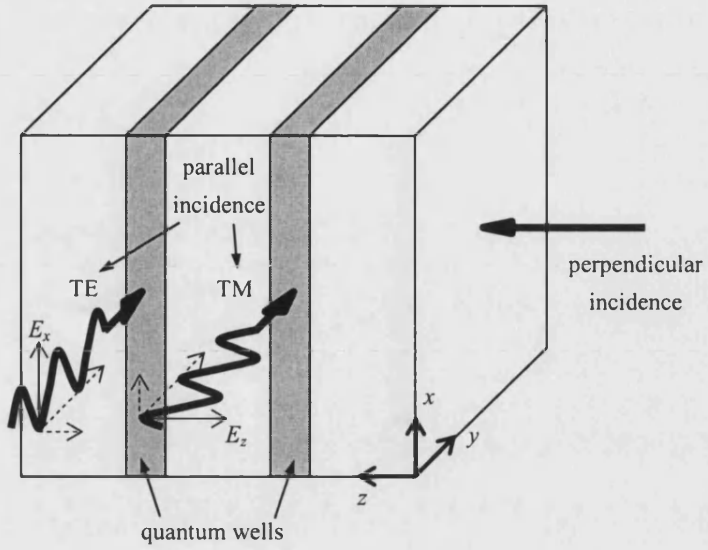

Figure 2.10: Different incident modes for possible photon absorption in the quantum wells.

even or odd quality) of the subscripting index number (n) of the confined state (E_n). The matrix element of optical dipole moment will be zero for transitions between two subbands with the same parity [83]. This is shown in the next chapter. Thus absorption is only permitted between states of different parity. This is called the parity selection rule and governs the transitions observed in optical absorption, irrespective of the polarisation state of the light.

For the simple isotropic band structure, as that is the assumption of III-V semiconductor in this work, both selection rules are essential to the occurrence of ISBA. However, it is important to stress that the selection rules governing the transitions do not hold strictly. For instance, the breakdown of polarisation selection can result from valence band mixing or by the use of anisotropic materials such as Si/SiGe [86-88]. Due to its strong dependence on the symmetry of the potential, the parity selection rule can be overcome by deliberately growing an asymmetric well or by applying bias to tilt the potential profile [15,83,84]. More detailed explanation and discussion of these selection rules will be provided in Chapter 3.

2.3 Advantageous Properties of Intersubband Transitions

2.3.1 Fast Relaxation Time

The foremost advantage of ISBT for optical modulation is the intrinsically ultrafast carrier dynamics. This enables the development of novel ultrafast optical devices which is potentially significant for advancing data rates in optical communication. The understanding of intersubband relaxation mechanism is particularly significant for ultrafast device applications.

At room temperature, the intersubband relaxation process is attributed by the rapid interaction between electrons and longitudinal optical (LO) phonons when the subband separation exceeds the LO-phonon energy [89], e.g. 36 meV for GaAs. This is known as Fröhlich interaction. If the subband separation is less than the LO phonon energy, e.g. in a large well width structure, the relaxation is dominated by the comparatively slow interaction of electrons with longitudinal acoustic phonons [90]. The transition rate for the former interaction (~ps) is about two orders of magnitude faster than that for the latter [91].

For ISBTs around the 1.55 μm communication wavelength (0.8 eV), the subband separation is much higher than the LO phonon energy (normally around 30~90 meV). It has been generally considered that the population relaxation time of ISBTs is determined by a two-step-process, as shown before in Fig. 1.2. First, the electron scatters from the upper subband to the lower subband by means of the interaction with a LO phonon; then the electron cools down to the bottom of lower subband via intrasubband scattering [10,89]. Hence, the overall intersubband relaxation time can be estimated by [10,12]

$$\tau_{\text{total}} = \tau_{\text{inter}} + \frac{E_{\text{ISBT}}}{\eta\omega_{\text{LO}}} \times \tau_{\text{intra}} \tag{2.1}$$

where τ_{inter} is the intersubband scattering time, E_{ISBT} the energy of ISBTs, $\hbar$ Planck's constant divided by 2π and ω_{LO} the angular frequency of the LO phonons.

For the InGaAs/AlAs quantum well structures, the intrasubband relaxation time (τ_{intra}) is ~0.1 ps and the AlAs-like interface mode phonon energy ($\hbar\omega_{LO}$) is ~47 meV [10,92]. The intersubband scattering time can be estimated from the reciprocal of the scattering rate (W). The scattering rate due to Fröhlich interaction of electrons with LO phonons is simplified to an analytical expression based on the perturbing potential approximation and is given by [93,94]

$$W = \frac{1}{2} W_0 \left(\frac{\eta\omega_{LO}}{E_1} \right)^{1/2} \left[\frac{1}{4-(\eta\omega_{LO}/E_1)} + \frac{1}{12-(\eta\omega_{LO}/E_1)} \right] = \frac{1}{\tau_{inter}} \qquad (2.2)$$

where

$$W_0 = \frac{e^2}{4\pi\eta} \left(\frac{2m^*\omega_{LO}}{\eta} \right)^{1/2} \left(\frac{1}{\varepsilon_\infty} - \frac{1}{\varepsilon_s} \right) \qquad (2.3)$$

is the basic rate for Fröhlich interaction, and ε_∞ and ε_s are the optical and the static dielectric permittivities, respectively.

The relaxation time for $In_{0.53}Ga_{0.47}As$/AlAs quantum wells as a function of the intersubband energy is calculated here from Eq.s (2.1), (2.2) and (2.3), and the result is given in Fig. 2.11. Measured results reported by Asano *et al* and Lutgen *et al* for the intersubband relaxation time of 2.7 ps and 1.3 ps for the transition at ~500 meV and ~260 meV, respectively, are also shown in Fig. 2.11 [10,95]. These theoretical results are in good agreement with the experimental results. However, Ghislotti *et al* observed a differential transmission decay of ~10 ps for a transition energy at 680 meV, compared to the overall relaxation time expected about 3.3 ps from the theoretical calculation [96]. They suggested that the longer relaxation time might be caused by the Γ-X coupling and the predominant fast Γ-Γ relaxation process has a decay constant of 6.5 ps.

In addition, for the low doping or undoped structures, the lower energy state can be easily bleached even by a weak input light. The absorption cannot occur until the electrons relax back to the bottom of lower subband. Therefore, the total relaxation time is important and limits the ultimate speed of operation of such structures. On the

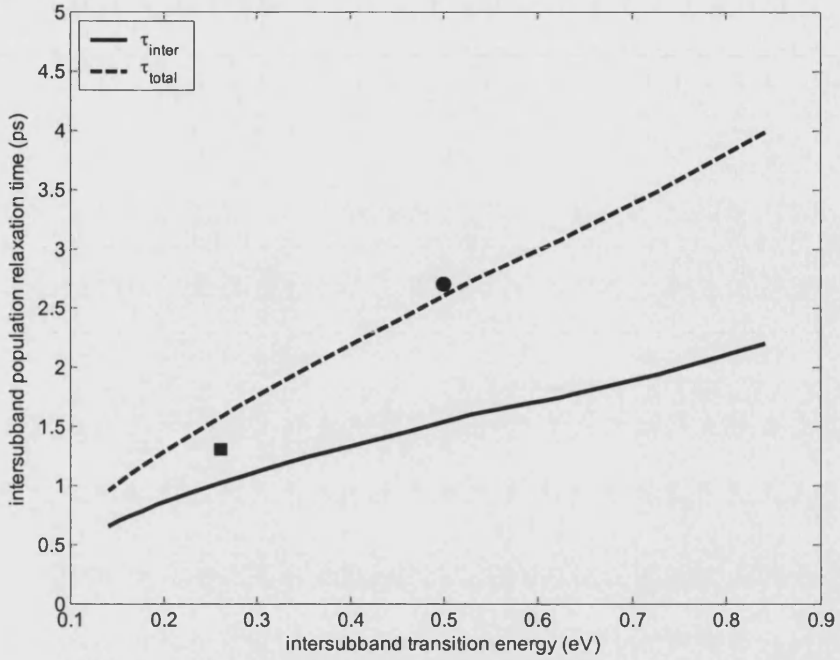

Figure 2.11: The intersubband energy relaxation time as a function of ISBT energy. The solid line represents as a calculation of the intersubband LO phonon scattering time, and the dashed line represents a calculation including both the intersubband scattering time and the intrasubband energy relaxation time. The round and square dots indicate the data adopted from ref [10] and [95], respectively.

other hand, for strongly doped structures, the lower energy state in ISBTs is almost completely occupied by electrons. Once the electron in upper subband is scattered to the lower subband, the absorption can take place. As a consequence, the operation speed of the heavily doped ISBA based modulators is governed essentially by electron intersubbband scattering rate. The theoretical relaxation time of 2.5~4 ps at 0.8 eV (1.55 μm wavelength) ISBT indicates its promise for ultrafast device applications aimed at optical communication system.

Furthermore, extensive measurements have been performed in the intersubband relaxation time for other group III-V semiconductors. Müller *et al* [97] measured the intersubband relaxation time of 14 ps in an undoped GaAs/AlGaAs DQW sample. They also suggested that the relaxation mechanism was associated with the carrier

scattering due to the strong dependence of the intersubband relaxation time on the carrier density. The ISBTs in hole subbands have also caught attention for developing optical devices, such as THz frequency sources. Bezant *et al* observed hole relaxation lifetimes of 20 ps and 55 ps for the LH1 to HH1 transition in GaAs/AlGaAs quantum wells by using pump-probe technique [98]. Tan *et al* have measured the electron intersubband lifetimes as short as 1.8 ps in asymmetric stepped GaAs/AlGaAs quantum structures [99]. Their result also shows that the intersubband lifetimes are related to the construction of quantum well structures.

ISBA recovery times are even shorter in group III-V nitride semiconductors. The relaxation times of carrier are typically of the order of 150~400 fs due to enhanced electron-phonon interaction [12,100,101]. Asano *et al* measured an extremely fast carrier relaxation time (~150 fs) in GaN/AlGaN quantum well structures based on ISBT via femtosecond pump-probe technique [102]. Gan *et al* observed an ultrafast intersubband hole relaxation process less than 350 fs in InGaN MQW laser diodes by using the optical selection rules in the wurtize crystalline structure and pump–probe polarisation configurations [103].

2.3.2 Wide Spectral Wavelength

ISBTs in semiconductor quantum well structures have been attracting significant attention because of the wide range of wavelengths over which their occurrence can be engineered. Inasmuch as ISBTs occur between confined electron levels in semiconductor heterostructures, the transition wavelength can be tailored to almost arbitrary wavelengths by artificially engineering the confinement of electrons, namely by adjusting the width and depth of the quantum wells. In other words, band gaps of conventional semiconductor devices are no longer limiting the design wavelength of a device, offering the possibility of creating a wide range of light sources or detectors using one material system. However, tuning is limited at short wavelengths by the band offset between the well and barrier materials limiting the depths of the wells that can be formed.

Using cubic III-V semiconductors, the shortest achievable wavelength ISBT between the ground and the first excited electronic states that could occur theoretically is the range 1.3~2 μm [104]. In practice, the well depth achievable is limited by the lattice mismatch between alloys of different composition that can be grown by one of the established epitaxial growth techniques like MOCVD or MBE [30-37]. However, in recent years, progress in the development of semiconductor heterostructures with large conduction-band discontinuity has enabled near-infrared ISBT in the optical-communication wavelength band (1.3~1.55 μm) in various material systems such as InGaAs/AlAsSb/AlSb and GaN/AlGaN/AlN quantum wells [11-13,17,25,85]. This has opened the possibility for optical devices that are significantly faster than conventional interband optical devices operating at telecommunication wavelength.

Photodetectors operating in the mid- to far-infrared region have usually been based on the interband transitions in InAs/GaAs, InSb or HgCdTe [105,106]. However, in recent years, photodetectors based on electron and hole ISBTs in MQWs and SLs have been studied widely because of the greater flexibility in the design of operating wavelength compared to those based on interband transitions. The intersubband technology in the mid-infrared has been highly developed, especially operating in the 3~5 and 8~12 μm wavelength ranges which have wide ranging applications including thermal imaging [107], medical imaging and remote temperature sensing [108]. Photodetection in the far-infrared wavelength region using ISBT has also attracted interest. The longest wavelength could be up to several hundred microns [109], where a wide range of applications include astrophysics, trace gas analysis and industrial process control [110,111]. The operation of quantum cascade lasers has been investigated and demonstrated in the far-infrared region, extending the operating range of these unipolar semiconductor lasers from 10 μm up to 88 μm [112-114]. To date, there has been very little work focusing on devices operating by ISBTs at the telecommunication wavelengths owing in part to limitations in materials technology. This is discussed in more detail in the next section.

2.4 Advances in Intersubband Transitions

The rapid development of the field in ISBTs is the result of a combination of novel physics ideas, new techniques for epitaxial growth to implement them and applications in electronics and optoelectronics based on those concepts. Photonic devices based on ISBT in quantum wells, such as quantum cascade lasers and quantum well infrared photodetectors, are among the examples of very successful applications.

2.4.1 Quantum Cascade Lasers

Quantum cascade lasers (QCLs) are one of the key devices based on ISBTs. They were predicted theoretically in 1970s by Kazarinov and Suris [115,116] and first realized experimentally in 1994 by Faist *et al* [18]. QCLs are unipolar intersubband devices which work on transitions between the first excited and the ground state in quantum well, as illustrated in Fig. 2.12. A typical structure is made up of periodic repetitions of two sections, one acting as injector-collector region, the other as active region. There are three important confined levels in the active region and are marked in the figure by 1,2 and 3. Each of the confined states originates from one of the wells. To create a population inversion between two confined states, one needs to provide for electron injection into a higher lasing state and depletion of a lower lasing state. Under a voltage bias, the potential in the doped region is almost flat. From the injector region, the electrons are injected into the upper laser energy level (level 3 in Fig. 2.12) of the active section. Here population inversion occurs and the laser transition takes place primarily to level 2. After that, the electrons lose energy via a non-radiative transition (between level 2 and 1 in Fig. 2.12). After undergoing lasing transitions in QCL, the electrons remain inside the conduction band and enter the next stage by tunnelling through to next active region due to the applied electric field. Then the processes are repeated in each subsequent period of the superlattice. A number of such cascade processes multiple photons are generated by single electron, which provides a high quantum efficiency of QCLs.

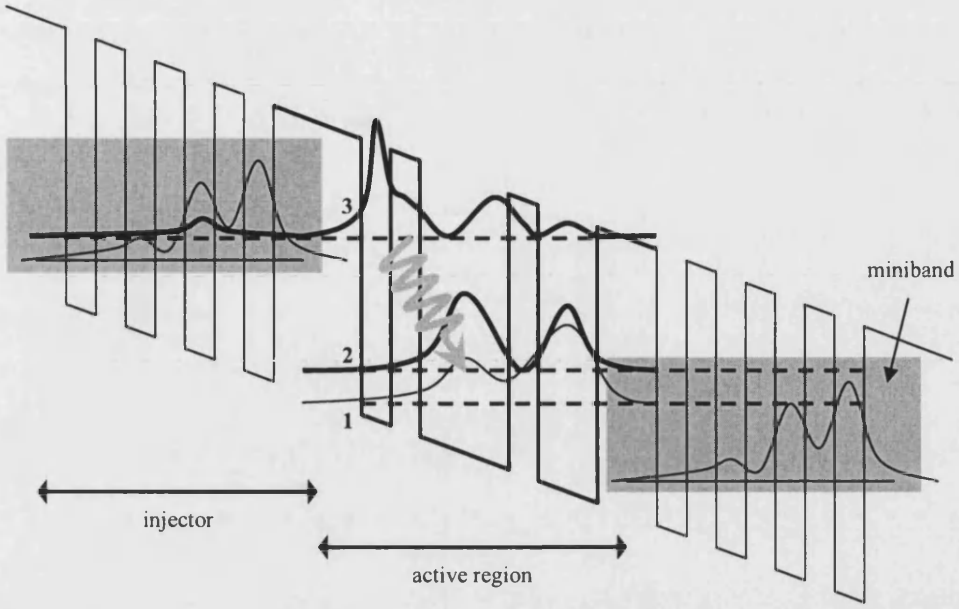

Figure 2.12: Schematic conduction band profile of a portion of a typical quantum-cascade-laser-structure. The wavy arrow indicates the transition responsible for the laser action. The solid curves represent the relevant wavefunctions.

Following these pioneering studies, the development of QCLs has been rapid. Firstly, QCLs have been realized in InP-based InGaAs/InAlAs and GaAs-based GaAs/AlGaAs multiple layer structures and these devices have become the source of choice in the mid-infrared wavelength range (3~20 μm) [117,118]. Recently, room temperature, continuous wave operation in QCLs grown by MBE has been demonstrated [119], and further improvements at high temperature have followed [120]. Laser action in the terahertz range (λ = 66 μm) has also been demonstrated [121].

2.4.2 Quantum Well Infrared Photodetectors

The most established intersubband technology is probably the quantum well infrared photodetector (QWIP) for detecting, measuring and imaging the patterns of thermal heat radiation emitted by objects. As the device most resembling the proposed ISBA optical modulator in terms of operating principle, the following review of QWIPs has much relevance to the research of EAMs described in this thesis.

The QWIP was first demonstrated by Levine *et al* in 1987 [122]. In most QWIP devices, a signal is generated when a quantum well absorbs infrared radiation. This excites electrons from the ground state to an excited state from which the excited electron is collected by an applied field, resulting in photocurrent, as shown in Fig. 2.13. ISBA and QWIPs for long wavelength applications have been investigated theoretically and experimentally [105,122,123]. The QWIP could be competitive with conventional detectors based on the interband transitions [105]. QWIPs have been designed based on transitions in the valence band as well as conduction band in MQWs and SLs. In general, QWIPs based on electron transitions show greater detectivity compared to the hole-based photodetectors. One of the reasons for this advantage is their lighter effective mass [123].

In addition, QWIPs are suitable for multicolour detection because their absorption wavelength can be tailored by varying device and material parameters and their intrinsic absorption line shape is narrow. QWIPs with two stacks of quantum wells, each designed to detect a different wavelength by varying the well width and depth, are the simplest two-colour detectors [124]. A four-colour QWIP has been demonstrated [125]. Four stacks of quantum well structures with four different detection wavelengths are sandwiched between three highly doped contact layers.

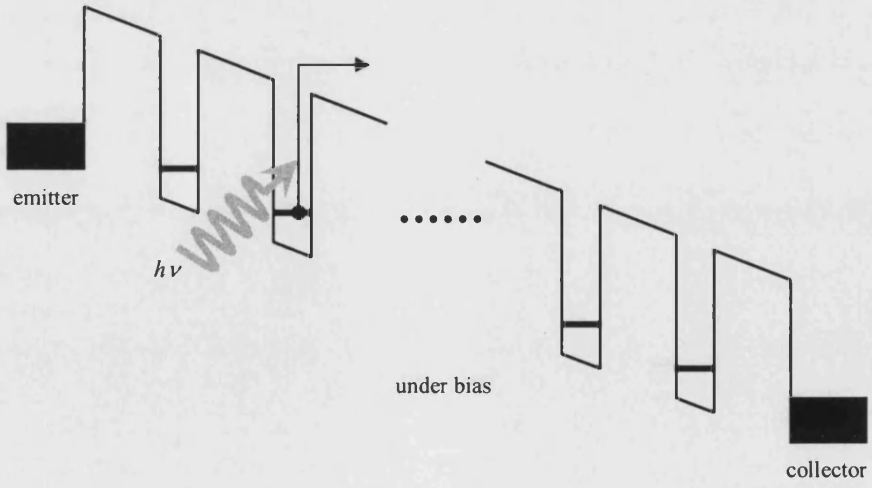

Figure 2.13: Schematic potential profile for QWIPs.

Peak detection wavelengths of this device are centred at 4.7, 8.5, 9, and 12.3 μm, respectively, and the peak detection wavelength can be tuned by the applied bias [125]. Since the polarisation dependence of the absorption process effectively requires light propagation parallel to the quantum well interfaces, the device sensitivity (responsivity) is not limited by the number of the quantum wells, but by the device length and optical confinement factor of the lightwave to the quantum well stacks.

2.4.3 Optical Modulators

Devices based on ISBTs in quantum wells have received considerable attention in the last few decades. However, most of the work has been devoted to lasers and detectors as specified in previous sections. Several types of ISBT based electro-optical modulators have been proposed and demonstrated [126,127]. For instance, one modulator concept is based on ISBA and a linear Stark shift. The strong ISBA is ensured by having a high doping density in the quantum wells, and the large linear Stark shift under an applied DC field is facilitated by using asymmetrical quantum wells which can be either in the form of a step quantum well or double quantum well with different well widths [128,129]. The modulation is achieved by adjusting the applied field to shift certain peak energies of the absorption spectra. In addition, another type of modulator is based on quantum interference that occurs between nearly resonant transitions in coupled quantum wells and can be used for modulating the light, known as the quantum interference modulator. This is because the oscillator strengths of the transitions from the two resonant states to a third state vary significantly and the change in oscillator strength consequently result in absorption that can be used for modulation.

Moreover, the EAMs which are often used in transmitters in optical fibre communications or to control the intensity of a laser beam via an electric voltage have been developed. Since the ISBA based devices have high attainable material absorption due to the large dipole moment and an inherent insensitivity to saturation

due to the fast carrier relaxation time, this enables the potential applications as EAMs. In semiconductor phase or intensity modulators the optical waveguide structure is normally a *p-n* or *p-i-n* waveguide. A ridge waveguide and a cross-sectional view of the waveguide with the expected electromagnetic field distribution are shown in Fig. 2.14. ISBA based modulators can also have an *n-n-n* structure in which a symmetrical applied voltage swing around zero bias is feasible in order to reduce the driving voltage for achieving high speed modulators [129].

The operation of an EAM is based on a change of the absorption spectrum caused by an applied electric field. When an external bias voltage is applied through the quantum-well region using a diode structure, the bias field almost totally appears in the depletion layer, where the optical mode is confined. The potential profiles are tilted and the positions of the quantised subbands are shifted. Therefore, the density of electrons confined in the wells is modified and consequently the carrier-related absorption spectrum is changed as the probability of an upward transition decreases. For achieving a high extinction ratio, the Stark effect in a quantum well structure is usually exploited.

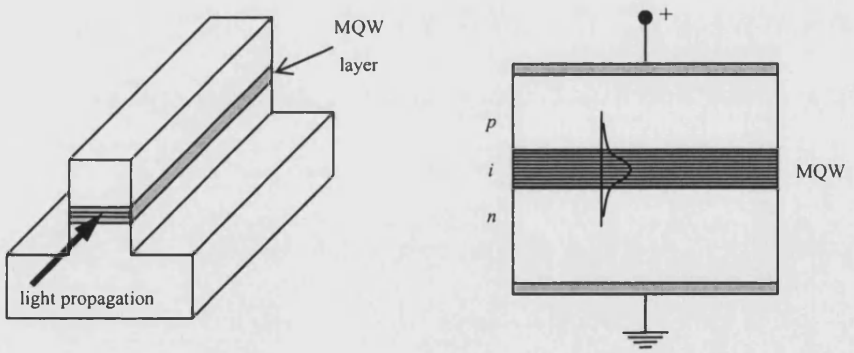

Figure 2.14: Typical quantum structures used for phase or intensity modulation: (a) a ridge waveguide and (b) cross-sectional view with optical field distribution indicated.

However, in actual EAMs or modulation doped heterojunctions, as mentioned in Section 2.1.2, the electron density and the potential profile are modified by the external bias in a very complicated way. Owing to the modulation doping, a 2DEG exists and this is altered by an external bias. The electric field in the depletion region is modified by the applied bias and the electron charge distribution. The charge distribution in turn is determined by the existing field. Therefore, the external bias, the applied electric field and the charge distribution are interactional. This problem can be solved by self-consistent modelling using the techniques described in the next chapter.

2.4.4 New Materials

With the conventional materials used for semiconductor optical devices, such as AlGaAs/GaAs, it is difficult to find a suitable material system for heterostructures in which the conduction band offset is large enough to accommodate ISBTs compatible with the optical communication wavelength band at 1.55 μm (0.8 eV). For the InGaAs/InAlAs system lattice-matched to InP, the conduction band offset is only about 0.5 eV. Therefore, the development of innovative semiconductor materials or highly strained InGaAs/InAlAs/InP is crucial to this prospective technology.

ISBTs at 1.55 μm wavelength have been demonstrated in a number of materials during the last couple of years. One of the most suitable systems is InGaAs/AlAsSb which can have a large conduction band offset of 1.75 eV. Mozume *et al* reported 1.45 μm wavelength ISBT in 2.0 nm-thick $In_{0.53}Ga_{0.47}As/AlAs_{0.56}Sb_{0.44}$ quantum wells grown lattice matched to InP substrates by using MBE [25]. Recently, InGaAs/AlAsSb has allowed the observation of ISBTs as short as 1.3 μm in 30-Å-wide quantum wells and an ultra-fast absorption recovery time of 685 fs at 1.55 μm was reported in coupled DQWs [11,130]. Recent publications have shown that short wavelength ISBTs in InGaAs/AlGaAs quantum wells can be achieved where room-temperature diode lasers are available [131]. These results show the potential of this material system for the ultra-high speed optical devices based on ISBA for use

in optical communication networks. However, the growth of these material systems requires further development.

GaN/AlGaN has drawn attention as another potential material system for the fabrication of devices based on ISBTs at communication wavelength because of their large conduction band offset (~2.0 eV) and large difference of refractive index between GaN and AlN [132]. The large refractive index step can result in optical waveguide devices with strong confinement of the optical field to the active region. Gmachl *et al* measured optical ISBA in structures specifically designed for 1.7 and 1.55 μm wavelengths [133,134]. In addition, the nitride semiconductor has very fast carrier dynamics. The relaxation times of carrier are typically of the order of 150~400 fs due to enhanced electron-phonon interaction [12,100,101]. These fast relaxation processes could provide the basis for optical modulators that are very resistant to absorption saturation (device operation at optical powers up to ~100 mW). However, growing device structures based on the GaN/AlGaN system for ISBT is challenging due to the lack of a lattice-matched substrate and the large lattice mismatch between GaN and AlGaN. Difficulties in doping AlN and the often unsatisfactory crystalline quality make achieving near infrared ISBTs [133,135] difficult.

Other material systems with potential for ISBT switch applications include II–VI semiconductors such as ZnSe/BeTe and CdS/BeTe. These heterostructures have a huge conduction band-offsets of ~2.3 eV for the former and ~3.1 eV for the latter [136-138]. These material systems can be grown with high structure quality on GaAs substrates by MBE, since both ZnSe and BeTe are closely lattice matched to the substrate. Strong ISBA at the wavelength of 1.55μm has been demonstrated by a 40-period (CdS/ZnSe)/BeTe quantum well [137]. Besides, the benefit from the huge conduction band offset the ZnSe/BeTe system has the advantage of its higher ionicity in ZnSe layers. Relaxation times monitored on a variety of (CdS/ZnSe)/BeTe quantum wells have indicated that ultrafast recovery times of ~1 ps without

exhibiting slow tail are achieved in the wavelength range of 1.8~2.2 μm [138].

Highly strained III-V semiconductors have also caught attention. A systematic study in very narrow InGaAs/AlAs quantum wells has shown that ISBT at wavelengths less than 2 μm is possible [94]. InGaAs/AlAs heterostructures have been drawing much attention as a key material system to the short wavelength ISBT. More recently, a near-infrared wavelength (1.55 μm) ISBT in $In_{0.53}Ga_{0.47}As$/ AlAs single quantum well on an InP substrate with a well width of 3 monolayers (MLs) has been reported by Smet *et al* [139]. However, the lattice mismatch between AlAs and the InP substrate is as large as 3.7%. It limits the thickness of AlAs barrier layer (≤10 ML) and number of quantum wells (≤10 periods) that can be grown without significant formation of misfit dislocations arising from exceeding the critical thickness of highly strained epitaxial layers [140]. This limitation can be avoided with a novel growth technique of growing an InGaAs buffer layer on a GaAs substrate because AlAs lattice matches close to GaAs. An ISBT wavelength of 1.90 μm in 7-ML-wide InGaAs/AlAs multiple quantum wells grown coherently on a semi-insulating GaAs substrate [141]. In this material system, the AlAs barrier layer can be thick enough and the growth of several periods of quantum wells is much easier to achieve.

2.5 Summary

In this chapter, the background and basic physical concepts of heterostructures have been discussed. The principal features of electrons in different quantum structures were reviewed. The properties of the heterostructures associated with practical devices were considered and the quantum-mechanical behaviour was stressed. The optical transitions in quantum well structures were then analysed with emphasis on ISBTs. The relaxation time of ISBTs has been theoretically estimated. The advantages of ISBTs were reviewed and it was shown that ISBTs make possible innovation and improvement in optoelectronic technologies. Finally, addition

information on advancing the study of ISBT, including two important applications to optical devices and new material for improving the ISBT performance, was reviewed.

From this review, several conclusions can be drawn regarding the proposed application of ISBT to optical modulation at 1.55 μm wavelength. First, the review of the literature reveals the concept is novel. Next such an innovation is dependent on the emerging materials technologies described in section 2.4.4. This combination of device innovation and reliance on advance in epitaxial growth technology creates a need for detailed device modelling to establish the technological requirements for feasibility. Finally since doping must be incorporated into the device structure and bias voltage applied, local variation in the electrostatic potential on the scale of the quantum wells must be expected. This in turn will influence the wavefunctions and occupancy of the confined particle states and hence optical absorption. This gives rise to a need for fully self-consistent solution of the coupled Poisson and Schrödinger equations. The next chapter describes the methods of such a calculation and other theoretical issues underpinning the modelling of ISBA and its potential application to a new type of optical modulator.

Theory and Modelling of Intersubband Absorption in Quantum Wells

CHAPTER 3

3.1 Introduction

In recent years there has been great interest in studying the optical and electrical properties of quantum structures utilizing intersubband transitions (ISBTs). In a device operating by ISBT, free carriers are required, and consequently, the structures are usually doped [142]. Many novel devices of interest involve single or coupled quantum wells and narrow regions of very heavy doping, so call δ-doping [143]. The rapid fluctuations in local charge density that occur in such structures give rise to correspondingly more rapid fluctuations in the electron potential. It has led to investigations of the effects of the doping and the electric field on the electrooptical properties of quantum well structures [144,145]. Therefore, for determining the electroabsorption spectra of these quantum well samples, the influence of doping and applied bias on electrostatic potential, electric field distribution and carrier concentration needs to be considered.

To model the effects of quantum confinement in such conditions, a self-consistent solution, which solves the Schrödinger equation for the wavefunctions and energy levels, and Poisson's equation for the electrostatic potential simultaneously, is required [63-66,146-148]. This solution provides calculations of the bound state energies (eigen values), the carrier wavefunctions (eigen functions), and carrier concentrations in the presence of confining potential variations. The self-consistent calculation is a well established technique and has been reported for a range of different structures. For instance, it has been widely used for modelling the 2DEG in HFETs [64-66,149]. It has been applied to calculate the subband structure and optical gain spectrum of a type-II quantum well laser by Liu *et al* [150] and the theoretical results of the modal gain of the quantum well laser showed a good agreement with the experimental data. It can also be used to estimate the charge control behaviour of a range of quantum well devices. Ramsteiner *et al* [151] have investigated the dependence of doping level on the depolarization shift of the absorption peak in GaAs/AlGaAs ISBTs. Ozturk *et al* [148,152] have theoretically studied the

energy-level structure in *n*-type δ-doped quantum wells in Si, for investigating the physics at extremely high doping density.

In this thesis, the theoretical investigation of ISBT in the presence of the internal forces due to the lattice as well as external forces due to applied voltage is primarily concerned with structures of the type shown in Fig. 3.1 (a). This assumed InP intrinsic-*n*-type (*i-n*) junction consists of an assumed Schottky contact at the surface, an intrinsic layer usually undoped or unintentionally doped to a very low level (n^-), and then a thick heavily doped *n*-type layer. The $In_xGa_{1-x}As$/AlAs quantum wells are embedded in the centre of the intrinsic region. The Schottky contact is assumed to simplify the modelling of the related effects of charge control and electric field distribution on intersubband absorption (ISBA).

The extension of the results to heterojunction *p-i-n* waveguide structures is straightforward as can be seen in Fig. 3.1 (b). The only requirement is to add the band edge variation with distance over the range $z \leq 0$ and then add this to the surface potential of the equivalent Schottky contact structure. With the electric field strength of potential known at $z = 0$, the band bending for $z < 0$ can be found by re-applying the procedure for solving Poisson equation under the assumption of no current flow. In the respect of ISBA-based modulators, *n*-i-*n* or *n*-n^--*n* type structures are widely used and therefore a symmetrical applied voltage around zero bias swing is feasible [129]. This is an advantage since lower driving voltages are achievable compared to the conventional *p-i-n* structure used for interband modulators which usually require a reverse bias. Hence, modelling the *i-n* region is important, as there can be different options for the capping layer.

The effects on the intersubband absorption coefficient of changing doping densities and the position of the doped regions, applying bias voltage, the quantum well parameters (width, depth and separation) and the number of wells in the structure

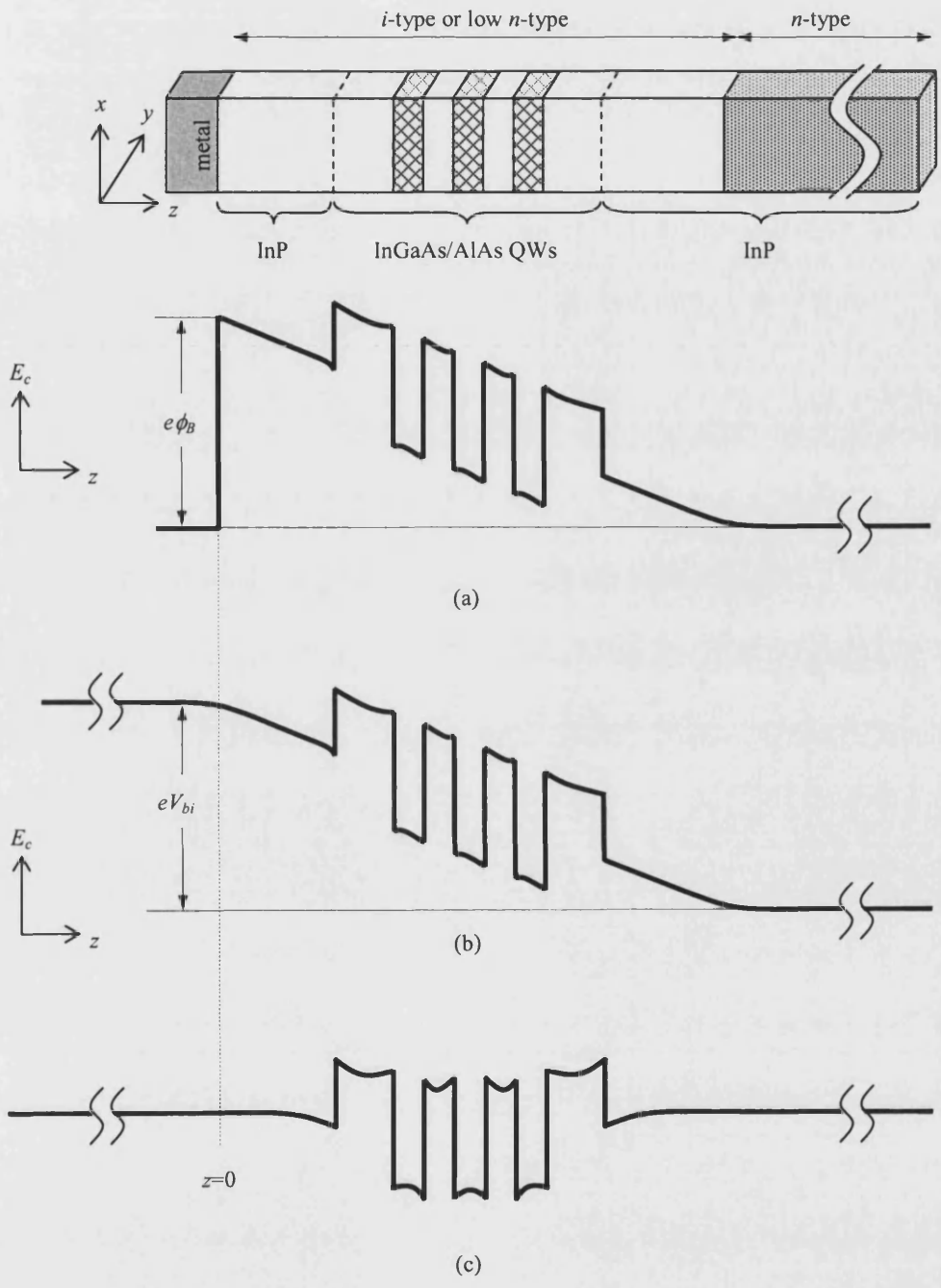

Figure 3.1: Schematic real space picture of (a) an InP *i-n* heterojunction with Schottky contact at the surface and its conduction band edge variation with position, where ϕ_B is the work function of the Schottky barrier height, (b) conduction band edge variation in a *p-i-n* junction, where V_{bi} is the built-in potential and (c) conduction band edge variation in a *n-i-n* junction. The InGaAs/AlAs quantum wells are embedded in the centre of the intrinsic region of the diodes.

were investigated. The model attempts to present a realistic description of the energy band structure of the quantum well including the influence of electric field and doping by solving Poisson equation. These band edge profile calculations are fundamental to this study and provide the framework necessary for the understanding and optimisation of the novel ISBT structures. The nature and interaction of subbands, which are calculated from Schrödinger equation according to the band structure, directly influence the optical properties of quantum well devices. Thus, an accurate modelling of quantum well structure ensures a precise and versatile way of determining the electroabsorption between different electron eigen states. In this chapter the basic physics necessary to describe the intersubbband transition in quantum wells is presented.

3.2 Schrödinger Equation for Quantum Well Structures

In dealing with quantum-mechanical systems, one aims to determine the wavefunction of a single electron or that of the whole system. The wavefunction in quantum mechanics is sufficient to describe a particle or even a system of particles. In other words, if the wavefunction of an electron system is determined, in principle, all macroscopic parameters that define the electronic performance of the device can be calculated.

3.2.1 Schrödinger Equation

The wavefunction Ψ of an electron or an electron system satisfies the principal equation of quantum mechanics, the Schrödinger equation [4],

$$\mathbf{H}\Psi(\mathbf{r},t) = i\eta\frac{\partial}{\partial t}\Psi(\mathbf{r},t) \tag{3.1}$$

where $\hbar = h/2\pi$ (h is Planck's constant, $h = 6.626\times10^{-34}$ J·s) and $\mathbf{H}$ is the Hamiltonian operator in the quantum mechanics system,

$$\mathbf{H} = -\frac{\eta^2}{2m}\nabla^2 + U(\mathbf{r},t) \tag{3.2}$$

In Eq. (3.2), the first term on the right hand side is the operator of the kinetic energy with the Laplacian operator ($\nabla^2 = \frac{\partial^2}{\partial x^2} + \frac{\partial^2}{\partial y^2} + \frac{\partial^2}{\partial z^2}$), m is the mass of the particle and $U(\mathbf{r},t)$ is the potential energy. $\Psi^*\Psi dV = |\Psi|^2 dV$ is to be identified as the probability that the particle will be found in the spatial volume element dV. Moreover, the wavefunctions are normalised over the whole volume V of the crystal,

$$\int_V \Psi^*(\mathbf{r},t)\cdot\Psi(\mathbf{r},t)dV = 1 \tag{3.3}$$

that is, the probability of finding the particle in the whole space is unity.

If $U(\mathbf{r})$ is time independent, one may separate the dependences of wavefunctions on the time and spatial coordinates as follows,

$$\Psi(\mathbf{r},t) = e^{-iEt/\eta}\phi(\mathbf{r}) \tag{3.4}$$

where $\phi(\mathbf{r})$ is a wavefunction of only spatial coordinates and E is the energy of a particle or of a system of particles. Since the complex modulus (magnitude) of the time coordinate is 1, the time-independent wavefunction $\phi(\mathbf{r})$ is also normalised, i.e. $\int_V \phi^*(\mathbf{r})\cdot\phi(\mathbf{r})dV = 1$. Substituting Eq. (3.4) into Eq. (3.1), results in the time-independent Schrödinger equation,

$$\left[-\frac{\eta^2}{2m}\nabla^2 + U(\mathbf{r})\right]\phi(\mathbf{r}) = E\phi(\mathbf{r}) \tag{3.5}$$

The solution of Eq. (3.5) may be in terms of quantized energy levels E_n with corresponding wavefunction $\phi_n(\mathbf{r})$ where n denotes the band index.

Further, a semiconductor crystal can be imagined as a set of ions located in the periodically arranged sites. A time-independent periodic potential $U(\mathbf{r}) = U(\mathbf{R}+\mathbf{r})$, therefore, is present and derives from the periodic Coulombic force of attraction arising from the ion cores experienced by a free electron within the semiconductor ($\mathbf{R}$ is a vector of the Bravais lattice, $\mathbf{R}=n_1\mathbf{a}_1+n_2\mathbf{a}_2+n_3\mathbf{a}_3$, $\mathbf{a}_1$,$\mathbf{a}_2$ and $\mathbf{a}_3$ are the lattice

vectors, n_1,n_2 and n_3 are integers). If $\phi(\mathbf{r})$ describes an electron moving in the crystal, $\phi(\mathbf{R}+\mathbf{r})$ will also be a solution to Eq. (3.5). Thus, $\phi(\mathbf{R}+\mathbf{r})$ will differ from $\phi(\mathbf{r})$ at most by a constant. The wavefunction can be expressed as a Bloch function due to this periodic potential $U(\mathbf{r})$ [153-155]

$$\phi_{n\mathbf{k}}(\mathbf{r}) = \frac{1}{\sqrt{V}} u_{n\mathbf{k}}(\mathbf{r}) e^{i\mathbf{k}\cdot\mathbf{r}} \tag{3.6}$$

where $1/\sqrt{V}$ is the normalising constant, n refers to the band index and $\mathbf{k}$ is a Bloch wavevector of the electron in the first Brillouin zone. The wavefunction $\phi_{n\mathbf{k}}(\mathbf{r})$ is usually called the Bloch function. $u_{n\mathbf{k}}(\mathbf{r})$ corresponds to the cell periodic part of the wavefunction which obeys the Bloch condition given by,

$$u_{n\mathbf{k}}(\mathbf{r}+\mathbf{R}) = u_{n\mathbf{k}}(\mathbf{r}) \tag{3.7}$$

3.2.2 The One-Electron Schrödinger Equation

In order to fully understand the optical and electronic properties of semiconductors, the behaviour of the electrons and holes needs to be described. This is fundamentally a very complicated problem and it is impractical to characterize each particle since there are ~10^{23} electrons/cm^3, all interacting with each other and with the numerous phonons which are the quanta of the lattice vibrations. However, most of the quantum phenomena can be described using a one-electron description, where the problem of the electron motion is simplified as if the electron is under some average potential due to the vibration of the lattice and the repulsive force of other particles in the system [44,154]. Physically measurable quantities, such as charge density, are then calculated by computing an appropriate statistical average over many electrons [44].

Quantum mechanically, the dynamics of an individual electron, which can be deduced from Eq. (3.1), is described by the one-electron Schrödinger equation,

$$i\eta\frac{\partial}{\partial t}\Psi_0(\mathbf{r},t)+\left[\frac{\eta^2}{2m_0}\nabla^2-U(\mathbf{r},t)\right]\Psi_0(\mathbf{r},t)=0 \qquad (3.8)$$

where m_0 is free electron mass (m_0 = 9.109×10^{-31} kg) and $\Psi_0(\mathbf{r},t)$ is called the wavefunction for the single electron. The wavefunction Ψ_0 is a complex quantity whose squared magnitude is proportional to the probability of finding the electron at a point in space ($\mathbf{r}$) at an instant of time (t). If the probability density $\Psi_0^* \cdot \Psi_0$ of a large number of electrons is summed, for example, one can interpret the result as the electron density. It will be noted that this one-electron description based on Eq. (3.8) is really an approximation to the far more complex dynamics of the multi-particle system of interacting electrons and phonons. The many-particle system will be explored later in this chapter and the comparison and relationship between these two systems will be discussed.

3.2.3 Effective Mass Equation

The effective mass equation, or also known as envelope function approximation, forms the foundation for much of semiconductor and device analysis. It was first suggested by Wannier [27] and elaborated on by Slater [28]. Later, a rigorous development of the equation and an extension to multiple bands was given by Luttinger *et al* [29]. One of the most substantial simplifications that has been made throughout the foregoing research is to assume that the band structure of the crystalline semiconductors can largely be ignored, retaining only the energy and effective mass at the extremity of each band. A spherical effective mass or an isotropic mass approximation, for example, is commonly used for electrons with energies close to the bottom of the conduction band $E_c(0)$ with wavevector $\mathbf{k}$,

$$E(\mathbf{k}) \approx E_c(0)+\frac{\eta^2}{2m^*}(k_x^2+k_y^2+k_z^2) \qquad (3.9)$$

where m^* is the effective mass.

The effective mass approach, which is extremely general, has proved to be a valuable

tool for studying electron devices by treating the problem of a crystal in a slowly varying external potential, $V_{ext}(\mathbf{r})$, which is superimposed on the lattice potential $U(\mathbf{r})$ [156-158]. Under this assumption, the wavefunction is a product of the slowly varying envelope function and the Bloch function of the local extremum in the host's band structure. Instead of solving the full Hamiltonian, including the ion cores, the valence and core electrons, and the external potential, one can solve a reduced Hamiltonian that includes only the band structure $E(\mathbf{k})$ and the external potential. The result is [28,29]

$$i\eta\frac{\partial}{\partial t}\psi(\mathbf{r},t)=[E(-i\nabla)+V_{ext}(\mathbf{r},t)]\psi(\mathbf{r},t) \tag{3.10}$$

where $E(-i\nabla)$ is the kinetic energy term. $E(-i\nabla)$ is further simplified to the second-order Taylor polynomial by substituting the operator $-i\nabla$ for the wave vector $\mathbf{k}$ in the energy-wave vector dispersion relationship $E(\mathbf{k})$ at Eq. (3.9), that is $E(-i\nabla)\approx E_c(0)-\frac{\eta^2}{2m^*}\nabla^2$. As a result, an equation similar to Schrödinger equation is obtained but in which the effective-mass m^* has replaced the free electron mass m_0. The result is,

$$i\eta\frac{\partial}{\partial t}\psi(\mathbf{r},t)=-\frac{\eta^2}{2m^*}\nabla^2\psi(\mathbf{r},t)+V_p(\mathbf{r},t)\psi(\mathbf{r},t) \tag{3.11}$$

where $V_p=E_C(0)+V_{ext}(\mathbf{r},t)$ is the interaction potential energy. The wavefunction $\psi(\mathbf{r},t)$ appearing in the effective mass equation is often called an envelope wavefunction, as it describes the behaviour of an electron over a volume much larger than the crystal unit cell.

Apart from the substitution of the effective mass m^*, which is measured from the bottom of the conduction band as clarified in Eq. (3.9), for the free electron mass m_0, Eq. (3.11) is mathematically identical to the one-electron Schrödinger equation (3.8). Note m^* should be considered as a material property that is analogous to the dielectric constant. The effective mass approximation has simplified the motion of an

electron in a periodic system of ion centres.

It should be noted that the effective mass equation does not give good results for high-energy electrons which are equivalent to the observation that the bands become quite nonparabolic for large values of the wavevector **k**. Detailed study of this will be given in Section 3.7. Overall this approximation has been widely shown to describe with good accuracy the behaviour of electrons in semiconductor quantum wells. This is the justification for applying many of the formulas derived for the quantum mechanics of free particles directly to conduction band electrons by making the simple replacement of the free electron mass m_0 by the effective conduction band electron mass m^*.

3.2.4 Many-Particle Systems

Although any semiconductor material consists of numerous electrons, holes, ions, etc., the major electrical and optical properties of semiconductor devices are generally determined by the electron subsystem. The features in many-electron subsystems that are absent in the classical description of the quantum physics are associated with the fact that particles are identical and that specifying and tracing the coordinates of a given electron are impractical. One approximation is to separate the electron subsystem and the lattice vibrations and consider them to be only weakly coupled. In the spirit of this approach, a many-electron subsystem which takes into account its interaction with the lattice vibrations needs to be studied. This is especially true, given that the structures considered in this work involve many electrons occupying the subbands of a quantum well structure.

The basic equations of quantum mechanics can be generalized to account for the behaviour of electrons in solids. An overview is presented here. Instead of the one-particle wavefunction $\Psi(\mathbf{r},t)$, a many-electron wavefunction is introduced to describe the system. This takes the form

$$\Phi(\mathbf{r}_1,\mathbf{r}_2,\mathbf{r}_3,...,\mathbf{r}_n,t) \tag{3.12}$$

where $\mathbf{r}_1$, $\mathbf{r}_2$, ..., $\mathbf{r}_n$ is the set of position vectors of the N electrons comprising the subsystem. Under the time-independent periodical potential assumption, the time-dependent wavefunction of the many-particle system in Eq. (3.12) can first be factorized by an exponential prefactor to define a time-independent wavefunction, φ, such that

$$\Phi = e^{-iEt/\eta}\varphi(\mathbf{r}_1,\mathbf{r}_2,\mathbf{r}_3,...,\mathbf{r}_n) \tag{3.13}$$

where E is the total energy of the many-particle system in a stationary state. In this stationary case, the time-independent function φ is determined by solving the many-particle Schrödinger equation,

$$H^{mp}\varphi(\mathbf{r}_1,\mathbf{r}_2,\mathbf{r}_3,...,\mathbf{r}_n) = E\varphi(\mathbf{r}_1,\mathbf{r}_2,\mathbf{r}_3,...,\mathbf{r}_n) \tag{3.14}$$

where H^{mp} is the many-particle Hamiltonian with superscript *mp*. In the simplest form, the electrons are assumed to be a set of single, non-interacting electrons, i.e. there is no Coulomb interaction between the electrons. Each electron is treated as individual and independent of the other electrons. Therefore, the many-electron Hamiltonian H^{mp} for the system can be approximated as a sum of one-electron Hamiltonians. Consequently, the exact eigen function will be a product function

$$\varphi(\mathbf{r}_1,\mathbf{r}_2,\mathbf{r}_3,...,\mathbf{r}_n) = \prod_{i=1}^{n}\psi_i(\mathbf{r}_i) \tag{3.15}$$

However, this approximation does not illuminate the interaction between electrons. Electron-electron interactions need to be included in the Hamiltonian by an additional potential energy term for the many-electron system. As a consequence, the many-particle Hamiltonian consists of the sum over single-particle Hamiltonians in the external field and the potential energy of the Coulomb interaction among these charged particles [44,159], yielding

$$H^{mp} = \sum_{i=1}^{N} H(\mathbf{r}_i) + \frac{e^2}{2\varepsilon}\sum_{i,j}\frac{1}{|\mathbf{r}_i - \mathbf{r}_j|} \tag{3.16}$$

Moreover, the total wavefunction must be antisymmetric with respect to the

interchange of any pairs of the particle coordinates. This is equivalent to stating that the electron must satisfy the Pauli Exclusion Principle in the same system. Such requirement was rectified by the Hartree-Fock approximation. For an N-electron system, the wavefunction can be written as a N×N determinant, known as a Slater determinant [44,160],

$$\varphi(\mathbf{r}_1,\mathbf{r}_2,\mathbf{r}_3,\ldots,\mathbf{r}_n)=\frac{1}{\sqrt{N!}}\begin{vmatrix}\psi_1(\mathbf{r}_1) & \psi_2(\mathbf{r}_1) & \Lambda & \psi_N(\mathbf{r}_1)\\ \psi_1(\mathbf{r}_2) & \psi_2(\mathbf{r}_2) & \Lambda & \psi_N(\mathbf{r}_2)\\ \mathrm{M} & \mathrm{M} & & \mathrm{M}\\ \psi_1(\mathbf{r}_N) & \psi_2(\mathbf{r}_N) & \Lambda & \psi_N(\mathbf{r}_N)\end{vmatrix} \tag{3.17}$$

where ψ_i are the normalised one-electron wavefunctions. The determinant of Eq. (3.17) is equal to zero unless all one-electron wavefunctions are different, i.e., each electron must occupy a distinct state. Substituting Eq. (3.17) into Eq. (3.14), multiplying each term on the left by the complex conjugate of wavefunction $\psi^*_{i\neq j}$, and then integrating over all coordinates, a system of coupled equations for the one-electron wavefunctions, which has N equations (i = 1,2,...N) and are called the Fock equations, can be then obtained [160]

$$(H+V_H-V_{EC})\psi_i(\mathbf{r})=E_i\psi_i(\mathbf{r}) \tag{3.18}$$

where the first term in the parentheses on the left-hand side is the single-particle Hamiltonian containing the kinetic energy and the external potential. The second term in the parentheses of Eq. (3.18) for a system of electrons acting on the i^{th} is given by,

$$V_H=\frac{e^2}{\varepsilon}\sum_{j\neq i}\int d\mathbf{r}'\frac{|\psi_i(\mathbf{r}')|^2}{|\mathbf{r}-\mathbf{r}'|} \tag{3.19}$$

V_H is the electrostatic potential created by all electrons except the i^{th} one acting on the i^{th} electron and is called the Hartree potential. In effect V_H reflects the average repulsive Coulombic interaction between the i^{th} electron and all the others in the ensemble. The overall potential must also represent the correlation between the position of i^{th} electron and the positions of all the other electrons ($j \neq i$) and the effect of swapping the subscript label of the wavefunctions. These corrections to the Hartree potential are included by the third term in the parenthesis on the left-hand

side of Eq. (3.18), where [44,160]

$$V_{EC}\psi_i(\mathbf{r}) = \frac{e^2}{\varepsilon}\sum_{j\neq i}\left[\int d\mathbf{r}' \frac{|\psi_j^*(\mathbf{r}')\psi_i(\mathbf{r}')|}{|\mathbf{r}-\mathbf{r}'|}\right]\psi_j(\mathbf{r}) \tag{3.20}$$

This term describes the electron exchange correlation and V_{EC} is known as the exchange-correlation potential. This exchange term is the manifestation of the Pauli Exclusion Principle. Thus the Hartree-Fock representation has described the motion of a single electron in an effective potential created by all other electrons of the system and shows the strong correlation of the motion of all electrons.

However, the Fock equations remain difficult to apply to solid-state problems because of the huge numbers implied in the summations in Eq. (3.19) and Eq. (3.20) their extreme complexity. Equation (3.18) can be simplified if the characteristic kinetic energy of electrons is much larger than the Coulomb interaction energy. Moreover, the electron interaction in subbands is significant essentially at high electron concentration [161]. The temperature effect on the Fermi energy is more important than the electron interaction and the latter may be considered as a small perturbation [162]. Besides, rectifying the electron interaction of the model would not introduce physics that will significantly alter the trends in the results described in this thesis. Therefore, the effect of exchange-correlation interaction on the subband energies is considered to be weak and can be neglected. As a result, instead of the Fock equations, the Hartree approximation for the one-electron state in a many-electron system is given:

$$(H + V_H)\psi_i(\mathbf{r}) = E_i\psi_i(\mathbf{r}) \tag{3.21}$$

where the Hartree potential V_H is the solution from the Poisson equation. The total energy of the N electron system is

$$E = \sum_{i=1}^{N} E_i \tag{3.22}$$

3.2.5 Quantum Well Structures

With the advent MOCVD and MBE, the ability to grow single atomic layers of semiconductor material has led to the production of abrupt heterojunctions. It is the band energy mismatch of the materials at the heterojunctions which creates a potential energy variation that acts as a quantum well and provides for confinement of carriers inside the well. The square quantum wells have the following idealized form of the conduction band potential illustrated in Fig. 3.2.

Mathematically, the potential energy in a quantum well is given by,

$$V(z) = \begin{cases} V_w & \text{for } z \in \text{well} \\ V_b = V_w + \Delta E_c & \text{for } z \in \text{barrier} \end{cases}, \tag{3.23}$$

where ΔE_c is the depth of the well. In the assumed structure shown in Fig. 3.1, the conduction band offsets of $In_{0.53}Ga_{0.47}As/AlAs$ and $In_{0.53}Ga_{0.47}As/InP$ including the strain effect are 1.3 eV [85,94,163] and 0.23 eV [164], respectively. The potential $V(z)$

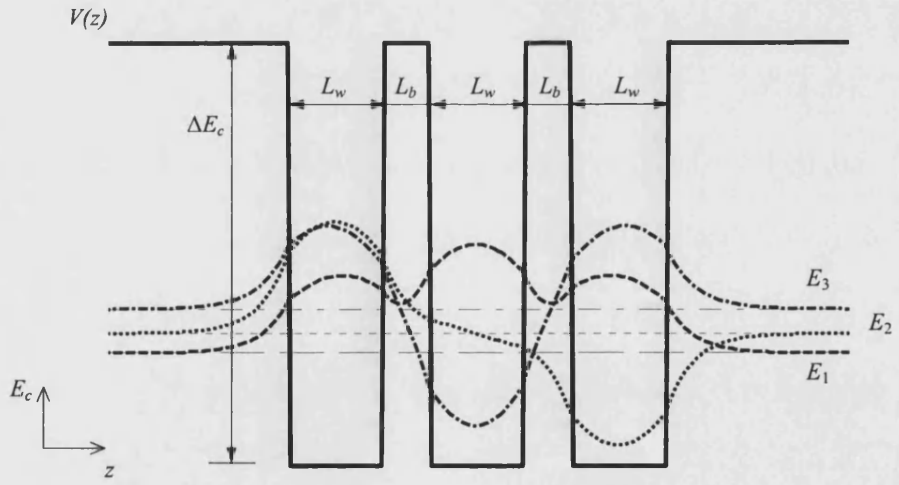

Figure 3.2: The position-dependent potential energy [$V(z)$] of a three-well structure and the quantum confined states, E_1, E_2 and E_3, with corresponding wavefunctions in energy-real space coordinates. L_w and L_b indicate the thickness of the wells and barriers respectively, a notation used throughout this work.

is a function of coordinate z only. In this case, the three-dimensional problem is reduced to a one-dimensional Schrödinger problem. According to the Eq. (3.5) and (3.11), the effective mass equation for a quantum well structure in Fig. 3.2 can be written as a time-independent effective-mass Schrödinger equation of the form [165]

$$\frac{\eta^2}{2m^*}\frac{d^2}{dz^2}\psi(z)+[E-V(z)]\psi(z)=0 \tag{3.24}$$

where E is the energy of the bound particle. Two types of solution to Eq. (3.24) are expected. The first is characterized by a discrete-energy spectrum for $E<V_b$ of bound states of electrons. The second corresponds to a continuous spectrum for $E>V_b$ of unbound states. In addition, $\psi(z)$ vanishes for bound states at $z\rightarrow\pm\infty$ or is finite for unbound states.

For the bound states $E<V_b$, the solution has the following form in the barrier

$$\psi(z)=A_i e^{-k_b z}+B_i e^{k_b z} \tag{3.25}$$

where $k_b=\sqrt{2m^*(V_b-E)/\eta^2}$ and is real, and subscript i is the barrier index. In the left-most barrier, A_i=1 and B_i=0, while in right-most region, A_i=0 and B_i=1. The solution inside the well is a simple combination of plane waves,

$$\psi(z)=C_j\cos k_w z+D_j\sin k_w z \tag{3.26}$$

where $k_w=\sqrt{2m^*(E-V_w)/\eta^2}$, and subscript j is the well index. Parameters A, B, C and D are determined or calculated by the boundary conditions.

Due to different material composition the effective mass is different for the well and barrier regions. The sudden change of the effective mass at the heterojunction interfaces requires the use of appropriate interface conditions to ensure that the continuity of the envelope wavefunction $\psi(z)$, and the effective mass weighted gradient $\frac{1}{m^*}\frac{d\psi(z)}{dz}$ across each heterojunction is continuous. More details will be discussed in the following section.

3.3 Numerical Solution for Arbitrary Shaped Quantum Well Structures

The solutions given in Eq. (3.25) and (3.26) are only valid for the piecewise constant potential $V(z)$ and run into trouble when applied to the structures of the type shown in Fig. 3.1. Such a potential profile is deformed by the doping and the external electric field. Details of the variation in potential profile will be discussed in the section 3.4 of Poisson solver. The aim of this work is to investigate and optimise the structures of the ISBTs based electroabsorption modulators which are usually modulation doped and operate under an applied voltage bias. Therefore, a solution for the arbitrary shaped quantum well structures is required. A Schrödinger solver based on the transfer matrix method [166-168] approach has been developed for this purpose.

3.3.1 Theory of Transfer Matrix Method

An arbitrary profile, $V(z)$, can always be approximated by a piecewise step profile, as shown in Fig. 3.3 as long as the original potential profile does not have singularities. The arbitrary shaped quantum well potential was first divided into a number of regions of equal width h, i.e. the incremental step size given by z_{i+1}-z_i. The actual potential energy distribution in each region was then approximated by a constant potential V_i, as shown in Fig. 3.3. The advantage of using the approximate profile becomes obvious when the method is applied to deformed quantum well structures under the external field. The accuracy of the bound energy states in this case is determined by the width of the step size (h).

The whole structure is divided into n regions of equal width and the single band effective mass equation is then solved in each divided region for the complete quantum well structure consisting of small regions. Since the effective mass and the potential energy are piecewise constant in each of these regions, the effective mass equation for the i^{th} region can be rewritten as

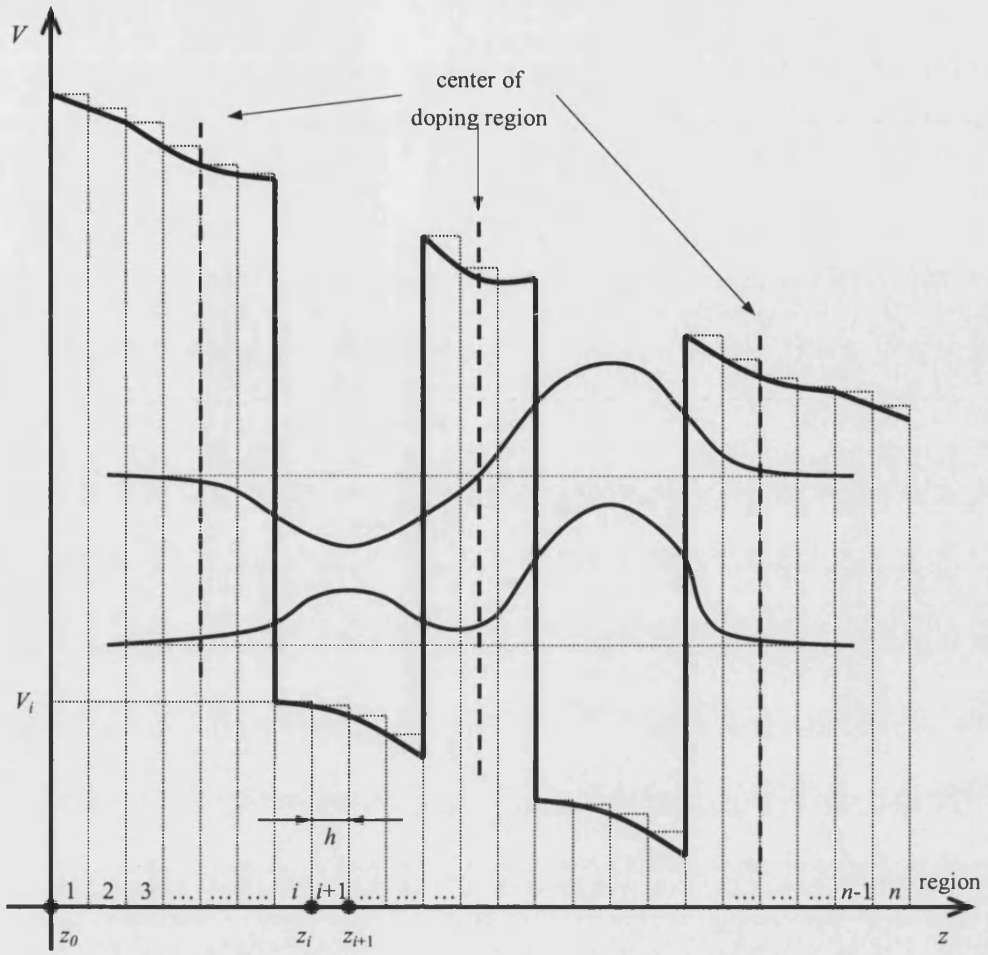

Figure 3.3: The potential profile of a quantum well structure with doping and external electric field. The dotted bars indicate the divided regions and the height of bars shows the constant potential in each region.

$$\frac{\eta^2}{2m_i^*}\frac{d^2}{dz^2}\psi_i(z)+(E-V_i)\psi_i(z)=0 \tag{3.27}$$

The solution of this equation is oscillatory when $E > V_i$, typically in the quantum well, and exponentially decaying when $E < V_i$, as typically occurs in the barrier region. This behaviour is similar to Eq. (3.25) and (3.26), and the result is given by

$$\psi_i(z)=\begin{cases}A_i\sin(\alpha_i z)+B_i\cos(\alpha_i z) & E>V_i\\ A_i\exp(\beta_i z)+B_i\exp(-\beta_i z) & E<V_i\end{cases} \tag{3.28}$$

where the piecewise constant of V_i is estimated form the calculated potential profile $V(z)$ by solving Poisson's equation in Section 3.4, and α_i and β_i are

$$\alpha_i = \sqrt{\frac{2m_i^*}{\eta^2}(E - V_i)}$$
$$\beta_i = \sqrt{\frac{2m_i^*}{\eta^2}(V_i - E)} \tag{3.29}$$

3.3.2 Boundary Conditions

Equations (3.28) are the general solutions for all regions in the quantum well structure in the piecewise approximation. The only parameters which need to be changed are the effective mass and the value of the potential energy and hence the nature of the solution, i.e. oscillatory or exponential. The next step is to match the wavefunctions of the i^{th} and $(i+1)^{th}$ regions at the interface between them. The interface conditions required in each interface are

$$\psi_i(z)\Big|_{z=z_i} = \psi_{i+1}(z)\Big|_{z=z_i} \tag{3.30}$$

$$\frac{1}{m_i^*}\frac{d\psi_i(z)}{dz}\Big|_{z=z_i} = \frac{1}{m_{i+1}^*}\frac{d\psi_{i+1}(z)}{dz}\Big|_{z=z_i} \tag{3.31}$$

Knowing the generalized solutions of the effective mass equation in the i^{th} and $(i+1)^{th}$ regions and also the connection between the two solutions at the interface, it is convenient to express the solution in a matrix notation

$$\begin{pmatrix} A_{i+1} \\ B_{i+1} \end{pmatrix} = M_i \begin{pmatrix} A_i \\ B_i \end{pmatrix} \tag{3.32}$$

where M_i is a 2×2 connection matrix. The coefficients of this matrix are obtained by applying Eq.s (3.30) and (3.31) and are given in appendix A.

Moreover, the wavefunction of the bound state must be well behaved. It means that the wavefunction must be normalizable or, in other words, the solutions are expected to be exponentially decaying in the two extreme ends of the quantum well structure since the substrate consists of barrier material. The requirement of the well behaved wavefunctions determines the initial and final values of the coefficients which are given by

$$\begin{cases} A_0 = 1\ ,\ B_0 = 0 \\ A_n = 0,\ B_n = 1 \end{cases} \tag{3.33}$$

A_0, B_0 represent the coefficient in the left-most region and A_n, B_n the coefficients in the right-most region.

3.3.3 Searching Confined States

The problem that remains to be solved is the computation of eigen-energies, E_n, of the bound energy states. If a value of E equals to the n^{th} eigen state E_n of the quantum well structure then using Eq. (3.28) and (3.32) along with the initial conditions $A_0 = 1$ and $B_0 = 0$, the corresponding wavefunction can be constructed. At the eigen-energy, this wavefunction must be well behaved as shown in Fig. 3.4 (a). Such a wavefunction is normalizable and decays exponentially in both substrate regions; in other words, $A_n = 0$ and $B_n = 1$ as mentioned in Eq. (3.32). However, if the energy E is a little too large or too small than E_n, the wavefunction does not tend to zero in the substrate but diverges to plus or minus infinity as shown in Fig. 3.4 (b) and (c), meaning that $A_n \neq 0$ and $B_n \neq 1$. Therefore, by calculating many different E, the correspondence relationship between E and A_n (B_n) can be revealed, i.e. $A_n = f_A(E)$ [$B_n = f_B(E)$]. Theoretically, these two coefficients, A_n and B_n, as a function of E can then be plotted and all the eigen-energies can be determined by searching for values of E such that $f_A(E) = 0$ and $f_B(E) = 1$ [167]. However, it can become impractical to determine the behaviour of A_n and B_n for all values of E by this method when there is only a small difference in bound energy levels, unless a careful search procedure for the roots of $f_A(E) = 0$ is applied. Therefore, a more efficient root finding procedure is required.

There are very simple numerical techniques which can provide the required information. Firstly, it is important to note that the wavefunctions consist of oscillatory and exponential functions, implying that each wavefunction has certain

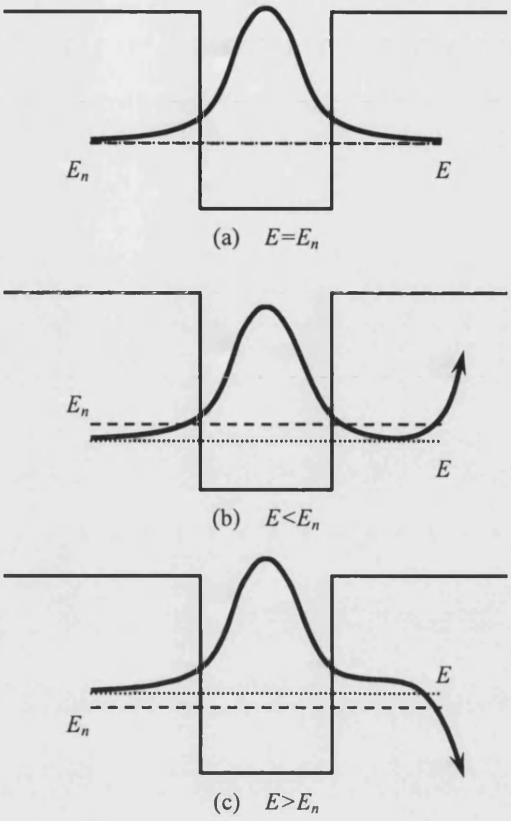

Figure 3.4: A trial energy E (dotted line) is (a) equal to, (b) less then and (c) greater than the bound-state energy E_n (dashed line). Only in the situation of $E=E_n$ a well-behaved wavefunction is produced. Otherwise, the wavefunction diverges to plus or minus infinity.

number of nodes where its value is zero along the z axis. Secondly, the n^{th} order eigen state is expected to have n-1 nodes in general. The first eigen state, for example, has no node and its value approaches zero only at both extreme ends of the structure. As a consequence, for the lower and upper bound of energies [E_{min} , E_{max}], where the wavefunctions at E_{min} and E_{max} has n-1 and n nodes respectively, there must be a bound state, i.e. eigen-energy, inside this range.

Therefore, the shooting method [169,170] is applied to solve the eigen value problem. The first step is to assume any arbitrary value of energy E_{trial} bound between E_{min} and E_{max}. The wavefunction corresponding to E_{trial} is then calculated by using the transfer matrix method. The initial value for the coefficients A_0 and B_0 is fixed but the final

value is determined by Eq. (3.32). At this stage the number of nodes in the wavefunction as well as the final value of coefficients is examined. The correct value of E_n must generate a wavefunction having (n-1) nodes and satisfying boundary conditions [Eq. (3.33)]. Until these two conditions are met, the value of E_{trial} is iteratively modified by a bisection algorithm, as illustrated in Fig. 3.5. Since the previous procedure of searching the notes can efficiently identify upper and lower limits [E_{min} , E_{max}], all the eigen value (root) can be found by iteration.

3.4 Poisson Equation for Quantum Well Structures

Insight into the energy distribution of charge carriers is necessary to gain an understanding of the optical and transport properties of semiconductors. Firstly, the total energy for electrons includes two terms: the kinetic energy which is given by the band structure and the potential energy due to the electrostatic potential. An accurate treatment requires a solution of Poisson's equations for the electrostatic potential. Secondly, in quantum well structures, external electric fields applied normal to the layer boundaries can alter the band diagram and the behaviour of charge carriers. Moreover, in the structure with modulation doping, the electrons excited from the donors accumulate at one side of the heterojunction giving rise to band bending. The effects of modulation doping and the applied voltage bias on the potential profile, electric field and the carrier concentration are studied in this section.

3.4.1 Poisson Equation

The one dimensional electrostatic potential, $\phi(z)$, in semiconductor heterostructure and quantum well devices can be calculated by solving the one dimensional Poisson's equation,

$$\frac{d}{dz}\left[\varepsilon(z)\frac{d\phi(z)}{dz}\right]=-\rho(z) \tag{3.34}$$

where z is the coordinate axis perpendicular to the junction is grown, $\varepsilon(z)$ is the position-dependent dielectric permittivity in each layer due to the different materials

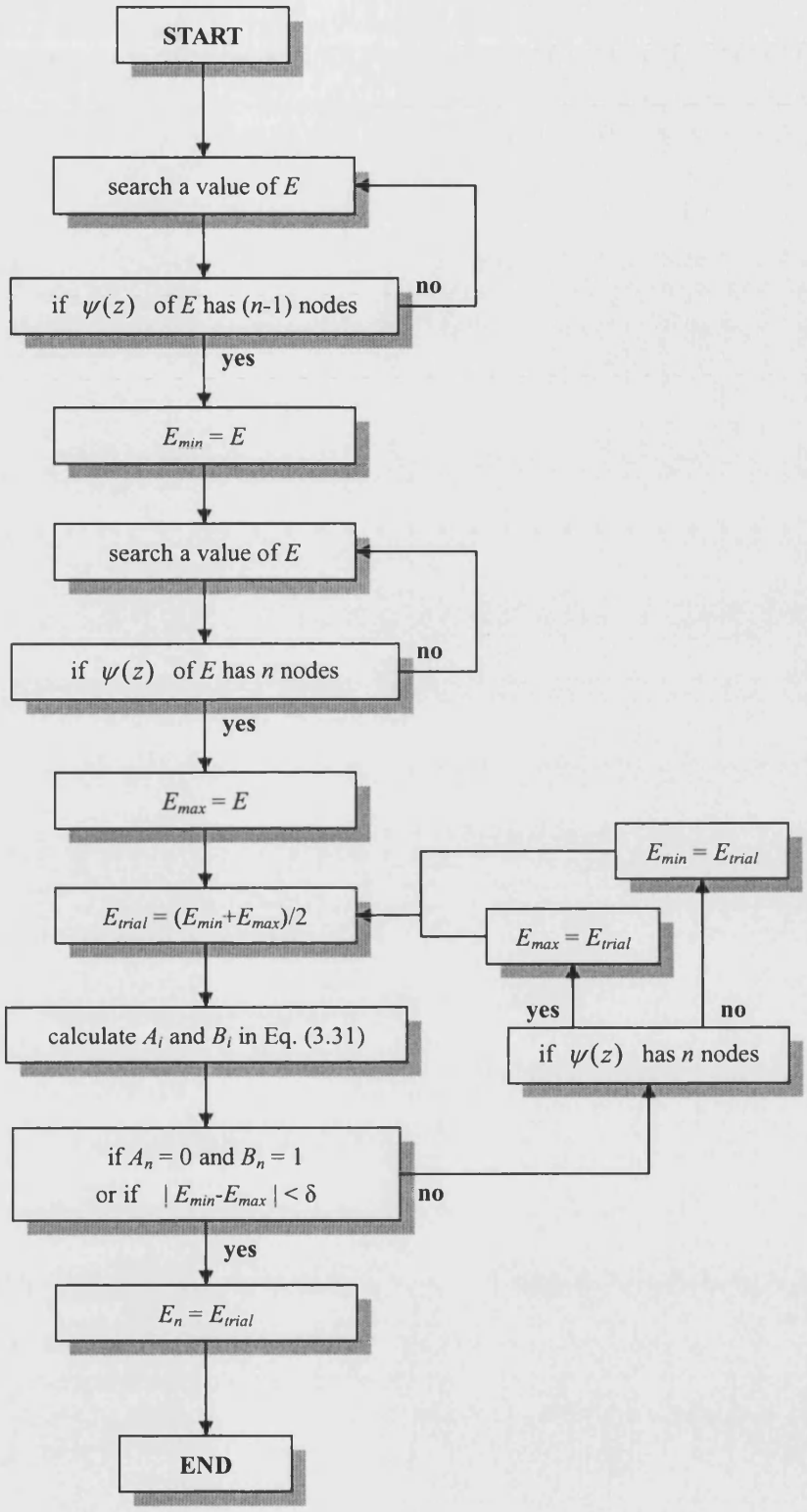

Figure 3.5: Flow chart of the Schrödinger procedure with an iterative method for calculating energy states (E_n) and wavefunctions (ψ_n) of quantum wells. δ is a small value to avoid overflowing, choosen as the floating point value in the program.

chosen in the structures and $\rho(z)$ is the charge density distribution given by [155],

$$\rho(z) = e[N_D^+(z) - N_A^-(z) + p(z) - n(z)] \tag{3.35}$$

where e is the charge of an electron (e = 1.602×10^{-19} C), $N_D^+(z)$ and $N_A^-(z)$ are the ionized donor and acceptor densities respectively, $n(z)$ and $p(z)$ are the electron and hole density in the conduction and valence bands respectively.

The electrostatic potential of the conduction band can be expressed in terms of the energy of an electron (E_c) found at the bottom of the conduction band

$$-e\phi(z) = E_c(z) - E_F \tag{3.36}$$

If there is no current flow, which is a reasonable assumption for reverse bias, the Fermi level, E_F, is constant through the device and can be taken as the reference level for the measurement of the electrostatic potential. The energy and potential are calculated in eV (electron volt) and V (volt), respectively.

The Poisson equation can be rewritten in terms of the reduced potential η as [155],

$$\frac{d}{dz}\left[\varepsilon(z)\frac{d\eta(z)}{dz}\right] = -\frac{e^2}{K_bT}[N_D^+(z) - N_A^-(z) + p(z) - n(z)] \tag{3.37}$$

where

$$\eta(z) = \frac{E_F - E_c(z)}{K_bT} = \frac{e}{K_bT}\phi(z) \tag{3.38}$$

is dimensionless. K_b is the Boltzmann's constant (K_b = 1.381×10^{-23} J/K) and T is the absolute temperature in Kelvin, and $K_bT \approx$ 25.8 meV at room temperature (300K). The effect of applied voltage (V) on the band edge variation and the electric field in the diode can be included by rewriting η as

$$\eta(z) = \frac{E_F - E_c(z) + V(z)}{K_bT} \tag{3.39}$$

where $V(z)$ is negative for reverse bias.

3.4.2 Equilibrium Concentration Relationships

In order to solve Eq. (3.37), it is first necessary to deduce the distribution of carriers in the conduction and valance bands. The desired distribution, as shown in Fig. 3.6, can be obtained by establishing the energy distribution of available band states and the ratio of filled to total states under equilibrium conditions. The average occupation of electron states for a system in thermal equilibrium is governed by the Fermi-Dirac distribution function, *f(E)* [155], which is a probability density function that specifies the ratio of filled to total allowed states at a given energy E, and is given by

$$f(E) = \frac{1}{1 + e^{(E-E_F)/K_bT}} \tag{3.40}$$

The number of holes in the valence band is determined by the fraction of unoccupied electron states, i.e. 1-*f(E)*. The density of states function, $g(E)$, defines the distribution of the total number of allowed states available to electrons per unit energy range centred at energy E and per unit volume of the crystal. The conduction and valence band densities of states near the band edges in bulk semiconductors are given by [155]

$$\begin{aligned} g_c(E) &= \frac{m_n^* \sqrt{2m_n^*(E-E_c)}}{\pi^2 \eta^3} \qquad E \geq E_c \\ g_v(E) &= \frac{m_p^* \sqrt{2m_p^*(E_v-E)}}{\pi^2 \eta^3} \qquad E \leq E_v \end{aligned} \tag{3.41}$$

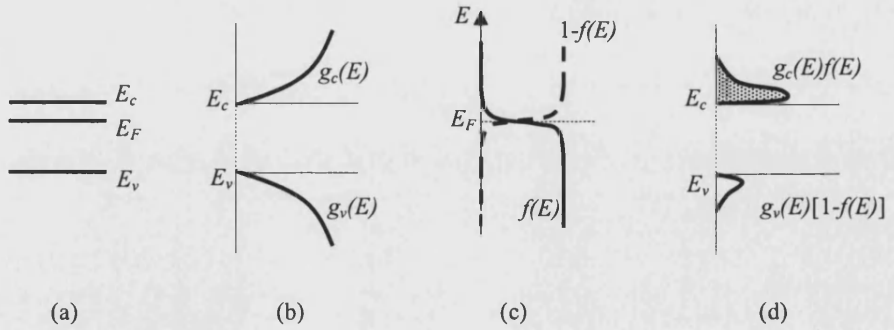

Figure 3.6: Sketches of the relationship between (a) the energy band edges, (b) density of states, (c) the occupancy factors and (d) the carrier distribution for a bulk semiconductor.

where m_n^* and m_p^* are the electron (n) and hole (p) density of states effective masses, E_c is taken to be the minimum electron energy in the conduction band and E_v the maximum hole energy in the valence band.

The electron and hole density in the conduction and valence band is given by:

$$n = \int g_c(E) f(E) dE \tag{3.42a}$$

$$p = \int g_v(E)[1 - f(E)] dE \tag{3.42b}$$

$n(z)$ and $p(z)$ can be written in terms of Fermi-Dirac integral $F_{1/2}$ as [155]

$$n(z) = N_c \frac{2}{\sqrt{\pi}} F_{1/2}(\eta) \tag{3.43a}$$

$$p(z) = N_v \frac{2}{\sqrt{\pi}} F_{1/2}(-\eta - \frac{E_g}{K_b T}) \tag{3.43b}$$

where $F_{1/2}(\eta) = \int_0^\infty \frac{\xi^{1/2} d\xi}{1 + e^{\xi - \eta}}$. The Fermi-Dirac integral requires numerical evaluation; however, several analytical approximations exist, one of which is presented in Appendix B and used in calculations in this thesis. The effective density of states, N_c and N_v in conduction and valence bands respectively, are given by [155]

$$N_c = 2\left(\frac{2\pi m_e^* K_b T}{h^2}\right)^{3/2} = 2.51 \times 10^{19} \left(\frac{m_e^*}{m_0} \frac{T}{300}\right)^{3/2} cm^{-3} \tag{3.44a}$$

$$N_v = 2\left(\frac{2\pi m_h^* K_b T}{h^2}\right)^{3/2} = 2.51 \times 10^{19} \left(\frac{m_h^*}{m_0} \frac{T}{300}\right)^{3/2} cm^{-3} \tag{3.44b}$$

where m_e^* and m_h^* are the effective mass of electrons and holes, respectively.

The ionized donor and acceptor densities are other essential terms in Eq. (3.36). In terms of the energy band diagram, donors and acceptors add allowed electron states in the band gap close to the conduction and valence band edges respectively, as shown in Fig. 3.7. Since the proportion of the ionized donor density to the total donor

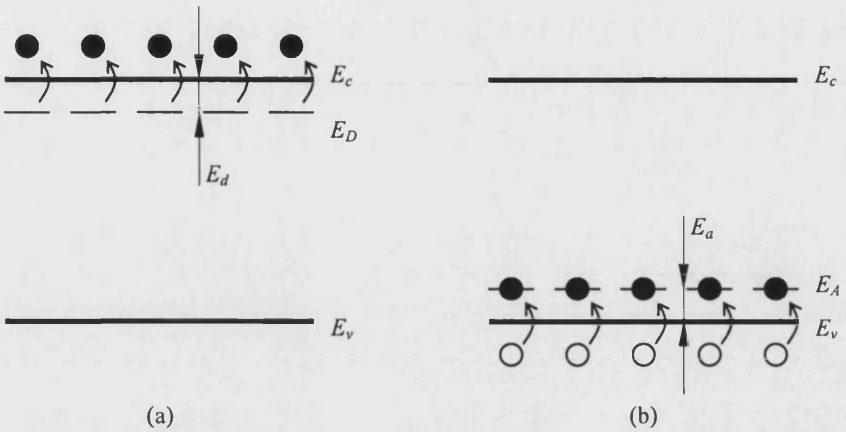

Figure 3.7: Energy-band diagram representation of (a) donors and (b) acceptors.

concentration (N_D^+ / N_D) represents the ratio of empty to total states at the donor energy E_D, and the proportion of the ionised acceptor density to the total acceptor concentration (N_A^- / N_A) corresponds to the ratio of electron filled to total states at the acceptor energy E_A, the dopant ionization expressions are [155]

$$\frac{N_D^+}{N_D} = \frac{1}{1 + g_D e^{(E_F - E_D)/K_b T}} \qquad g_D = 2 \tag{3.45a}$$

$$\frac{N_A^-}{N_A} = \frac{1}{1 + g_A e^{(E_A - E_F)/K_b T}} \qquad g_A = 4 \tag{3.45b}$$

where g_D and g_A are the donor- and acceptor- site degeneracy factors, respectively. These factors arise because the statistics of filling band gap levels differs slightly from the statistics of filling energy band levels. Therefore, the ionized donor [$N_D^+(z)$] and acceptor [$N_A^-(z)$] densities are given by [155]

$$N_D^+(z) = \frac{N_D(z)}{1 + 2\exp\left[\eta(z) + \frac{E_d}{K_b T}\right]} \tag{3.46a}$$

$$N_A^-(z) = \frac{N_A(z)}{1 + 4\exp\left[-\eta(z) - \frac{E_g}{K_b T} + \frac{E_a}{K_b T}\right]} \tag{3.46b}$$

where E_d and E_a represent the ionization energy for the donors and acceptors. In InP the energy levels of commonly used donors and acceptors are respectively $E_d = 7meV$ [171] and $E_a = 31meV$ [172]. The doping densities in p and n regions are given by N_A and N_D respectively, which are functions of position due to the different doping in the structure.

3.4.3 Quantum Wells in an intrinsic-n-type Junction

Now considering the structure shown in Fig. 3.1, quantum wells are embedded in the middle of the intrinsic layer in an *i-n* diode with a Schottky contact used to modulate the electric field (F), as shown in Fig. 3.8. The structure is shown with a negative bias V_A on the Schottky contact, which has a work function of ϕ_B with respect to the intrinsic region. When the *p-i-n* junction is considered, the built-in voltage is V_{bi}. If a high donor density ($\sim 10^{18}/cm^3$) exists in the n-type region and a low donor density ($\sim 10^{15}/cm^3$) occurs in the intrinsic region of the diode, then $p(z) \approx 0$ and $N_A^- \approx 0$ due to the n-type doping in the whole structure. Therefore, the problem is simplified and becomes straight forward to solve, and Eq. (3.36) can be approximated as follows,

$$\frac{d}{dz}\left[\varepsilon(z)\frac{d\eta(z)}{dz}\right] = -\frac{e^2}{K_bT}[N_D^+(z) - n(z)] \tag{3.47}$$

For the InP, AlAs and $In_{0.53}Ga_{0.47}As$, the dielectric constants, ε, in these materials are 9.61, 8.16 and 11.09 [14,173,174], respectively. Since there are quantum wells present in the structure and the energy of the particle is quantized along one direction, all electrons in the wells occupy the different bound states for motion in the z direction but remain free in the x-y plane inside the wells. Therefore, inside the quantum well the two dimensional density of electrons is given by [148]

$$n_{2d} = \frac{m^* K_bT}{\pi\eta^2}\sum_i |\psi_i|^2 \ln\left[1 + \exp\left(-\frac{E_i - E_F}{K_bT}\right)\right] \tag{3.48}$$

where ψ_i can be obtained by solving the Schrödinger equation presented in Section 3.3. Outside the quantum well the density of electrons n_{3d} is given by Eq. (3.42a).

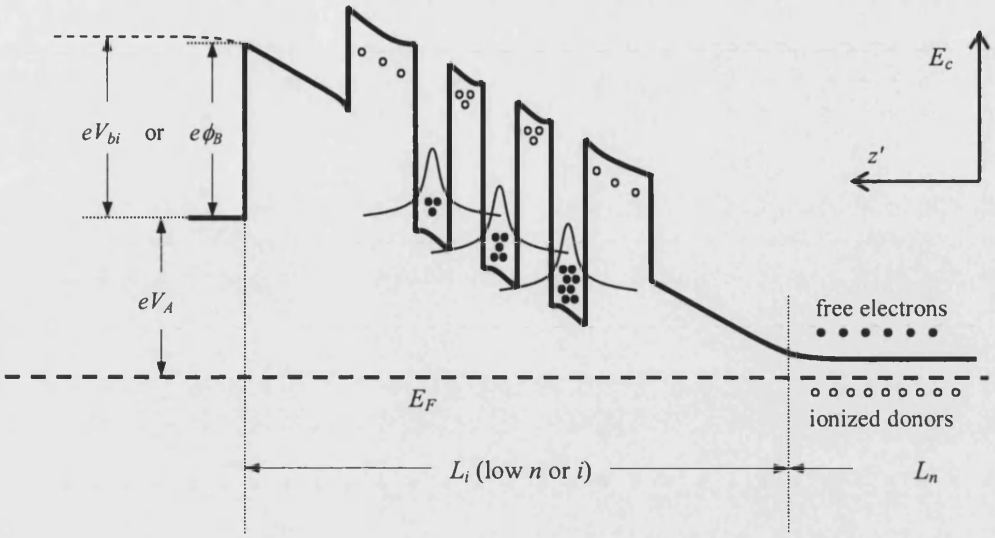

Figure 3.8: Sketch of band diagram and carrier distribution. The solid and open circles indicate the free electrons and ionized donors respectively.

Therefore, the Poisson equation can be written as:

$$\frac{d}{dz}\left[\varepsilon(z)\frac{d\eta(z)}{dz}\right] = -\frac{e^2}{K_b T}[N_D^+(z) - n_{3d}(z) - n_{2d}(z)] \tag{3.49}$$

where N_D^+ is local density of ionized donors, n_{3d} the 3D electron density, n_{2d} the 2D electron density. Inside the wells $n_{3d}(z)$ is set to zero to account for the effect of quantisation on the energy states available to the electron. Outside the quantum wells both $n_{3d}(z)$ and $n_{2d}(z)$ contribute to the free electron density. Note that $n_{2d}(z)$ is only large inside the well and in those parts of the barriers closer to the wells.

3.5 Numerical Solution of Poisson Equation

The shooting method is used again for solving Poisson equation with appropriate boundary conditions. For a given surface potential, the surface field which yields the correct values of potential and electric field at the other boundary is determined by an iterative process.

3.5.1 Differential Equation Solver

The Runge-Kutta method for a second order equation, $y''=f(x,y,y')$, which was given by Collatz [175] has been proved to be an effective method for solving Poisson's equation [176]. The Runge-Kutta scheme is of fourth order locally. When applying this method to Poisson's equation (3.49), this implementation has a right hand side independent of x and y', i.e. $\eta''=f(\eta)$, and there is some redundancy in the evaluation of the terms. For the given values of $\eta(z_0)$ and $\eta'(z_0)$, one can estimate the value $\eta(z_0+h)$ and $\eta'(z_0+h)$ as follows

$$\begin{cases} K_1=\dfrac{h^2}{2}f(\eta(z_0)) \\ K_2=\dfrac{h^2}{2}f(\eta(z_0)+\dfrac{h}{2}\eta'(z_0)+\dfrac{K_1}{4}) \\ K_3=\dfrac{h^2}{2}f(\eta(z_0)+\dfrac{h}{2}\eta'(z_0)+\dfrac{K_1}{4})=K_2 \\ K_4=\dfrac{h^2}{2}f(\eta(z_0)+h\eta'(z_0)+K_3) \end{cases} \tag{3.50}$$

$$\begin{cases} \eta(z_0+h)=\eta(z_0)+h\eta'(z_0)+\dfrac{1}{3}(K_1+K_2+K_3) \\ \eta'(z_0+h)=\eta'(z_0)+\dfrac{1}{3h}(K_1+2K_2+2K_3+K_4) \end{cases} \tag{3.51}$$

Therefore, with the given field and potential at a position z_0, the next step of the numerical Poisson solver is to find out the reduced potential and electric field at the next point $z_1 = z_0+h$. Iteratively, the reduced potential and electric field can be determined at any point $z = z_i$.

3.5.2 Boundary Conditions

In order to obtain the numerical solution of the Poisson equation given by Eq. (3.49), the use of boundary conditions is required. To identify these conditions one needs to carefully consider the behaviour of the charge distribution inside the diode. The net charge is zero at the extreme end of the diode in the *n*-type regions and therefore the electrostatic potential is constant. This is the first boundary condition which

determines the maximum value for the reduced potential satisfying the Poisson's equation and is given by,

$$N_D^+(z)\Big|_{\eta=\eta_{max}} = n(z)\Big|_{\eta=\eta_{max}} \tag{3.52}$$

Using the approximate function for the Fermi-Dirac integral in Appendix B, the solution of Eq. (3.52) is given by

$$\eta_{max} = \ln\left(\frac{-b+\sqrt{b^2+4ac}}{2a}\right) \tag{3.53}$$

where

$$\begin{cases} a = \dfrac{4N_c}{\sqrt{\pi}}\exp(\eta_d) \\ b = \dfrac{2N_d}{\sqrt{\pi}} - 0.27N_D \\ c = -N_D \\ \eta_d = \dfrac{E_d}{K_bT} \end{cases} \tag{3.54}$$

Wilson *et al* [176] have derived a simple expression relating the electric field at point z with the potential at z by integrating the Poisson's equation. This can improve the running time of the Poisson solver. It is valid for a region of n-type semiconductor (or p-type with suitable changes) with constant doping level and is given by

$$\frac{d\eta}{dz} = \pm\sqrt{\frac{2e^2}{\varepsilon K_bT}}\left\{\frac{2}{\sqrt{\pi}}N_cF_{3/2}(\eta) + N_D\ln[g+\exp(-\eta-\eta_d)] + c_n\right\}^{1/2} \tag{3.55}$$

where g is the ground state degeneracy of the donor impurity level and $g = 2$ for the n-doped region, c_n is the constant of integration and $F_{3/2}$ is the Fermi-Dirac integral (see Appendix B). Equation (3.55) is only valid for the calculation of the initial value of electric field in the n-doped regions at thermal equilibrium but not a general solution of the field in the whole structure. Evaluating Eq. (3.55) requires an appropriate value for the constant c_n. This is obtained by noting that in the flat-band region deep in the n-type layer

$$\frac{d\eta}{dz}\Big|_{\eta=\eta_{max}} = 0 \tag{3.56}$$

This is the second boundary condition and, as stated, is used to determine the

constants of integration of Eq. (3.55). The values calculated from Eq. (3.53) and (3.56) are used to determine the first values applying to the Runge-Kutta method. Therefore, the shooting calculation starts from the *n*-type region to the Schottky contact through the intrinsic region as illustrated in Fig. 3.8.

Furthermore, the perpendicular electric displacement vector, $\mathbf{D}_z = \varepsilon_0\varepsilon_r\mathbf{F}_z$,must be continuous at every interface where no surface current flow is assumed. For this reason, the requirement is to match the electric displacement of the i^{th} and $(i+1)^{th}$ regions at the interface between them. The interface condition of this is given as

$$D_i(z_i) = D_{i+1}(z_i) \tag{3.57}$$

Therefore, the interface condition required at each heterojunction is

$$\varepsilon_i \left.\frac{d\eta_i}{dz}\right|_{z=z_i} = \varepsilon_{i+1} \left.\frac{d\eta_{i+1}}{dz}\right|_{z=z_i} \tag{3.58}$$

3.5.3 Self-Consistent Schrödinger-Poisson Approach

The main objective of solving the Poisson equation is to calculate the carrier concentration and the electric field distribution in the quantum wells under external bias conditions. However, the individual quantum wells support a few eigen states in the conduction and valence band, and when occupied by carriers, their presence in the intrinsic region will alter the net charge distribution. This means that the Poisson and Schrödinger solvers are interactive: the distribution of two-dimensional electrons in quantum wells is required in the Poisson solver for the accurate calculation of potential profile, while the potential profile is essential for the Schrödinger solver for calculating correct wavefunctions. Thus, one needs to solve both the Poisson and Schrödinger equations alternately until the solution is self-consistent. Under these circumstances, the Poisson's equation without any quantum wells is solved first. The quantum well profile is then introduced in the intrinsic region and, depending upon the lateral position, the field in each well is estimated from the field distribution calculated in the previous iteration.

A flow chart of the numerical procedure is shown in Fig. 3.9. The electric field and potential distribution in an *i-n* diode are first simulated by the numerical solver based on the Poisson equation. Then, transition energy calculations using the transfer matrix method are performed by applying Schrödinger equation to the quantum well potentials that are deformed as a consequence of the total electric field. The next step involves updating the charge density in the Poisson solver to include the 2DEG in the wells and recalculating the potential profile. The iteration is stopped when the result approaches a constant value, i.e. the self-consistent solution.

The self-consistent Schrödinger-Poisson calculation mentioned above was developed in MATLAB and is simple to use. It has been applied to the design and analysis of various quantum well structures. The software can be used to calculate the bound states and corresponding wavefunctions under external field conditions and various doping conditions. Additional information about the physics of quantum wells, such as the optical transition energies and their oscillator strengths for the structure, can be extracted by understanding the wavefunction behaviour with varying field strength. This self-consistent technique has been extensively employed here in understanding the physics of isolated quantum wells, and weakly and strongly coupled quantum well structures, as described in the next chapter.

3.6 Absorption Coefficient for the Conduction Intersubband Transition

With the accurate solution of bound state energies and corresponding wavefunctions from the self-consistent Schrödinger-Poisson solution, one can then start the calculation of the bound-to-bound intersubband absorption coefficient. The absorption process from an initial subband (i) with energy E_i to final subband (f) with energy E_f is shown in Fig. 3.10. The transition rate W (s^{-1}) for the absorption or emission of a phonon with a given interaction potential V_p is given by the Fermi

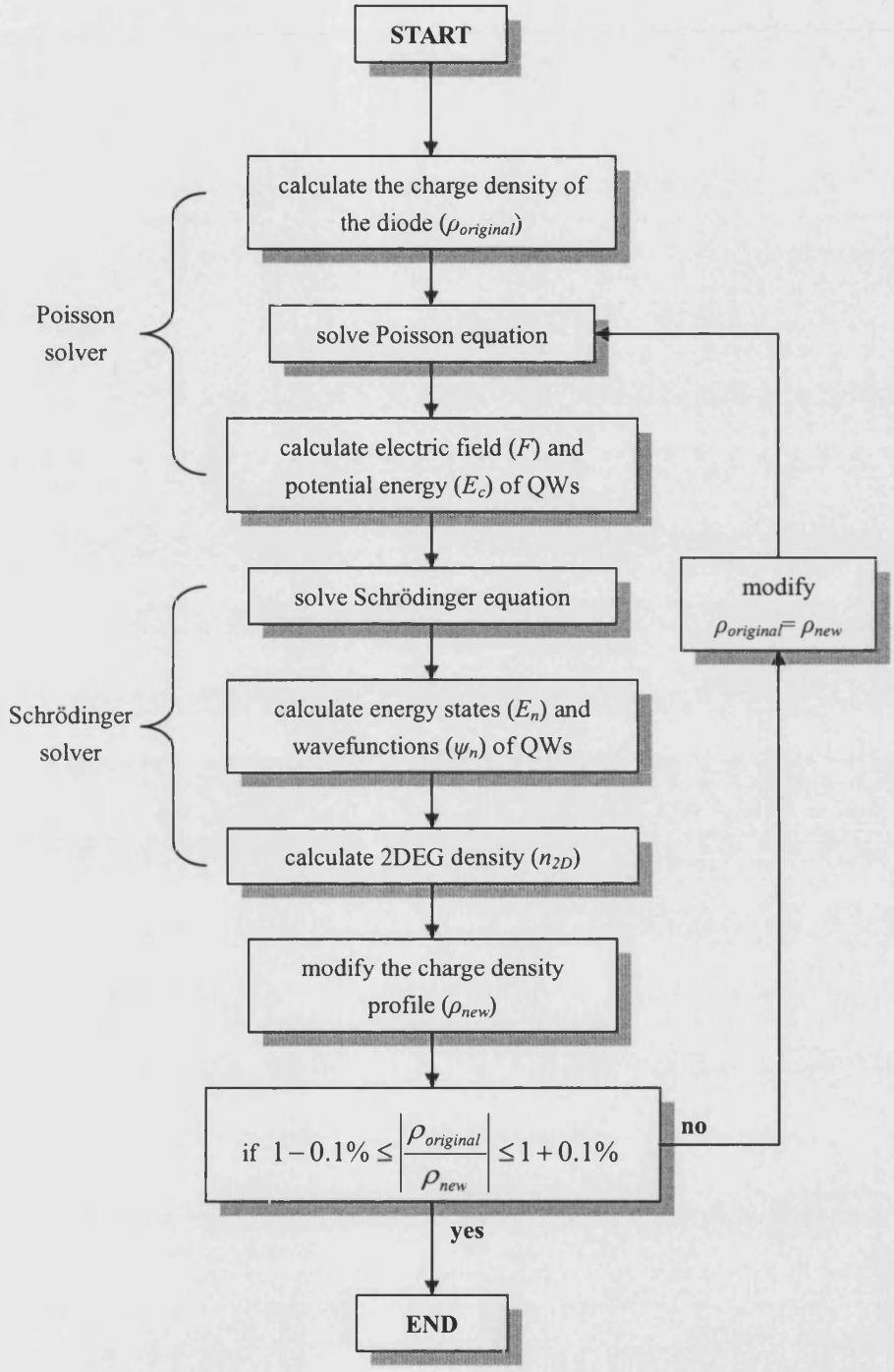

Figure 3.9: Flow chart of the iterative methods of self-consistent Schrödinger-Poisson approach in this thesis.

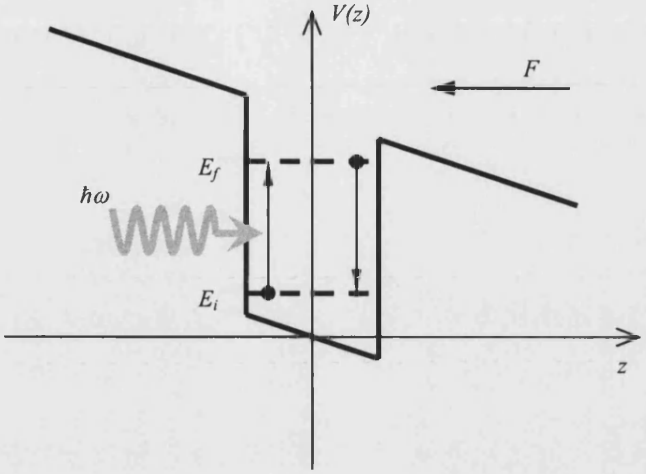

Figure 3.10: Potential energy profile for a quantum well subject to an electric field F in the presence of incoming radiation with photon energy $\hbar\omega$.

golden rule as [4,43]

$$W_{i\leftrightarrow f} = \frac{2\pi}{\eta} |< \Psi_f | V_p | \Psi_i >|^2 \, \delta(E_{if} \, \mu \, \eta\omega) \tag{3.59}$$

where the matrix element $< \Psi_f | V_p | \Psi_i >= \int \Psi_f^* V_p \Psi_i d\mathbf{r}^3$, δ is the Dirac delta function, $E_{if} = E_f - E_i$, E_i and E_f are the energies of the initial and final subbands, respectively, the 'μ' in the δ function takes '-' for absorption and '+' for emission and ω is the angular frequency of incident photon. In a one-dimensional structure, the wavefunctions Ψ_i and Ψ_f may be written as

$$\begin{cases} \Psi_i = \dfrac{1}{\sqrt{S}} u_c(\mathbf{r}) \exp(i\mathbf{k}_{//} \cdot \boldsymbol{\rho}) \phi_i(z) \\ \Psi_f = \dfrac{1}{\sqrt{S}} u_{c'}(\mathbf{r}) \exp(i\mathbf{k}'_{//} \cdot \boldsymbol{\rho}) \phi_f(z) \end{cases} \tag{3.60}$$

where S is the surface area, ϕ_i and ϕ_f are envelope functions of the initial and final states, respectively, u_c and $u_{c'}$ are Bloch functions, $\mathbf{k}_{//}$ and $\mathbf{k}'_{//}$ refer to the 2D wave vectors of an electron in the x-y plane and $\boldsymbol{\rho}$ refers to the in-plane position vector perpendicular to z axis. Taking into account the probability that the initial state is occupied and the finial state is empty, the total upward transition rate $R_{i\rightarrow f}$ and the total downward transition rate $R_{i\leftarrow f}$ per unit volume ($s^{-1}cm^{-3}$) in the crystal is

$$\begin{cases} R_{i\to f} = \dfrac{2}{V}\sum_{\mathbf{k}_{//}}\sum_{\mathbf{k'}_{//}} W_{i\to f} f(E_i)\left[1-f(E_f)\right] \\ R_{i\leftarrow f} = \dfrac{2}{V}\sum_{\mathbf{k}_{//}}\sum_{\mathbf{k'}_{//}} W_{i\leftarrow f} f(E_f)\left[1-f(E_i)\right] \end{cases} \tag{3.61}$$

where $f(E_i)$ and $f(E_f)$ are the Fermi-Dirac distributions given in Eq. (3.40) which denote the Fermi occupational probabilities for electrons in the initial and final subbands, respectively, the prefactor "2" takes into account the sum over spins.

The absorption constant, α (cm^{-1}), is the fraction of the absorbed photon energy versus the intensity of the incident radiation per unit distance, and can be written as

$$\alpha = \frac{\eta\omega \times \text{number of transitions per unit volume per second}}{\text{incident photon energy per unit area per second}} \tag{3.62}$$

Now, the absorption constant must take into account all the allowed transitions that a photon of energy $\hbar\omega$ can undergo. The net upward transition rate (the absorption rate minus the emission rate) per unit volume can be written as

$$\begin{aligned} R &= R_{i\to f} - R_{i\leftarrow f} \\ &= \frac{2}{V}\sum_{\mathbf{k}_{//}}\sum_{\mathbf{k'}_{//}} \frac{2\pi}{\eta} |< \Psi_f | V_p | \Psi_i >|^2 \, \delta(E_{fi} - \eta\omega)\left[f(E_i) - f(E_f)\right] \end{aligned} \tag{3.63}$$

The optical intensity S (W/cm^2) of the incident photons per unit area per second is $\frac{n_r\omega^2 A_0^2}{2\mu c}$. Therefore, in terms of transition rates in quantum well structures, the absorption constant must be the sum over all transitions between the occupied initial states and non-occupied final states and can be written as [84]

$$\alpha = \sum \frac{\eta\omega R}{S} = \sum_{i<f}\left[\eta\omega R \Big/ \left(\frac{n_r\omega^2 A_0^2}{2\mu c}\right)\right] \tag{3.64}$$

where n_r is the refractive index, A_0 is the amplitude of the vector potential **A** of the incoming light, μ is the permeability.

Since the envelope functions ϕ_i and ϕ_f are slowly varying in comparison with the periodic-cell function, u_c, the matrix element in Eq. (3.59) may be written approximately as [177,178]

$$\begin{aligned} &< u_{c'}\phi_f \mid V_p \mid u_c\phi_i > \\ &\approx < u_{c'} \mid V_p \mid u_c >_{cell} < \phi_f \mid \phi_i > + < u_{c'} \mid u_c >_{cell} < \phi_f \mid V_p \mid \phi_i > \end{aligned} \tag{3.65}$$

where the subscript "*cell*" indicates that the scalar product has been evaluated over a unit cell. In the case of direct interband transitions, the second term in Eq. (3.65) reduces to zero since the cell-periodic parts of the two different bands at the same point of the Brillouin zone are orthogonal, i.e. $< u_{c'} \mid u_c > \approx 0$ [178]. On the other hand, the first term becomes zero for transition within the same band, because ϕ_i and ϕ_f are eigen functions of the same effective mass Hamiltonian and are orthogonal, i.e. $< \phi_f \mid \phi_i > \approx 0$ and $< u_{c'} \mid u_c > \approx 1$ [177]. Therefore, for ISBTs the matrix element reduces to

$$< \psi_f \mid V_p \mid \psi_i > \approx < \phi_f \mid V_p \mid \phi_i > \tag{3.66}$$

By using the electric dipole approximation associated with the $\boldsymbol{k}\cdot\boldsymbol{p}$ perturbation theory, the matrix element in Eq.(3.66) reduces to [4,84]

$$< \phi_f \mid V_p \mid \phi_i > = -\frac{eA_0(E_i - E_f)}{2i\eta} \boldsymbol{\varepsilon}_\lambda \cdot < \phi_f \mid \mathbf{r} \mid \phi_i > \tag{3.67}$$

where $\boldsymbol{\varepsilon}_\lambda$ is the polarization unit vector of the incident photon. The envelope functions ϕ_f and ϕ_i are functions of z only and are orthogonal to each other. As a consequence, only the matrix element $< \phi_f \mid z \mid \phi_i >$ remains since both $< \phi_f \mid x \mid \phi_i >$ and $< \phi_f \mid y \mid \phi_i >$ are zero. Therefore, ISBTs are allowed only for radiation polarized perpendicular to the layers. This is known as the polarization selection rule. Thus the absorption coefficient can be simplified and expressed as [84]

$$\alpha(\eta\omega) = \frac{\pi\omega\mu ce^2 \cos^2\theta}{n_r} \sum_{i<f} (N_i - N_f) < z >^2 \delta(E_{if} - \eta\omega) \tag{3.68}$$

where

$$< z > = < \phi_f \mid z \mid \phi_i > = \int \phi_f \cdot z \cdot \phi_i dz \tag{3.69}$$

$$\begin{cases} N_i = \frac{2}{V}\sum_{\mathbf{k}_{//}} f(E_i) = \frac{m^* K_b T}{\pi\eta^2 L}\ln(1+e^{(E_F-E_i)/K_bT}) \\ N_f = \frac{2}{V}\sum_{\mathbf{k}'_{//}} f(E_f) = \frac{m^* K_b T}{\pi\eta^2 L}\ln(1+e^{(E_F-E_f)/K_bT}) \end{cases} \tag{3.70}$$

$N_{i\,(f)}$ is the electron density of i^{th} (f^{th}) subband, θ is the angle between the polarization vector ε_λ and normal to the quantum well.

Again, the polarization selection rule can be revealed from the value of $\cos^2\theta$. For the polarization vectors parallel to the interface, $\cos^2\theta = 0$, which means the transition is prohibited. However in this work, only the polarization vector perpendicular to quantum well is considered, i.e. $\cos^2\theta = 1$. In a symmetric quantum well structure, Eq. (3.69) implies another selection rule: for transitions between two subbands with the same parity of the band index, the matrix element is zero, i.e. these transitions are forbidden. The transitions are possible only between states with different parity. This is known as the parity selection rule. However, it has to be noted that these limitations of transitions are under the assumption of simple isotropic bands and symmetric quantum well structures, as mainly considered in this work. The selection rules would break down in various situations, such as using anisotropic materials [87], growing asymmetric wells [99] and applying bias [84] to the structures, as mentioned in Chapter 2.

In addition, when one takes into account the line broadening, i.e. the scattering relaxation is included, the δ-function may be replaced by a normalised Lorentzian function [179], i.e. $\delta(E_{if}-\eta\omega) \to \frac{\Gamma/2\pi}{(E_{if}-\eta\omega)^2+(\Gamma/2)^2}$ where Γ is the line width or full-width at half-maximum (FWHM), the factor π has been included such that the area under the function is properly normalised: $\int\delta(E_{if}-\eta\omega)d(\eta\omega)=1$. Equation (3.68) can then be written as

$$\alpha(\eta\omega) = \frac{\omega\mu ce^2 m^* K_b T}{\pi\eta^2 L n_r} \sum_{i<f} \ln\left\{\frac{1+\exp[(E_F - E_i)/K_b T]}{1+\exp[(E_F - E_f)/K_b T]}\right\} \times < z >^2 \frac{(\Gamma/2)}{(E_{if} - \eta\omega)^2 + (\Gamma/2)^2} \quad (3.71)$$

For the InGaAs/AlAs material system, it has been reported that $\Gamma \approx 30$ meV [96,130] and this value has been used in all simulations in this work. The peak of the absorption occurs therefore at a photon energy $\hbar\omega = E_{if}$, i.e. the separation between the subbands. Parameter values in Eq. (3.71) that are generally used are [180]: $m^* = (m_w^* L_w + m_m^* L_b)/(L_w + L_b)$ where $m_w^* = 0.043 m_0$ and $m_b^* = 0.15 m_0$ [181]; $n_r = (n_w L_w + n_b L_b)/(L_w + L_b)$ where $n_w = 3.43$ and $n_b = 2.89$ [14,174].

3.7 Band Nonparabolicity Effects in ISBT

3.7.1 Band Nonparabolicity Effect

In practice, most of the electronic properties of a semiconductor are defined by the lowest minimum of the conduction band and the top maximum of the valence band. In the simplest effective mass formalism [Eq. (3.9)], the energy band variation in **k** space is treated as parabolic (dashed line Fig. 3.11), which is valid only very close to the high symmetry points of **k** space. Electrons are assigned an effective mass that is the inverse of the second derivative of the energy, $m^* = (\frac{\partial^2 \varepsilon_k}{\partial k^2})^{-1}$, evaluated at the conduction band minimum. For low energy electrons, this single-band approximation is appropriate for many semiconductors. For example, the conduction band in GaAs has a singly degenerate band minimum at the Γ point, with $m^* \approx 0.067 m_0$. However, this parabolic approximation does not give good results for narrower direct band gap semiconductors ($E_g \leq 1$ eV) [182,183], or in general for high-energy electrons in the effective mass equation [184,185]. For values of **k** far from the minimum of the conduction band, the energy deviates from the simple quadratic expressions and nonparabolicity occurs [185,186] (solid line in Fig. 3.11). The deviation of the real

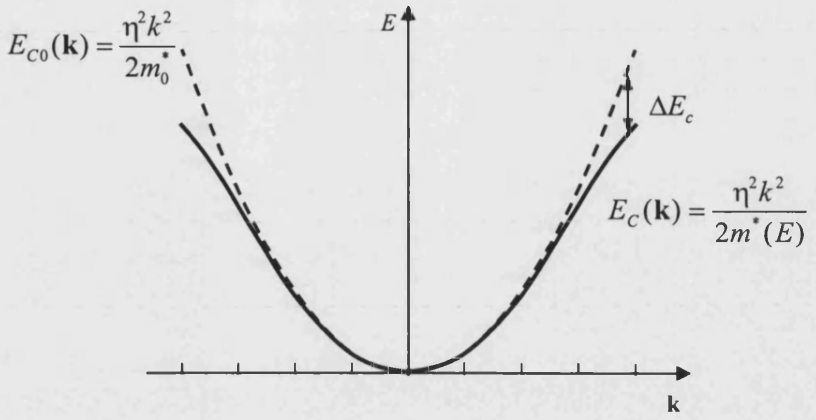

Figure 3.11: Band nonparabolicity effect on conduction band energy dispersion.

band from the parabola is called the energy band nonparabolicity. In order to obtain accurate eigen-energies for higher energy electrons in the effective mass approximation, the nonparabolicity of the conduction band must be taken into account.

3.7.2 Energy Dependent Effective Mass Approximation

One way to overcome this problem is to consider the electron effective mass to be a continuous function of electron energy [187]. The effect of band nonparabolicity is then taken into account by using the energy-dependent effective mass $m^*(E)$ based on $\boldsymbol{k}\cdot\boldsymbol{p}$ perturbation theory [188]. This is given by,

$$E_C(\mathbf{k}) = \frac{\eta^2 k^2}{2m^*(E)} \tag{3.72}$$

where

$$m^*(E) = m_0^*(1 + \alpha_{non}E) \tag{3.73}$$

where α_{non} is the nonparabolicity parameter, and $m_0^* \equiv m^*(0)$ refers to the mass when E=0. With this correction, the validity of the effective-mass approach can be extended to higher energies. In particular, it provides a reasonable approximation to the full-band density of states in the conduction band of silicon up to almost 2eV

[189]. From the two-band Kane model [186], the energy scale for nonparabolicity is set by the bandgap, E_{gap}, as $\alpha_{non} = 1/E_{gap}$. This expansion can be continued to higher orders in energy. For the correction of nonparabolicity, expressions with additional parameters containing terms up to fourth order in k have been reported [184].

In this thesis, only the first-order energy correction to the effective mass in quantum well structures is considered. This correction depends on a single parameter, which can be easily determined by comparing model predictions with experimental results. By using the energy dependent effective mass approximation based on Bastard's three band model, the energy-dependent effective masses are given by [186]

$$\begin{aligned} m_w^*(E) &= m_{0,w}^*\left(1+\frac{E}{E_{g,w}+\Delta_w/3}\right) \\ m_b^*(E) &= m_{0,b}^*\left(1-\frac{V_b-E}{E_{g,b}+\Delta_b/3}\right) \end{aligned} \tag{3.74}$$

where $E_{g,w}$ and $E_{g,b}$ are the energy gaps between the conduction and the light-hole valence bands in the well and barrier materials, and Δ_w and Δ_b are the energy splitting between the light-hole and split-off valence bands in the well and barrier materials, respectively. For the material system chosen in this thesis, $E_{g,w}$ = 0.816 eV, $E_{g,b}$ = 2.95 eV [190,191], Δ_w = 0.33 eV and Δ_b = 0.28 eV [181].

The nonparabolicity causes a lowering of subband edge energies of higher subbands and the effect becomes substantial for the highest subband edges. For instance, there is about 60 meV less in intersubband transition energy when including the band nonparabolicity effect in calculations for the 5.0 nm wide InGaAs/InAlAs quantum well with 0.5 eV band offset. For the deeper InGaAs/AlAs quantum well, such effects on the transition energy will be more significant and vital. Therefore, the nonparabolicity need to be included as compared to the exchange-correlation or the depolarization shift with normally ~10 meV changes [151,161,214].

3.8 Validity of the Model

Having developed the self-consistent Poisson-Schrödinger approach and the correction of nonparabolicity, the next step is to check the validity and accuracy of the models. The self-consistent approach is applied and compared to the case of $In_{0.53}Ga_{0.47}As$/ $In_{0.52}Al_{0.48}As$ MQW structures [192]. It is also applied to the case of InGaAs/AlAs quantum structures [94]. The material parameters used in the calculations are the same as those used in reference 94 and 192. The objective of this exercise was to test the envelope-function approximation including the band nonparabolicity correction by investigating the discrepancy of the subband energies and transition energies in different material systems. The results of simulations are shown in Fig. 3.12. Also shown for comparison is the calculated eigen values reported in the literature. The model described here produced excellent agreement. The advantages of the model developed in this chapter are that it gives the numerical wavefunctions and eigen states under different conditions of applied electric field and doping, and accurately treats the effect of nonparabolicity of subbands on the effective mass.

3.9 Summary

To determine the electric field dependent effects in ISBA, a model for subband energy levels using an envelope-function approximation and taking band nonparabolicity into account is developed in this chapter. The physics of quantum confined structures are first discussed in Section 3.2. The effective mass approximation, which is widely used in device analysis, is also described in this section. This approach is applied to solve for the conduction band states in quantum wells numerically in section 3.3. The theory of the Poisson solver is described in Section 3.4. The model is applied to the structure above for the simulation of the net charge, electrostatic potential and electric field distribution in this structure and the numerical solver is presented in Section 3.5. In section 3.6 the method of calculating the optical absorption coefficient for bound-to-bound ISBTs is presented. In addition,

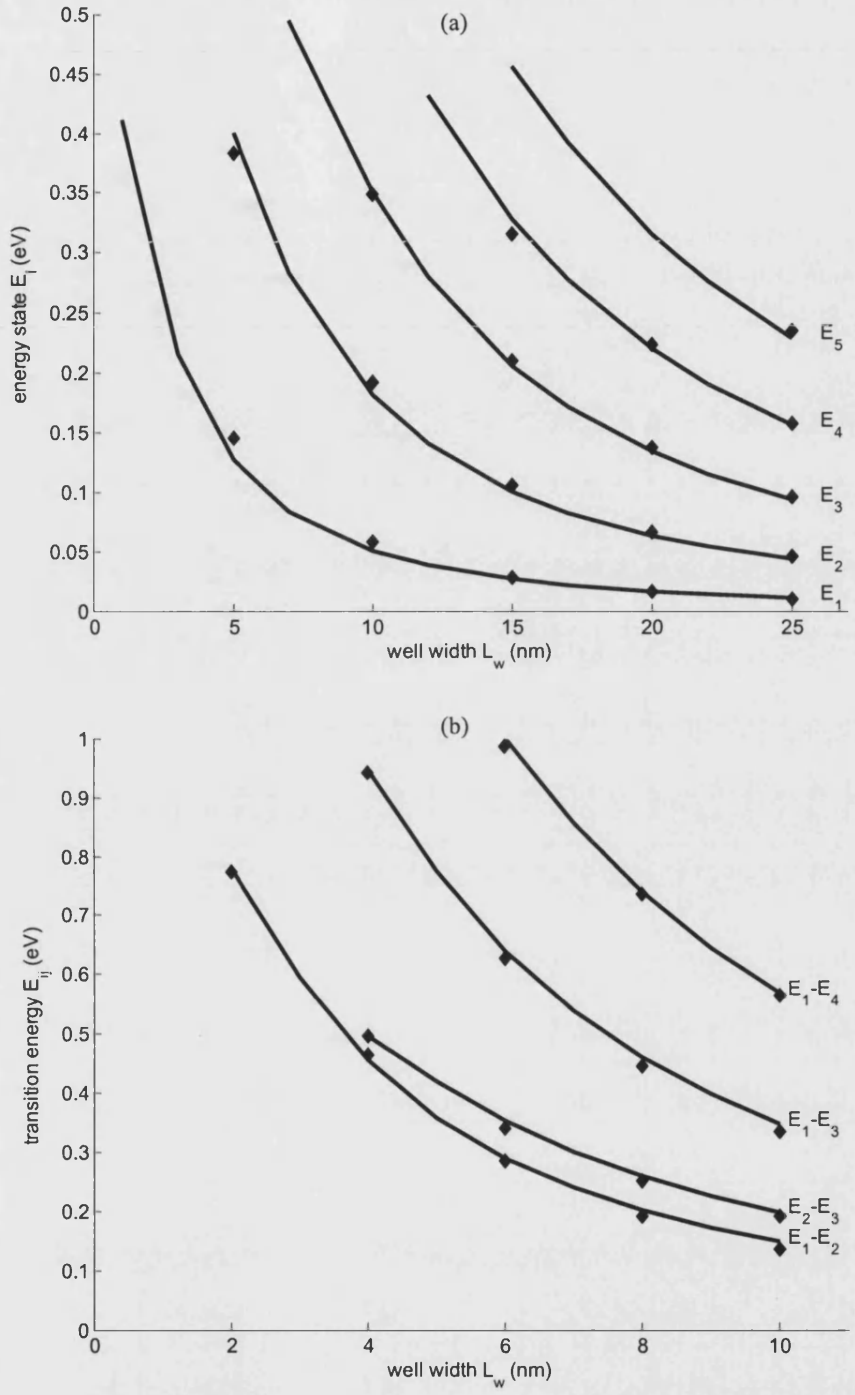

Figure 3.12: (a) The subband energies of InGaAs/InAlAs and (b) the transition energies between subband levels of InGaAs/AlAs quantum well structures as a function of well width. The lines are the theoretical results of the self-consistent model taking into account band nonparabolicity. The solid diamonds indicate data adopted from ref. [94] and [192].

nonparabolicity is included in the calculation to account for the correct dependence of the absorption coefficient in Section 3.7. Finally, the accuracy and validity of the model developed is compared to other literature results in Section 3.8.

CHAPTER 4

Simulation Results

4.1 Introduction

Based on the model and numerical solvers developed in last chapter, the electro-absorption modulation of different structures is calculated and compared in this chapter. Briefly, the calculations were performed by iteratively solving the Poisson and Schrödinger equations until the result approaches stable values. Then, with the accurate confined energies and envelope wavefunctions, the intersubband absorption coefficient can be calculated by using widely accepted material parameters which were given in previous chapter. Thereby, the electroabsorption can be completed by calculating intersubband absorption (ISBA) under different external conditions.

The assumed quantum well structures used in the calculation consisted of $In_{0.53}Ga_{0.47}As$ well(s) (one, two or three wells according to specified structures in the following sections), two thick outer AlAs barriers (spacers) with a constant thickness of 10.0 nm on the both sides confining all quantum wells, and may also include thin inner AlAs barrier(s) separating the wells in all simulations. To distinguish these two types of AlAs layers, hereafter, the former was called "outer barrier" and the latter called "inner barrier". In the following simulations, all wells will have the same thickness, L_w, and all inner barriers will have the same thickness, L_b. They are the two free structure parameters to be optimised. The example of a three well structure is shown in Fig. 4.1 to demonstrate the definitions of outer barriers, quantum wells and inner barriers, their parameters and symbols used in later discussions.

The whole well and barrier construction was embedded in the middle of the intrinsic InP region [see Fig. 3.1 (a)]. Both inner and outer barriers were considered as prospective areas to insert modulation doping. In all simulations presented in this chapter, the modulation doping in the selected barrier(s) constituted an n-doped sheet of 1.0 nm thickness with a doping density (N_D) and located in the centre of corresponding AlAs layers as shown in Fig. 4.1, i.e. the distances between the well-barrier interface and the centre of the doped sheet located for inner and outer

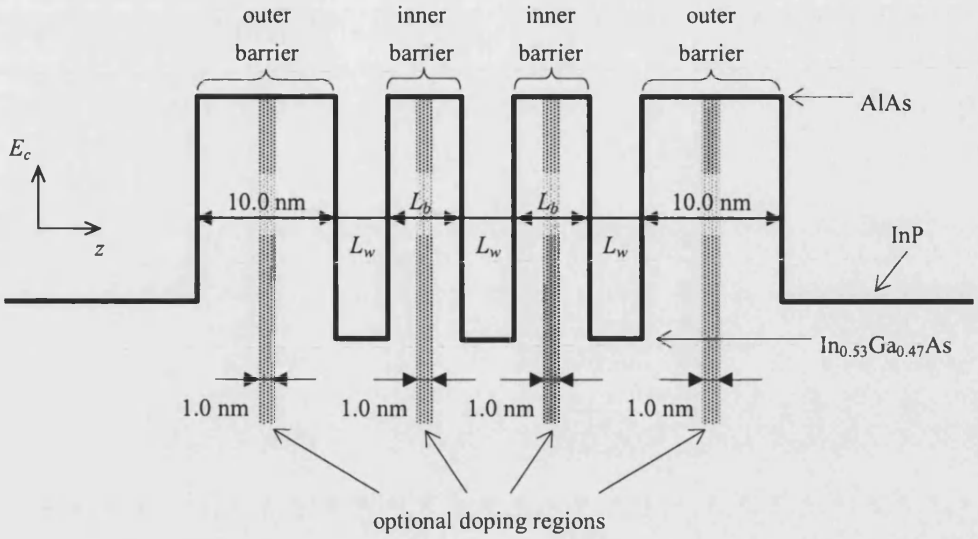

Figure 4.1: The schematic potential profile of quantum wells embedded in the middle of intrinsic region. The well width (L_w) and the inner barrier width (L_b) are variable while the thickness of the outer barriers (10.0 nm) and the doping layers (1.0 nm) are constants in all simulations.

barrier were $L_b/2$ and 5.0 nm, respectively. The rest of the intrinsic region was consider to have a uniformly low *n*-type doped of $1\times10^{15}/cm^3$ due to residual unintentional doping, instead of considering an ideal intrinsic region which was free of carriers. For the modulation doping, there are two free parameters: the doping density and the doping location. In the case of no modulation doping applied to any barrier, the structure is described as "undoped". The *n*-type region of the *i-n* junction was assumed as being uniformly doped to 1×10^{18} donors/cm^3 in all structures. The self-consistent approach was then applied to these $In_{0.53}Ga_{0.47}As$/AlAs quantum well structures, the material parameters of which were given in the Chapter 3. A step size of 0.1 nm was used as the distance increment in all numerical simulations. Adopting a smaller step size had little effect on the results discussed in this chapter.

The main objective of the Poisson solver developed in the previous chapter is to calculate the potential profile, the field distribution and the net charge concentration throughout the Schottky diode, which can be considered as a limiting case of a *p-i-n*

or an *n-i-n* diode as indicated in Fig. 3.1. The reduced potential (η) and the conduction band profile (E_c) can be converted into each other simply by multiplying a constant according to Eq. (3.38). The electric field (F) is proportional to the first derivative of reduced potential with respect to distance while the net charge (ρ) to the second derivative, i.e. $F \propto \frac{d\eta}{dz}$ and $\rho \propto \frac{d^2\eta}{dz^2}$, respectively. These simulation results are variable and depend on initial conditions, such as applying external bias, doping locations and doping densities.

In the case of a fully depleted diode, if heavy doping levels are assumed in the *p*- and *n*-type regions of the diode, a uniform electric field can be assumed throughout the intrinsic region and the presence of quantum wells in the intrinsic region will not alter the electric field distribution much compared to the case of a diode without the quantum wells. But when excess carriers are present in the intrinsic region, which will be the focus in this work, the field distribution is non-uniform implying that different field strength will occur in each quantum well. For research and practical purposes, the field strength used in any graph is chosen as the average value inside the quantum wells. For simplification, the "electric field" mentioned in the following sections actually means the "average electric field strength across the quantum wells" (F_{av}). Since the electric field is perpendicular to the quantum well, its sign can indicate the direction of electric field. A positive value denotes the field directed towards plus infinity along *z* axis (the epitaxy growth axis) while a negative field is one directed towards minus infinity.

A three-well structure was simulated and illustrated in Fig. 4.2 as an example for showing the correlation between η, E_c, F and ρ. The numerical result for the structure was performed under F_{av} equalled to 0 V/μm and -15 V/μm. As can be observed clearly, the reduced potential in Fig. 4.2 (a) resembles the potential profile in Fig. 4.2 (b) but with an upside-down shape due to the negative constant factor in Eq. (3.38).

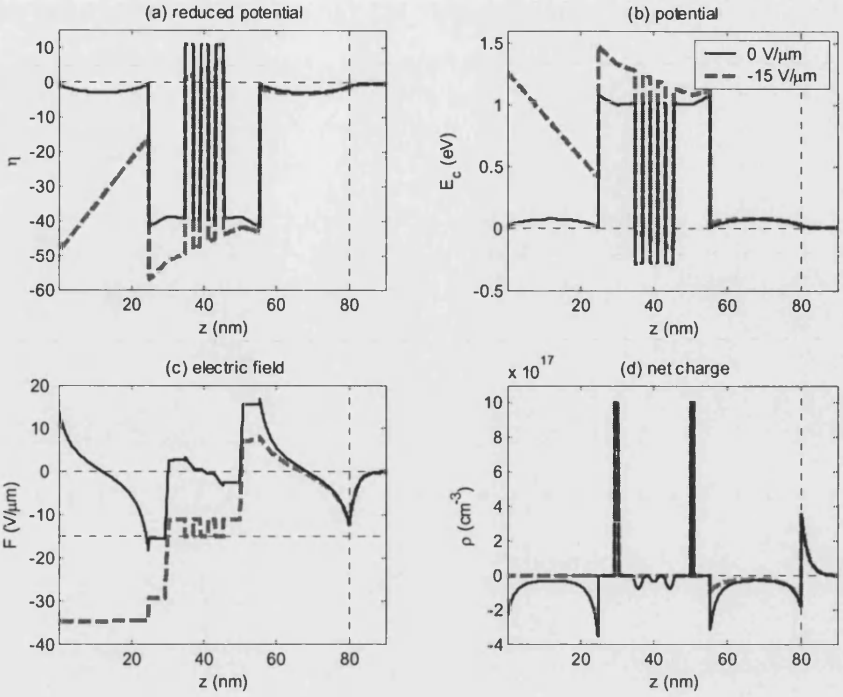

Figure 4.2: (a) The reduced potential, η, (b) the potential profile of conduction band, E_c, (c) the electric field, F, and (d) the net charge distribution, ρ, under the average field strength across the wells (F_{av}) to zero (solid line) and -15 V/μm (dashed line). The vertical dotted line at z = 80 nm indicates the interface of the *i-n* junction.

The potential slowly attained a constant value in the *n*-type region. The position-dependent electric field in the structure is shown in Fig. 4.2 (c), and net charge distribution (sum of negative electron and positive ionised donor densities) in Fig. 4.2 (d). The dielectric constant steps between different materials causes the step changes in electric field as shown in Fig. 4.2 (c). The presence of carriers in the intrinsic region alters the net charge distribution significantly. The net charge curve at F_{av} = 0 V/μm in Fig. 4.2 (d) clearly demonstrates the existence of the two dimensional electrons in the wells. This accumulation of the carriers in the wells vitally affects the electric field.

There is electric field jump at the interfaces due to the piecewise constant of dielectric permittivity, indicating the interface condition given in Eq. (3.58). At zero

field, the potential near the quantum wells was symmetric, but varied non-linearly with distance. In addition, the average electric field strength was zero only in the middle well, while the well on the left hand side had a positive value (~2.1 V/μm) and the one on the right hand side had a negative value (~ -2.1 V/μm) in this particular case [solid line in Fig. 4.2(c)]. When the average electric field in the wells reached -15 V/μm, an increase in the average electron potential in the wells was clearly observed. The electric field in each well was approximately the same due to the low density of electrons gathered in the wells. In effect, the structure was fully depleted when this average field strength was achieved across the wells in the designated negative field direction.

As mentioned in Chapter 3, the numerical Poisson solver started from the *n*-type region and calculated in sequence from right to left in the scenario illustrated in Fig. 4.2. The first input value in the solver is η_{in} and the last output value η_{out}, which is the reduced potential in the interface between the intrinsic region and Schottky contact. The value η_{out} can be converted into the surface potential, V_{surf}, again by using Eq. (3.38). According to the shooting method used in Poisson solver, each different η_{in} started from the flat band condition deep inside in the *n*-type region of the diode will result in a different but physically valid surface potential (valid to within the numerical error). Each potential profile also corresponds to a valid average value of electric field inside the wells. Therefore, by choosing a series of suitable value of η_{in}, electroabsorption spectra under different electric field can be computed efficiently without iteration, which is unlike the case of pre-defined values of surface potential. This enables a computationally efficient determination of the voltage (i.e. surface potential) dependence of the optical and electrical properties of the various structures considered. Figure 4.3 shows V_{surf} and F_{av} as a function of η_{in} of the three-well structure given in Fig. 4.2. As an example, when η_{in} = -0.395717, V_{surf} = 0.75 eV and F_{av} = -10.4 V/μm in this structure. Structure properties for a defined value of surface potential, e.g. corresponding to -1 V bias applied on the Schottky contact, can be

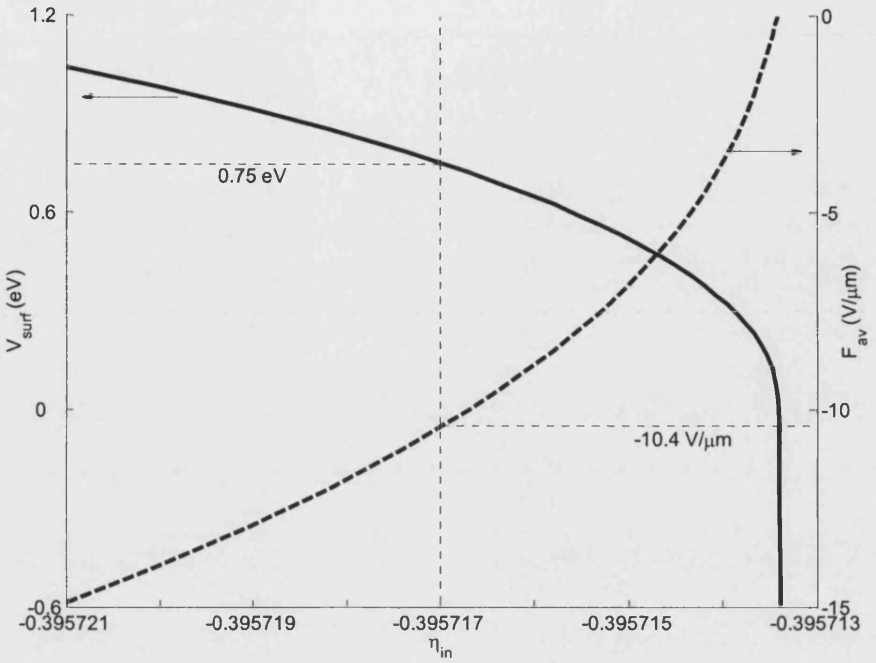

Figure 4.3: Output surface potential (V_{surf}) and average electric field across the well (F_{av}) as a function of input reduced potential (η_{in}).

found either by interpolation or by iteratively varying η_{in} until a self-consistent solution is obtained. Notably, the results in Fig. 4.3 show non-linear, hence nontrivial, relationships between V_{surf} and η_{in}, and F_{av} and η_{in}. This demonstrates the need for a robust self-consistent computational method. The detail of these non-linear relationships will depend on the inclusion of modulation doping.

4.2 Simulations of Single Quantum Well (SQW) Structures

The simplest structure, the single quantum well (SQW), was first investigated. The well width is one of the key parameters for determining the energy of the intersubband absorption peak. Since the 1.55 μm communication wavelength (0.8 eV) is at the core of this work, the influence of well width on the transition energy is shown in Fig. 4.4 for selecting a suitable well width. In order to achieve intersubband

transitions (ISBTs) at 0.8 eV in a SQW structure, the required well width will be determined by the transition E_i - E_f. Based on the band offset and effective mass data [163,164,181], 0.8 eV transitions can be achieved by the following well widths for $In_{0.53}Ga_{0.47}As$/AlAs SQWs pseudomorphically grown on InP substrate: 2.2 nm (E_1-E_2), 5.0 nm (E_1-E_3), 5.5 nm (E_2-E_4) and 7.6 nm (E_1-E_4). These possibilities will be discussed in detail in the following sections.

4.2.1 Effects of Well Width (L_w) on ISBA in SQWs

Three structures with different well width were carefully selected to investigate the electric-field-induced modulation of ISBTs at input photon energies of 0.8 eV. The structures compared in this section were 2.2 nm, 5.0 nm and 7.6 nm wide InGaAs SQW, all confined by two 10.0 nm wide AlAs outer barriers. These well widths were chosen as being representative of structures that demonstrate significant physics behind ISBA modulation. The 5.5 nm was not selected because of the negligible absorption near 0.8 eV and this justification will be given later in this section. No modulation doping was applied to all three structures and the whole intrinsic region was uniformly low n-type doped to $1\times10^{15}/cm^3$ as commented before.

SQW structures with well width of 2.2 nm, 5.0 nm and 7.6 nm, in which 2, 3 and 5 bound states are generated, can support superficially 1, 3 and 10 different transitions between various pairs of confined particle states, respectively. With reference to Fig. 4.4, it can be seen that ISBA at 0.8 eV should occur in principle between the E_1 and E_2 states, between E_1 and E_3 states and between E_1 and E_4 states in the 2.2 nm, 5.0 nm and 7.6 nm wide well, respectively. Figure 4.5 shows the normalised absorption spectra of these three structures at F_{av} = -1 V/μm. For 2.2 nm and 5.0 nm well widths, there is only one peak in both absorption spectra. This arises from the E_1-E_2 transition. On the other hand, two absorption peaks are observed for the 7.6 nm wide SQW. These correspond to the transitions E_1-E_2 and E_1-E_4. In these structures, it turns out that ISBA is significant only between certain initial and final states.

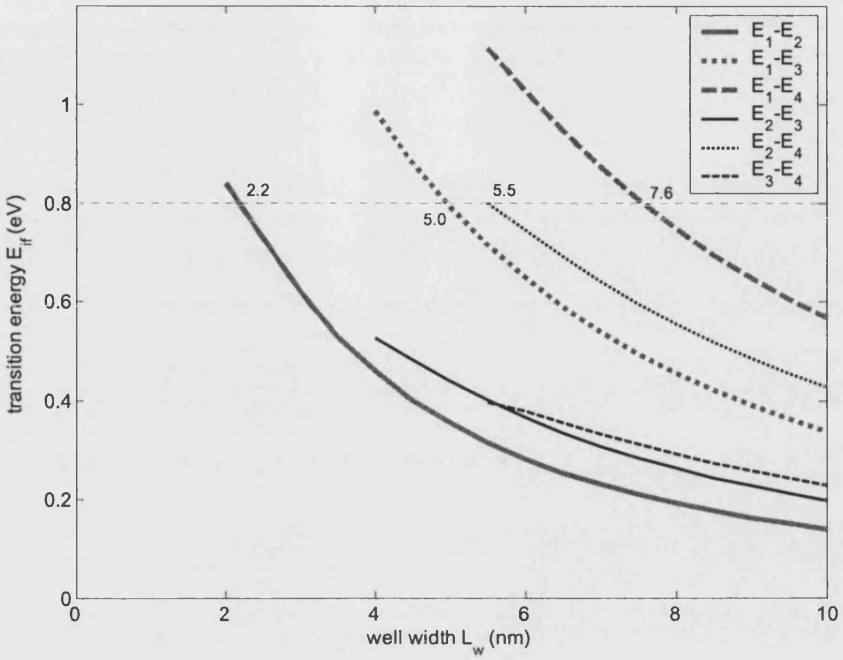

Figure 4.4: Calculated transition energies (E_{if}) as a function of well width (L_w) in the $In_{0.53}Ga_{0.47}As$/AlAs SQW.

Referring to Fig. 4.4, the energy states E_1 and E_3 should provide a possibility of ~0.8 eV transition in the absorption spectra in the 5.0 nm SQW. However, such transition is actually restrained and not observed in Fig. 4.5 due to the parity selection rule. The same restriction on ISBTs applies in the 5.5 nm SQW and therefore its simulation was not repeated. Unlike the 5.0 nm SQW, an observable peak near 0.8 eV is achieved in the 7.6 nm SQW. However, the absorption intensity at 0.793 eV (E_1-E_4 transition) is only about one eighth of the strongest absorption at 0.204 eV (E_1-E_2 transition). The oscillator strength of E_1-E_2 transition is estimated about 30 times stronger than that of E_1-E_4 transition [193]. The difference in the value of the absorption peaks arises from the difference in the optical matrix elements of the E_1-E_2 and E_1-E_4 transitions [see Eq. (3.69)]. Similar to the E_1-E_3 transition in the 5.0 nm SQW, the E_1-E_3 transition in the 7.6 nm SQW (~0.5 eV) was also inhibited. In general, the prohibition and the different strengths of the ISBA depend on the value

of optical matrix elements between the confined particle states. In turn, the optical matrix elements are governed by the parity selection rule for the weak electric field in symmetrical structures. This is discussed further later in this section.

Moreover, Fig. 4.5 shows that dominant ISBA takes place between the lowest two energy states, i.e. E_1-E_2, and this transition energy decreases with increasing the well width, which occurs at 0.800 eV (1.55 μm), 0.355 eV (3.49 μm) and 0.204 eV (6.08 μm) in the 2.2 nm, 5.0 nm and 7.6 nm SQWs, respectively. As a consequence, utilising the transition between the lowest two energy bands is the most efficient configuration in ISBA modulators. Due to the weak modification of the transition energies by the electric field in SQWs, the spectral position of the absorption peak, when determined by the well width dependent E_1-E_2 transition, can be estimated from Fig. 4.4.

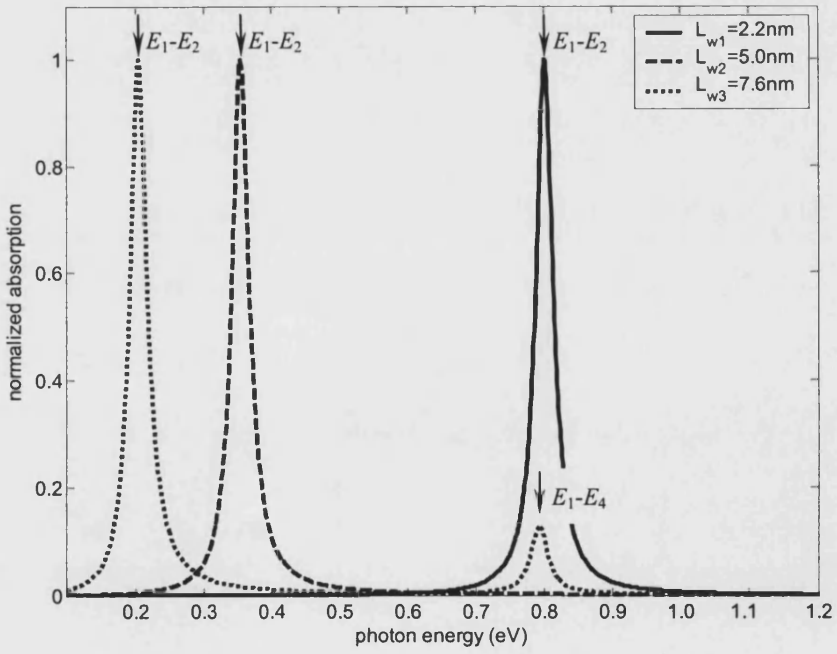

Figure 4.5: Normalized absorption spectra of three undoped structures: 2.2 nm, 5.0 nm and 7.6 nm wide SQWs. The average electric field is at -1V/μm.

For gaining insight into the similarities and differences in the characteristics of these three SQW structures relying on electric field, four important factors that contribute to the ISBA of 2.2, 5.0 and 7.6 nm SQW are shown in Fig.s 4.6, 4.7 and 4.8 respectively in the range of F_{av} = 0 ~ -15 V/μm. The four sub-plot graphs in each figure correspond to the electric field dependence of (a) the transition energy (E_{if}), (b) the maximum absorption coefficient [max(α_{if})], (c) the absolute value of optical matrix element or overlap integral ($|<\psi_f|z|\psi_i>|$ or $|<z>|$) and (d) the Fermi occupancy ratio ($\ln\left\{\frac{1+\exp[(E_F-E_i)/k_BT]}{1+\exp[(E_F-E_f)/k_BT]}\right\}$) between the initial state (i) and final state (f) for each ISBT. The Fermi occupancy ratio is proportional to the electron density difference (N_i - N_f) with a constant of the effective density of states [see Eq. (3.70)] and is selected to reveal the importance of occupation of state in ISBA. Since the Fermi energy (E_F) is chosen as the reference energy level throughout the structure, i.e. E_F = 0, the Fermi occupancy ratio is dominated essentially by the values of E_i and E_f. According to Eq. (3.71), the matrix element and Fermi occupancy ratio are the two governing factors in determining the value of absorption coefficient while the rest are constant values. Inspection of sub-plots (c) and (d) in Fig.s 4.6 - 4.8 will reveal the significance of each contribution to the electroabsorption modulation.

For the 2.2 nm SQW, there was about 0.56 meV decrease (Stark shift) in the energy at which the maximum of the absorption peak occurs as F_{av} changed from 0 to -15 V/μm as shown in Fig. 4.6 (a). This electric field dependence of the transition energy is very small compared to the Quantum-Confined Stark Effect (QCSE) observed for interband transitions in a quantum well [22,54,60]. In Fig. 4.6 (b), the maximum absorption decreased almost linearly on a logarithmic scale, which means α is exponential decay versus F_{av}. Moreover, the optical matrix element remained basically the same in Fig. 4.6 (c) while the Fermi occupancy ratio was dramatically changed in Fig. 4.6 (d), again almost linearly on a logarithmic scale. By comparing Fig.s 4.6 (b) and (d), the variations in the absorption intensity and Fermi occupancy

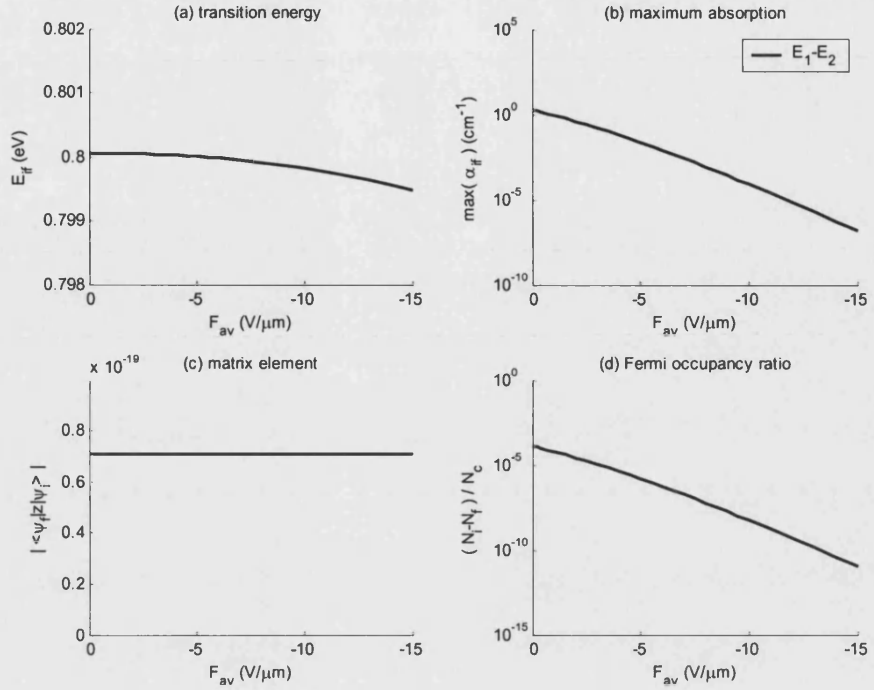

Figure 4.6: The electric field dependence on (a) transition energy, (b) maximum absorption, (c) optical matrix element and (d) Fermi occupancy ratio in an undoped 2.2nm SQW.

ratio with electric field are close to each other. Therefore, it is concluded that the change in the Fermi occupancy ratio with electric field is the dominant mechanism in the characteristics of the electroabsorption modulation in this structure.

For the 5.0 nm SQW, when the F_{av} increased from zero to -15 V/μm, there were 1.6 meV blue shift, 1.4 meV blue shift and 0.2 meV red shift in the transition E_1-E_2, E_1-E_3 and E_2-E_3, respectively, as shown in Fig. 4.7 (a). Again, compared with the QCSE, the field-dependent energy shift is negligible, although somewhat larger than for the 2.2 nm wide SQW. In Fig. 4.7 (c), the value of $|< z >|$ for the E_1-E_3 is zero at F_{av} = 0, giving as a consequence the extremely weak absorption strength near zero electric field shown in Fig. 4.7 (b). Although the matrix element of E_1-E_3 transition appears to increase dramatically depending on the raise of field strength, it is in fact a very small change when compared to the $|< z >|$ for E_1-E_2 and E_2-E_3 (note the scale

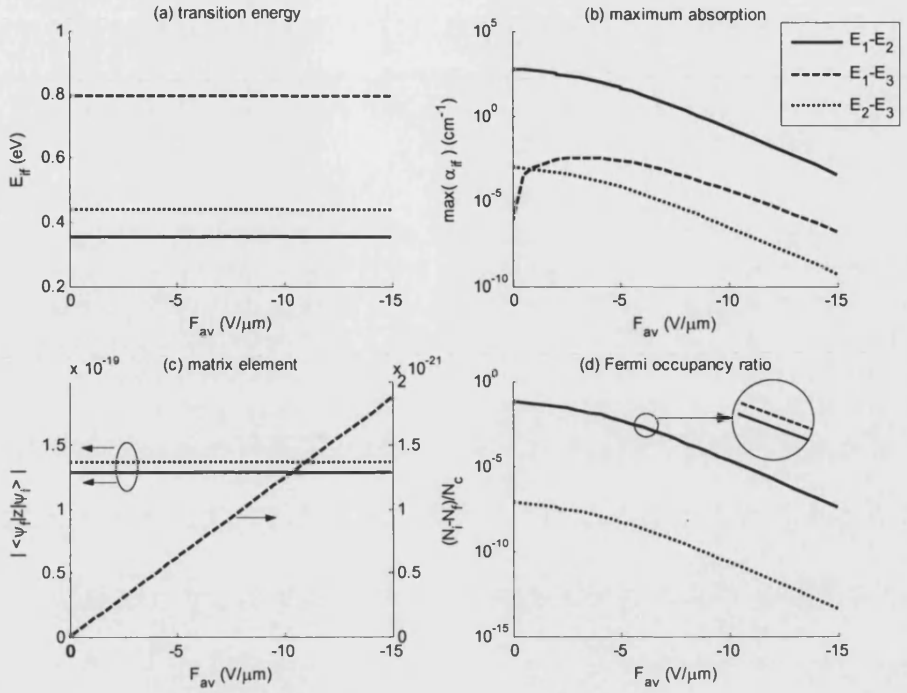

Figure 4.7: The electric field dependence on (a) transition energy, (b) maximum absorption, (c) optical matrix element and (d) Fermi occupancy ratio for different ISBTs in an undoped 5.0nm SQW.

change). As a consequence, the trend of the maximum absorption for the E_1-E_3 transition first increases with increasing electric field and then decreases at higher field in Fig. 4.7 (b). However, its contribution to absorption is always several orders of magnitude smaller than that of the dominant E_1-E_2 transition.

For the 7.6 nm SQW, there are 10 possible transitions between two different states. In order to clearly show the dominant mechanism, the absorption between excited states (i,f > 1) is much weaker than that from the ground state (i = 1) to excited states (f > 1) and hence is neglected in Fig. 4.8. Over the same range of applied electric field as in the two structures above, the transition energies of E_1-E_2, E_1-E_3, E_1-E_4 and E_1-E_5 were increased by 5.80, 5.15, 4.90 and 3.21 meV, respectively. By associating with the results in 2.2 and 5.0 nm SQW, it shows that the energy shift caused by the applied electric field is stronger in the wider well structure. This arises from the

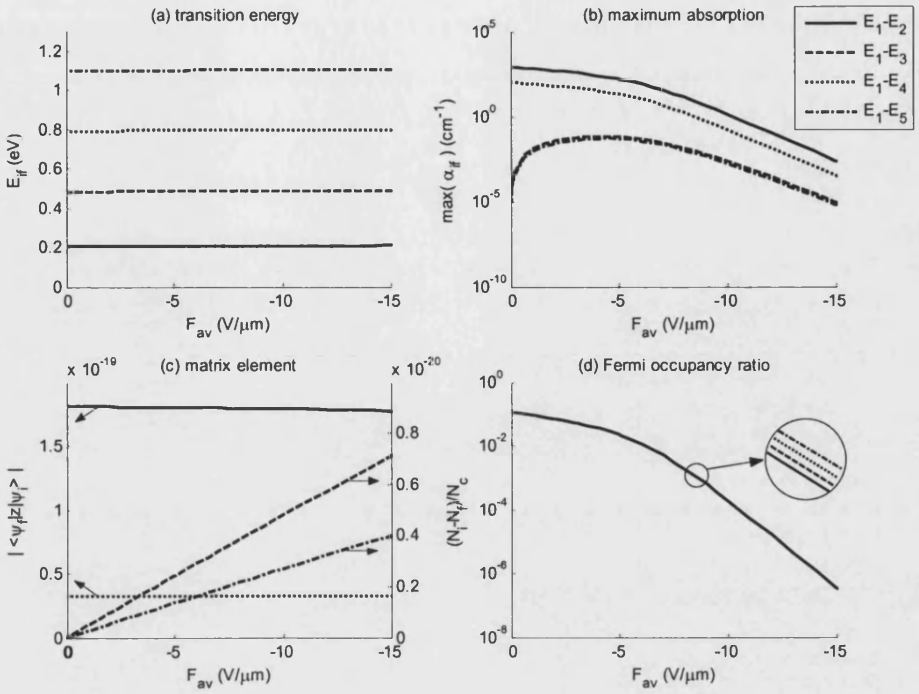

Figure 4.8: The electric field dependence on (a) transition energy, (b) maximum absorption, (c) optical matrix element and (d) Fermi occupancy ratio in an undoped 7.6nm SQW. Only the transitions from ground state (E_1) to excited states (E_2, E_3, E_4 and E_5) are shown.

greater freedom of the envelope wavefunctions to distort in a wider well as an electric field is applied. The enhanced wavefunction distortion reflects the increase in stored electrical energy ($\frac{1}{2}D \cdot F$, where D is the displacement vector and F the electric field) that arises from the effective charge distribution in the well and rearranges itself on applying the electric field. Again in Fig. 4.8 (b), for $F_{av} \approx 0$, the transitions E_1-E_3 and E_1-E_5 are forbidden corresponding to the zero values of $|< z >|$ in Fig. 4.8 (c). By comparing Fig.s 4.7 (d) and 4.8 (d), one can see that the Fermi occupancy is high only in the initial state at ground state (E_1) in the ISBA, which is an important factor to achieve large absorption. Besides, with the same initial state (E_i), different final states (E_f) have only a slight effect on Fermi occupancy ratio because of the almost empty excited states. Therefore, in order to increase the absorption rate, making E_i smaller, i.e. closer to the Fermi energy, is a more efficient

way in all three structures owing to the dominant contribution of the change in the Fermi occupancy ratio of the ground state with electric field to the absorption modulation.

The presence of an assumed background doping in the *i-n* diode means that even with a zero bias applied to the structure, there is still an electric field across the SQW. In the structures considered in Fig.s 4.6 - 4.8, the background doping in the wide intrinsic region was assumed to be 1×10^{15} donors/cm^3. With such low doping, a surface potential of $V_{surf} \approx 0$, or a low value, gives rise to only a very small electric field across the well. Consequently, the potential profile across the well is virtually symmetrical.

In the symmetrical quantum well structure, the envelope wavefunction is either symmetric or anti-symmetric function with respect to the bisection plane of the well (a *x-y* plane parallel to the well-barrier interfaces) corresponding to the parity of the confined energy band's index, as mentioned in Chapter 3. The envelope functions ψ_f and ψ_i are functions of z only and are orthogonal to each other. The bisection plane of the quantum wells is set as the origin for calculating the matrix element $|< z >|$. Thus, the value of $|< z >|$ is equal to zero when the index i and f have the same parity. This is the parity selection rule as mentioned in Chapters 2 and 3. However, when electric field increases and breaks the symmetrical potential profile, the symmetry of the envelope functions is also broken. The examples of the low optical matrix elements of E_1-E_3 in 5.0 nm SQW, and E_1-E_3 and E_1-E_5 in 7.6 nm SQW are the embodiment of the parity selection rule due to the unfavourable symmetry of the envelope wavefunctions. As a consequence, the variation of $|< z >|$ in parity-forbidden transitions reveals the extent in which the field effect causes the selection rule to break down. By the same token, electric field induced distortions of the envelope functions will also cause a change in the probability of parity-allowed transitions which normally decreases as field strength increases.

In the SQW structures considered above, the results show that the breakdown in the parity selection rule for both allowed and forbidden transitions has only a small effect on the absorption strength of the ISBTs. In general, the behaviour of absorption peak within all structures shows a good agreement to the Fermi occupancy ratio. Only transitions forbidden by the parity selection rule near zero field showed significant increase in absorption strength but this absorption remained several orders of magnitude lower than that of the allowed transitions, even at their peak strength.

According to the calculations and results presented, the well width should be chosen near 2.2 nm, which is about 8 monolayers (MLs) in the $In_{0.53}Ga_{0.47}As$/AlAs material system, for achieving 1.55 μm wavelength ISBT. This well width is larger than the experimentally measured value. For instance, Smet *et al* [139] have reported an ISBT wavelength of 1.55 μm for 3 ML-thick InGaAs/AlAs quantum well but his result is difficult to reproduce theoretically. Sung *et al* have demonstrated peak energy of ISBA as large as 720 meV (1.72 μm) for 6 ML-thick $In_{0.6}Ga_{0.4}As$/AlAs MQW structures with a linearly graded InGaAs buffer layer [85], which is congruous with the result of 1.798 μm wavelength (690 meV) for 6ML-thick $In_{0.53}Ga_{0.47}As$/AlAs previously proposed by Hirayama *et al* [194], and the result of 1.72 μm wavelength for 6 ML-thick $In_{0.7}Ga_{0.3}As$ quantum well with composite $In_{0.55}Al_{0.45}As$–AlAs barriers later reported by Georgiev *et al* [195]. In addition, an ISBT wavelength of 1.9 μm in 7 ML-thick [141] and a transition energy of 680 meV in 8 ML-thick [96] InGaAs/AlAs MQW grown coherently on a GaAs substrate have also been reported.

The difference between the measured and the calculated results could be caused by different degrees of strain relaxation in the strained layer structures used in the reported experiments. Strain relaxation will not only change the band gaps but also the actual band offset value (1.1 eV ~ 1.3 eV) [94] which can become less than the theoretical value of 1.3 eV used in this thesis. Consequently, the energy levels change from their theoretical values.

Also, monolayer fluctuations about the mean position of the heterojunction can occur at each well-barrier interface during epitaxial growth. In such narrow quantum wells, even monolayer fluctuations in well width can have a significant effect on the energy levels of the confined electron states. This could be another contributing reason for the discrepancies of ISBT energies between the reported measurements and the theory used in here. However, changing the well width from 2.2nm by ±1 ML in the test structures used in this work will not alter the main conclusions in the sections that follow, except for the exact position of the absorption peaks.

Additionally, the thin AlAs barriers in the experiments, normally 3~9 MLs in which the envelope wavefunctions can penetrate through, may lead to lower confined energies, while the thick outer barrier chosen in the simulation can confined electrons in the wells more completely and with comparatively larger confined energies.

Moreover, the coupling and the transfer of the indirect band-gap configuration in the Γ conduction-band state of the InGaAs well to the X conduction-band state of the AlAs barrier (Γ-X) on ISBT has been reported and may affect the thickness of the well to achieve a large transition energy [96,196]. Scattering from states derived from the Γ-valley to states associated with the X-valley can then impacts on ISBTs. Further studies are necessary to clarify these points and provide a more accurate model to simulate the ISBT energies.

4.2.2 An Undoped SQW with L_W = 2.2 nm

The optimal well width for achieving 0.8 eV transition energy in $In_{0.53}Ga_{0.47}As$/AlAs SQW structures in the AlAs layers is 2.2 nm. The assumed undoped SQW structure in the simulation consisted of a 2.2 nm InGaAs well and two 10.0 nm AlAs outer barriers. Figure 4.9 shows the conduction band profile, confined energy states and their envelope wavefunctions under the field strength of 0, -5 and -10 V/μm found

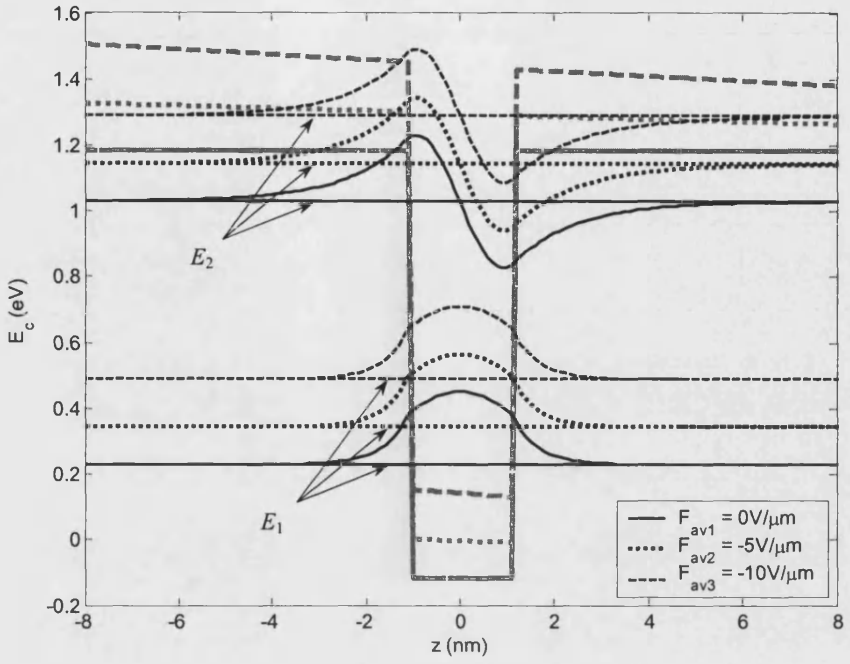

Figure 4.9: Potential profile, subband energies and envelope wavefunctions under different average field strength across the well in the 2.2nm undoped SQW.

from the self-consistent calculation. It shows that the potential profile is lifted up when the reverse average electric field strength increases. This can be explained straightforward by considering a reverse voltage applied to the diode. With this reverse bias, the surface potential on the Schottky contact [or the *p*- (*n*-) type region as shown in Fig. 3.1] increases and therefore the strength of the electric field in the intrinsic region rises. At stronger field strengths, i.e. higher surface bias, the energies of bound states (E_n) increase with respect to the reference level E_F, which corresponds to the decrease of Fermi occupancy ratio in Fig. 4.6 (d), while the shape of their envelope functions basically remains unchanged, which gives rise to the unchanged optical matrix elements in Fig. 4.6 (c).

Having calculated the subband energies and their envelope wavefunctions from the self-consistent model, the absorption coefficient can then be computed by applying Eq. (3.71). A three-dimensional plot of electroabsorption spectra versus photon

energy versus electric field is shown in Fig. 4.10. The data were obtained for field strengths from 0V/μm to -10 V/μm and photon energies in the range from 0.6 eV to 1.0 eV. The ISBA spectra are sensitive to the change in electric field, decaying dramatically and non-linearly with increasing the electric field strength. However, the energy of the absorption peak and the shape of the spectra essentially remain unchanged. In other words, the electric field has a strong effect on the intensity of absorption but only a weak influence on the transition energy in this SQW structure, as previously shown in Fig. 4.6(a). The absence of a Stark shift originates from the negligible distortion of the wavefunction with electric field in such a narrow quantum well, as shown in Fig. 4.9.

With this three-dimensional plot of the variation in absorption with electric field and photon energy, many other results can be deduced. For example, differential

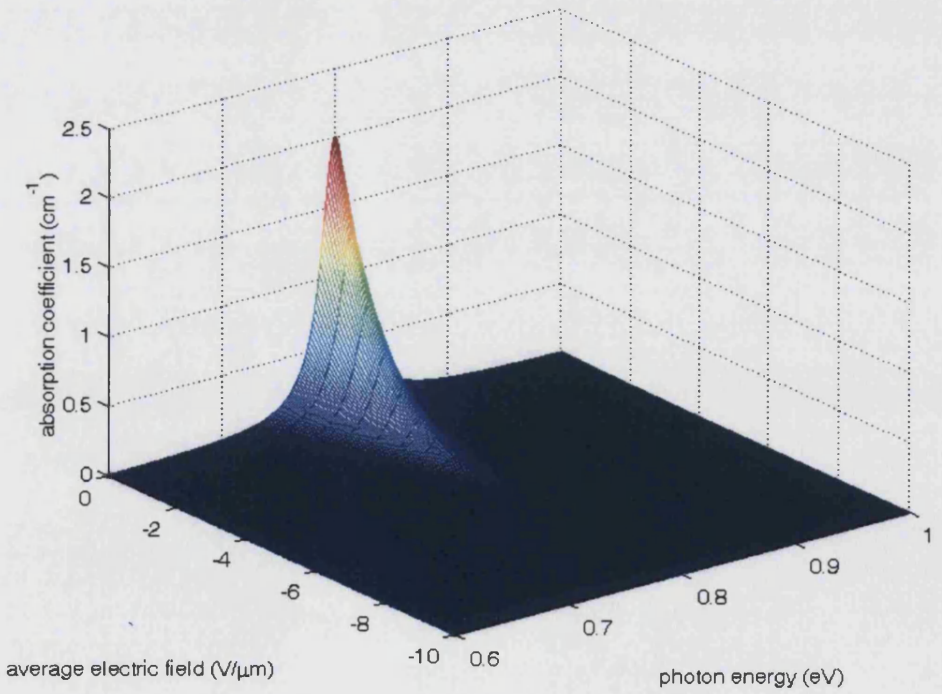

Figure 4.10: A 3D plot of absorption coefficient versus electric field versus photon energies of an undoped 2.2 nm-wide InGaAs/AlAs SQW.

absorption spectra ($\Delta\alpha$) for step changes in field strength of ΔF_{av} = -1 V/μm starting from zero to a maximum field strength of -4 V/μm are shown in Fig. 4.11. These data show that the changes in absorption are more pronounced at low applied electric fields in the structure simulated. Such plots enable the identification of optimum operating conditions in a possible modulator operating by ISBA. In order to utilise large differential absorption for a good performance of a modulator, a sensible threshold voltage and operating bias are necessary due to the correspondence between the surface potential and electric field as observed in Fig. 4.3. The structure considered here is suitable only for operation about a low quiescent built-in voltage and therefore would be effective only for structures with relatively wide depletion (intrinsic) regions where the built-in field at zero applied bias is low. Overall the large predicted absorption changes that can be induced by small changes in electric

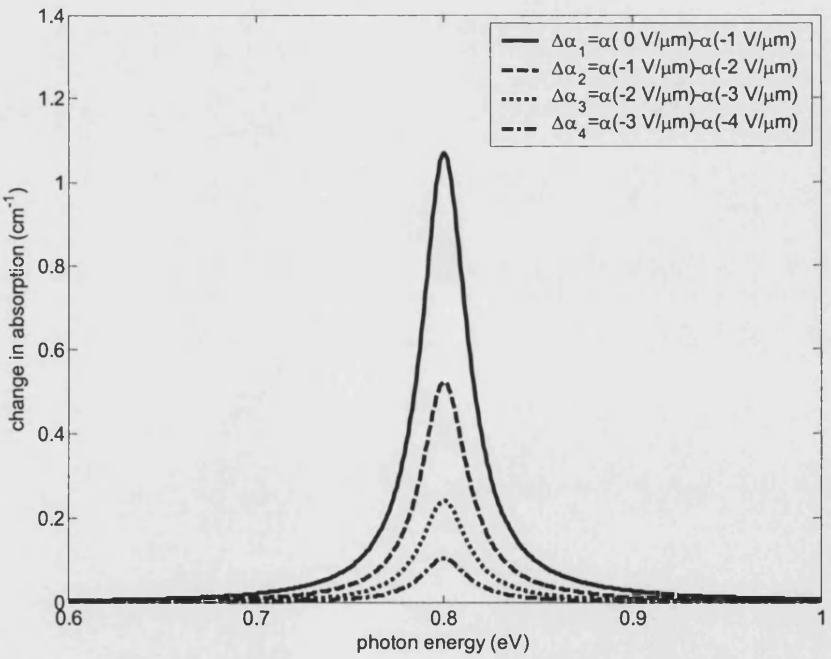

Figure 4.11: Differential absorption coefficient of a 2.2nm SQW with no modulation doping in barriers. The electric field is changed from -1 V/μm to -5 V/μm with a fixed ΔF_{av} = -1V/μm.

field strength indicate that low voltage optical modulators operating by ISBA are feasible. However, optimization of the structures for practice device operation under low current is required. This is explored in the following sections.

4.2.3 Effects of Modulation Doping in SQWs

The studies presented above only discussed the undoped quantum well structures, or precisely uniform low *n*-doped throughout the intrinsic layers. In practice, the quantum well devices are often doped [142-145]. For instance, Mozume and Georgiev have reported the photoluminescence spectra of InGaAs/AlAsSb SQW which significantly depend on the doping position and doping concentration [197]. Further, the results in previous section demonstrate that the variation in the electron occupancy of the ground state (i = 1) with electric field makes the dominant contribution to absorption modulation. Therefore, modulation doping is likely to have a major effect on electric field induced variations in ISBA. This effect is now explored thoroughly by considering the introduction of modulation doped regions with donor density varying from a low doping level ($1\times10^{17}/cm^3$) to a high one ($5\times10^{18}/cm^3$) and also by varying positions of the doped regions in the structures.

Firstly, in order to reveal the performance of modulation doping on ISBA, 2.2 nm SQW structures with different doping position but with uniform doping density throughout the selective regions were simulated. For a SQW structure, there are two optional AlAs barriers for introducing modulation doping with reference to Fig. 4.1, resulting in three cases: doped in one (left/right) outer barrier only and both outer barriers, as illustrated in Fig.s 4.12 (b), (c) and (d). In all three cases, every modulation doping sheet was 1.0 nm thick and was located in the centre of corresponding AlAs barrier, i.e. L_d = 5.0 nm, as shown in Fig. 4.12.

In order to demonstrate a reasonable comparison, the same amount of donors is applied to these three structures. Therefore, $N_D = 1\times10^{18}$ donors/cm^3 for doping in

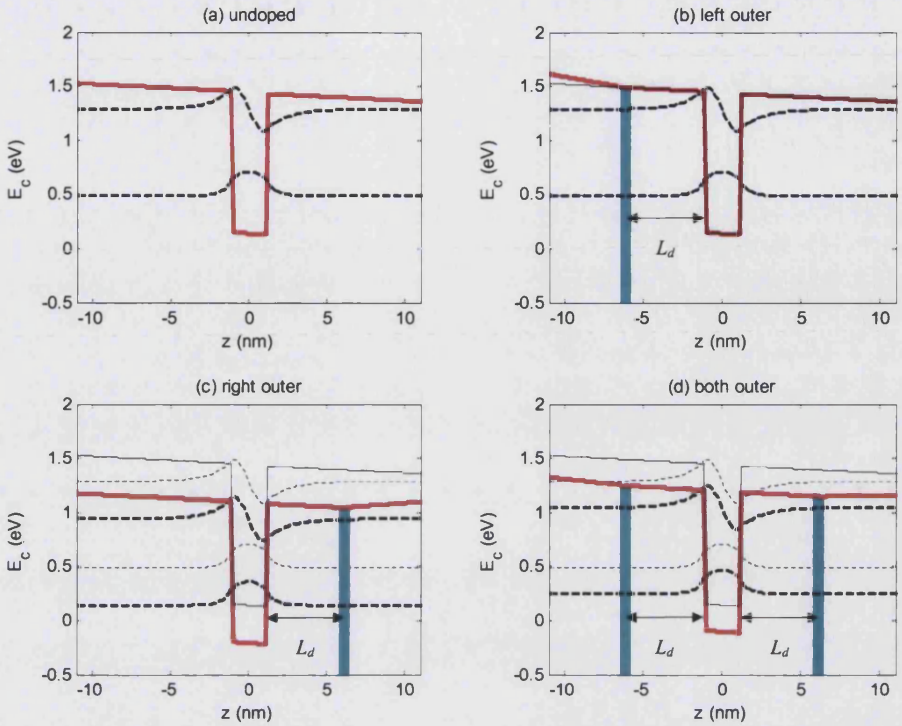

Figure 4.12: The conduction band profile (solid red line) and wavefunctions (thick dashed line) of 2.2 nm SQWs with (a) no modulation doping, (b) doped in the left outer barrier to N_D=1×10^{18}/cm^3, (c) doped in the right outer barrier to N_D=1×10^{18}/cm^3 and (c) doped in both outer barriers to N_D=5×10^{17}/cm^3. The zero amplitude positions of the envelope functions coincide with the subband energies. The thin solid and dashed lines indicate the undoped case for comparisons. Each modulation doping layer (blue line) is 1.0 nm thick and the distance between the central plane of the doping layer and the well-barrier interface (L_d) is 5.0 nm. All structures are under F_{av} = -10V/μm bias.

one barrier [Fig.s 4.12 (b) and (c)], and N_D = 5×10^{17} donors/cm^3 for the both outer barriers case [Fig. 4.12 (d)]. The resulting potential profiles and envelope functions for 0.8 eV ISBTs are compared with the case of an undoped SQW for the same average electric field strength across the well, here F_{av} = -10 V/μm. Note the surface potential required to achieve the -10 V/μm average field strength varies from structure to structure, as shown in Table 4.1.

Compared to the undoped situation in Fig. 4.12(b), it is clearly revealed that doping in the left outer barrier does not cause any significant change in subband energies and in the envelope wavefunctions when both structures at F_{av} = -10 V/μm. This type of

modulation doping only has a negligible effect on the conduction band profile to the right of the doped region, as illustrated by the difference between the red solid and thin solid lines in Fig. 4.12 (b). The main change in the potential profile occurs between the doped layer and the (assumed) Schottky contact at $z = 0$, where the potential is raised about 0.7 eV as can be seen from Table 4.1. This reflects the higher surface potential needed to overcome the screening effect of the ionised donors in the doped layer in order to produce the same electric field strength in the well as in the undoped SQW case. When this raised surface potential is converted to the applied bias on the structure, it represents a larger reverse bias being applied.

	undoped	left outer	right outer	both outer
V_{surf} (eV)	0.7223	1.4256	0.3554	0.8305

Table 4.1: The surface potentials of SQW structures at different modulation doping conditions given in Fig. 4.12.

Unlike the case of the left outer barrier, a doped region of the same width and donor density but located in the right outer barrier in Fig. 4.12 (c), has an enormous change of the potential profile. Under the same field strength at -10 V/μm, the conduction band profile is lower and the surface potential is ~0.37 eV less than those in the undoped case. It is because the net electric field across the well is constituted by the applied electric field due to the reverse bias and the built-in electric field due to the ionised donors in the structure. Since a reverse bias is applied to this structure, the screening effect is significant only on the right hand side of the doped region. However, the quantum well is on the left-hand side of the doped region in this structure. As a result, the built-in electric field across the well in this structure is enhanced rather than depressed. In order to achieve the same net field strength as in the undoped structure, a lower surface potential is required to balance the enhancement of the built-in electric field. The descent of the potential profile will also result in smaller values of confined energies in the well. According to Eq. (3.71), the Fermi occupancy ratio is expected to rise and consequently a large absorption

coefficient is expected in this structure.

In Fig. 4.12 (d), the same total amount of donors as in Fig.s 4.12 (b) and (c) were separated into two equal portions and inserted in both AlAs barriers. By comparing Fig.s 4.12 (c) and (d), it is found that doping in both outer barriers and the right outer barrier have similar effect. Although the potential profile also has a large drop around the well, somewhat weaker than the right outer barrier case, the change in V_{surf} is smallest (~0.1 eV) among these three doping cases. This is due to the mixed effects of the two modulation doped regions inserted in the quantum well structure. The left region causes the screening effect to the quantum well and raises the surface potential, whilst the right one induces a negative field across the well and lowers the potential profile throughout the structure. Therefore, these two doping layers tend to counteract each other at the surface potential but together drive down the potential energy around the well at the same field strength. Again, like the right outer barrier doping case, the absorption under the same field strength would be increased due to the depression of the conduction band edge towards the Fermi level when comparing to the undoped structure.

(1) Doping Locations

Although the results given above have briefly shown the effects of the doping location on SQW structure, they are partly caused by the rather high doping density. For clarifying the importance of doping regions in the effect on absorption spectra, the previous three cases of 1.0 nm wide doped regions in the left barrier, in the right barrier and in both barriers [Fig.s 4.12 (b), (c) and (d)] have been considered again but this time with a very low density of donors. The doping density chosen in all these designated "low doped" structures was 1×10^{17} donors/cm^3 for the reason that the potential profile was basically unchanged. Therefore, the effect on ISBA of incorporating low levels of modulation doping derives from the location of the doped layers.

Figure 4.13 shows the effect of the doping position on the differential absorption spectrum at the change of electric field from -1 V/μm to -2 V/μm across the well. Positioning the doping in the left outer barrier leaves differential absorption coefficient substantially unchanged compared to undoped structure. This is because the increased surface potential depletes the SQW of electrons in order to produce the same field strength as in the undoped case. The doping in the right outer and both outer cases have nearly the same increase and enlarge the value of absorption peak to about three times stronger than the other cases. These results are implicit in Fig.s 4.12 (c) and (d) but become explicit in Fig. 4.13. It is concluded that for the SQW even a low modulation doping level could remarkably affect the absorption spectra.

It is noted that, since the same three-dimensional doping density is used in all these low modulation doped structures, for the case of modulation doping in both outer

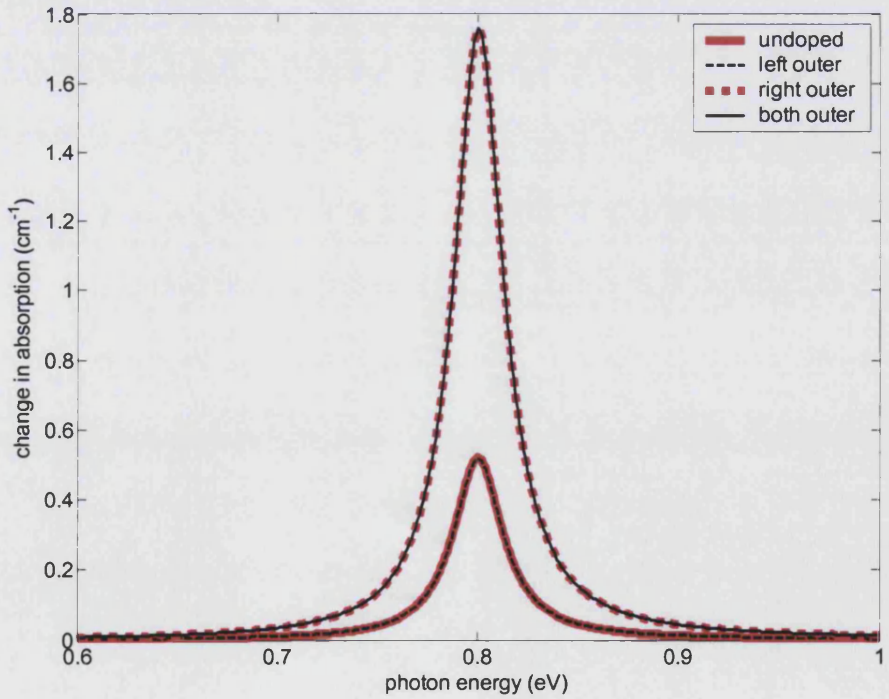

Figure 4.13: The influence of doping regions on the differential absorption spectra for electric field changed from -1V/μm to -2V/μm. The same doping density, 1×10^{17} donors/cm^3, is applied to the three modulation doped structures.

barriers it doubles the amount of donors compared with structures with modulation in only one (left/right) outer barrier. However, compared to modulation doping in right outer barrier only, the extra doping in the left outer barrier of both outer barriers doping does not alter the absorption spectrum much. Therefore, for the bias condition used, it is considered that doping in the left outer barrier causes only almost no effect on the energies of confined states and their envelope functions, resulting in the nearly unchanged absorption spectrum, but causes only a small lift-up on the potential profile in the high energy side, resulting in the higher surface potential.

The behaviour of the absorption spectra as a function of electric field given above is essentially based on the view of physics. As revealed previously, the doping in the left outer barrier leaves the ISBA unaltered compared with the undoped cases for the same average applied field across the SQW, but required a higher surface potential to achieve this condition. In practice, modulators are worked under applied voltage. The relationship between the surface potential and applied bias in the Schottky diode considered in this work, as shown in Fig. 3.8, can be expressed as: $V_{surf} = (\phi_B - V_A)e$, where ϕ_B is the Schottky barrier height and V_A applied bias on the structure. For a Schottky contact formed by the vacuum evaporation of gold on to the *n*-type InP, $\phi_B \approx 0.5$ V [198-200]. When a *p-i-n* or *n-i-n* junction is considered instead of a Schottky diode, ϕ_B can be replaced by the built-in potential, V_{bi}, due to the electric field formed in the diode to prevent diffusion. If the acceptor density (N_A) in *p*-type layer and the donor density (N_D) in *n*-type layer both are 1×10^{18} /cm^3, one can calculate $V_{bi} \approx 1.3$ V by using Boltzmann statistics and the depletion approximation. On the other hand, if an *n-i-n* junction is assumed and both sides of *n*-type layers have the same donor density, $V_{bi} \approx 0$ V due to the symmetry of the unbiased potential profile. Therefore, the use of the concept of surface potential remains valid for the design of devices because it directly relates to the applied bias on the structures.

For comprehensively understanding the doping effect in this area, the variation in

average electric field strength across the well with the surface potential (F_{av}-V_{surf}) and the dependence of maximum absorption coefficient on the surface [max(α)-V_{surf}] are plotted for several combinations of doping position and doping density in Fig. 4.14. The vertical dotted lines in Fig. 4.14 indicate the assumed ϕ_B in the Schottky diode and the approximate V_{bi} in *p-i-n* and *n-i-n* junction structures. Therefore, each electron-volt fluctuation in the unbiased surface potential (ϕ_B and V_{bi}) represents ±1V applied to the structures. In other words, V_{surf} changing from 0.5 eV to 1.5 eV is equivalent to bias voltage applied to the structure changing from 0 to -1 V in the case of a Schottky-contacted structure or from +0.8 V to -0.2 V in a *p-i-n* diode structure, containing a single isolated 2.2 nm wide $In_{0.53}Ga_{0.47}As$/AlAs quantum well grown on InP.

In these graphs, the three cases of the doping conditions considered are the same as in Fig. 4.12. The extra case of doping in both outer barriers to N_D = 1×10^{18} donors/cm^3 is also shown. This is based on the view that a higher electron concentration is always required in a practical device to maximise the occupancy of the ground state energy level and thereby maximise the absorption. It is difficult to simulate III-V semiconductors with donor densities much above ~1×10^{18}/cm^3 using the model described in Chapter 3 for complex, such as numerical noise and overflow. Further, above such doping densities many body effects like impurity band formation become profound [201] and some of the assumptions underlying the solution of Poisson's equation become invalid. Rectifying these shortcomings of the model using a first principles approach is beyond the scope of this project and would not introduce physics that will significantly alter the trends in the results described in this thesis. For example, since virtually all of the donors are ionised for the bias conditions considered, the impact of impurity band formation on the carrier statistics would be minimal. Therefore, if a high doping density can be realized in one barrier, it is feasible to fabricate the same density to the other barriers in order to increase the Fermi occupancy of the confined states.

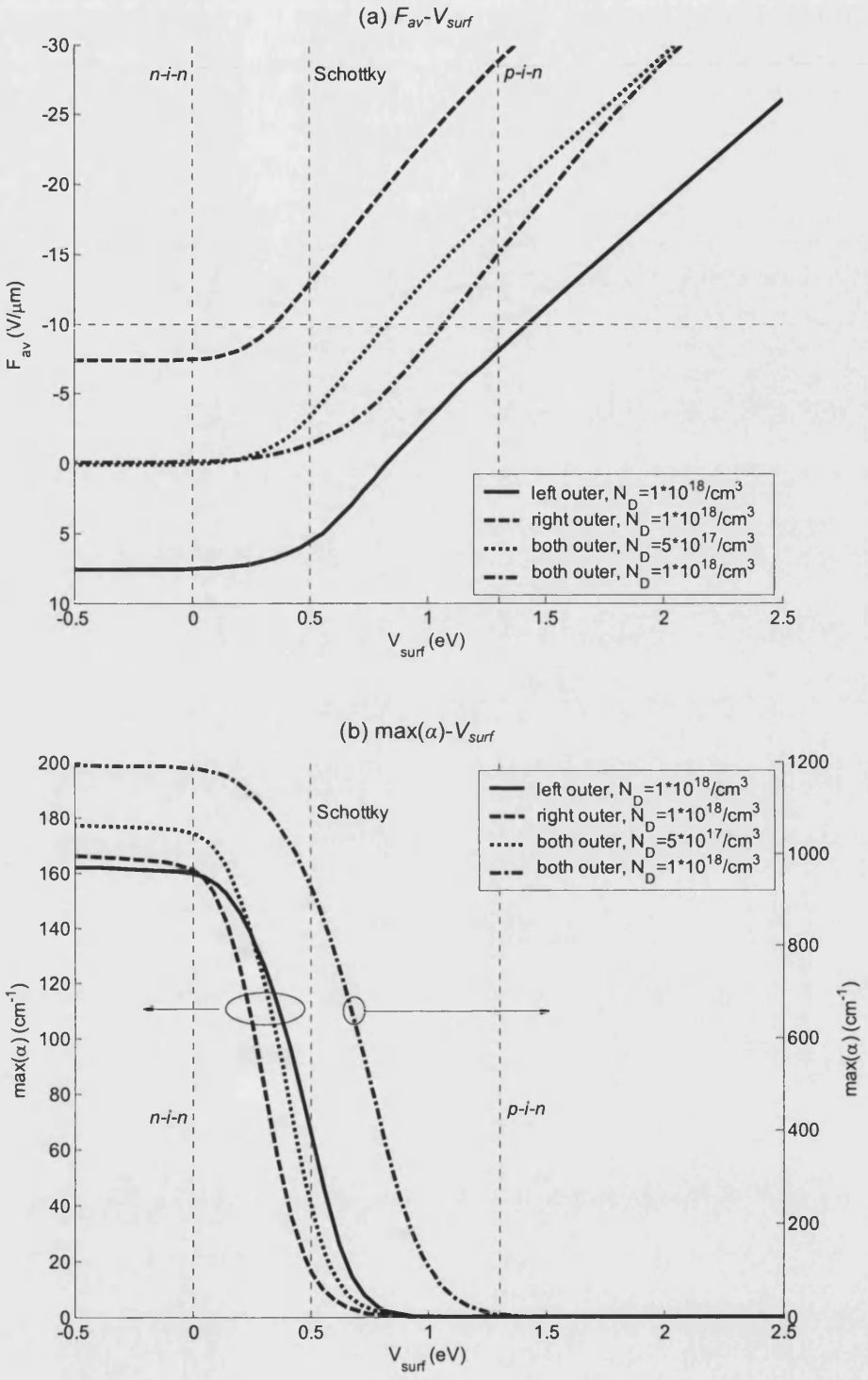

Figure 4.14: The variation of (a) average field strength across the well, F_{av}, and (b) the maximum absorption, max(α), as a function of the surface potential, V_{surf}, at different doping conditions. The vertical dotted line indicates the assumed barrier height for the metal-semiconductor junction and the built-in potential energy for *p-i-n* and *n-i-n* junctions.

For all the cases in Fig. 4.14 (a), the incorporation of the modulation doping gives rise to a non-linear relationship between V_{surf} (equivalently the applied bias combined with ϕ_B or V_{bi}) and F_{av}. The variation in electric field as a function of surface potential has the same form: for low V_{surf}, F_{av} is virtually unchanged (defined as flat field region) whilst for high V_{surf}, F_{av} varies linearly (defined as linear field region). The cause of the flat field region is because the two-dimensional electron gas (2DEG) inside the well is sufficient large to screen the structure to the right of the SQW and therefore the electric field across the well remains at a constant value at the low V_{surf}. As V_{surf} increases to some threshold level, the 2DEG density starts to fall and the electric field starts to penetrate the SQW, giving rise to a finite average field within it. Once some threshold surface potential is exceeded, F_{av} increases almost linearly with V_{surf} as the SQW is fully depleted. Also, the threshold in each structure is different and this could be critical for the operating condition of devices if there are bias restrictions, for example as occur in high speed operation where low switching voltages are required.

The maximum absorption coefficient, max(α), as a function of surface potential for the four structures is shown in Fig. 4.14 (b). Since the absorption spectrum in the 2.2 nm wide SQWs has a single peak, which is composed of E_1-E_2 transition only, and electric field has merely a small effect on the transition energy E_{12}, the variation of max(α) with bias can be used to estimate the change of whole spectrum. The max(α)-V_{surf} characteristic has a near step shape in all structures. For the same amount of donors in the three cases given in Fig. 4.12 (i.e. the total donor density = $1\times10^{11}/cm^2$), the largest values of max(α) that can be achieved are almost the same. However, it has to be noted that these comparable values of max(α) occur at different average field strength. The comparisons given previously in Fig. 4.12 and Table 4.1 were based on the same field strength, which is the horizontal dotted line in Fig. 4.14 (a). The additional case of doping in both barriers to 1×10^{18} donors/cm^3 has been considered in Fig. 4.14 (b). This structure has just twice the total amount of donors than the other three structures but the largest value of max(α) is more than six times

the one in the lower doped devices, demonstrating once again the dominant contribution of the ground state occupancy in determining ISBA in modulated doped SQWs. Further, this result shows that the peak absorption is non-linearly proportional to the total number of donors incorporated in the structures. This has revealed the importance of the charge control in the enhancement and modulation of ISBA.

On the other hand, for EAMs based on the structures shown in Fig. 4.12, the consequence of using a Schottky contact, *p-i-n* junction or *n-i-n* junction can be observed clearly. The *n-i-n* junction can be considered as in the "off" state at zero applied voltage, due to the large absorption at zero bias, and reverse bias is needed to turn the EAM "on". On the other hand, the *p-i-n* junction is the other way round. The unbiased Schottky contacted device is in an indeterminate state somewhere between the "off" and "on" states. A forward bias can fully turn the structure "off" and a reverse bias for "on". In the SQW simulated here, the Schottky contact has an advantageous of a smaller driving voltage by using the applied voltage swing around zero bias. However, one can adjust the doping density in the *p*- and *n*- type region to modify the built-in voltage and may even locate the unbiased condition to utilise symmetrical applied voltage. Since the *p-i-n* and *n-i-n* situations are analogous to the Schottky diode, with the only difference being in its bias condition, the Schottky diode is selected as the focus structure in the following simulations to simplify the description of the results.

By comparing Fig. 4.14 (a) with (b), some important conclusions can be drawn. For the flat field region, the absorption coefficient of E_1-E_2 transition remains large, but only weak absorption modulation occurs as the V_{surf} increases due to the weak fluctuation in electric field in the SQW. For the linear field region, the assumed SQW structures are fully depleted, which means very few electrons are confined in the well and therefore the absorption coefficient is small and again weak modulation of ISBA occurs. For future discussion, these two regions are called the weak modulation

regions. The large electroabsorption modulation takes place in the corner region of the characteristic between the flat field region and the linear field region in Fig. 4.14 (a). This is revealed in Fig. 4.14 (b), as the rapid change of max(α) occurs over the corner between the flat and the linear field regions in Fig. 4.14(a). For future discussion, this is called the corner of the F_{av}-V_{surf} characteristic or strong modulation region. This is crucial to optimise the operating conditions.

(2) Doping Density

The effect of the doping density needs to be further investigated since the above results have shown the significance of the position of the doping in ISBA. Asai *et al* have proposed the dependence and importance of doping density on ISBA in the uniformly doped InGaAs/InAlAs MQWs [144]. The doping level will cause the Fermi energy level to vary in quantum wells and consequently changes the strength of ISBA. For simplification, the approximation of a constant Fermi energy (no current flow) for all doping density is considered in this work.

For demonstrating the behaviour of doping density in the structure, the surface potential dependence of the average electric field strength across the well and maximum absorption coefficient as a function of doping density for modulation doped in both AlAs barriers are illustrated in Fig. 4.15. The simulated structures have the same locations and thickness of the modulation doped regions as the one shown in Fig. 4.12 (d). There are two important results that need to be pointed out from the Fig. 4.15 (a). First, the field strength at which the flat field region occurs becomes increasingly negative as N_D in the modulation doped layers increases. Second, the corner of F_{av}-V_{surf} becomes more slowly varying and the linear region starts from a larger threshold voltage when N_D is raised. These are caused by the stronger internal electric field across the well due to the higher doping density. Further, a larger applied bias is required to overcome the screening effect of the higher density of electrons in the quantum well and hence to deplete the structure.

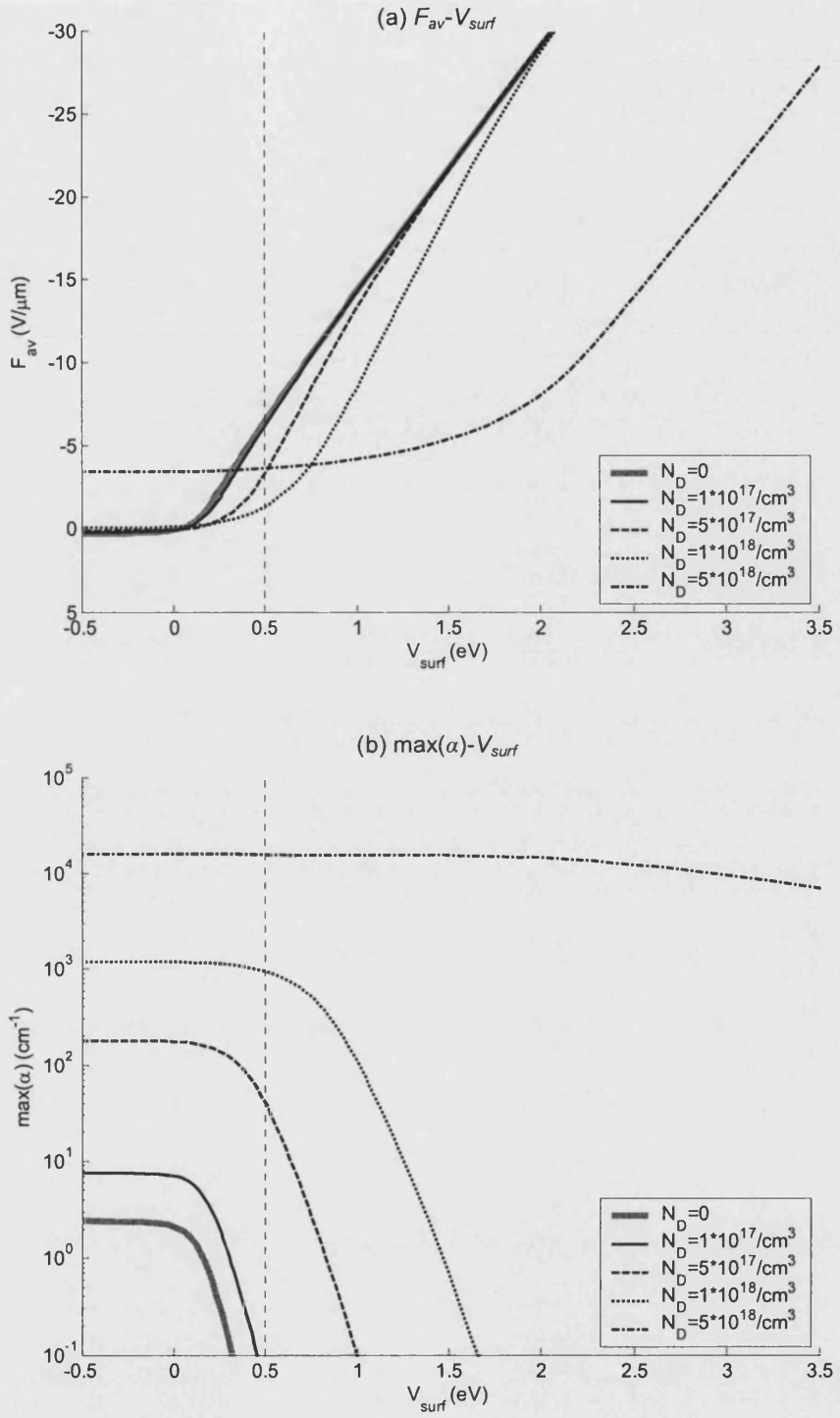

Figure 4.15: The variation of (a) average field strength across the well, F_{av}, and (b) the maximum of absorption, max(α), as a function of the surface potential, V_{surf}, at different doping density (N_D). All structures are doped in both outer AlAs barriers. The vertically dotted line indicates the barrier height (ϕ_B) at the metal-semiconductor junction.

As can be seen in Fig. 4.15 (b), increasing N_D causes a strong enhancement in the absorption. At $N_D = 1\times10^{18}/cm^3$, for example, the absorption strength is increased by almost three orders of magnitude compared with the undoped structure. However, when a very large doping density is applied to the structure, e.g. $N_D = 5\times10^{18}/cm^3$, the absorption peak is large but decreases very slowly as the field strength increases. Consequently, achieving a large differential absorption spectrum requires the application of a very large reverse electric field to the most highly doped structure. This is not optimised for high speed electro-optic modulators. Therefore, a trade-off between absorption change and bias change is required for high-speed, voltage-induced optical modulation by ISBA in a modulation doped SQW. The donor density is the parameter requiring optimisation by modelling.

Finally, if the three device configurations shown in Fig. 4.14 are reconsidered in here, with the use of a Schottky contact at zero bias, the structure with low modulation doping is "on" while the one with high modulation doping is "off". For very high doping, above $1\times10^{18}/cm^3$, a *p-i-n* junction appears to have a better operating characteristics since the built-in voltage can be placed in the strong absorption modulation region by selecting the suitable doping density in *p*- and *n*-type region then utilising swing voltage around zero bias. Also the alloy composition in the *p*- and *n*- contact layers can be adjusted, which is necessary in any case to create an optical waveguide, so that the band offsets to the *i*- layer contribute favourably to the built-in potential. On the other hand, the unbiased *n-i-n* junction has opposite features to the *p-i-n* junction. Therefore, the doping density and doping location combined with the configuration of the SQW can optimize the performance and operation of the devices.

(3) Energy Shift

Further, the wavelength at which the absorption peak occurs is also critical in determining the behaviour of a possible optical modulator operating by ISBA modulation. In order to clarify the influence of doping conditions in 2.2 nm wide

SQW, Table 4.2 shows the effect of the doping location on the energy of E_1-E_2 transitions and on their absorption strength at an average applied field of -10 V/μm for N_D = 1×10^{17} and 1×10^{18}/cm^3. These data reveal that the variation in doping condition, density and regions, only has a negligible effect on the transition energy but has a very strong influence on the maximum absorption coefficient in some certain cases such as doping in both outer barriers.

SQW, L_w = 2.2nm, F_{av} = -10V/μm		**transition energy E_{12} (meV)**	**peak absorption max(α) (cm^{-1})**
undoped		799.8252	~0
$N_D = 1\times10^{17}$/cm^3	**both sides**	799.8249	0.0031
	left side	799.8253	~0
	right side	799.8250	0.0031
$N_D = 1\times10^{18}$/cm^3	**both sides**	799.7733	184.6181
	left side	799.8256	~0
	right side	799.7729	184.3230

Table 4.2: The transition energy of E_{12} and the absorption strength of the peak [max(α)] in 2.2nm SQW structures under different doping conditions at F_{av} = -10 V/μm.

(4) An Optimized SQW Structure

Finally, according to the above study, a SQW structure is designed, which is modulation doped in both outer barriers with 1nm-wide n-type layers to 1×10^{18} donors/cm^3, and its absorption spectra is given in Fig. 4.16. Since the modulation doping is applied to both AlAs layers, the structure has a fine dynamic F_{av}-V_{surf} characteristic, which ensures a sharp corner region for sensitive voltage control of the ISBA. The high doping density ensures a large absorption coefficient, which is about 600 times larger than the undoped structure. Moreover, larger differential absorption spectra can be achieved by a small field change, as shown in Fig. 4.16 (b).

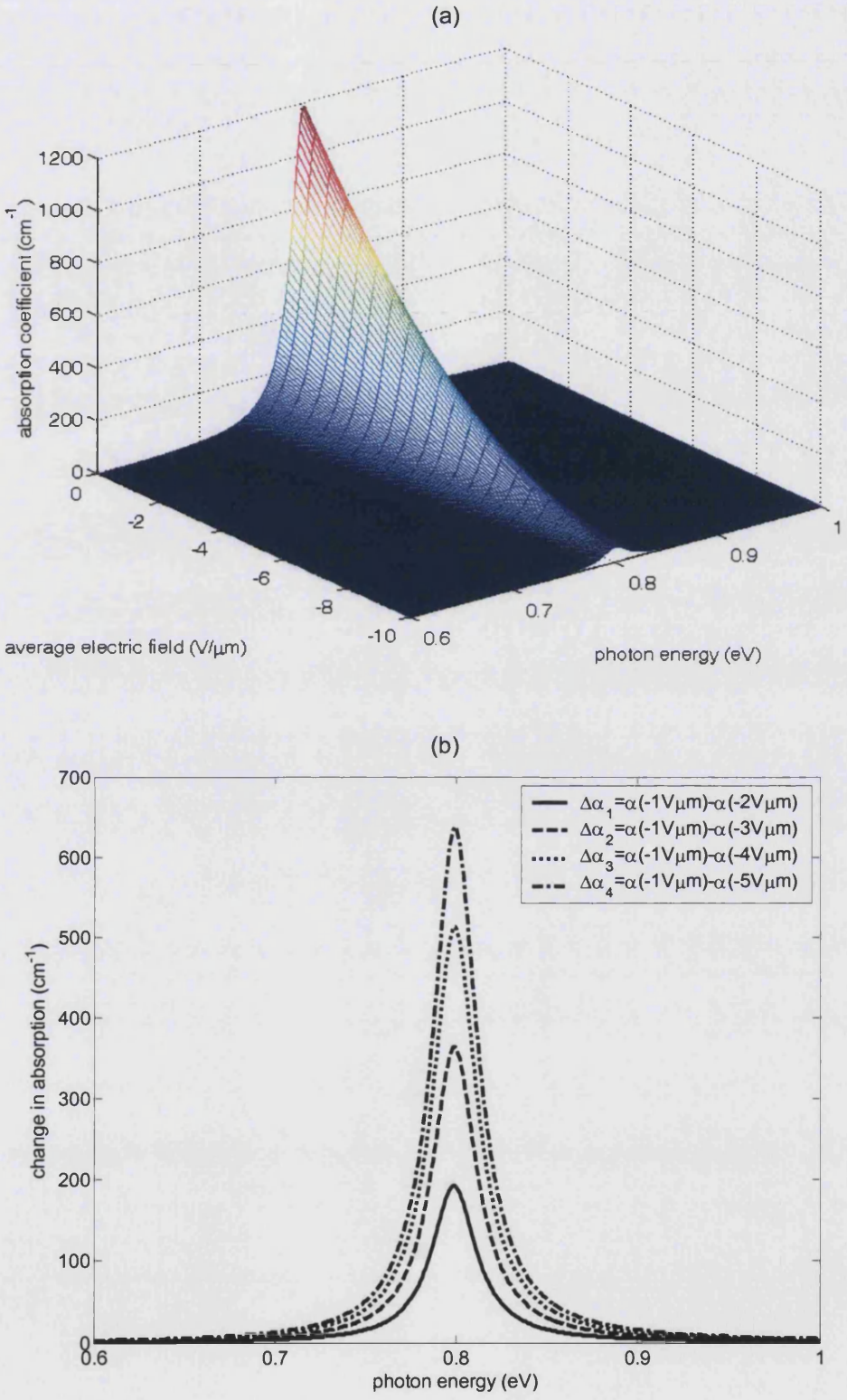

Figure 4.16: (a) A 3D plot of absorption coefficient versus photon energy versus electric field and (b) differential absorption spectra for the change of electric field for various field strengths assuming a starting field strength of F_{av} = -1 V/μm in a SQW structure with modulation doping to 1×10^{18} donors/cm^3 in both outer barriers.

4.3 Simulations of Double Quantum Well (DQW) Structures

In this section, the self-consistent Poisson-Schrödinger approach is applied to the design of double quantum well (DQW) structures, which have been shown to be significant for the flexibility in tailoring quantised energy levels, optical matrix elements and carrier relaxation processes [202-204]. For instance, the coupled quantum well concept has been demonstrated to be effective for achieving fast optical response [17,202,205]. Since the use of narrow well width can result in a decrease in absorption intensity [141,203], DQW structure has been used to obtain a higher ISBT energy, i.e. shorter transition wavelength, without further reducing the well width in SQW structures [85]. The well width chosen for all DQW structures in this section was 2.2 nm, the same as in the main simulations of ISBA in SQWs, for the benefit of making comparisons between them later. Different inner barrier widths have been considered, as specified in subsequent sections. The rest of structures had the same dimension as mentioned in Section 4.1.

In general, since two bound states are confined in a 2.2nm SQW, there are in total four energy states in a DQW and therefore six possible transitions can be produced. This is shown in Fig. 4.17. The transitions are classified into two groups: transitions from the ground states to excited states (E_1-E_3, E_1-E_4, E_2-E_3 and E_2-E_4 transitions) and transitions between states of the same origin (E_1-E_2 and E_3-E_4 transitions). Since the short wavelength ISBTs, i.e. large transition energies, are the focus of this work, the former are essential and studied in detail.

In SQW structures, ISBTs only take place inside the same well which is known as a vertical transition. However, in the DQW structure, due to the tunnelling of envelope wavefunctions, the effective charge distribution of a confined state inside a well can be estimated by the integrated probability of the corresponding wavefunction. In order to reveal the characteristics of ISBTs in DQW structure, two types of transitions need to be considered: the vertical transition in which the effective charge

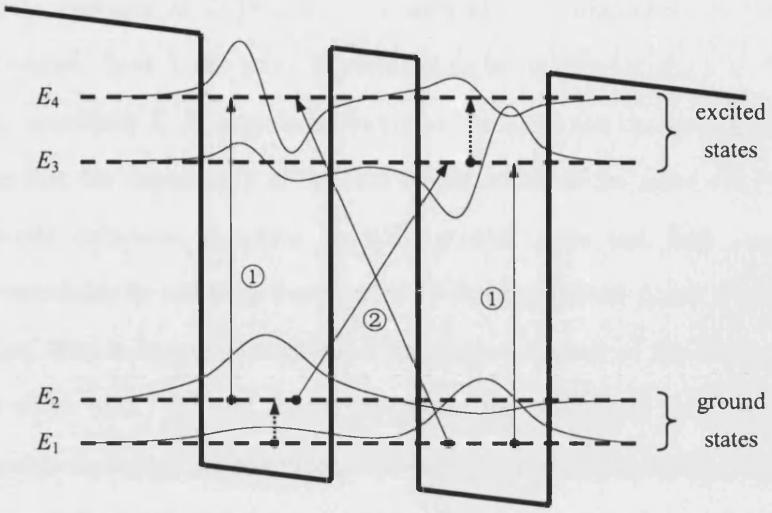

Figure 4.17: Different types of ISBTs in a DQW structure under reverse field: transitions from ground states to excited states (solid arrows) and transitions between the states of the same origin (dotted arrows). The former are classified into two groups: ① vertical transitions (E_1-E_3 and E_2-E_4) and ② diagonal transitions (E_1-E_4 and E_2-E_3).

distribution of initial and final states are mainly confined in the same well and the diagonal transition between the two wells. This is also shown in Fig. 4.17. In principle, when a reverse electric field is applied to a DQW structure, the E_1 and E_3 states localise in the well on the right-hand (low energy) side while the E_2 and E_4 in the left-hand side one (high energy) in the sense illustrated in Fig. 4.17. As a result, the vertical transitions describe the transitions E_1-E_3 and E_2-E_4, whilst E_1-E_4 and E_2-E_3 are diagonal transitions.

4.3.1 Effects of Barrier Width (L_b) on ISBA in DQWs

The focus of the work reported here is the feasibility of applying ultra-fast ISBTs as the basics of high speed optical modulation at 1.55 μm communication wavelength. Regarding a DQW with a constant well width of 2.2 nm in the following calculations of all DQW structures, the barrier width (L_b) determines the coupling between the wells and therefore becomes the crucial part in determining the absorption peak of the structure. The influence of L_b on the characteristics of the DQW was studied first.

The transition energies of DQWs as a function of L_b is illustrated in Fig. 4.18, in which the electric field in the wells is assumed to be absent, i.e. $F_{av} = 0$. Firstly, the energies of transitions E_1-E_2 and E_3-E_4 decrease to zero as the barrier width increases. This shows that the degeneracy of the two bound states of the same origin between the two wells enhances, resulting in both ground state and first excited state becoming two-fold. In addition, there are only three confined states when $L_b < 0.7$ nm (~3MLs). This is because the E_4 subband reaches the top of the barrier height at the barrier width of 0.7 nm and is pushed up into the continuum states if the barrier width is further decreased. In this circumstance, optical transition occurs between the bound states in the well and the extended continuum states above the top of the barrier. Such bound to effectively free transition, whilst contributing to absorption modulation, are not considered further in this work. This is because the carrier dynamics will involve either drift under the applied field or recapture of the free electron by the quantum wells, or both, thereby altering the charge relaxation rate.

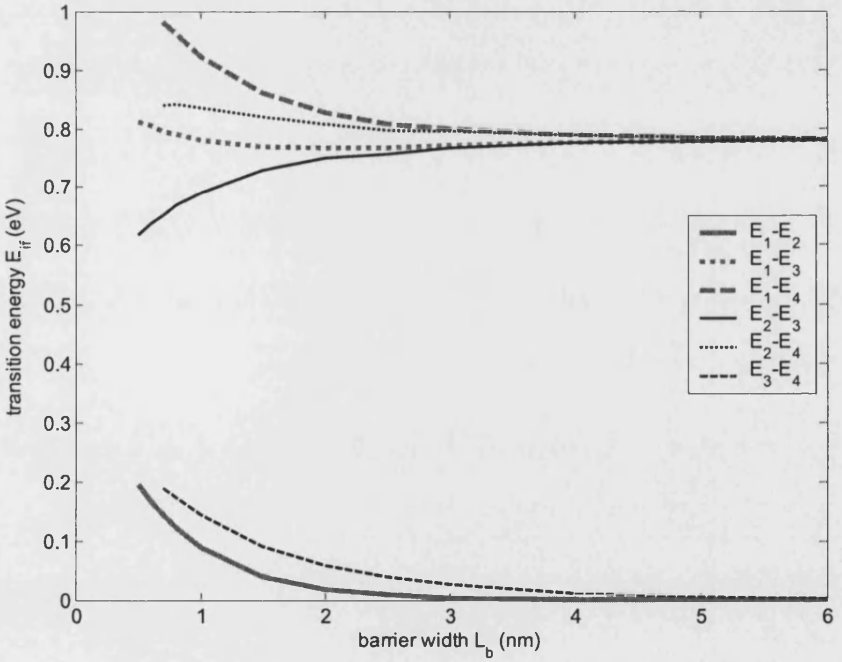

Figure 4.18: Calculation transition energies (E_{if}) as a function of barrier width (L_b) in the InGaAs/AlAs DQW with $L_w = 2.2$ nm.

Furthermore, since the transition around 0.8 eV is at the core of this work, transitions from the ground states (E_1, E_2) to first excited states (E_3, E_4) remain the attention in DQW structures. Owing to the results given above, absorption spectra of DWQs with the thickness of the inner barrier varied as a parameter from 1.0 nm to 5.0 nm with 1.0 nm step value are illustrated in Fig. 4.19 for $F_{av} \approx 0$ V/μm. With $L_b = 1.0$ nm, two peaks are observed with the higher energy peak at 0.923 eV (E_1-E_4 transition) markedly more dominant than at 0.692 eV (E_2-E_3 transition). Increasing L_b causes the two peaks to move together in energy, following the trend shown in Fig. 4.18 with the absorption strength of the E_1-E_4 transition decreasing and that of the E_2-E_3 transition increasing. For $L_b = 3.0$ nm, the absorption strength of these two peaks is pretty much equal. For $L_b \geq 4.0$ nm, the two peaks have merged into a single peak, indicating the quantum wells have become decoupled, again as can be inferred from

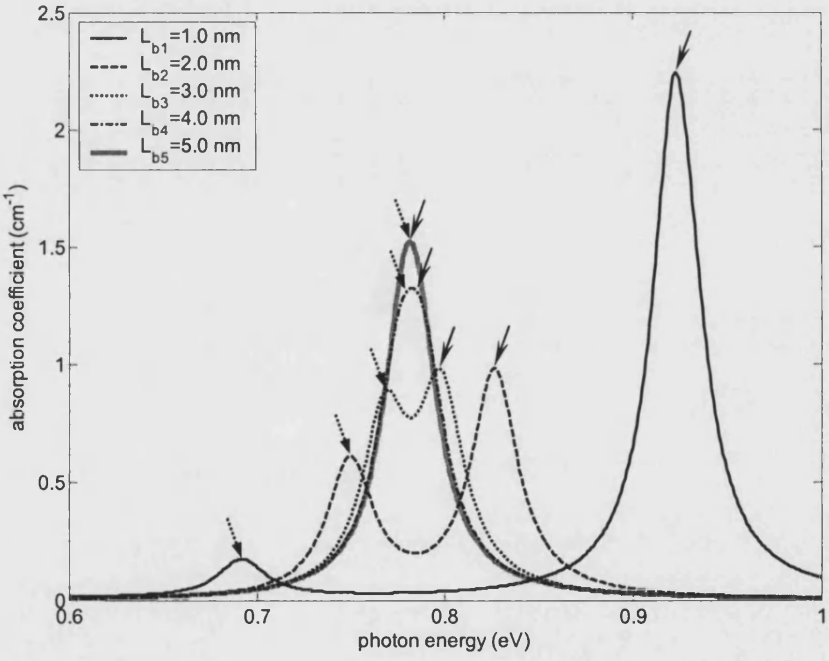

Figure 4.19: The influence of barrier width, which ranges from 1.0 nm to 5.0 nm, on intersubband absorption spectra of DQWs with $L_w = 2.2$ nm for the average electric field across the well(s) at 0 V/μm. The solid and dotted arrows indicate the energies of E_1-E_4 and E_2-E_3 transitions respectively.

Fig. 4.18. For all five different barrier widths, only two of the four transitions in the range from 0.6 eV to 1.0 eV identified in Fig. 4.18 have significant absorption strength. This indicates that some of the transitions in DQW structures are disallowed by the parity selection rule.

In general, the difference of the absorption peak and absorption intensity shown in Fig.4.19 is caused by the splitting of the two-fold degenerate energy levels in DQWs. The energy splitting as mention in Chapter 2 is determined by the overlap of the envelope wavefunction, which is the outcome of the inner barrier width. The two absorption peaks in the case of the 1.0 nm inner barrier have huge difference in the absorption energy and the absorption strength. This occurs due to the extremely strong coupling between the two wells. In the 2.0 nm case, two sharp absorption peaks are observed. The coupling is still strong in this structure and the result is representative. Since the two peaks occur near 0.8 eV, this structure is of interest and will be studied in detail later. The coupling becomes moderate in 3.0 nm barrier width. Although two peaks can still be observed, their spectral resolution is small. The structures with a 4.0 and 5.0 nm barrier width show only a weak coupling effect between the two wells, and only a single peak in the absorption spectra can be observed for the broadening parameter used, which is very similar to the SQW situation. However, the absorption spectra in the DQWs of 4.0 nm and 5.0 nm wide inner barrier have the full-width at half-maximum (FWHM) of ~38.5 meV and ~32 meV, which are larger than the assumed Lorentzian line width of 30 meV [see Eq. (3.71)]. For a wide FWHM in the absorption spectrum composed of E_1-E_4 and E_2-E_3 transitions, it indicates that the difference between the peak energies of the Lorentzian components remains significant. Therefore, the FWHM can be used as a guideline to evaluate the coupling strength between the two wells. One can also expect that the absorption spectra of the structure with a barrier width around 3.0 and 4.0 nm would have one wide peak with in some situations, a secondary shoulder. The 5.0 nm case was chosen to illustrate the negligibly coupled circumstances and will be described as such in later comparisons with the strongly coupled DQW with 2.0

barrier width.

Details of the effects of electric field and doping conditions on DQWs with 2.0 nm and 5.0 nm wide barriers will be given in the following sections. In order to distinguish the two coupled cases, the strongly coupled DQW is denoted as C-DQW and the weakly coupled one as 2QW.

4.3.2 An Undoped C-DQW (L_w = 2.2 nm, L_b = 2.0 nm)

The influence of electric field on the ISBA for the C-DQW structure determined above (L_w = 2.2 nm, L_b = 2.0 nm) is calculated and illustrated in Fig. 4.20. The Stark shift in the transition energy can be observed in Fig. 4.20 (a) and is much stronger than the case of SQW. As a consequence, an absorption peak can shift with respect to the selected incident photon energy, contributing to the absorption modulation. Further, the transition energies of the diagonal ISBTs (E_1-E_4 and E_2-E_3) move away from the ~0.8 eV whilst those of the vertical ISBTs (E_1-E_3 and E_2-E_4) approach to a value near 0.8 eV as the electric field increases. This is because a strong electric field is necessary to break the coupling effect in such a C-DQW structure. Once the field is strong enough and the localisation of envelope wavefunctions is significant, the DQW structure can then be considered as two separated SQWs and therefore the vertical transition become dominant as the quantum wells become decoupled, like the case of the SQW structure [4].

Fig. 4.20 (b) shows that the diagonal ISBTs (E_1-E_4 and E_2-E_3) are important at low field strength, whilst the vertical transition E_1-E_3 becomes the dominant ISBT when the field strength, $|F_{av}|$, exceeds 8V/μm owing to the combined effect of the variation with field in the overlap matrix element, as shown in Fig. 4.20 (c), and the continuous decrease in the Fermi occupancy ratio in Fig. 4.20 (d). At $F_{av} \approx 0$, the vertical transitions are forbidden and only the diagonal transitions are allowed [see Fig. 4.20 (c)]. This is because the optical matrix elements modify the transition

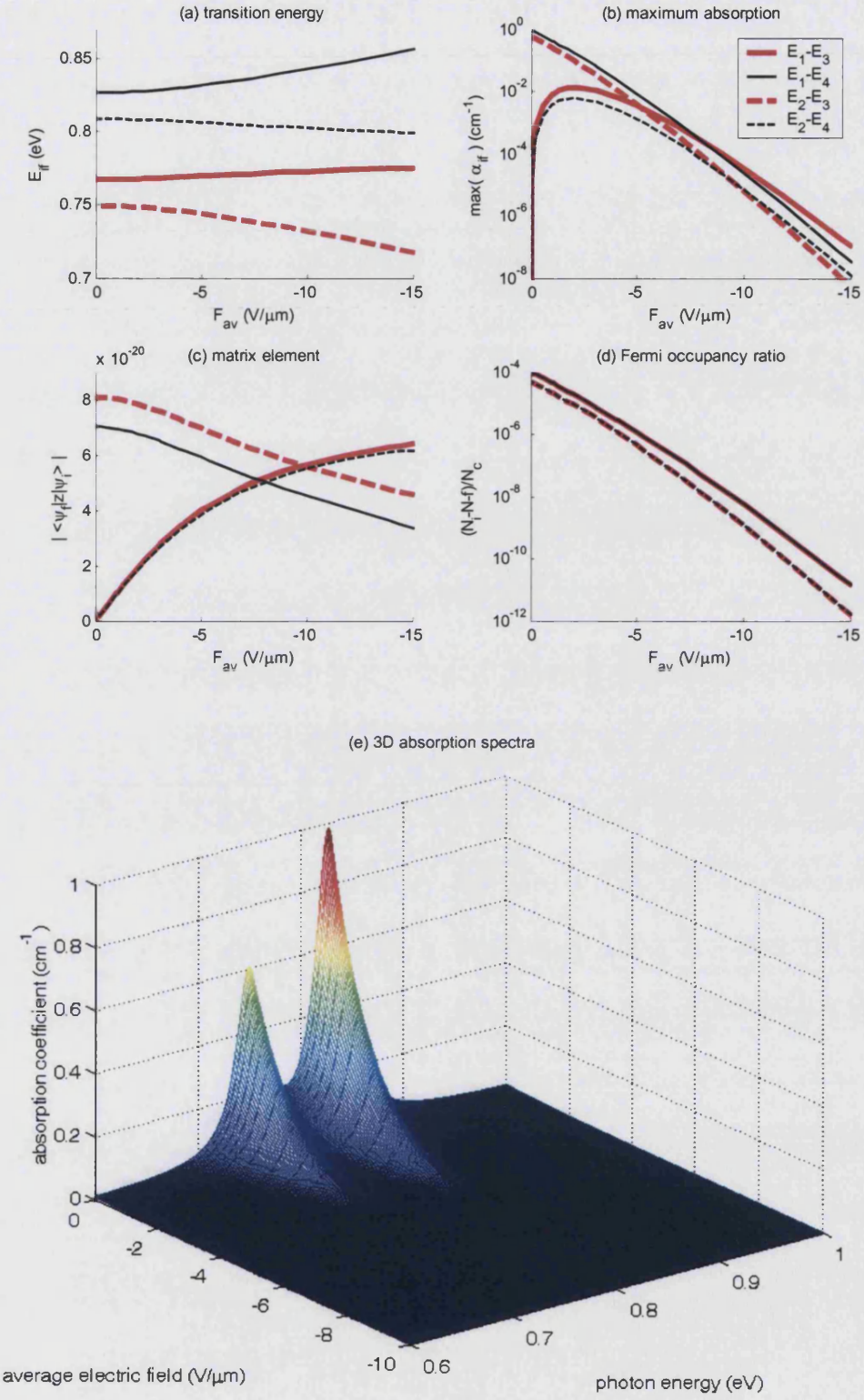

Figure 4.20: (a) The transition energy, (b) the maximum absorption coefficient, (c) the optical matrix element, (d) the Fermi occupancy ratio and (e) the 3D electroabsorption spectra ($\Sigma\alpha_{if}$) as a function of average electric field across the well for different transitions in an undoped C-DQW.

possibility and only the transitions between two band indices with different parity (i.e. the diagonal transitions) have a nonzero value, in line with the parity selection rule. However, the matrix elements of the vertical transitions increase along the applied electric field whilst those of the diagonal transitions decrease. This causes the break down of parity-forbidden transitions and restraint of parity-allowed transitions. For the vertical transitions, the absorption peak increases dramatically first at a small range near zero of field strength, then it decreases as the field strength continuously increases. The behaviour of the vertical transition E_1-E_3 is representative of such changes with the applied electric field. As Fig. 4.20 (b) shows, the intensity of the E_1-E_3 absorption starts exceeding the diagonal E_2-E_3 absorption at about -5V/μm. Then, E_1-E_3 transition becomes the dominant ISBA when field strength $|F_{av}|$ exceeds 8V/μm.

In order to clarify the characteristics of electroabsorption modulation of the C-DQW, the absorption spectra at applied field strengths of -1, -5 and -10 V/μm are shown in Fig. 4.21. The spectra near 0.8 eV are decomposed into its Lorentzian components so that the contribution of each transition to the total ISBA spectrum can be easily observed. In Fig. 4.21 (a), the electric field applied to the structure is relatively weak, which results in a fairly symmetrical potential profile as shown in the inset. Consequently, the values of the matrix elements of the vertical transitions are small owing to the parity selection rule, and the two peaks in the spectrum are then mainly contributed by the Lorentzian components of the diagonal E_1-E_4 and E_2-E_3 transitions.

As the field strength increases, the symmetric character of the band profile and the envelope functions is lost. The originally symmetrical potential profile is tilted and the wavefunctions of the two lowest energy states start localising into the individual wells at F_{av} = -5 V/μm, as shown in the inset of Fig. 4.21 (b). This then causes the breakdown of the parity selection rule and subsequently the values of matrix

(a) F_{av} = -1 V/μm

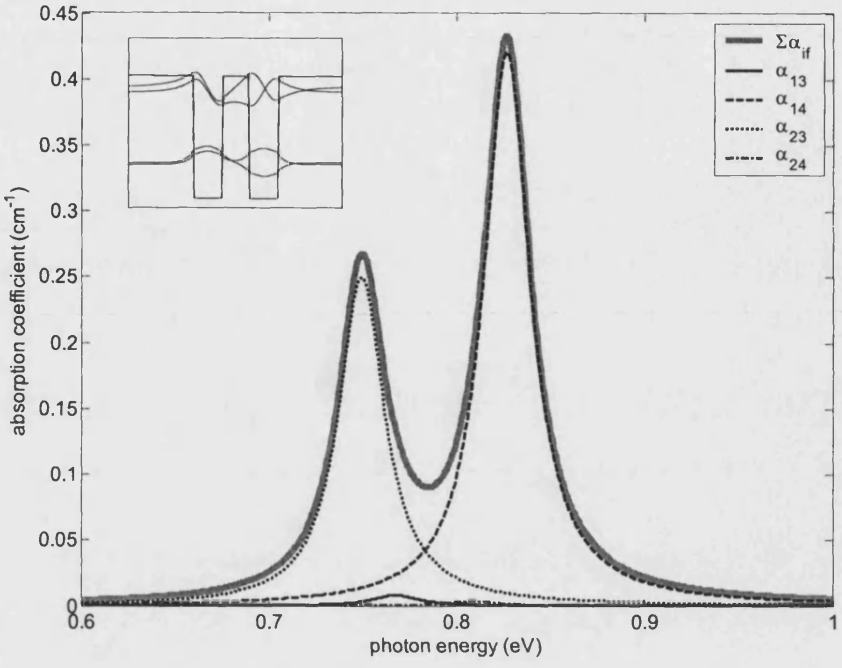

(b) F_{av} = -5 V/μm

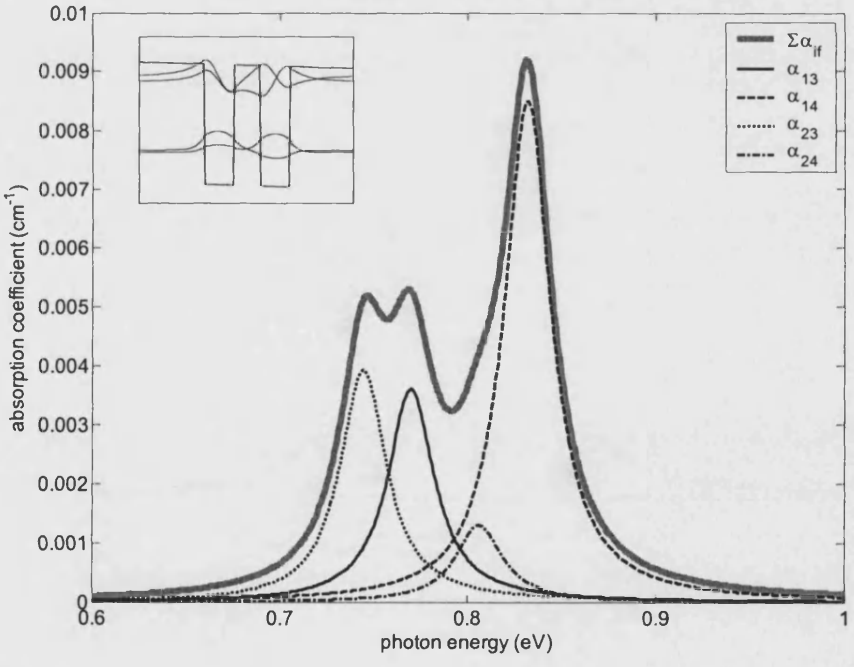

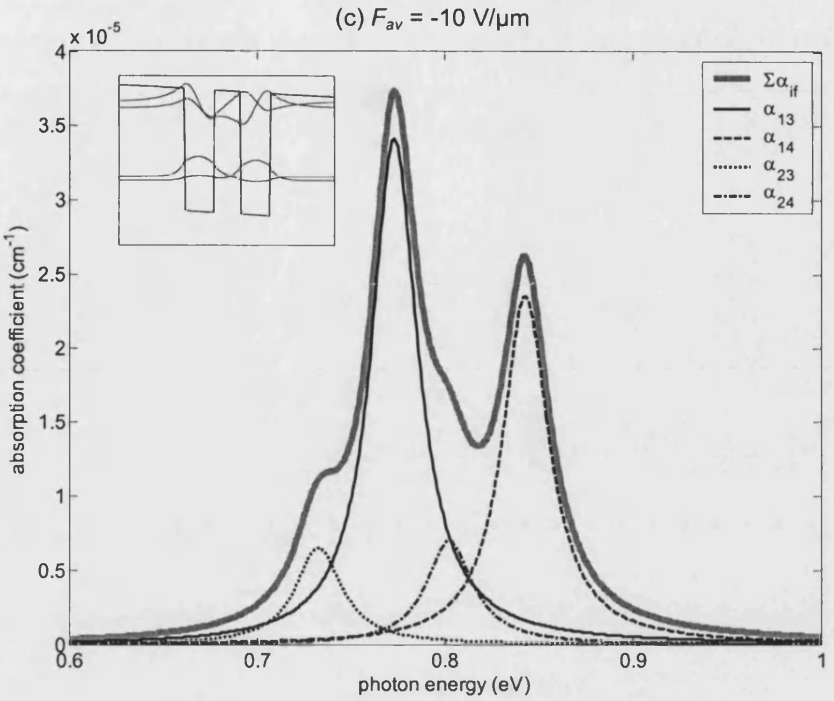

Figure 4.21: Decomposition of the absorption spectra for average field strength of (a) -1 V/μm, (b) -5 V/μm and (c) -10 V/μm into its Lorentzian components. The thick solid line is the sum of the decomposed components. The inset shows the potential profile and the envelope wavefunctions of the confined states. The zero amplitude positions of the envelope functions coincide with the subband energies relative to the bottom of the wells. Note the change in the scale factor of the vertical axes of parts (a), (b) and (c) of this figure.

elements are comparable for all ISBTs. As a result, in the low energy feature (~0.75 eV) transition E_1-E_3 becomes more dominant than transition E_2-E_3 as both absorption peaks decrease in strength, but at different rates as can be observed in Fig. 4.20 (b). The high energy feature at ~0.83 eV has a low energy shoulder. When comparing to the -1V/μm situation in Fig. 4.21 (a), the shape of the spectrum in Fig.4.21 (b) is very different owing to the different rate at which the intensities of the individual Lorentzian components associated with the different transitions vary with changing the applied field.

At F_{av} = -10 V/μm in Fig. 4.21 (c), the localisation of the envelope wavefunctions of the two lowest energy states is very strong but the wavefunctions of the excited states

still extend to the neighbouring well as shown in the inset. It implies that very strong field strength is required to fully decouple such a C-DQW structure. Although both matrix elements of the vertical transition are large, only the E_1-E_3 transition is dominant in the absorption spectra and the diagonal transition E_1-E_4 still remains the next most prominent peak. This is because the amplitude of the Fermi occupancy ratio of the E_2-E_3 transition decreases much faster than that of the E_1-E_4 transition. For the E_2-E_3 transition, the decrease of the Fermi occupancy ratio is more rapid than the increase of its matrix element, resulting in the strong decrease of the maximum absorption. Moreover, by comparing Fig.s 4.20 (b) and (d), it can be seen that the Fermi occupancy ratio is the principal factor affecting the absorption in the strong field region.

In general, the various features of the field dependence of ISBA in the undoped C-DQW structures are the combined effects of the break down of parity selection due to the increase of matrix elements and the monotonic decrease of the Fermi occupancy ratio due to increasing the reverse bias applied to the structure. The E_1-E_4 and E_2-E_3 transitions are the major Lorentzian components contributed to the absorption lineshape at $F_{av} \approx 0$, because of their large optical matrix elements. As the electric field increases, the parity selection rule is broken causing a variation in the optical matrix elements. Therefore, the vertical transition E_1-E_3 produces the dominant contribution to the overall absorption spectrum. Yet, the diagonal transition E_1-E_4 remains a strong, if secondary, contribution to the overall ISBA at -10 V/μm. At even stronger electric fields, e.g. -20 V/μm, the structure is still not fully decoupled and remains a significant absorption peak owing to the size of its optical matrix element. It is concluded that the electroabsorption modulation in C-DQW is more complex than the SQW structure owing to the significant effects of the optical matrix elements in the ISBA. However, whilst the changes in the optical matrix elements of the various transitions govern the shape of the absorption band, the Fermi occupancy still governs its overall strength.

4.3.3 Effects of Modulation Doping in C-DQWs

(1) Potential Profile

The C-DQW structures with same dimensions discussed in previous section were chosen to investigate the dependence of modulation doping on ISBA. There are several combinations for siting the modulation doped regions in a DQW since three optional doping areas can be selected. The influences on the potential profile, the confined state energies and the corresponding envelope wavefunctions in different doping situations with reference to the undoped case are shown in Fig. 4.22. In order to show a clear separation in the potential profile, a high doping density of 1×10^{18} donors/cm^3 was chosen for all simulations discussed here. Each modulation doping sheet was located in the centre of its corresponding AlAs layer, as illustrated earlier in Fig. 4.1.

Compared to the undoped case [Fig. 4.22 (a)] under the same field strength, the modulation doping in the left outer barrier in Fig. 4.22 (b) shows little influence in all aspects, similar to the result of SQW in Fig. 4.12 (b). With same amount of donors for the modulation doping applied in the inner or the right outer barrier, as in Fig.s 4.22 (c) and (d), the potential profile is bent downwards and consequently the energies of the confined states are closer to the Fermi level. In this circumstance, the absorption coefficient is increased, referring to Eq. (3.71). By comparing Fig.s 4.22 (c) and (e), (d) and (g) or (f) and (h), all three groups show that modulation doping in the outer-left barrier has little effect on the potential profile and the envelope wavefunctions when the same field strength is applied. On the other hand, locating the modulation doping in the inner barrier or in the outer-right barrier has a strong effect, pulling the wells down towards the Fermi level to increase their occupancy. Locating the doping in the outer-right barrier has the strongest effect, but overall modulation doping in all three AlAs barriers gives the most promising outcome.

(2) Absorption Spectrum

In order to clarify the effect of the position of modulation doping on the ISBA, the

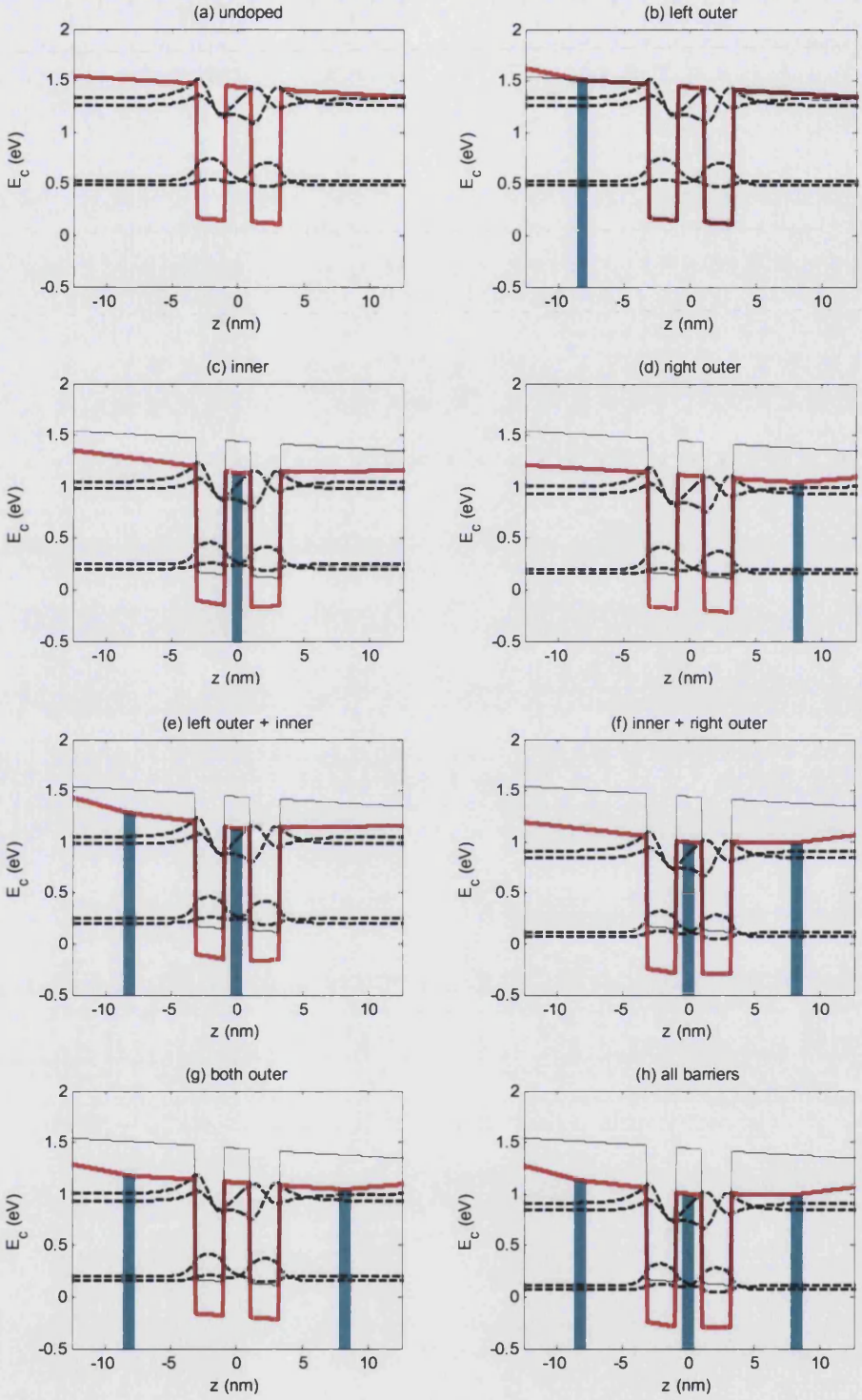

Figure 4.22: The influence of modulation doping locations on conduction band profile (solid red line) and wavefunctions (dashed line) of C-DQWs. Each modulation doping layer is 1.0 nm thick and $N_D = 1\times10^{18}$ donors/cm^3, as indicated by the vertical blue lines. All the structures is under F_{av} = -10 V/μm. The potential profile of the undoped structure (thin solid line) is also plotted for comparisons. The zero amplitude positions of the envelope functions coincide with the subband energies.

absorption spectra of five representative cases from Fig. 4.22 are given in Fig. 4.23 with the locations of the modulation doping specified in the inset. Further, another five similar situations but with a low doping density of 1×10^{17} donors/cm^3 are also applied to the same doping locations, to explore the effect of doping density on the absorption spectra of C-DQWs. The same order in the enhancement of the absorption with respect to the position of the doped regions is observed for the two different doping densities. While the low doping density (1×10^{17}/cm^3) does not alter the potential profile much, the results are still significant. For example, the absorption of the structure with modulation doping in all three barriers is over ten times stronger than the undoped structure. For the high doping density cases, the enhancement in the absorption compared with the undoped and low doped structure is more remarkable. The magnitude of absorption coefficient has increased several orders of magnitude compared to the same doping location but with a low doping concentration.

By comparing the "inner" to the "left outer + inner" cases or the "inner + right outer" to "all barriers" cases in both doping levels, it clearly shows that the extra modulation doping in the left outer barrier results in an essentially unchanged absorption spectrum compared to just inserting doping in the inner barrier, or right outer barrier or both. It has to be noted that these comparisons are based on the same average field strength across the C-DQW, but the surface potential needed to produce this average field strength can be very different. Moreover, positioning the same amount of donors in the right outer barrier can increase the absorption coefficient more than putting the same sheet density of donors in the inner barrier. By combining these two doping locations without increasing N_D, i.e. only doubling the donors in the structure, one can increase the intensity of absorption spectrum by over an order of magnitude. This shows that the location of the modulation doped region can powerfully change the strength of ISBA. The results also clearly demonstrate that using higher doping density in the doping regions increases the absorption intensity across the spectrum, as in the case of the SQW.

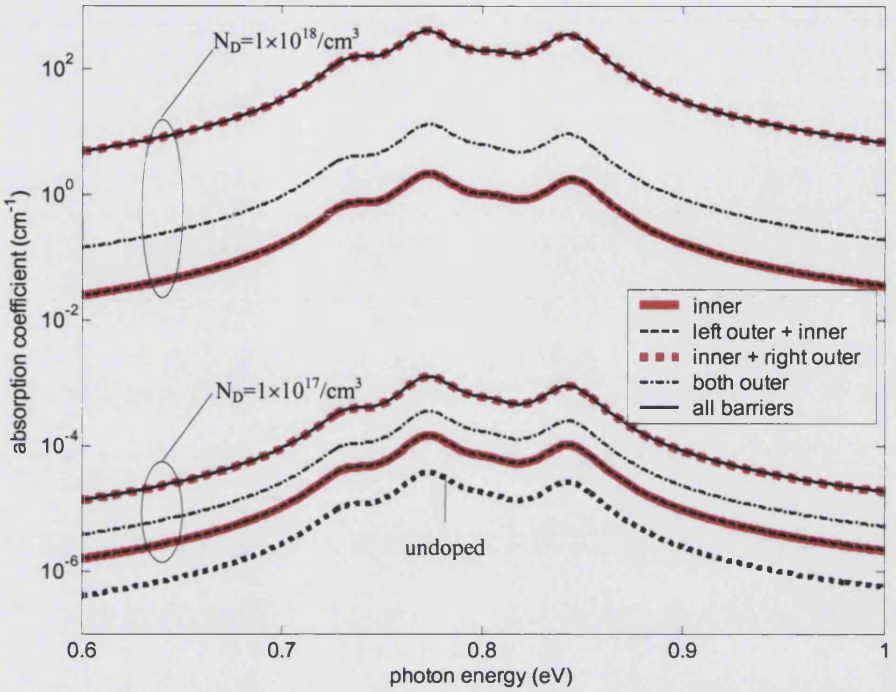

Figure 4.23: The combined influence of the doping location and doping concentration on the absorption spectra of C-DQWs. Undoped and two levels of the doping density, 1×10^{17} donors/cm^3 and 1×10^{18} donors/cm^3 in the 1nm-wide *n*-type regions, are considered. The absorption spectra are at F_{av} = -10 V/μm for all cases.

(3) Transition Energy Shift

For all doping cases in Fig. 4.23 the peak absorption occurs at more-or-less the same energy. This shows that modulation doping has little effect on the transition energy, which is a critical parameter for modulators. Since all the cases with low doping density have nearly the same transition energies as in the undoped structure, only the influence of doping locations on the transition energy at high doping concentration is listed in Table 4.3. As can be observed from the table, the maximum shift in the absorption peak is about 2~3 meV, compared to the undoped structure. However, transition energies are modified more strongly by electric field (Stark shift) in C-DQW structures compared with the SQW, as commented previously (Fig. 4.20). The influence of modulation doping on the transition energy shift is small, compared with the effect of the built-in electric field. However, designing a modulator to work

C-DQW L_w = 2.2nm, L_b = 2.0nm, F_{av} = -10V/μm		transition energy (meV)			
		E_{13}	E_{14}	E_{23}	E_{24}
Undoped		773.0	842.8	732.5	802.3
$N_D = 1\times10^{18}/cm^3$	**left outer**	773.0	842.8	732.5	802.3
	inner	772.9	844.8	733.4	805.2
	right outer	772.9	842.8	732.5	802.5
	left outer + inner	772.9	844.7	733.4	805.2
	inner + right outer	772.1	842.8	734.2	805.0
	both outer	772.9	842.8	732.5	802.3
	all barriers	772.1	842.8	734.3	805.0

Table 4.3: The influence of the location of doped regions on the transition energies of C-DQW structures. The doping density is 1×10^{18} donors/cm^3 and field strength -10 V/μm for all structures.

at given energy, the effect of the built-in field along on the transition energy should be taken into account for the accurately unbiased condition.

(4) Surface Potential

Finally, for clarifying the dependence of externally applied bias on the internal characteristics, i.e. the electric field and the absorption spectra, the connection between the surface potential and the electric field (F_{av}-V_{surf}) is shown in Fig. 4.24 (a) for different doping situations illustrated in Fig. 4.22. Since the diagonal transition E_1-E_4 and the vertical transition E_1-E_3 are the dominant ISBT in weak and strong field respectively, the maximum value of these Lorentzian components of the overall absorption spectra as a function of surface potential are illustrated in Fig.s 4.24 (b) and (c).

The doping location produces a strong effect on the extent of the flat field region (the weak modulation region) in Fig. 4.24 (a). When the doped regions are symmetrically sited, the structure appears to have an average applied field strength close to zero at the limit of this region whilst the asymmetric siting of the doped layers creates quite

a strong built-in field. In the other weak modulation region, the slope of the linear field region changes considerably for the various doping conditions. The absorption modulation region lies between the flat field region and the linear field region. The onset for this modulation region and the voltage range over which it occurs varies considerably with the location of the modulation doping. For sensitive absorption modulation, sharp bending after achieving the onset voltage is required. Locating the doping in the inner barrier only or in one or other of the outer barriers gives rise to the sharpest corner in the characteristic. Hence single locations of the modulation doping result in a more sensitive voltage control than multi-layer doping.

Fig. 4.24 (b) shows that doping in either outer barrier has basically the same improvement on maximum absorption of the E_1-E_4 transition [max(α_{14})]. However, locating the modulation doped region in the inner barrier has the strongest enhancement in max(α_{14}) among the structures with the same amount of donors added in. Doping in the left outer barrier can push the strong modulation region of max(α_{14}) towards the positive surface potential side, i.e. towards the negative reverse bias due to the barrier height of 0.5 eV for the Schottky contacted structure (indicated as the vertical dotted line in Fig. 4.24), whilst doping in the right one towards the negative side. Placing the donors at the different possible locations can affect the driving voltage of modulators. For example, siting the doping in the inner barrier only creates a device requiring forward bias to produce the "off" state, whereas doping in the inner and right outer barriers creates a device that requires bias swings around zero to produce "off" and "on" state. When *p-i-n* and *n-i-n* junctions, as shown in Fig. 4.14, are considered, forward bias is typically necessary for the former one while reverse bias for the latter. Therefore, for a certain device configuration, the doping location is important for its desired operating conditions.

For the vertical transitions, the absorption coefficient has a maximum value at a certain range of electric field strength, i.e. applied bias voltage, as shown in Fig. 4.20 (b). In Fig. 4.24 (c), the maximum absorption of the E_1-E_3 transition [max(α_{13})] is

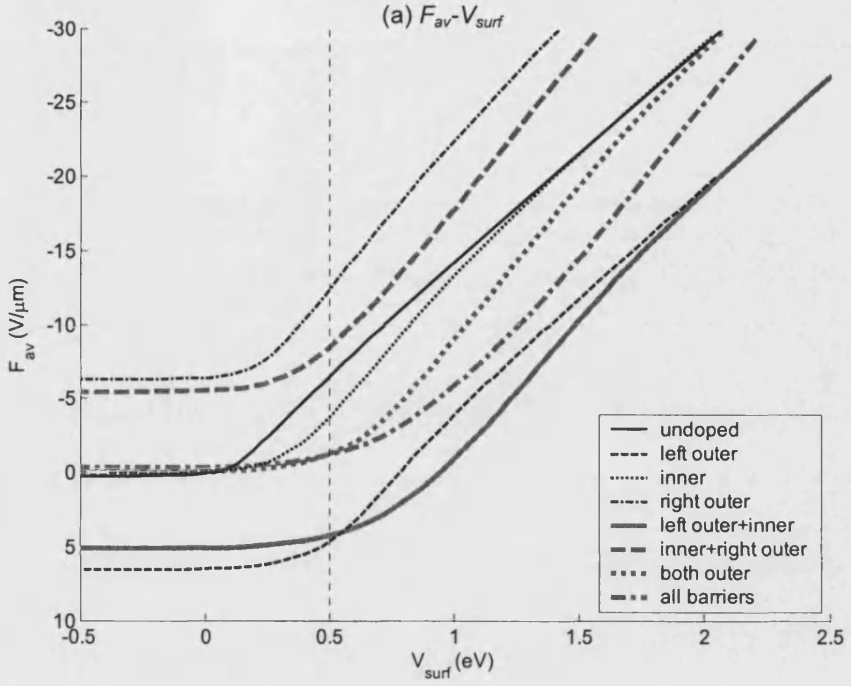
(a) F_{av}-V_{surf}
F_{av} (V/μm)
V_{surf} (eV)
undoped
left outer
inner
right outer
left outer+inner
inner+right outer
both outer
all barriers

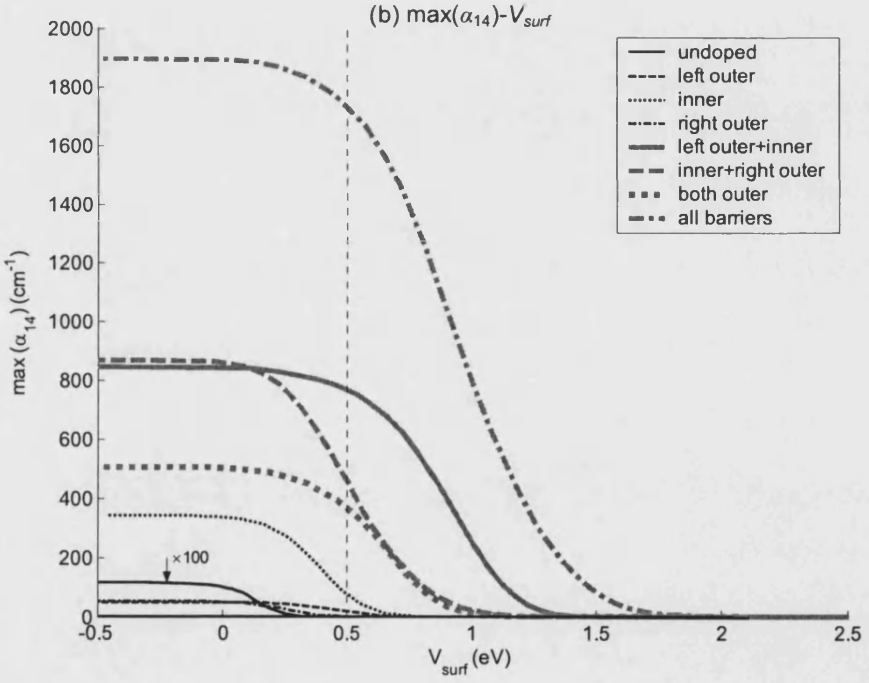
(b) max(α_{14})-V_{surf}
max (α_{14}) (cm^{-1})
×100
V_{surf} (eV)
undoped
left outer
inner
right outer
left outer+inner
inner+right outer
both outer
all barriers

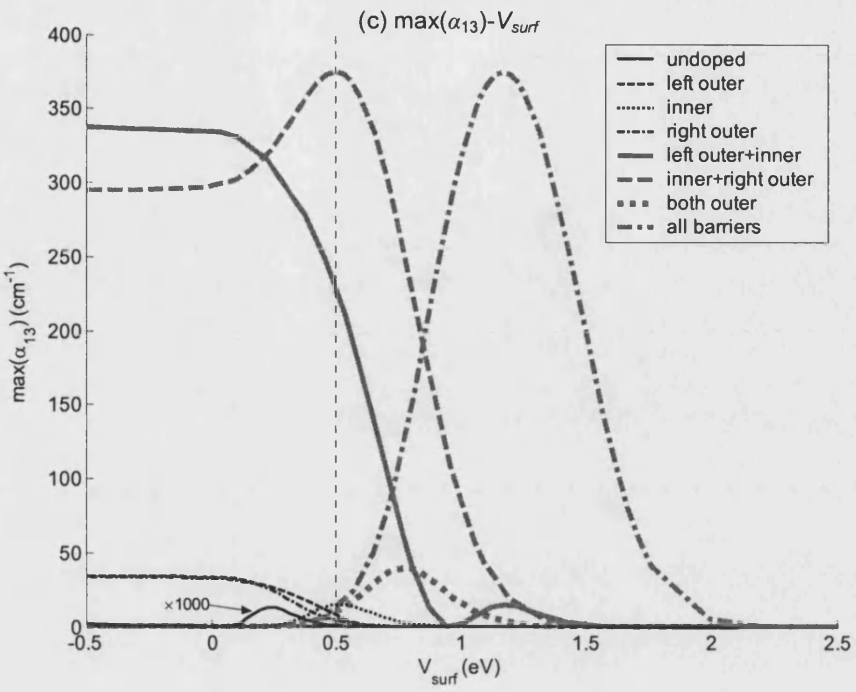

Figure 4.24: The influence of doping locations on (a) the average field across the well (F_{av}-V_{surf}), (b) the maximum absorption coefficient of diagonal transition E_1-E_4 [max(α_{14})-V_{surf}] and (c) the maximum absorption coefficient of vertical transition E_1-E_3 [max(α_{13})-V_{surf}] as a function of surface potential. Each modulation doping layer in AlAs was assumed to be uniformly doped to 1×10^{18} donors/cm^3 and 1.0 nm wide.

illustrated. The max(α_{13})-V_{surf} characteristic is very different from the max(α_{14})-V_{surf} characteristic in Fig. 4.24 (b). The max(α_{13}) appears to have a peak at particular surface voltage, which shows a strong dependence on the location of the doped layer or layers. Moreover, the enhancement of max(α_{13}) also depends strongly on the doping location. This absorption peak is caused by the combination of the increase of the matrix element of the vertical transition and the decrease of Fermi occupancy ratio as reverse bias increases. In principle, the behaviour of the maximum absorption associated with the vertical transition E_1-E_3 is not straightforward and therefore it requires detailed simulations as used here for its evaluation.

In general, the location of the modulation doping shows significant effects on the F_{av}-V_{surf} and max(α_{if})-V_{surf} characteristics especially in defining the surface potential

for the onset of bias induced change in absorption, i.e. the corner or onset voltage in the average field strength versus surface potential characteristics, and the built-in electric field across the wells (corresponding to the flat parts of the curves). For all different locations for applying the modulation doping, positioning donors in all AlAs barriers with a large doping density appears to have the best result for electroabsorption modulation in terms of enhancing the absorption intensity due to the enhanced occupancy of the ground state, but at the cost of some reduction in voltage sensitivity.

(5) An Optimized C-DQW Structure

Summing up the effects of modulation doping on ISBT in C-DQWs, an example of a good performance structure for modulators is given in Fig. 4.25. It is an $In_{0.57}Ga_{0.43}As$/AlAs C-DQW with L_w = 2.2 nm, L_b = 2.0 nm and modulation doping of $N_D = 1\times10^{18}$ donors/cm^3 in all AlAs barriers. The structure has strong ISBA and its absorption spectra are sensitive to the electric field. This ensures large differential absorption spectra with respect to the change in electric field. These features can be easily observed from Fig. 4.25 (a). Moreover, the maximum absorption given above in Fig. 4.24 is a function of the certain transition, such as E_1-E_3 and E_1-E_4. However, these transition energies are not constant and shift according to the electric field, as shown in Fig. 4.25 (b).

For a practical modulator, the incident light will have specified photon energy. Therefore, the absorption coefficient for carefully selected photon energies versus electric field is given in Fig. 4.25 (c). The functions of absorption at 0.747 and 0.827 eV show very good performance as the field strength increases. Although the vertical transition E_1-E_3 undergoes a rapid absorption change, as seen in Fig. 4.24 (c), it in fact only has a small effect on the overall absorption modulation due to the extended Lorentzian tail of the line broadening effect of the E_1-E_4 and E_2-E_3 transitions.

(a) isometric view

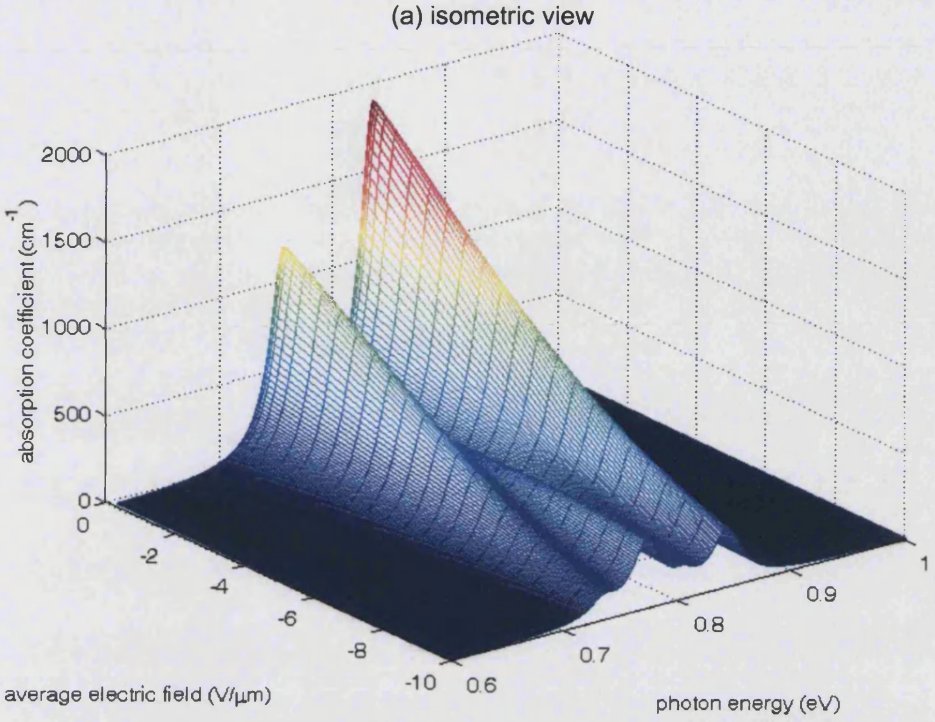

(b) top view

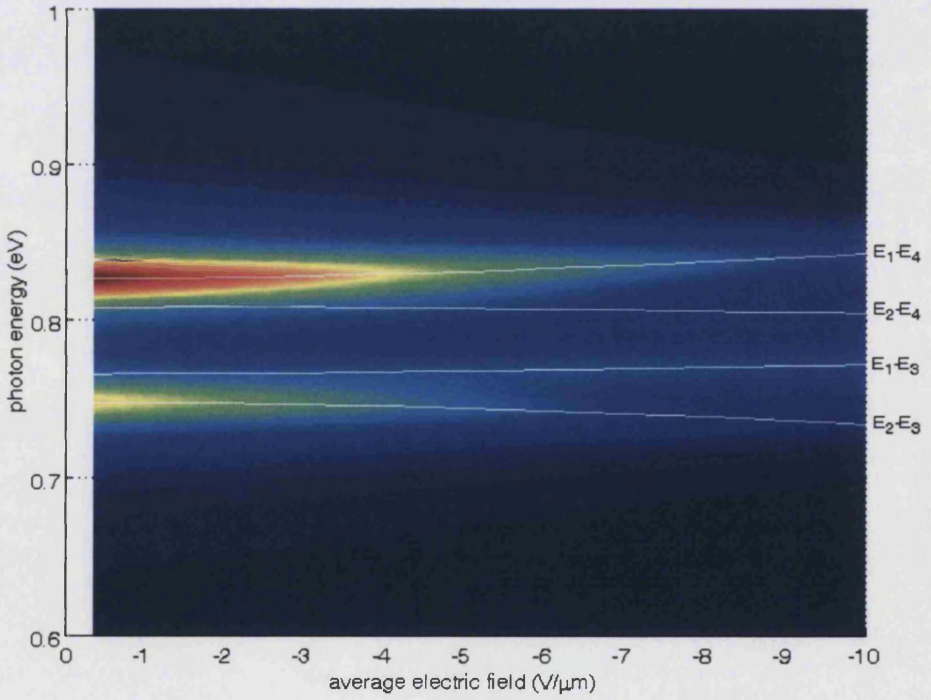

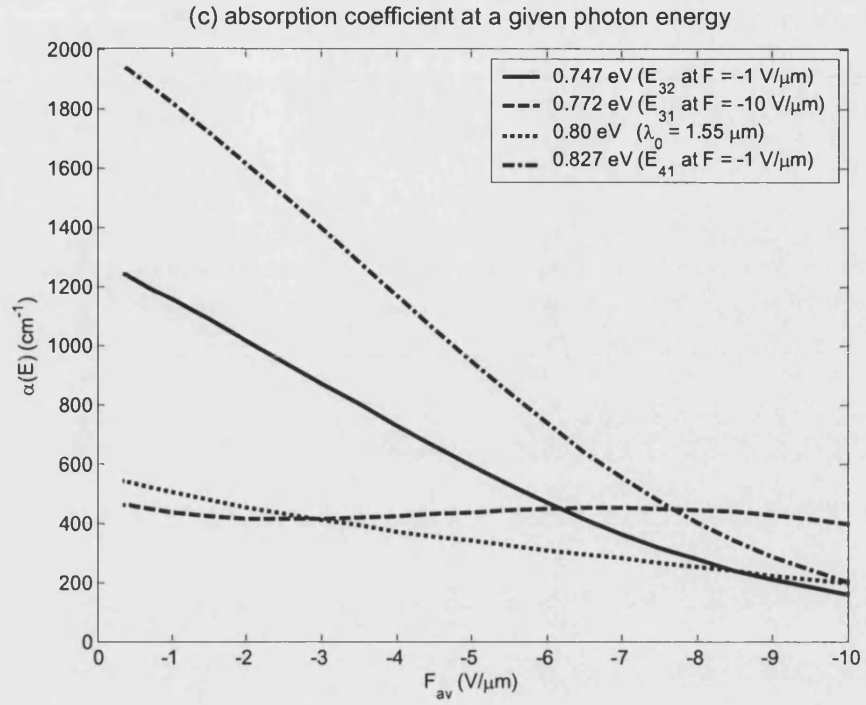

Figure 4.25: The 3D absorption spectra from different viewpoint: (a) isometric view and (b) top view with four transition energies, and (c) the absorption coefficient at certain photon energies as a function of electric field in a C-DQW with modulation doping to 1×10^{18} donors/cm^3 in all barriers.

Therefore, for the modulators based on the C-DQW, in order to achieve a large different absorption spectrum under a small change on the applied bias, utilising the ISBA modulation based on the diagonal transitions produces a superior outcome. Owing to the simultaneous electroabsorption from both the E_1-E_4 and E_2-E_3 transitions, which occur at weakly voltage dependent energies above and below 0.8eV, an EAM based on this C-DQW structure will efficiently modulate a range of wavelengths in a narrow band about 1.55 μm (equivalent to 0.8 eV) as well at the designated wavelength.

4.3.4 An Undoped 2QW (L_w = 2.2 nm, L_b = 5.0 nm)

Similar studies were performed for the negligibly coupled DQW (2QW), in order to explore the cross-over region from strongly coupled quantum wells (SL) behaviour

to multiple modulation doped SQWs (MQW) behaviour. Such discussion is given in Section 4.5. The transition energy, absorption strength, absolute value of optical matrix element, the Fermi occupancy ratio and the electroabsorption spectra are given in Fig. 4.26 for the undoped 2QW. The shift in transition energy, E_1-E_4 and E_2-E_3, are very sensitive to applied electric field in Fig. 4.26 (a). However, the effect of these shifts on the shape of the absorption band of the modelled structure is insignificant for the following reasons.

First Fig. 4.26 (c) reveals that whilst the matrix elements of the E_1-E_4 and E_2-E_3 transitions are large at zero field across the wells, their values rapidly decline whilst those of the E_1-E_3 and E_2-E_4 transition rapidly grow to the extent that for $|F_{av}| > 0.05$ V/μm the latter becomes the larger. Now, the occupancy factors for transitions from E_1, the lowest energy state, are consider much larger than those involving transitions of E_2 for applied field of strength $|F_{av}| > 3$ V/μm as Fig. 4.26 (d) reveals. Whilst the matrix elements vary rapidly with field, this change, being an order of magnitude or so between -0.5 V/μm and -15 V/μm, becomes of only marginal significance at best when compared with the changes in the occupancy factors over the same range of applied fields. Therefore, once the initial rapid changes in the matrix elements have occurred, at fields strength -1 V/μm in this undoped structure, the absorption modulation with electric field is largely governed by the occupancy factor of the dominant E_1-E_3 transition, as Fig. 4.26 (e) shows.

The Fermi occupancy ratio [Fig. 4.26 (d)] has comparable value for all transitions at weak electric field and undergoes a difference of several orders in magnitude between initial states at $i = 1$ and $i = 2$ as the field strength increases. The similar value is caused by the degeneracy of subband energies at zero field, resulting in basically the same energies (two-fold) in ground states and excited states, while the distinct value is due to the tilted potential caused by the applied bias and results in a large energy difference between the two initial energy states (E_1 and E_2). In general, the phenomena presented above are owing to the minor energy split by the weak

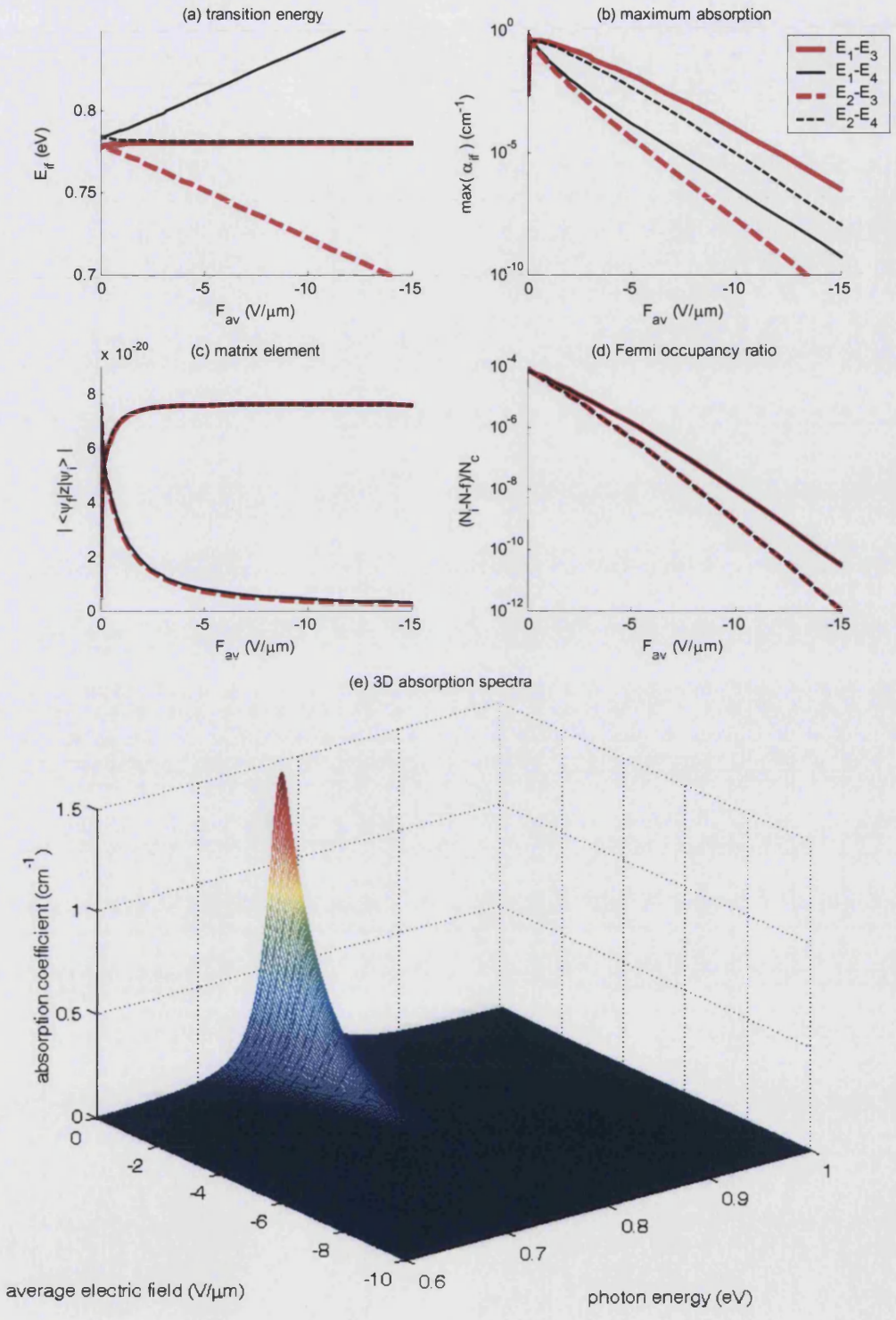

Figure 4.26: (a) The transition energy, (b) the maximum absorption coefficient of each transition, (c) the optical matrix element, (d) the Fermi occupancy ratio and (e) the 3D electro-absorption spectra ($\Sigma\alpha_{if}$) as a function of electric field in an undoped 2QW.

tunnelling, and the subsequent strong localisation of the envelope wavefunctions together with the unequal ground state energies by the applied field.

After the envelope wavefunctions are localised, the vertical transitions E_1-E_3 and E_2-E_4 dominate the ISBA. Meanwhile the transition energies E_{13} and E_{24} are almost equal. In this circumstance, there is only one sharp peak in the absorption spectra which can be considered as a superposition of the absorption strengths of two SQWs. This is expected due to the weak coupling effect. However, the tunnelling of envelope functions still results in ~0.02 eV shift of the absorption peak compared with the behaviour of an isolated SQW structure (Fig. 4.6). This is caused by the shift integral due to the overlap of envelope wavefunctions indicated in Section 2.2.1. Therefore, the central absorption wavelength shifts from 1.55 μm in SQW to 1.59 μm in 2QW. This is a potentially significant detuning for device operation in multi-wavelength communication systems and must be taken into account in designing any practical device.

For clarifying the localisation dependence on the structure characteristics, an absorption spectrum is decomposed into its Lorentzian components arising from the individual ISBTs in Fig. 4.27. In the case of 2QW, the localisation of envelope wavefunction proceeds rapidly starting from small field strength. As can be noticed in the inset of Fig. 4.27, the wavefunctions of both ground states and excited states are strongly localised even at F_{av} = -2 V/μm. This is contrary to the C-DQW case shown in Fig. 4.21, in which the wavefunctions are not fully localised even at field strength as large as -10 V/μm. Only the vertical transition is important in this situation as can be observed from the localised wavefunctions and also from the negligible value of the optical matrix elements of the diagonal transitions [Fig. 4.26 (c)], and therefore the DQW structure can be considered as effectively two SQWs even at low field strength. However, in this two SQW structure, the vertical ISBTs have unequal strength in which the well at the lower potential energy side shows a

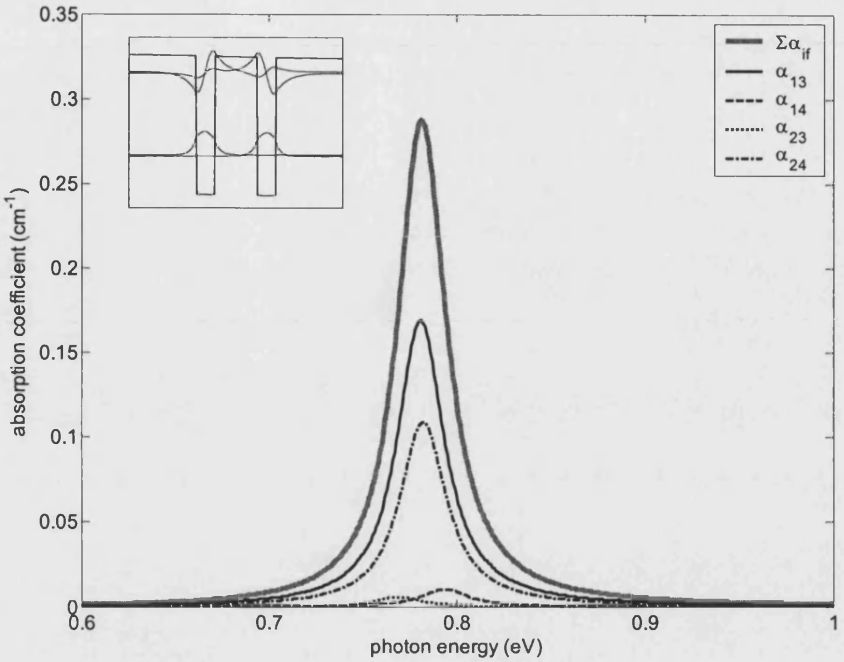

Figure 4.27: Decomposition of the absorption spectra into its Lorentzian components at F_{av} = -2V/μm. The inset shows the potential profile and the subband energies with their envelope wavefunctions. The zero amplitude positions of the envelope functions coincide with the subband energies relative to the bottom of the wells.

stronger absorption than the other one. This arises from the difference in the ground state energies which gives rise to a difference in the Fermi occupancy factors for the E_1-E_3 and E_2-E_4 transitions despite their near degeneracy from a quantum mechanical point of view.

4.3.5 Effects of Modulation doping in 2QWs

It has to be noted that the studies of 2QW presented above focus on the field dependence only. The surface potential, i.e. the applied bias, is important to determine the operating conditions as a function of modulation doping conditions. With the same regions selected in previous C-DQW (see Fig. 4.22), the effects of incorporating a high density of modulation doping on the ISBA in the 2QW have been considered. Since changing the doping density mainly results in changing the

magnitude of the absorption, only the case of 1.0 nm wide layer(s) doped with 1×10^{18} donors/cm^3 has been considered. The results are given in Fig. 4.28.

The influence of the location of the modulation doping on the F_{av}-V_{surf} characteristics is illustrated in Fig. 4.28 (a). When one compares Fig. 4.28 (a) to Fig. 4.24 (a), both C-DQW and 2QW have very similar F_{av}-V_{surf} curves for the corresponding doping locations. When the modulation doped regions are symmetrically distributed with respect to the central plane of the quantum wells, the field strength in flat region of the F_{av}-V_{surf} curves is nearly zero. As the total number of donors in the structure increases, the corner of F_{av}-V_{surf} (the modulation region) moves to higher V_{surf} and is flatter, i.e. a larger bias voltage is required to fully deplete the 2DEG inside the wells. Therefore, it is concluded that the F_{av}-V_{surf} features, i.e. the low and high modulation regions, are essentially controlled by the doping profile.

Owing to the negligibly extended envelope wavefunctions, the energies of the two dominant vertical ISBTs generally remain at the same value, as Fig. 4.27 shows. Therefore, the two corresponding Lorentzian components have merged into a single peak, resulting in a similar absorption lineshape to the situation of SQWs. Due to the occurrence of this single absorption peak in 2QWs, the variation in its intensity accurately describes the overall absorption modulation ($\Sigma\alpha_{if}$) with applied voltage. As a result, only the maximum overall absorption as a function of surface potential [max($\Sigma\alpha_{if}$)-V_{surf}] is shown in Fig. 4.28 (b). The enhancement of ISBA is ~1.5 times greater than the diagonal transition of C-DQW for the same amount of modulation doping, as seen in Fig. 4.24 (b). For the same amount of donors applied to the structure, doping in the inner barrier improves the max($\Sigma\alpha_{if}$) much more than inserting the same amount of donors in the left/right outer barrier. Moreover, doping in the inner barrier combined with either outer barrier enhances the max($\Sigma\alpha_{if}$) more than locating the doping in both outer barriers. However, with the same doping density, doping in all barriers has the strongest effect due to the fact that the total number of donors in the structure is the highest. This is similar to the SQW and

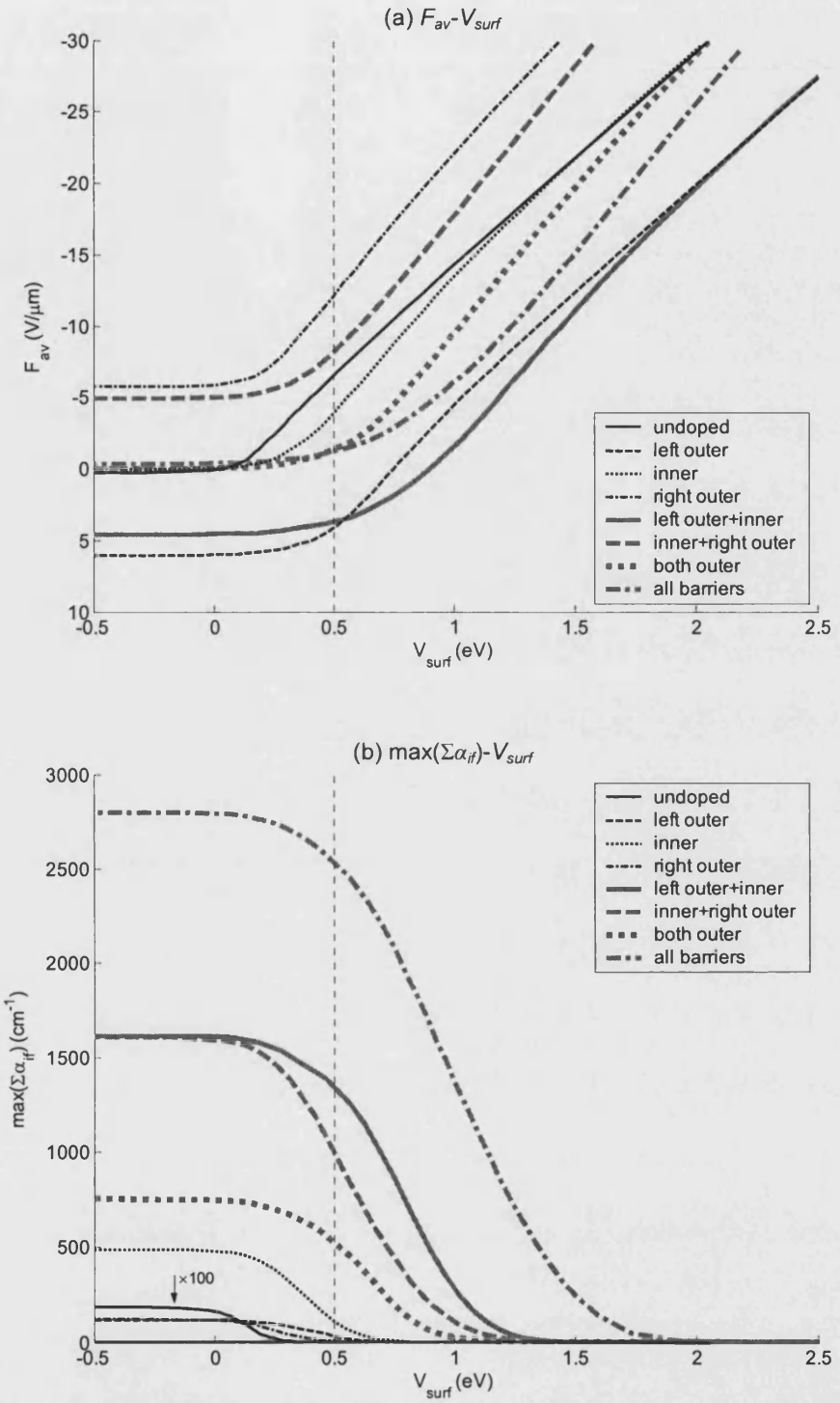

Figure 4.28: The influence of doping locations on (a) the electric field across the well (F_{av}-V_{surf}) and (b) the maximum absorption coefficient of the total ISBA [max($\Sigma\alpha_{if}$)-V_{surf}] as a function of surface potential of a 2QW. Each modulation doped region was assumed to be uniformly doped to 1×10^{18} donors/cm^3 and 1.0 nm wide. Note, doping in two (three) barriers doubles (triples) the total amount of donors in the structure.

C-DQW cases. In general, it shows that the improvement in the absorption rate is crucially related to the location of modulation doped regions when having the same doping density.

(4) An Optimized 2QW Structure

Summarising the features of 2QW structures, an optimised structure for the EAM, assuming a limit of modulation doping of layers containing $N_D = 1\times10^{18}$ donors/cm^3, would have such doped layers in all AlAs barriers. Its electroabsorption spectra are illustrated in Fig. 4.29 (a). The spectra contain a single absorption peak centred on a photon energy of ~0.78 eV, whose ISBA is mainly comprised by the vertical transitions E_1-E_3 and E_2-E_4 as shown in Fig. 4.29 (b). The transition energies E_{13} and E_{24} approach to the same value as the electric field increases due to the rapid localisation of wavefunctions to the individual wells. The intensity of the absorption peak declines strongly and monotonically as the applied electric field increases. As such, the characteristics are very different from the C-DQW (Fig. 4.25), but are very similar to those of the SQW (Fig. 4.16). Quantitatively, the absorption strength of the 2QW is more than twice that of the SQW. This reflects not only the doubling of the number of absorption wells, but also the effect of the extra modulation doped layer inserted in the inner barrier enhancing the Fermi occupancy ratio of the lowest energy levels in the two wells.

In order to reveal the similarity and difference of the absorption features of SQW and 2QW, the Fermi occupancy ratio of two vertical components (E_1-E_3 and E_2-E_4) in the 2QW is compared with the only ISBT in an SQW (E_1-E_2) in Fig. 4.30. This comparison is valid because the Fermi occupancy ratio dominates the characteristics of the ISBA in both cases, as the optical matrix elements remain basically unchanged once the wavefunctions have localised in the 2QW cases. As can be seen, the Fermi occupancy ratio of transition E_1-E_3 of the DQW structure decreases gently compared to the others. Moreover, the values of Fermi occupancy ratio for E_1-E_2 in SQW and E_2-E_4 in 2QW are direct proportion in the whole range of electric field in Fig. 4.30.

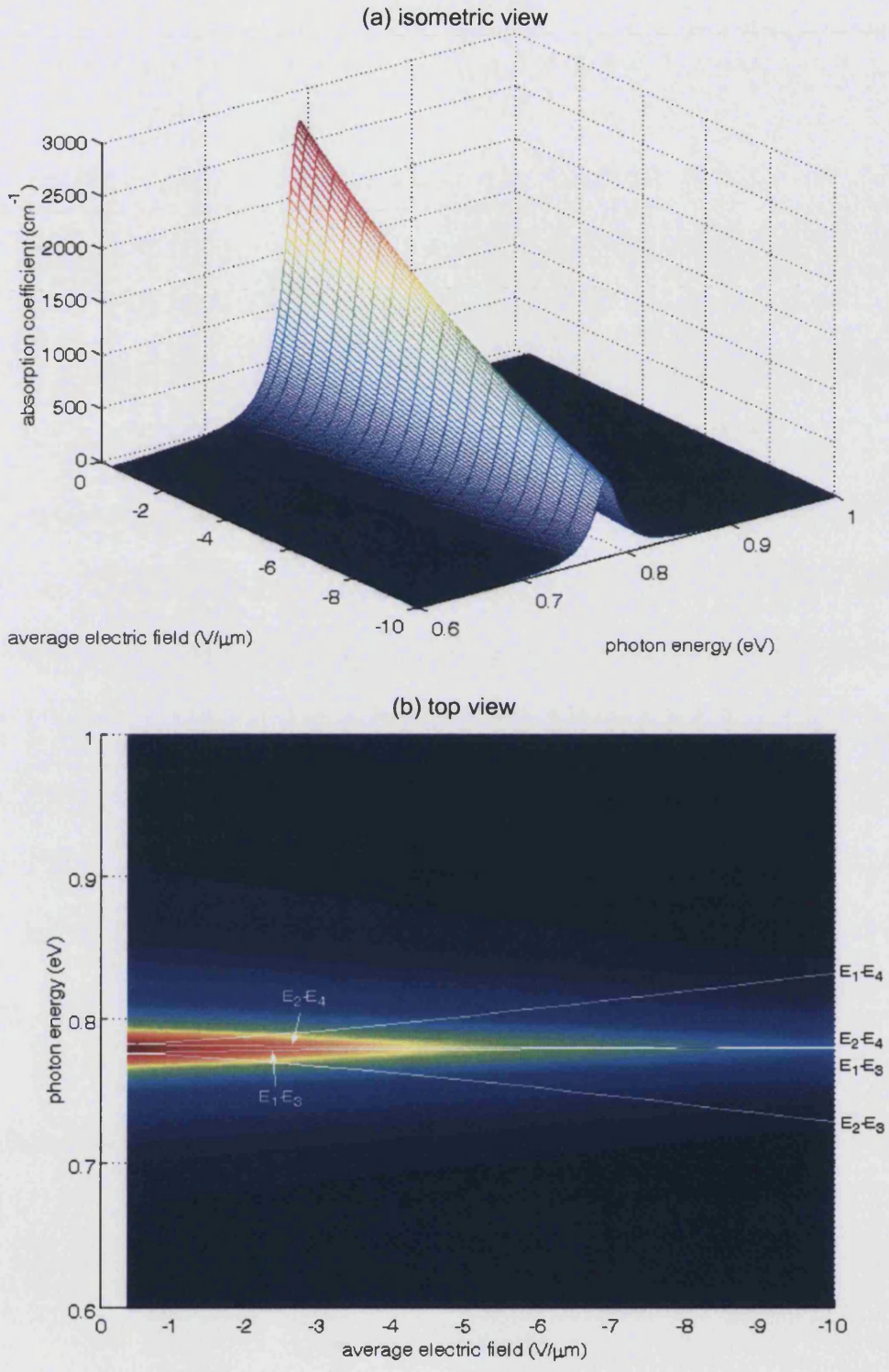

Figure 4.29: The 3D absorption spectra from different viewpoint: (a) isometric view and (b) top view with four transition energies (solid lines) as a function of electric field in a 2QW with modulation doping to $1\times10^{18}/cm^3$ in all barriers.

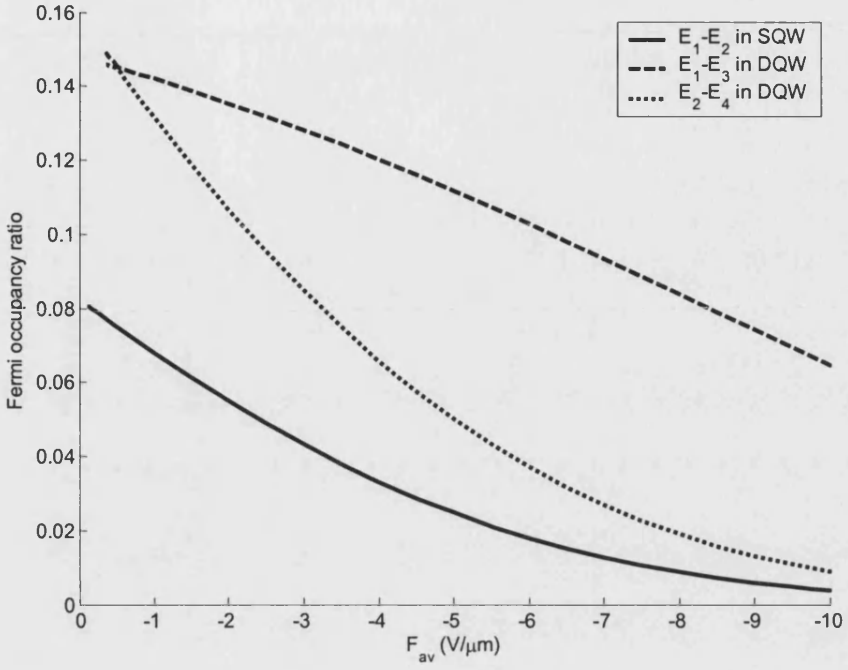

Figure 4.30: The Fermi occupancy ratio as a function of electric field of the transition E_1-E_2 in SQW and the vertical transitions E_1-E_3 and E_2-E_4 in 2QW.

Therefore, for the 2QW, in the situation of strong field, the total absorption coefficient ($\Sigma\alpha_{if}$) is mainly contributed by E_1-E_3 transition. This is because the screening effect of the left-hand well on the right-hand well when bias is applied to the contact. The left-hand well depletes more rapidly than the right-hand well as V_{surf} increases. Consequently, it contribution to the total absorption decreases more quickly. This behaviour gives some insight to the ISBA behaviour of a modulation doped MQW. It is expected that the total absorption strength of the MQW will decline as the wells deplete in sequence. This behaviour contracts with that of interband absorption in a MQW with a constant applied electric field, where each well contributes equally to the total absorption. In general, controlling the electron density in the quantum wells by varying the depletion field will have the dominant effect on the absorption modulation.

4.4 Simulations of Triple Quantum Well (TQW) Structures

In this section, the self-consistent approach is applied to the study of ISBA in triple quantum well (TQW) structures, which are less commonly used [206-208]. However, the TQW structures are investigated because of the potentially strong electroabsorption modulation by means of the large variation in their optical matrix elements, which have been observed in DQW structures. The addition of a third coupled well is expected to enhance this behaviour and any Stark shift. In addition, the possibility of TQW in multi-wavelength communication system is explored owing to the various transition energies that can occur in such structures. Furthermore, by extending the study from SQW and DQW to TQW, one can logically draw the estimated electroabsorption features to the SL and the MQW structures.

Like the DQW structures, two types of the TQW structures will be discussed, the strongly coupled TQW (C-TQW) with L_w = 2.2 nm and L_b = 2.0 nm, and the weakly coupled TQW (3QW) with L_w = 2.2 nm and L_b = 5.0 nm. Effects of different doping conditions on these two types of TQW structures are considered first. In addition, the characteristics of C-TQW and 3QW will be studied and compared with SQW, C-DQW and 2QW individually.

4.4.1 Effects of Modification Doping in TQWs

There are many options for inserting modulation doping in TQW structures due to the selection and the combination of the two inner and two outer barriers. Among all the options, seven representative cases were considered and compared with the undoped situation in Fig. 4.31. Fig.s 4.31 (b) - (e) clarify the general effects caused by inserting the modulation doping in each of the barriers in turn. Fig.s 4.31 (f) and (g) show a contrast between doping the inner and doping the outer barriers on the slope of the well potential, while doping in all barriers [Fig. 4.31 (h)] demonstrates the most substantial alteration to the potential profile. The assumed structures

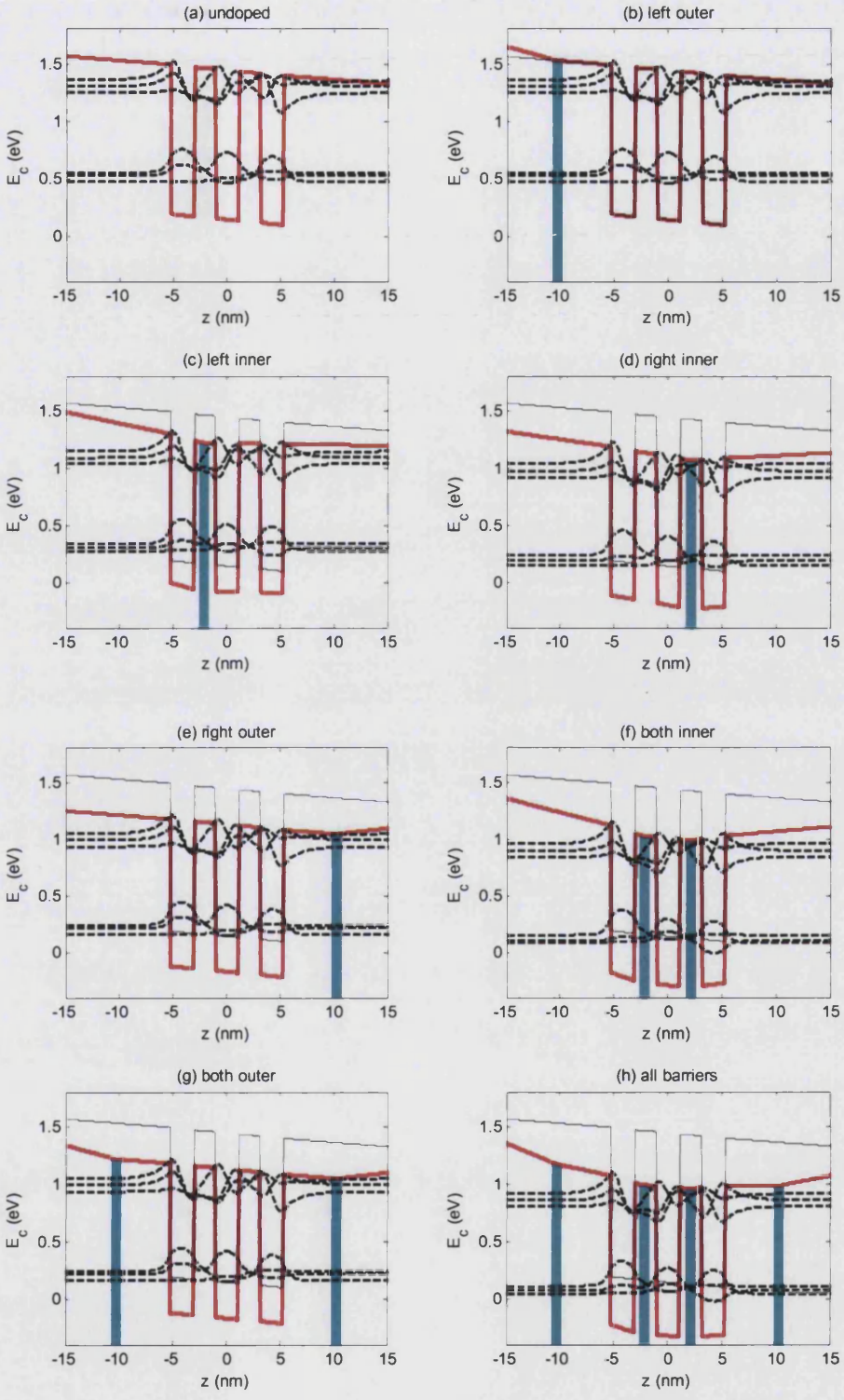

Figure 4.31: The conduction band profile (solid red line) and wavefunctions (dashed line) of C-TQWs with different doping regions (vertical blue line) as indicated in legends. Each modulation doping layer is 1.0 nm thick and N_D = 1×10^{18} donors/cm^3. The undoped case (thin solid line) is also plotted for comparison. All the structures is under F_{av} = -10V/μm. The zero amplitude positions of the envelope functions coincide with the subband energies.

illustrated in the charts were C-TQWs with modulation doped sheet(s) of 1.0 nm width containing a doping concentration of 1×10^{18} donors/cm^3 at F_{av} = -10 V/μm. The high doping density was selected for the simulations in order to visibly distinguish the potential profiles between the doped and undoped structures. For the 3QW, the effects on the potential profile and confined energies are analogous with the C-TQW cases and thereby not repeated.

As can be predicted from the conclusions given previously in SQWs (Fig. 4.12) and DQWs (Fig. 4.22), the potential profile has a very strong dependence on the positions and the number of the modulation doped regions. By comparing Fig.s 4.31 (b) - (e), doping in the right barrier, i.e. the barrier at lower potential energy, can bring down the potential profile more at the same field strength than the left one due to the screening effect. Placing donors in the inner barrier(s) [Fig.s 4.31 (c), (d), (f) and (h)] modifies the well potential in a non-linear manner, which means unequal field strength in the wells, compared to doping only the outer barrier(s) [Fig.s 4.31 (b), (e) and (g)].

Since the potential profile is shifted by the modulation doping under the same field strength, the confined particle energies and corresponding envelope wavefunctions are simultaneously affected. Consequently, the absorption coefficient will be modified. In order to investigate distinctly the influence of the doping conditions on the electroabsorption modulation, both C-TQW and 3QW structures are studied at the weak (1×10^{17} donors/cm^3) and strong doping density (1×10^{18} donors/cm^3) respectively for all the different doping locations shown in Fig. 4.31.

(1) Weak Doping Density

For clarifying individually the importance of the location of modulation doped regions on the absorption spectra for both C-TQWs and 3QWs, a low doping concentration of 1×10^{17} donors/cm^3 that hardly alters the potential profile was selected to recalculate all cases shown in Fig. 4.31. The effects of the location of the

modulation doping are significant, as shown in Fig. 4.32. The graphs show the calculated differential absorption spectra for changes in the applied electric field from -1 V/μm to -2 V/μm for (a) a C-TQW (L_b = 2.0 nm) and (b) a 3QW (L_b = 5.0 nm) with the locations of modulation doped regions shown in Fig. 4.31 and with the same other conditions except the change in doping density.

In the C-TQW structures [Fig. 4.32 (a)], three ISBA peaks, 0.842 eV, 0.787 eV and 0.726 eV, can be observed but the resolution of the peaks is low. The absorption band extends over a wider range of photon energies when compared with SQW in Fig. 4.13 and C-DQW in Fig. 4.23. The increased width of the absorption band arises from the occurrence and the superposition of multiple transitions due to the electron wavefunctions extending across all three wells. The low resolution of the absorption peaks is the result of the line broadening effects of using Lorentzian function in Eq. (3.71). In the case of the weakly coupled structures (L_b = 5.0 nm), the FWHM, or line width, of the absorption peak is ~40 meV in Fig. 4.32 (b), which is wider than the theoretical value (Γ = 30 meV) chosen in the Lorentzian function. This occurs because the peak comprises of three transitions that are too closely spaced in energy to be resolved for the broadening assumed in the calculation. Therefore, what appears as a single peak is in fact three overlapping Lorentzian components of slightly different central energy. More discussion about the effects of FWHM on ISBA will be presented in Section 4.5.1. In general, the coupling (tunnelling) phenomena play a major role in determining the shape of the absorption spectrum in both types of TQW: multiple peaks in a broad spectrum for the C-TQW, or a single peak but a larger amplitude for the 3QW.

By comparing all different arrangements of the modulation doping demonstrated in SQWs (Fig.s 4.13), DQWs (Fig.s 4.23) and TQWs (Fig.s 4.32) at the same field strength, it can be observed that doping in the left outer barrier hardly changes the absorption spectra and has little influence on the potential profile. Positioning the modulation doping in the right outer barrier has the largest effect on absorption

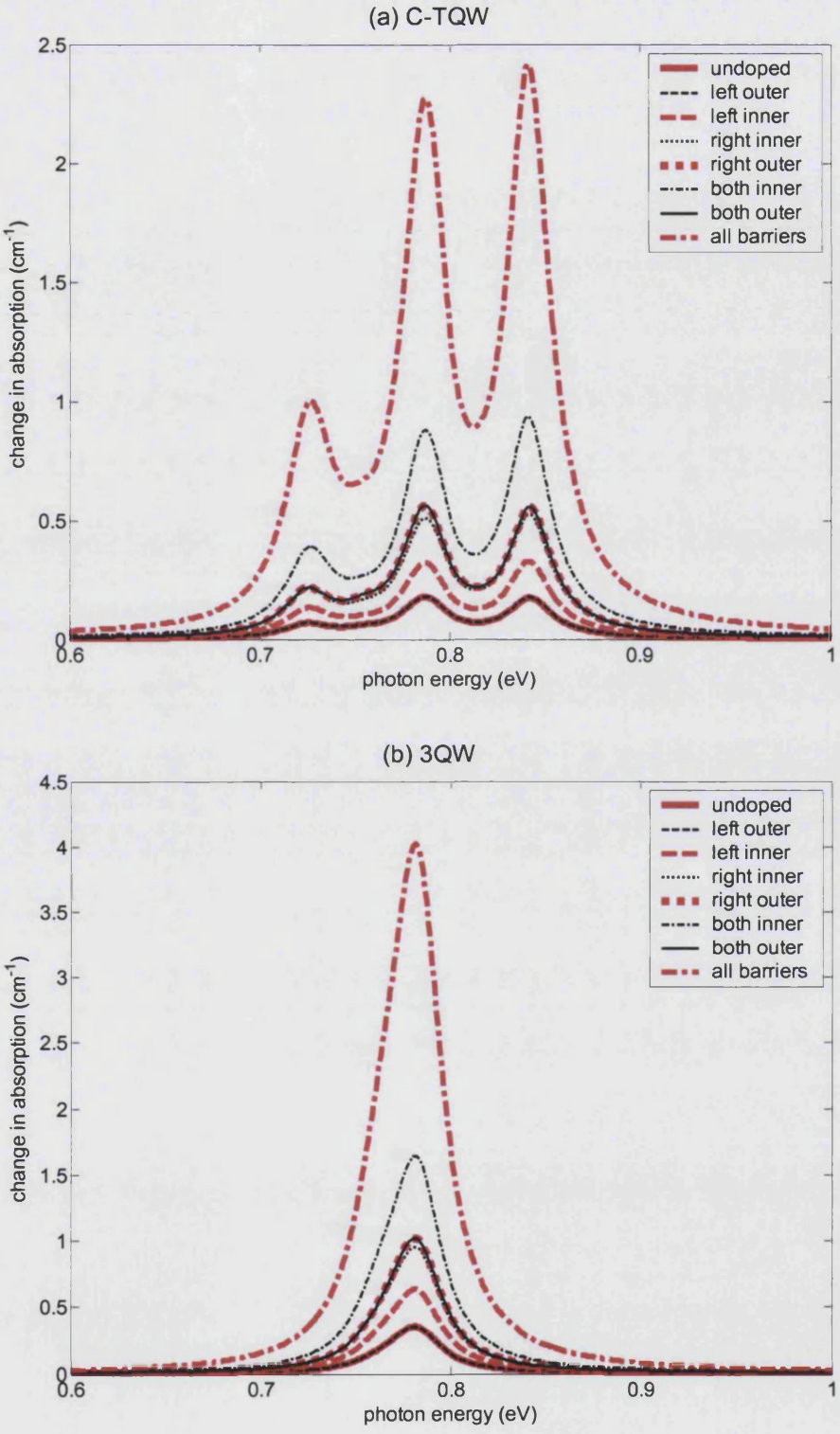

Figure 4.32: The differential absorption spectra of (a) C-TQW and (b) 3QW as a function of doping regions for the change of electric field from -1V/μm to -2V/μm. The modulation doping density is 1×10^{17} donrs/cm^3 for all doped structures.

spectra compared to other barriers with the same amount of donors under the same field strength. Inserting the doping in one or other of the inner barriers has an effect between the left and right outer barriers. This corresponds to the evaluation of the data in Fig.s 4.12, 4.22 and 4.31 for the changes in potential profiles of the SQW, C-DQW and 2QW with modulation doping. In fact, the order of the effectiveness of the locations of the modulation doping in enhancing ISBA is the same for both TQW types. The strongest improvement of absorption occurs for both TQW types when the modulation doping is inserted in all the barriers. Further, over 10 times stronger absorption can be achieved by applying such a low doping density in all barriers than that of the undoped structure.

(2) Strong Doping Density

After considering the locations of modulation doped regions at low doping density, similar studies are performed for high doping density. The same locations for placing donors but with a larger doping density (1×10^{18} donors/cm^3) in the inner and outer barriers for C-TQW structure were considered. Due to the complexity of the lineshape of the absorption spectrum in the C-TQW structures, as seen in Fig. 4.32 (a), the electroabsorption modulation is not dominated by a single transition. To determine the overall spectra correctly as a function of electric field or surface potential, several important transitions need to be considered at the same time. For simplified discussion, the electroabsorption modulation is studied later only in a particular C-TQW case in this section.

The F_{av}-V_{surf} characteristics for different C-TQWs were investigated and the results are shown in Fig.4.33. The F_{av}-V_{surf} shows that the sharpness of the corner region has the following sequence: the undoped C-TQW has the sharpest corner, followed by the single barrier doping cases and the both inner/outer barrier doping cases, while the all barrier doping case has the more gently varying corner region. Further, when the modulation doping is symmetrically inserted into the structure, one can achieve about zero field at the flat field region, while the asymmetrically doping results in a

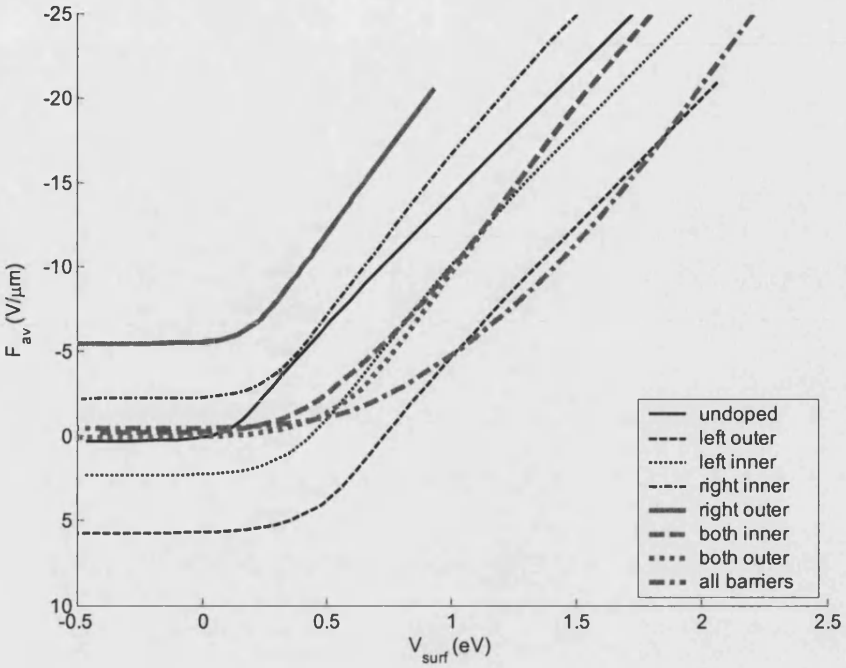

Figure 4.33: The influence of doping locations on the electric field across the well (F_{av}-V_{surf}) as a function of surface potential of a C-TQW. Each modulation doped region was assumed to be uniformly doped to 1×10^{18} donors/cm^3 and 1.0 nm wide.

large built-in electric field. Thus, the doping location and the number of doped layers have significant effects on the F_{av}-V_{surf} curves for C-TQW. This will influence any pre-bias that may be needed in a working modulation.

The same doping locations were considered for the 3QW and the simulation results are shown in Fig. 4.34. The F_{av}-V_{surf} curves of 3QWs in Fig. 4.34 (a) are analogous to those of C-TQWs in Fig. 4.33 and therefore the influence of the doping location on the sharpness of the corners and the strength of electric field are almost the same. The reason for the behaviour shown in Fig. 4.33 has already been discussed. By comparing the characteristics of F_{av}-V_{surf} in the SQW [Fig. 4.14(a) and Fig. 4.15(a)], the DQW [Fig. 4.24 (a) and Fig. 4.28 (a)] and the TQW [Fig. 4.33 and Fig. 4.34 (a)], it can be seen that the shape of the F_{av}-V_{surf} curves mainly depend on the location of the doped layers and the amount of donors (the sum of doping regions or the doping

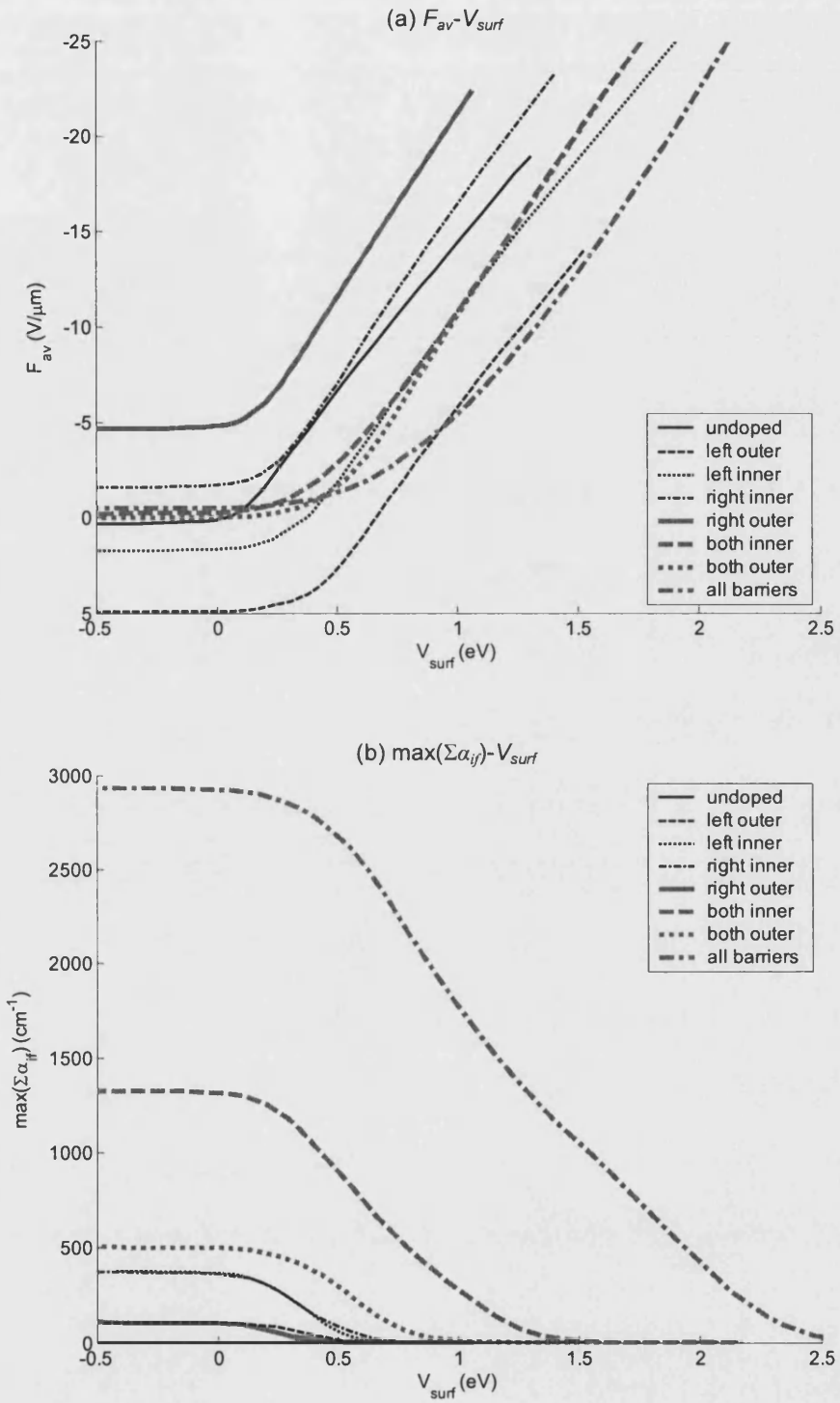

Figure 4.34: The influence of doping locations on (a) the electric field across the well (F_{av}-V_{surf}) and (b) the maximum absorption coefficient of the total ISBA [max($\Sigma\alpha_{if}$)-V_{surf}] as a function of surface potential of a 3QW. Each modulation doped region was assumed to be uniformly doped to 1×10^{18} donors/cm^3 and 1.0 nm wide.

density), rather than the structure's configuration, i.e. width and number of well and barrier width.

For weakly coupled quantum well structures, the ISBTs mainly occur vertically within the same well. As a consequence, the transition energies of the Lorentzian components in 3QW are very close and merge into a single peak in the total absorption spectra. Therefore, the overall absorption intensity of the whole spectrum [max($\Sigma\alpha_{if}$)] as a function of V_{surf} can be used to estimate the electroabsorption. The flatness or the sharpness of the corner of the curves in Fig. 4.34 (a) also reflects on the range of V_{surf} required to modulate max($\Sigma\alpha_{if}$) from its peak value to zero, as shown in Fig. 4.34 (b). The increase in the largest value of max($\Sigma\alpha_{if}$) is strongly related to the number of doped layers, i.e. the amount of the donors. However, increasing the number of wells from two to three does not cause a pro-rata increase in the total absorption. This will be discussed later in the context of an MQW. The positions of the doped regions also affect the absorption strength, with modulation doping inserted in the inner barrier generally causing the largest increase in absorption. In addition, the more the donors incorporated in the structure, the larger applied voltage is required to transform the overall absorption intensity. Therefore, there is a loss in the sensitivity of the electroabsorption modulation for a large amount of donors. Detailed comparison of the sensitivity of applied bias for the weakly coupled quantum well structures will be given in Section 4.5.2.

4.4.2 Modulation doped TQWs

Based on the behaviour of modulation doped TQWs presented above, it is expected that increasing the total amount of donors in the structure will enhance the Fermi occupancy ratio and subsequently improve ISBA, as in the SQW and DQW. As a result, both the C-TQW and 3QW structures with a large doping concentration of 1×10^{18} donors/cm^3 in all barriers, resembling the situation in Fig. 4.31(h), has been studied in detail separately and the results are presented in the following sections.

(1) An Optimized C-TQW Structure

First, the C-TQW structure which was doped to $1\times10^{18}/cm^3$ in all barriers was simulated. As commented, the electroabsorption behaviour in C-TQW is complicated. For clarifying such behaviour, the transition energy, absorption intensity, absolute value of optical matrix element and the Fermi occupancy ratio as a function of electric field are given in Fig. 4.35.

Fig. 4.35 (a) shows the variation of the transition energies (E_{if}) versus applied field. The energy shift in the absorption peak is very sensitive to electric field, in contrast to the SQW which has a negligible red shift, and is much stronger than the energy shift in the C-DQW structure. Fig. 4.35 (b) shows the absorption intensity for each transition [max(α_{if})] as a function of electric field. The behaviour of max(α_{if}) in Fig. 4.35 (b) is the combined outcome of the contribution from the matrix elements in Fig. 4.35 (c) and the Fermi occupancy ratio in Fig. 4.35 (d). At low applied field strengths ($|F_{av}| < 3$ V/μm), three dominant peaks occur in the ISBA spectrum (E_1-E_6, E_2-E_5 and E_3-E_4). While the amplitude of these peaks decreases dramatically with increasing field, the absorption amplitudes of E_1-E_5 and E_2-E_4 transitions increase first and then decrease, and the absorption peak of E_1-E_4 transition continuously grows in strength as electric field increases. Due to the characteristics of E_{if} and max(α_{if}), electroabsorption modulation in a C-TQW is consequently complicated.

The breaking of the parity selection rule at higher field strengths can be observed clearly in Fig. 4.35 (c). The parity-forbidden (at zero field) transition E_1-E_5 increases significantly in absorption strength and even dominates the absorption spectra when the field strength, $|F_{av}|$, is greater than 5.4 V/μm. It shows that the parity selection rule is important only for a weak electric field but breaks down in a strong electric field owing to the field induced distortion of the wavefunctions. In addition, the role played by the value of optical matrix element in determining the contribution of a given transition to the overall absorption is important not only at $F_{av} \approx 0$ but also at large field strengths. This contrasts with the situation in the SQW and even the

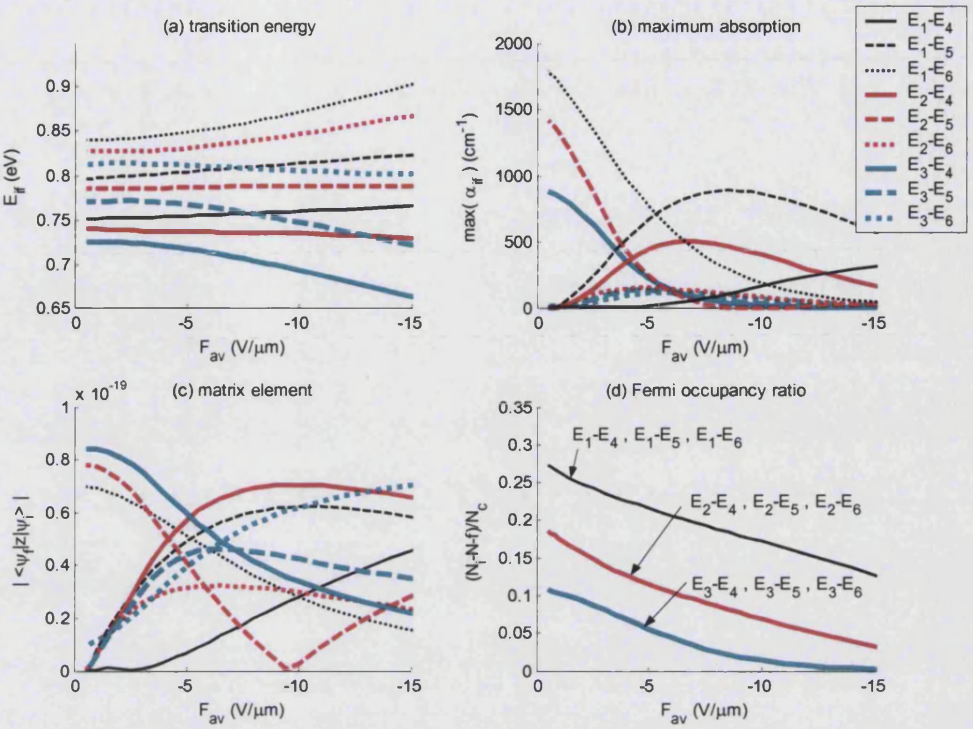

Figure 4.35: (a) The transition energy, (b) the maximum absorption coefficient of each transition, (c) the optical matrix element and (d) the Fermi occupancy ratio and as a function of electric field of a C-TQW structure with modulation doping to $1\times10^{18}/cm^3$ in all barriers.

C-DQW where the Fermi occupancy is dominant for the well width considered. Absorption for transition E_2-E_5, for example, is forbidden at around F_{av} = -9.5 V/μm due to the zero value of its matrix element and starts to increase when electric field exceed that limit. Moreover, there is another limitation of the parity selection rule in which only three transitions are clearly resolved at the low field. The absorption strengths of transitions E_1-E_4 and E_3-E_6 are expected to be large according to the selection rule but their values of optical matrix element are in fact very small. This shows that the normal parity selection rule is only obeyed in the simple symmetric structures like SQW and DQW and also near zero field.

Due to the multiple transition energies and the unequal absorption strength, both of which non-linearly vary as a function of the applied field, these effects result in the complicated lineshape and complicated evolution of lineshape with electric field

illustrated in Fig. 4.36. The three-dimensional plot of absorption coefficient versus photon energy versus electric field for the C-TQW is shown in Fig. 4.36 (a). The change of the absorption spectra as a function of electric field is dramatic and complex compared with that of strongly modulation doped SQWs and C-DQWs. In addition, Fig. 4.36 (b) shows that the spectral positions of the absorption peaks vary non-linearly with electric field. In order to reveal the absorption change at certain fixed photon energies for practical device operation, Fig. 4.36 (c) shows the electric dependence of absorption coefficient for the photon energy near 0.8 eV. The absorption coefficient at 0.79 and 0.84 eV decreases dramatically while at 0.81 eV the absorption coefficient rises then falls as the electric field increases. Therefore, multi-wavelength modulation is achievable for the C-TQW structures but only at specific structure dependent wavelengths.

The unique features in C-TQW are essentially caused by the unequal field strength in three wells because of the modulation doping placed in inner barriers. Due to the high doping density and the strong screening effect, the minimum average field strength across the wells is about -0.5 V/μm ($V_{surf} \approx 0.043$eV). However, only the average electric field strength in the middle well is -0.47 V/μm close to the overall mean value, whilst the field strengths in the left and the right side well are -9.13 V/μm and +8.1 V/μm, respectively, which is qualitatively similar to the circumstances shown in Fig. 4.2 (c). Therefore, it follows that the localisation of envelope wavefunctions in two side wells can be stronger than the middle well at the low field. This is especially true in the case of weak coupling as will be seen in the next section.

The effect of the electric field on the envelope wavefunctions of the three lowest energy states is shown in Fig. 4.37. The energy spacing of these states is not on a correct energy scale for the clarity of plotting the wavefunctions. As can be seen in Fig. 4.37, the envelope wavefunction starts to localise in the corresponding well as

(a) isometric view

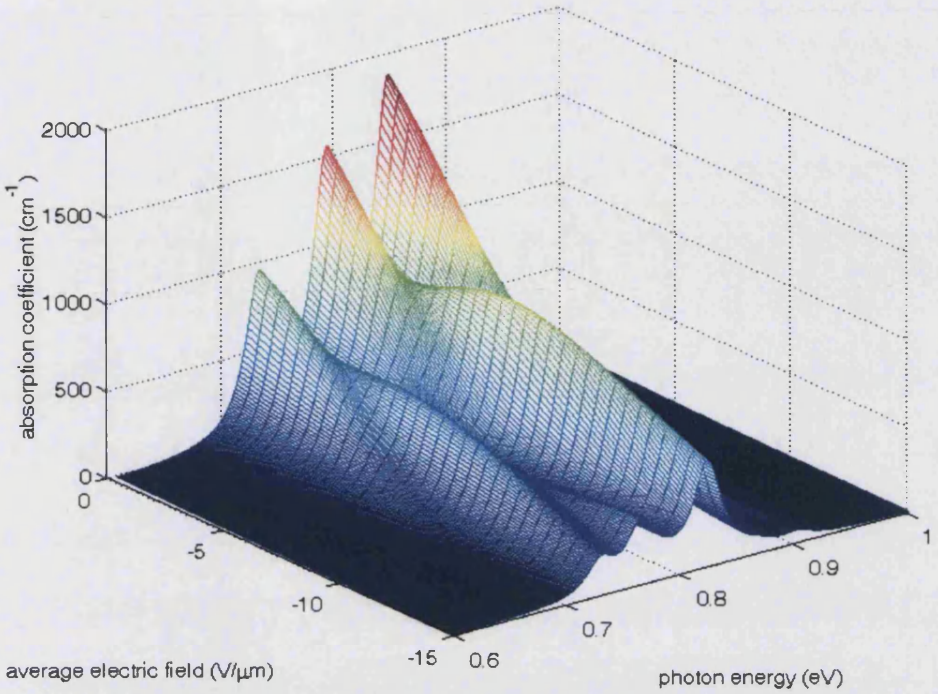

(b) top view

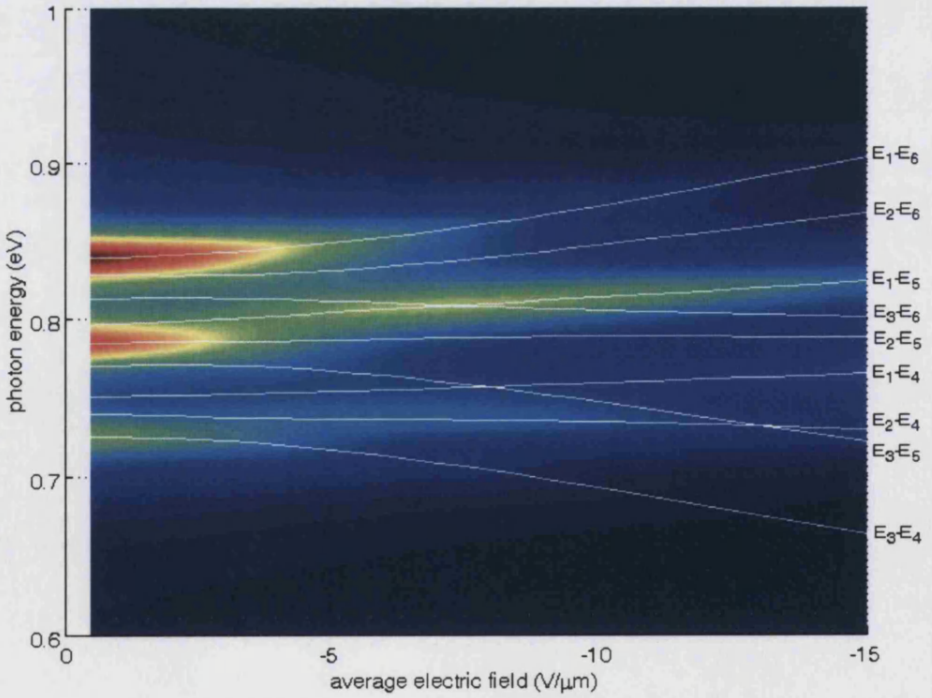

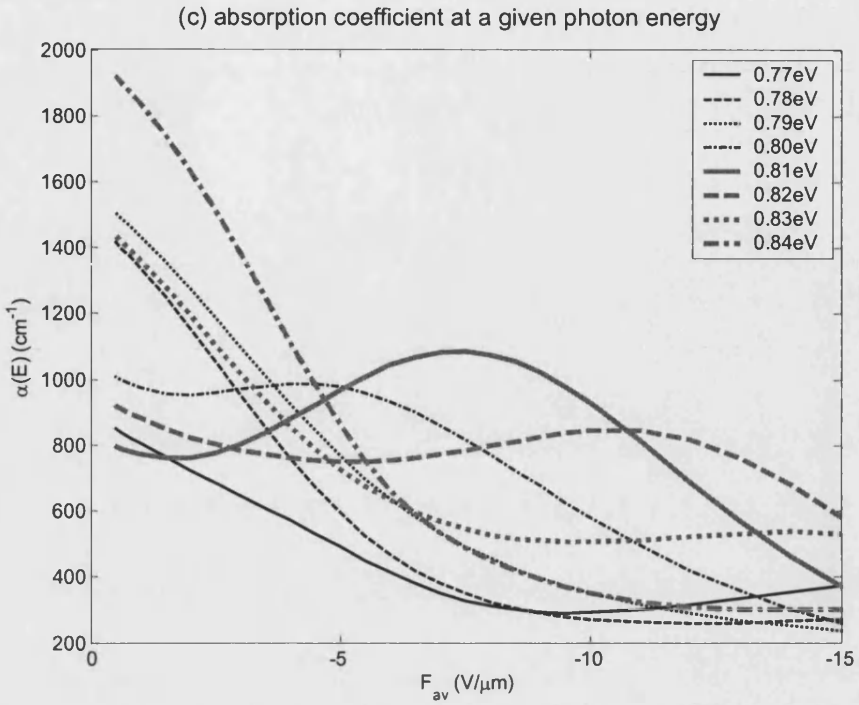

Figure 4.36: The 3D absorption spectra from different viewpoint: (a) isometric view and (b) top view with transition energies, and (c) the absorption coefficient at certain photon energies as a function of electric field of a C-TQW structure with modulation doping to $1\times10^{18}/cm^3$ in all barriers.

the electric field increases. When a small reverse bias is applied to the structure, the electric field in the left well increases to a larger negative value and the potential energy of the well is raised. Then the wavefunction of the E_3 bound state tends to localise increasingly in this well. However, wavefunctions of E_1 and E_2 states still tend to remain extended across the central and right-hand wells. The increasing electric field modifies further the separation between subbands, and causes stronger localisation, and thus the transition energies and the absorption peaks change in magnitude. In conclusion, for thin barriers in TQW structures, the wells are strongly coupled and the interwell wavefunctions tend to extend across the whole three well structure at low applied field strength. The subsequent localisation of, in particular, the three lowest energy wavefunction contributes to the complex field dependence of ISBA in C-DQWs which are caused by these strong tunnelling phenomena and the modulation doping.

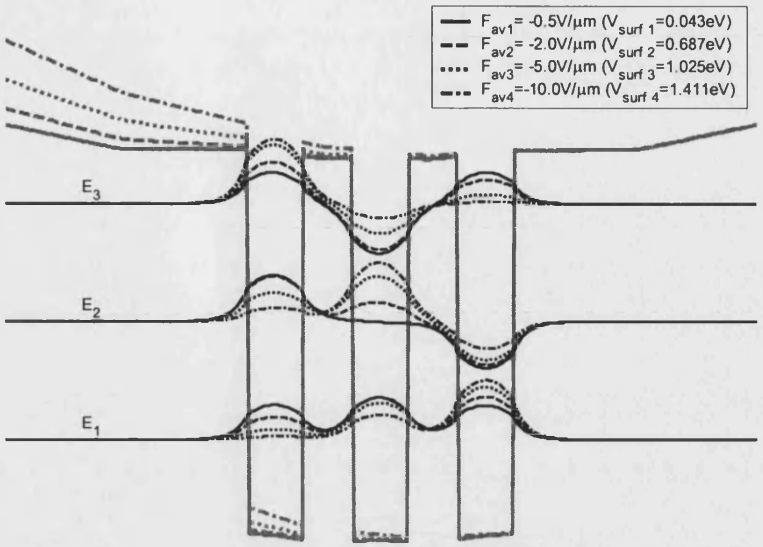

Figure 4.37: The conduction band profile and the wavefunctions of the ground states in C-TQW under different field strength. The confined states in this graph are not in the valid energy scale.

(2) An Optimized 3QW Structure

Next, the variation of the absorption spectra in a 3QW structure of modulation doping to a density of 1×10^{18} donors/cm^3 in all barriers with applied electric field and photon energy is shown in Fig. 4.38. Due to the wide inner barriers, the wells are effectively decoupled and the electroabsorption behaviour approaches to that of three isolated SQWs. Although reasonably large differential absorption spectra can be anticipated from the three-dimensional absorption spectra shown in Fig. 4.38 (a), the decrease of the whole absorption spectra is not as sharp as in the SQW (Fig. 4.16) and DQW (Fig. 4.29) structures. This is because the sequential screening effect of the wells as each depletes in turn starting with the well nearest the Schottky contact. This screening results in a different field strength occurring across each well. The change of the confined stated by the applied bias is different in each well until the whole structure is fully depleted. As a consequence, the absorption contributed by each well differs through the structure, with the absorption strength becoming progressively

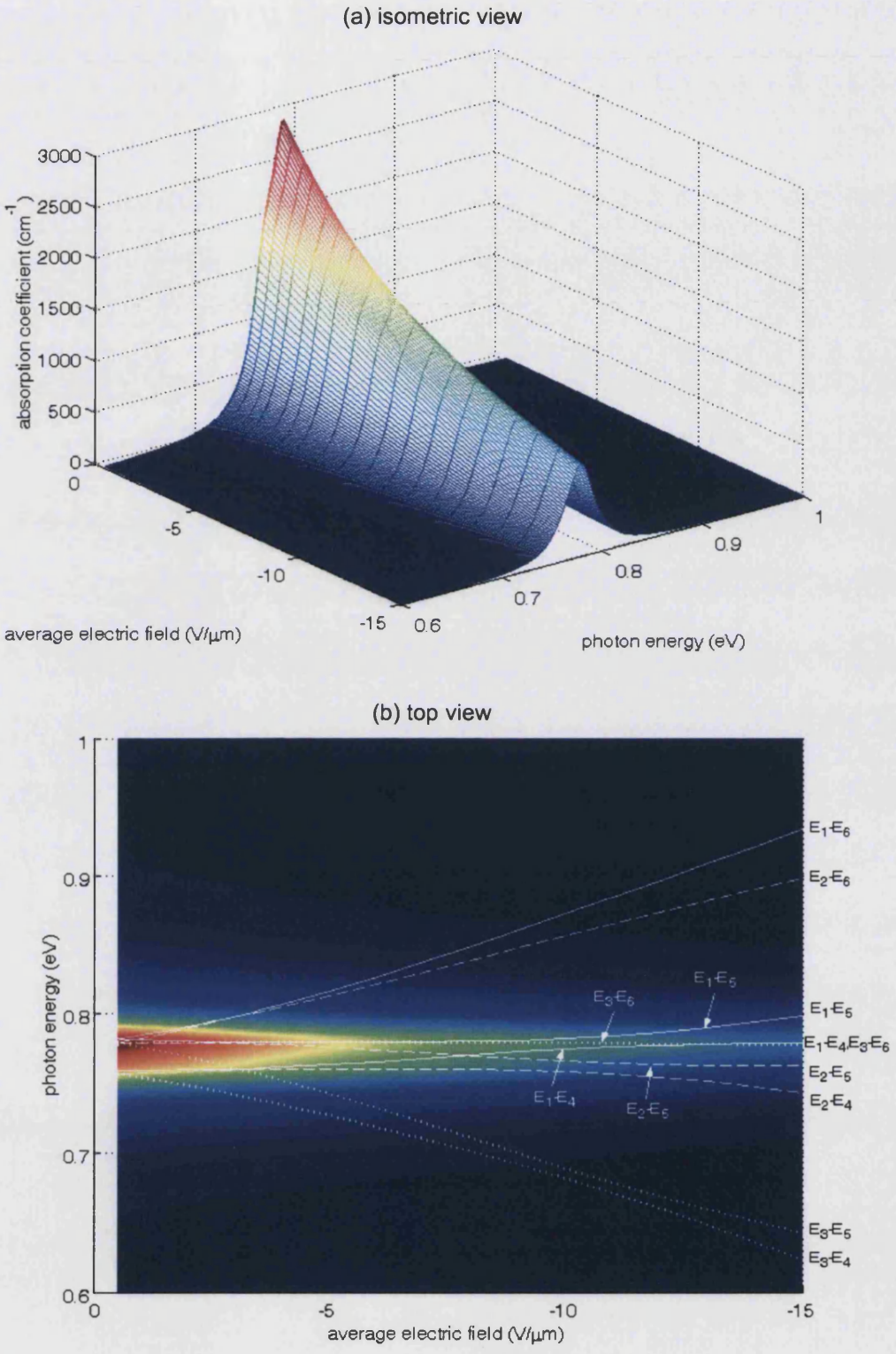

Figure 4.38: The 3D absorption spectra from different viewpoint: (a) isometric view and (b) top view with transition energies of a 3QW structure with modulation doping to $1\times10^{18}/cm^3$ in all barriers.

stronger with increasing distance of the well from the Schottky contact.

By associating the transition energies in Fig. 4.38 (b), one can easily observe that there is always about 0.02 eV difference between the two strongest transition components (E_1-E_4 and E_2-E_5 at field strength from -1 to -2.5 V/μm, E_1-E_5 and E_2-E_4 from -3.3 to -10 V/μm, and E_1-E_4 and E_2-E_5 stronger than -11 V/μm). The little difference in transition energies is an outcome of the small energy splitting from the weak coupling. For the line broadening ($\Gamma = 30$ meV) considered in the calculations, all the Lorentzian components superpose on each other owing to the small energy difference in the vertical transitions to form a single absorption peak near 0.8 eV. Such small energy difference between the Lorentzian functions will create a weak shoulder in the single peak. As a result, the FWHM (line width) of the whole absorption spectrum becomes wider as commented before in relation to the results in Fig. 4.32.

In order to clearly demonstrate the degeneracy of subbands and localisation shift between the wells as the electric field changes, the potential profile and the envelope functions of ground states of the 3QW structure with modulation doping comprising 1nm-wide *n*-type layers doped with 1×10^{18} donors/cm^3 at field strength of -1.5, -2.7 and -5.0 V/μm (equivalently at surface potentials of 0.551, 0.728 and 0.963 eV, respectively) are shown in Fig. 4.39. The energy states in the graph are not plotted on the correct energy scale to clarify the behaviour of the wavefunctions. Theoretically at zero field, the potential profile is symmetrical about the centre of the middle well with the two side wells having a higher potential energy than the middle well owing to the strong internal electric field derived from the modulation doped layers. As a result of the internal field, the lowest average electric field strength is achieved at about -0.5 V/μm in the structure given in Fig. 4.38. Even with such a low value of average electric field, the symmetric potential is tilted and one of the ground states is already localised in the left well due to weak coupling and the unequal strength of the electric field in each well. When the average electric field increases from -1.5 V/μm

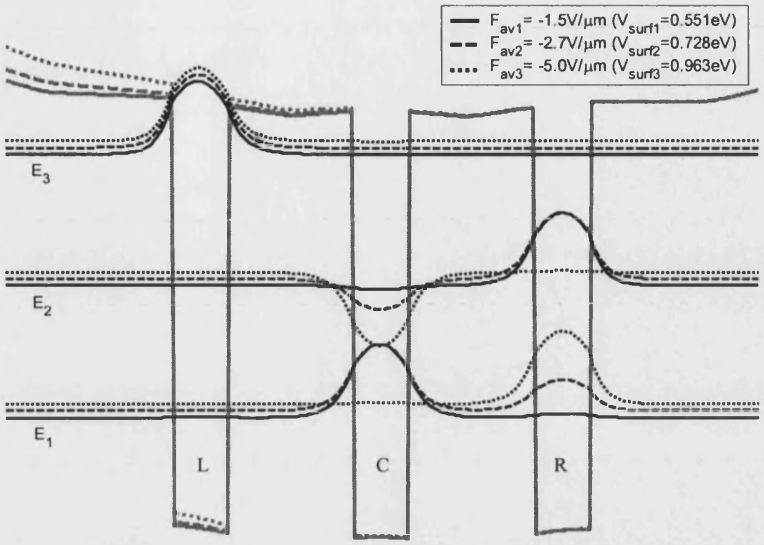

Figure 4.39: The conduction band profile and the wavefunctions of the ground states in a 3QW under different field strength and corresponding surface potential. The confined states in this graph are not in the valid energy scale.

to -5.0 V/μm, the electric field in the left-hand well, F_L, takes a large negative value while F_C and F_R, the field strength in the central and the right-hand wells, are more equal but a different direction. At a suitable field strength (around -2.7 V/μm when V_{surf} = 0.728 eV), $F_C+F_R \approx 0$, and a strong resonance tunnelling (quantum interference) occurs between E_1 and E_2. Consequently, the optical matrix elements of E_1 and E_2 change rapidly at this point. Once the electric field exceed this particular value, the wavefunction of the lowest energy state (E_1) localises in the right-hand well. However, the absorption peaks are contiguously spaced in energy, too close to be resolved. As a result, the absorption change in different ISBTs cannot be distinguished in the overall electroabsorption spectra.

In summary, like the 2QW structure, the absorption spectra in the 3QW considered here are largely the result of vertical transitions within the three effectively separate wells. The different ISBT energies and the absorption change are produced by degeneracy and the localisation of wavefunctions. Therefore, despite the weak

tunnelling in the wide barrier structure, it still results in some important characteristics and the coupling effect has to be taken into account to reveal these features.

4.5 Comparisons and Discussion of Modulation Doped Quantum Well Structures

For the design of EAMs, large differential absorption is crucial. The strongly coupled and weakly coupled quantum well structures presented above shows their feasibility of the application to optical modulation. Although the strength of ISBA generally rises as the number of the well increases, the central wavelengths in strongly and weakly coupled structures are different from the original transition energy designed for SQW. In order to observe the electroabsorption at 1.55 μm communication wavelength (0.8 eV), the absorption coefficient of the previous optimized structures with modulation doped in all barriers (check Fig.s 4.16, 4.25, 4.29, 4.36 and 4.38) is shown in Fig. 4.40. The absorption strength is similar in all the structures. Therefore, increasing the number of the well cannot achieve a better absorption rate at the fixed wavelength without adjusting the central absorption peak by modifying other structural parameters. Again, the splitting and shifting of the subband energy caused by the tunnelling are significant and need to be considered in designing devices. However, both strongly and weakly coupled quantum well structures have very different characteristics of electroabsorption and are explored further individually.

4.5.1 Strongly Coupled Quantum Well Structures

In order to extend the understanding of SL and draw an analogy between the strongly coupled quantum well structures, an extra structure of five quantum wells (L_w = 2.2 nm and L_b = 2.0 nm) are considered. The strongly coupled quintuple quantum well (C-QQW) structure with modulation doping to $1\times10^{18}/cm^3$ in all barriers are calculated and compared with the absorption spectra of modulation doped SQW,

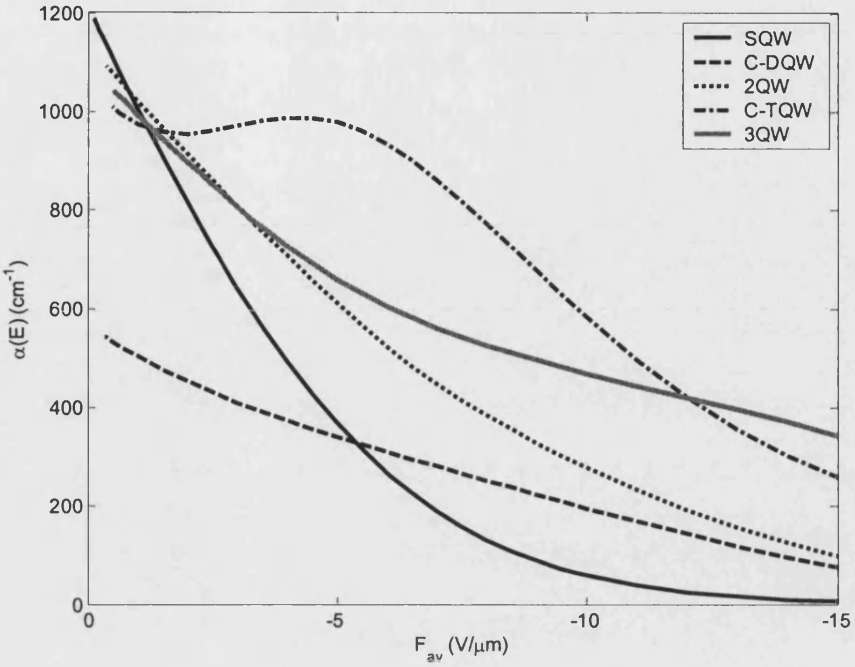

Figure 4.40: The absorption coefficient (α) at 0.8 eV photon energy (1.55 μm wavelength) as a function of average field strength (F_{av}) in various modulation doped structures.

C-DQW and C-TQW in Fig. 4.41.

As can be seen in Fig. 4.41, the absorption spectrum extends over a wider range of photon energies, from ~0.7 to ~0.9 eV, as the well number increases. For all strongly coupled structures, there is absorption peak occurring at energy higher than 0.8 eV in SQW because of the splitting of confined energy states. In other words, a wider well width can be used for strongly coupled quantum well structures to achieve the same required wavelength (0.8 eV) as in SQW structures [85]. This could make the structure technologically easier to fabricate, as well as reduce the impact of interface roughness on device characteristics. For those material systems that are unsuitable for growing narrow wells, strongly coupled quantum well structures provides another option to achieve the required wavelength. However, strong coupling is necessary in those structures, which means a thin barrier is needed to be fabricated and the structures may be still challenging to grow.

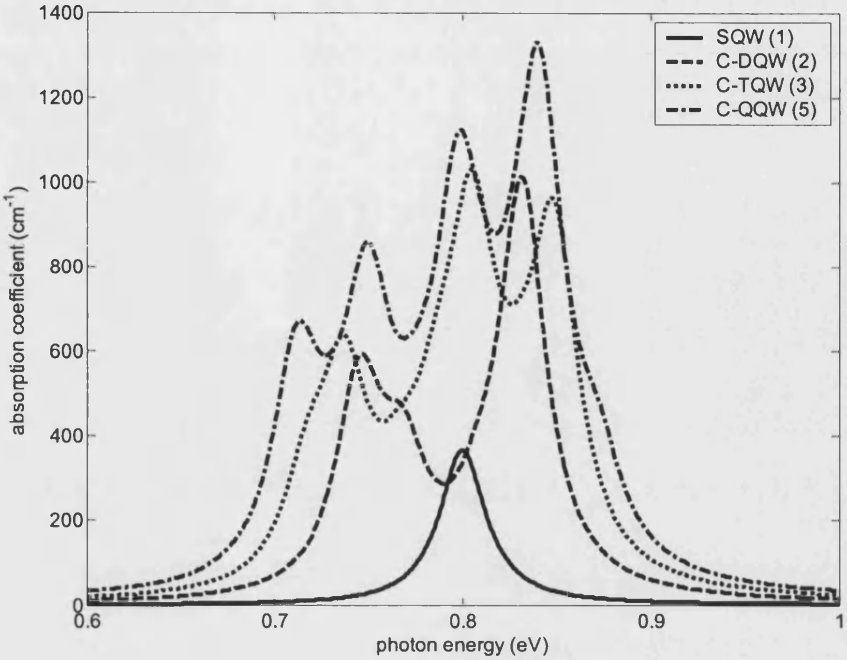

Figure 4.41: The absorption spectra of a SQW, a C-DQW, a C-TQW and a C-QQW at F_{av} = -5 V/μm. All structures are modulation doped in all barriers to 1×10^{18} donors/cm^3.

Along with the multiple absorption peaks as the number of wells increases in Fig. 4.41, the resolution of the peaks is diminishing. This is because of the smaller energy difference between the multiple transition energies. Clearly, the onset of the formation of a broad, near featureless absorption band will depend on the line broadening achieved in practice. As the number of wells increases, more transitions occur near 0.8 eV. When the number of strongly coupled quantum wells is sufficient large, a SL and its minibands are formed. From the results in Fig. 4.41, it can be concluded that the absorption band of SLs will be broad and featureless since the ISBA occurs between two minibands. In the presence of a large electric field, the minibands break into an energy ladder of discrete levels, which is known as a Wannier-Stark ladder. For clarifying such behaviour, further investigation based on techniques such as Kronig-Penney model or the tight banding approximation [4,42,44] is required, but this is beyond the scope of this thesis. Therefore, instead of large absorption change near a certain wavelength for a small perturbation of voltage

bias, bipolar differential absorption spectra are anticipated for some bias conditions in SLs as absorption will increase in some parts of the absorption band and decrease in others.

As mentioned, the sharpness of the peaks that can be observed will also be limited by the line broadening in a strongly coupled structure. The influence of the broadening is shown in Fig. 4.42 for different light width in the Lorentzian function of the absorption spectrum of modulation doped C-TQW as an example. For a very narrow line width (Γ = 20 meV) for the Lorentzian function, the intensity of absorption peaks is larger and the resolution of the peaks is high. With such a narrow line width, the contribution to the absorption band from normally forbidden transitions become more easily resolved even at low applied field strength. On the other hand, a large line width results in a low contrast absorption spectrum. For Γ = 70 meV, the three well structure already results in a spectrum with low resolution of absorption peaks, which is expected to show electroabsorption behaviour similar to that of SLs. Therefore, the line width is an important parameter for achieving sharp absorption spectra.

Since the transition energies in the coupled quantum well structure are shifted under an applied electric field, i.e. Stark shift, adjusting the bias applied to the structure is an alternative way for tuning absorption wavelength. Such an effect could open the possibility of designing some infrared optical devices. Indeed, one type of intersubband modulator has already been proposed based on such a Stark shift [128,129]. However, asymmetric coupled quantum well structures are normally used in these Stark shift modulators to exploit a linear Stark shift.

Although the change of absorption amplitude by the applied electric field at a particular energy may be small, a large fluctuation in differential absorption spectra ($\Delta\alpha$) can be achieved in a wide range of photon energy in modulation doped quantum

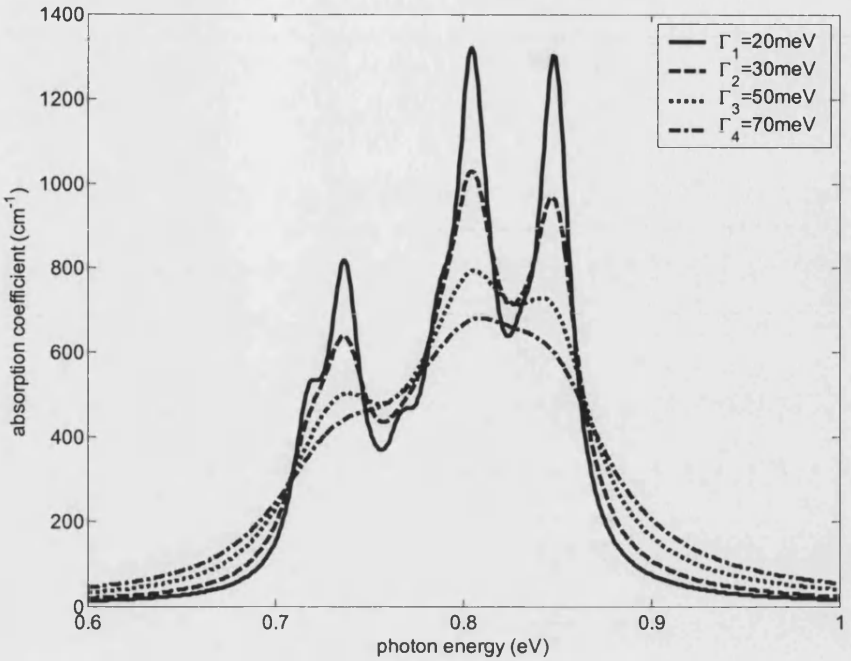

Figure 4.42: The influence of the line width (Γ) of Lorentzian function on the intersubband absorption spectrum as for a modulation doped C-TQW at F_{av} = -5 V/μm.

wells. The variation in $\Delta\alpha$ creates the potential for achieving a large change of refractive index of the medium which is called the electrorefraction effect. The change in refractive index Δn due to electrorefraction is calculated from the electroabsorption $\Delta\alpha$ by using the Kramers-Kronig relation [4]. The Kramers-Kronig relation can be written as,

$$\Delta n(E_p) = \frac{\eta c}{\pi} \int_0^\infty \frac{\Delta\alpha(E)}{E^2 - E_p^2} dE \tag{4.1}$$

where, E_p is the photon energy, $\Delta\alpha(E) = \alpha(E, F_2) - \alpha(E, F_1)$, F_1 and F_2 are the initial and finial electric field strength, respectively.

The results of the electrorefraction modulation for SQW, C-DQW and C-TQW are demonstrated in Fig. 4.43. The Δn as a function of photon energies is shown in Fig. 4.43 (a). For SQW, the curve is essentially antisymmetric about a photon energy of

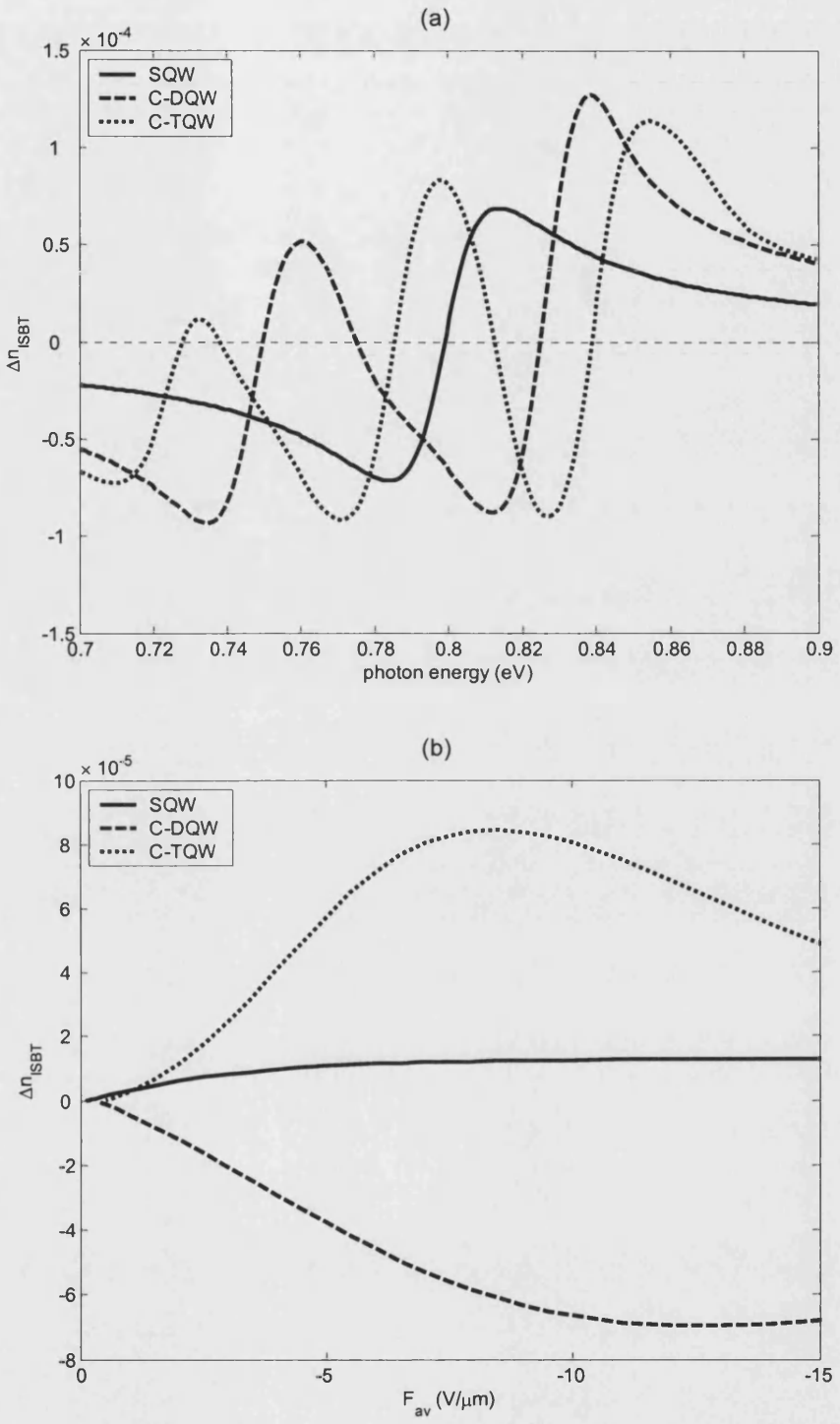

Figure 4.43: (a) The change of refractive index from ISBT (Δn_{ISBT}) as a function of photon energy at electric field varied from 0 to -10 V/μm; (b) Δn_{ISBT} at 0.8 eV photon energy as a function of electric field for SQW, C-DQW and C-TQW.

0.8 eV, which is the central absorption energy. The refractive index at 0.8 eV basically remains unchanged as seen in Fig. 4.43 (b) due to the symmetrical change in absorption coefficient around 0.8 eV. When the C-DQW or C-TQW is considered, the Δn has very different characteristics. For instance, the refractive index near 0.8 eV has a positive change while the changes around 0.77 and 0.83 eV are negative for the C-TQW. Also, Δn varies non-monotonically as a function of electric field and has a maximum change at a particular field strength. Therefore, strongly coupled quantum well structures can be used as phase or polarization modulators based on the electro-refractive effect associated with ISBA [209].

4.5.2 Weakly Coupled Quantum Well Structures

It has been shown that the 2QW and 3QW have wider scope than the strongly coupled quantum well structures for the application to EAMs. Two further weakly coupled quantum well structures, the five (5QW) and seven well (7QW) with L_w = 2.2 nm and L_b = 5.0 nm, are considered in here in order to analyse the behaviour of electroabsorption in a modulation doped MQW.

The simulated absorption spectra of the SQW and four weakly coupled quantum well structures comprising two, three, five and seven quantum wells are shown in Fig. 4.44, all structures with modulation doping comprising 1nm-wide n-type layers doped with 1×10^{18} donors/cm^3 in all barriers. It can be easily observed that there is only a single peak in all spectra, as demonstrated and commented previously for the 2QW and 3QW. Due to the wide barrier width, the tunnelling is weak in all structures. The energies of dominant absorption are closely spaced in energy since the dominant vertical transition takes place in each well between the ground state and the excited state. Consequently, in the weakly coupled structures, the consequential characteristics of these structures approach to the SQW cases with a single somewhat broadened absorption peak.

Moreover, it has to be noted that the peak energies constantly shift from 0.8 eV in

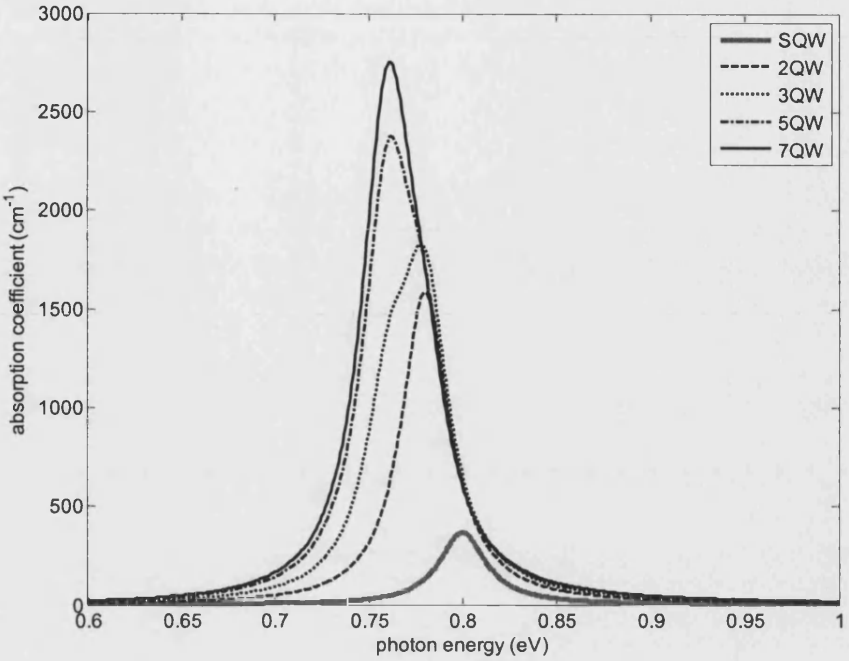

Figure 4.44: The absorption spectra of a SQW and four weakly coupled structures (2QW, 3QW, 5QW and 7QW) at F_{av} = -5 V/μm. All structures are modulation doped in all barriers to 1×10^{18} donors/cm^3.

SQW to 0.76 eV in 7QW. This is caused by the lifting the degeneracy of the transition energies and the change in confined energies due to the coupling, which has been explained previously Section 2.1.1 by the shift integral and a transfer integral in DQW. Therefore, this changing of the position of the absorption peak is essentially related to the width of the barrier. Although the coupling between the wells is weak, it is still sufficient to engender an energy shift in the absorption peak. This small energy shift is important and needs to be considered when designing EAMs.

The variation in the intensity of the absorption peak shown in Fig. 4.44 can be used to estimate the performance of weakly coupled structures. In Fig. 4.45, max($\Sigma\alpha_{if}$) is calculated as a function of V_{surf} for five different structures with modulation doped in all barriers. The maximum absorption, which occurs around -0.5 eV $\leq V_{surf} \leq$ 0.5 eV,

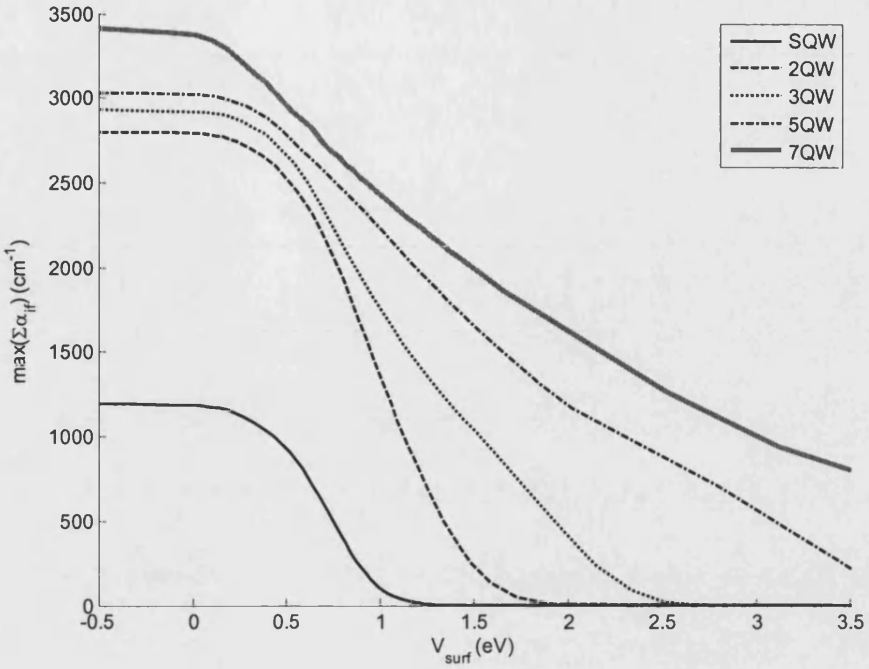

Figure 4.45: The peak intensity of overall absorption spectra [max($\Sigma\alpha_{ij}$)] as a function of surface potential (V_{surf}) for SQW and the four weakly coupled structures (2QW, 3QW, 5QW and 7QW).

increases as the well number increases. However this increase is sub-linear. Such improvement is a combined result from increasing the amount of donors and the number of wells. Although the enhancement of the absorption strength is sub-linear with the number of wells, one should bear in mind that the overlap integral between the active region, where ISBA occurs and the mode profile of a guided light beam are different in these structures. For instance, the 2QW and 3QW would have about twice or three times the effective optical cross-section of the SQW. As a consequence, the light absorption will be stronger. In general, MQWs comprising such weakly or independent wells are more ideal for the application of EAMs than strongly coupled structures, since the peak absorption is higher and the absorption change versus applied voltage is well behaved, as Fig. 4.45 shows.

For the EAMs based on the MQWs, the balance between the peak absorption and voltage sensitivity is crucial. Table 4.4 lists the voltage change required to achieve an

80% to 20% change in the absorption strength in the structures detailed in Fig. 4.45. Note the absolute maximum absorption strength will vary from structure to structure, as will the optical confinement factor. However, given that these factors can be compensated by changing the length of the device, the data in Table 4.4 is representative of the likely voltage sensitivity of an EAM operating by ISBA using the types of deep, narrow quantum wells considered here. Such values clearly show that larger voltage bias is needed to fully deplete electrons from a large number of wells. However, the number of quantum wells in the MQW is important for EAM design since a large number will achieve a better optical overlap, or confinement factor. Therefore, a trade-off between absorption intensity and the operating sensitivity is required for high-speed, voltage-induced EAMs by ISBA in a modulation doped MQWs.

	SQW	2QW	3QW	5QW	7QW
$\Delta V_{80\%\sim20\%}$ (eV)	0.408	0.637	1.160	2.110	3.109

Table 4.4: The potential change from 80% to 20% of the highest absorption intensity for different weakly coupled quantum well structures shown in Fig. 4.45.

Having raised the issue of the change of refractive index (Δn) for strongly coupled structures, the same calculation of Kramers-Kronig relation in Eq (4.1) is performed for the SQW and the four weakly coupled structures, corresponding to the 80% to 20% change in the absorption strength given in Table 4.4. As can be observed in Fig. 4.46 (a), all the Δn as a function of photon energy have a similar shape but shift to a lower energy for the larger number of wells. The function Δn has a zero value near the central absorption peak of the spectra given in Fig. 4.44.

Due to the constantly negative values of differential absorption spectra ($\Delta\alpha$) and the symmetrically change of refractive index to the central absorption peak for weakly

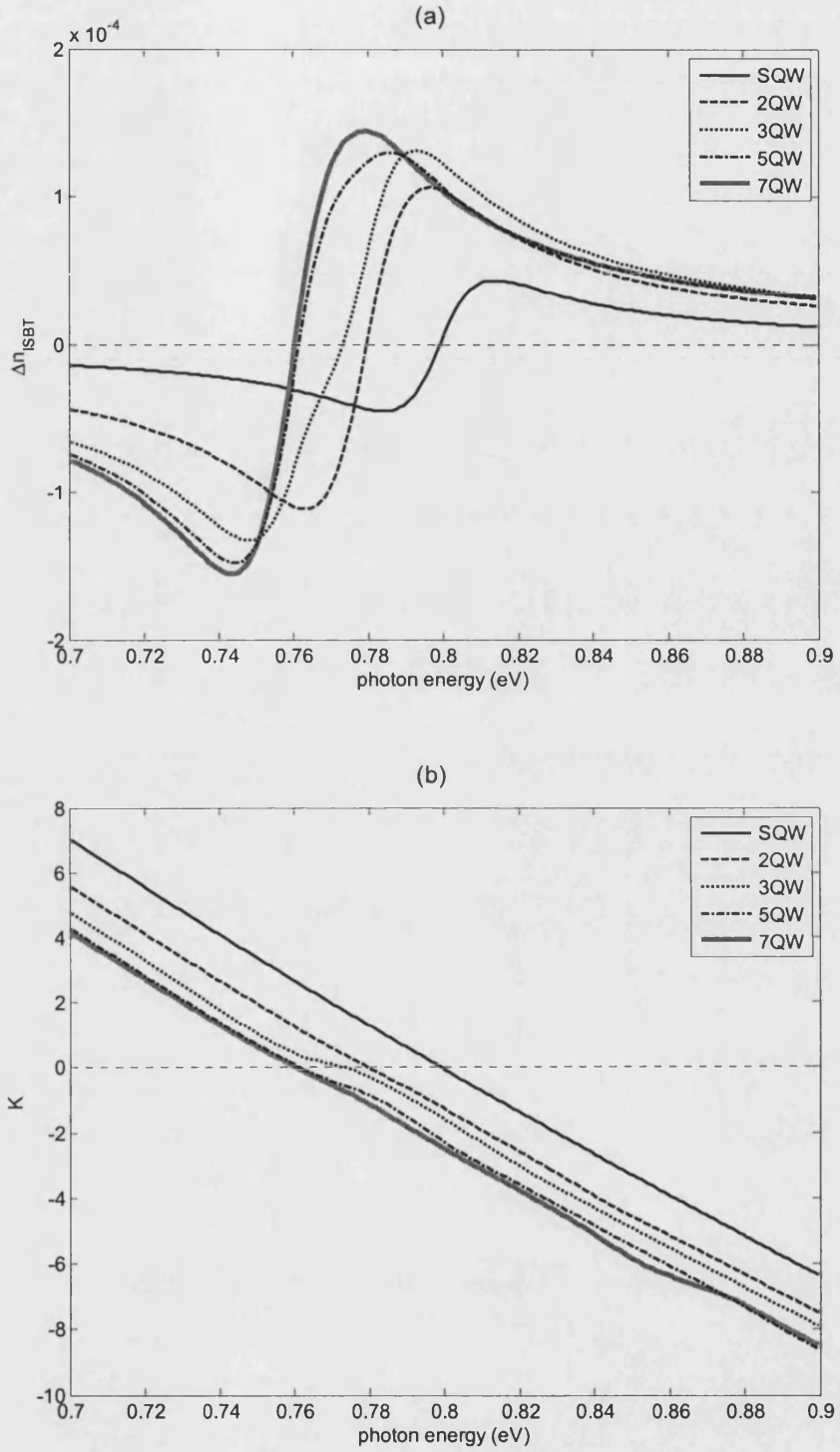

Figure 4.46: (a) The change of refractive index from ISBT (Δn_{ISBT}) and (b) the chirp parameter (K) as a function of photon energy at absorption strength varied from 80% to 20% for modulation doped structures given in Fig. 4.45.

coupled structures, one can expect to achieve bipolar chirp parameter around the wavelength of absorption peak. It has to be noted that the negative chirp is highly desirable from a system point of view for compensating fibre dispersion [78,210,211]. The chirp parameter is defined by [210]

$$K = \frac{4\pi}{\lambda} \times \frac{\Delta n(\lambda)}{\Delta \alpha(\lambda)} = \frac{2E}{\eta c} \times \frac{\Delta n(E)}{\Delta \alpha(E)} \tag{4.2}$$

where λ and E are the wavelength and energy of the light. The simulation results are shown in Fig. 4.46 (b). The chirp parameter for all structures is basically linear as a function of photon energy but with a small energy shift for different structures. This offset corresponds to the energy shift of the absorption peak in weakly coupled structures caused by the weak but not negligible tunnelling effect. As can be seen in Fig. 4.46 (b), one can tune EAMs based on weakly coupled structures to have a positive or negative chirp parameter straight forwardly, simply by adjusting the operating wavelength near the absorption peak. This effect provides EAMs operating by ISBA in weakly coupled deep narrow quantum wells a significant prospective advantage in fibre-based optical telecommunication networks.

4.6 Summary

A systematic study of the ISBA in various doping conditions in InGaAs/AlAs SQW, DQW and TQW structures is presented. To determine electronic properties such as the confining potential, the subband energies and the envelope wavefunctions, the self-consistent calculation of Poisson-Schrödinger equations was used. The absorption spectra as a function of electric field were simulated for strongly coupled and negligibly coupled structures with different modulation doping. According to the calculation, the modulation doping in structures has a significant influence in their ISBAs. The magnitude and position of the absorption peaks for ISBTs are very sensitive to the applied electric field in strongly coupled structures. The negligibly coupled structures have similar characteristics to the SQW structure but are not

identically same. The limitation of the parity selection rule at nonzero electric field and strongly coupled TQW is discussed. The internal estimated electroabsorption features for strongly coupled and weakly coupled quantum wells, and the cross over comparison between them have been studied. The results can be used in structure design.

Conclusions and Scope for Further Research

CHAPTER 5

5.1 Conclusions

This thesis is devoted to study the modelling of electric-field-induced modulation of intersubband absorption (ISBA) for the application in short-wavelength near 1.55 μm. It has elucidated the roles of the electric field on electron occupancy in quantum wells and the transition energies on intersubband transitions (ISBTs) for $In_{0.53}Ga_{0.47}As/AlAs$ quantum well structures with different coupling strength. Further, this work explores in detail the entire influence of applied bias voltage associated with modulation doping on ISBA. Such a systematic study of electroabsorption based on ISBTs had not been investigated before the work described in this thesis.

In the first chapter of this thesis, an overview of modelling ISBT based quantum well structures, particularly in their applications to electroabsorption modulators (EAMs) and the motivation for the work, were presented. EAMs based on ISBA are starting to draw considerable interest for fulfilling the requirements of ultrafast optical communications systems.

To assist the understanding of the methods for simulations, which were presented and utilised in this thesis, Chapter 2 reviewed key physics and properties of quantum well structures versus conventional semiconductor structures. It is required to enhance the absorption magnitude of the short-wavelength ISBTs in order to enable practical device applications. Therefore, the effects of modulation doping in quantum heterostructures were reviewed, since donors have to be introduced to provide carriers for the *n*-type electronic ISBTs. By focusing on the characteristics of ISBTs, the various types of transition and the selection rules were described. Finally, the advantageous features of ISBTs, e.g. the fast relaxation time and the wide range of transition wavelengths, and the novel applications and the development of some interesting devices were presented.

The principal theory and numerical solutions used in this thesis were derived in detail

in Chapter 3. In order to calculate the absorption coefficient of quantum well structures, the effects of modulation doping and applied bias on the density of electrons residing in the well and hence the strength of the ISBA, self-consistent solutions of the Poisson and Schrödinger equations are required. Firstly, a one-dimensional model based on transfer matrix method was developed to solve the single electron Schrödinger equation for calculating the confined state energies and their envelope wavefunctions in an arbitrary potential profile. The potential profile is obtained by solving Poisson's equation. A numerical model based on the Runge-Kutta method was then presented to calculate the potential and field distributions inside the device active region. By inputting the band edge profiles of the doped structures back into the Schrödinger solver, confined states were evaluated for different quantum well types, doping conditions and applied bias. Furthermore, an investigation into the effect of subband nonparabolicity based on an energy-dependent effective mass approximation was carried out and then matched with data adopted from the published literature.

Finally, simulation results and comparisons between different structures were presented and discussed in Chapter 4. The systematic study of ISBTs in InGaAs/AlAs material system has demonstrated the feasibility of ISBA based EAMs at communication wavelengths. Not only the absorption magnitude but also the transition wavelength of electric field induced modulation had been investigated in various quantum well structures, mainly single, double and triple quantum well structures with varying degrees of inter-well coupling. The essential results of the research can be naturally split in several major parts and summarized as follows.

First of all, the effects of modulation doping have been studied in depth. The absorption intensity of ISBA can be controlled simply by adjusting the electron density in a quantum well. Therefore, the doping density and the amount of doping regions are crucial parameters because of their significant influence on the Fermi occupancy of confined states. Placing the modulation doped regions at different

locations with the same amount of donors distinctly modifies the absorption-voltage characteristic of a given quantum well structure. This significantly affects the optical absorption at the same field strength but produces comparable enhancement of the overall absorption intensity. The transition energy shift resulting from varying the location of the modulation doping and density is small compared to the field effect, but is a notable factor in designing devices. The total amount of donors, i.e. the combination of doping density and doping layers, has a significant impact on the operating sensitivity of applied bias. Therefore, the trade-off between the absorption intensity and sensitivity of modulation is critical in designing devices.

Moreover, the effects of the average electric field across the quantum well(s) (F_{av}), or equivalently surface potential (V_{surf}), on ISBA have been investigated. The F_{av}-V_{surf} curves can be effectively used to estimate the strong electroabsorption modulation conditions for different structures. Also the characteristics of F_{av}-V_{surf} are significant in device operation and important in selecting the structure configuration such as Schottky contact, *p-i-n* or *n-i-n* junction when engineering device designs for particular applications, for example when accounting for the bias swing available in a system.

The Fermi occupancy constantly decreases as the surface potential or the negative field strength increases. This implies that the absorption intensity decreases in principle. This is also the dominant effect in determining the modulation rate of ISBA in the quantum well structures considered. In addition, the parity selection rule is broken by the applied external electric field. This is caused by the modification of the optical matrix elements as a result of the asymmetric potential profile. In general, the absorption intensity of the ISBT can efficiently be controlled by means of adjusting the electron density in a quantum well or the optical matrix elements via applied field or bias.

The influence of applied electric field on the subband energies, which is the

well-known Stark shift, has only a weak effect on the transition energies of narrow isolated quantum wells, but has a large impact on strongly coupled quantum well structures. The Stark shift plays a significant role in determining the shape of the absorption band. Furthermore, the localization of wavefunctions in different bound energy states is very dependent on the electric field strength and causes electrons to accumulate in different part of the structure.

Last but not least, a comprehensive investigation on the effect of the structural parameters of quantum wells has been carried out. Selecting the suitable well width and the barrier width are crucial in ISBA since the former determines the central transition energies and the latter determines the coupling (tunnelling) strength between the wells. The wavefunction tunnelling introduces the splitting and shifting of confined states and therefore results in determining the lineshape of absorption spectra.

For the strongly coupled quantum well structures, the optical matrix elements vary, often rapidly, as the bias changes and therefore results in a complex absorption spectra. They are prospective structures for multi-wavelength absorption. Weakly coupled quantum well structures are more suitable for EAMs than strongly coupled structures because the transition energy is almost the same in each nearly isolated well and the absorption change per volt applied is large. The absorption edge can be controlled over a wide range of applied electric field, or equivalently external voltages.

Further investigation on electrorefraction and the chirp parameter has been performed for the structures up to seven wells. The strongly coupled structures show a significant electrorefractive effect which can be used as phase of polarization modulators. The bipolar chirp parameter around the central absorption peak is achieved in the weakly coupled quantum well structures, which shows the potential application in fibre-based optical telecommunication networks.

To summarize, a comprehensive study of short-wavelength intersubband transition in InGaAs/AlAs system on InP substrate has been performed. The design and implementation of ISBT around 1.55 μm (0.8 eV) are achieved in the case of strong electroabsorption modulation. The theoretical research explored clearly demonstrates the feasibility of an intersubband modulator as a candidate for the high speed and low voltage modulators of the future. Further, the simulation results also provide insight into the optimum design of EAMs based on ISBA.

5.2 Scope for Further Research

The investigation described in this thesis has met its primary objectives, namely to establish the feasibility, from simulations, of strong electroabsorption modulation of ISBTs at telecommunication wavelengths and the role of modulation doping in improving the electroabsorption properties. In spite of these positive results, further work is needed to confirm from measurement the electroabsorption and electrorefraction associated with ISBA in InGaAs/AlAs quantum wells to compare with the simulation results.

In practice, quantum well devices are often heavily doped in order to obtain sufficiently large absorption coefficients. The single particle approximation breaks down at high carrier concentrations of a few $10^{12}/cm^2$. In such case, several many-body effects, e.g. exchange-correlation Coulomb interaction, depolarization and exciton-like effects [212-214], become important for the calculation of the spectral position of the absorption peak and change the characteristics of modulators. For instance, coupling between the ISBTs at different **k** wavevectors is induced by the Coulomb interaction between the electrons occupying different confined states. The Coulomb interaction also introduces an additional back-driving force for the carriers and therefore results in shifting the position of the transition energy towards the higher photon energies, i.e., the shorter peak absorption wavelength [215-217].

These many-body effects affect the shape of the intersubband absorption band, narrowing the absorption line width and modifying the absorption peaks. Therefore, a more complete model needs to be developed for taking into account of many-body effects, since the future focus is likely to be on heavily doped structures to achieve stronger ISBA.

One of the main simplifications in the simulation presented in this thesis is the assumption of no photo-current throughout the diode. Under this assumption, the Fermi level in the structure is constant and was selected as the reference energy level in calculating the confined energy states and the absorption coefficient. With the assumption of reverse bias, the currents are usually small and therefore the approximation is satisfactory. However, forward bias can be useful and the photo-current in *n-i-n* structures can be large for most bias conditions. Consequently, the model developed here, whilst useful for determining the underlying physics and trends, is limited for accurately simulating the device characteristics. In reality, when the device is under large forward bias, there is a gate current. This implies that the Fermi level will bend through the depleted region and is voltage dependent [218]. With this correction considered, the characteristics of the electroabsorption modulation will vary. For instance, the shape of absorption band of strongly coupled quantum well structures will be modified and the electroabsorption modulation rate in weakly coupled structures should be milder due to the stronger contribution of left hand side wells to the overall ISBA of an MQW. Clarification of such effects will require detailed simulation based on an improved model.

Although the strongly coupled quantum well structures show less efficient electroabsorption modulation than MQWs, the Stark shift is large in these structures and the shape of the absorption band varies dramatically. The multiple C-DQW or C-TQW could be useful for modulators based on the combination effect of the absorption lineshape and energy shift. Therefore, there are some alternative approaches to design and fabricate intersubband modulators, such as the Stark

modulator, the quantum interference modulator or electro-optics modulators based on electrorefraction. However, asymmetric quantum well structures in which the wells may have either unequal thickness or different materials, or both, are more efficient for achieving the linear Stark shift or strong quantum interference [126-129]. In order to simulate multiple asymmetric C-DQW or C-TQW structures, a more flexible structure configuration will be needed to improve the modelling.

With a focus on achieving high modulation speeds and large absorption modulation, it is also important to have tight confinement of any guided lightwaves to the MQW, as the required interaction length (modulator length) is inversely proportional to the confinement factor of the optical field to the quantum well layers. For EAMs based on the conventional rib waveguide structures, as shown in Fig. 2.14, substrates with lower refractive index than the core region are required. Moreover, the number of the wells needs to increase to achieve tight optical confinement. Therefore, the optical design of an effective single mode dielectric waveguide, for example using the weighted index method [219,220], will be of significant interest owing to its application in estimating the optical confinement. As the results have shown, increasing the number of quantum wells can achieve large absorption rate and but also results in a requirement for the applied voltage to deplete the quantum well structures. At high modulation speeds, voltage is a limiting factor [129,221,222]. An improved model that can exactly simulate the optical confinement for the quantum wells needs further investigation. Alternatively, Holmstrom *et at* have proposed two possibilities to achieve waveguides, one based on the plasma effect and the other based on surface plasmons at a metal/semiconductor interface, with a very tight confinement for mid-infrared wavelengths [221]. Whilst free carrier absorption will cause excess loss in waveguides formed by doping, surface plasmons may have advantages for low voltage operation. Therefore, an evaluation of a surface plasmon guided wave ISBA modulator would be of interest.

Appendix A

Matrix Coefficients for Transfer Matrix Method

Condition I: $E < V_i, E < V_{i+1}$

$$M_i(1,1) = \frac{1}{2}\left(1+\frac{\beta_i m_{i+1}^*}{\beta_{i+1} m_i^*}\right)\exp[(\beta_i - \beta_{i+1})z_i]$$

$$M_i(1,2) = \frac{1}{2}\left(1-\frac{\beta_i m_{i+1}^*}{\beta_{i+1} m_i^*}\right)\exp[(-\beta_i - \beta_{i+1})z_i]$$

$$M_i(2,1) = \frac{1}{2}\left(1-\frac{\beta_i m_{i+1}^*}{\beta_{i+1} m_i^*}\right)\exp[(\beta_i + \beta_{i+1})z_i]$$

$$M_i(2,2) = \frac{1}{2}\left(1+\frac{\beta_i m_{i+1}^*}{\beta_{i+1} m_i^*}\right)\exp[(-\beta_i + \beta_{i+1})z_i]$$

Condition II: $E < V_i, E > V_{i+1}$

$$M_i(1,1) = \left[\sin(\alpha_{i+1}z_i)+\frac{\beta_i m_{i+1}^*}{\alpha_{i+1} m_i^*}\cos(\alpha_{i+1}z_i)\right]\exp(\beta_i z_i)$$

$$M_i(1,2) = \left[\sin(\alpha_{i+1}z_i)-\frac{\beta_i m_{i+1}^*}{\alpha_{i+1} m_i^*}\cos(\alpha_{i+1}z_i)\right]\exp(-\beta_i z_i)$$

$$M_i(2,1) = \left[\cos(\alpha_{i+1}z_i)-\frac{\beta_i m_{i+1}^*}{\alpha_{i+1} m_i^*}\sin(\alpha_{i+1}z_i)\right]\exp(\beta_i z_i)$$

$$M_i(2,2) = \left[\cos(\alpha_{i+1}z_i)+\frac{\beta_i m_{i+1}^*}{\alpha_{i+1} m_i^*}\sin(\alpha_{i+1}z_i)\right]\exp(-\beta_i z_i)$$

Condition III: $E > V_i, E < V_{i+1}$

$$M_i(1,1) = \frac{1}{2}\left[\sin(\alpha_i z_i) + \frac{\alpha_i m_{i+1}^*}{\beta_{i+1} m_i^*}\cos(\alpha_i z_i)\right]\exp(-\beta_{i+1} z_i)$$

$$M_i(1,2) = \frac{1}{2}\left[\cos(\alpha_i z_i) - \frac{\alpha_i m_{i+1}^*}{\beta_{i+1} m_i^*}\sin(\alpha_i z_i)\right]\exp(-\beta_{i+1} z_i)$$

$$M_i(2,1) = \frac{1}{2}\left[\sin(\alpha_i z_i) - \frac{\alpha_i m_{i+1}^*}{\beta_{i+1} m_i^*}\cos(\alpha_i z_i)\right]\exp(\beta_{i+1} z_i)$$

$$M_i(2,2) = \frac{1}{2}\left[\cos(\alpha_i z_i) + \frac{\alpha_i m_{i+1}^*}{\beta_{i+1} m_i^*}\sin(\alpha_i z_i)\right]\exp(\beta_{i+1} z_i)$$

Condition IV: $E > V_i, E > V_{i+1}$

$$M_i(1,1) = \sin(\alpha_i z_i)\sin(\alpha_{i+1} z_i) + \frac{\alpha_i m_{i+1}^*}{\alpha_{i+1} m_i^*}\cos(\alpha_i z_i)\cos(\alpha_{i+1} z_i)$$

$$M_i(1,2) = \cos(\alpha_i z_i)\sin(\alpha_{i+1} z_i) - \frac{\alpha_i m_{i+1}^*}{\alpha_{i+1} m_i^*}\sin(\alpha_i z_i)\cos(\alpha_{i+1} z_i)$$

$$M_i(2,1) = \sin(\alpha_i z_i)\cos(\alpha_{i+1} z_i) - \frac{\alpha_i m_{i+1}^*}{\alpha_{i+1} m_i^*}\cos(\alpha_i z_i)\sin(\alpha_{i+1} z_i)$$

$$M_i(2,2) = \cos(\alpha_i z_i)\cos(\alpha_{i+1} z_i) + \frac{\alpha_i m_{i+1}^*}{\alpha_{i+1} m_i^*}\sin(\alpha_i z_i)\sin(\alpha_{i+1} z_i)$$

Appendix B

Fermi-Dirac Integral

The Fermi-Dirac integral of order j is defined as [223]

$$F_j(\eta) = \frac{1}{\Gamma(j+1)} \int_0^\infty \frac{\varepsilon^j}{1+e^{\varepsilon-\eta}} d\varepsilon$$

where Γ is Gamma function and $\Gamma(x) = \int_0^\infty t^{x-1} e^{-t} dt$. Blakemore [223,224] has given an approximate function for the Fermi-Dirac integral of order 1/2

$$F_{1/2}(\eta) = \begin{cases} \dfrac{e^\eta}{1+0.27e^\eta} & \eta \le 1.3 \\ \dfrac{4}{3\sqrt{\pi}} (\eta^2 + \dfrac{\pi^2}{6})^{\frac{3}{4}} & \eta \ge 0.7 \end{cases}$$

The relative error of the function is within 3% of the actual integral. Similar the approximate function for $F_{3/2}$ [225] is

$$F_{3/2}(\eta) = \frac{1}{1+0.16e^\eta} \qquad \eta \le 0$$

The relative error of the function is less than 2% for the negative values of η.

Bibliography

[1] OIDA Predicts Growth in Optical Communications Market and Projects Trends into Year 2015 (2005)

[2] C. T. A. Brown, M. A. Cataluna, A. A. Lagatsky, E. U. Rafailov, M. B. Agate, C. G. Leburn and W. Sibbett, "Compact laser-diode-based femtosecond soruces," New J. Phys., Vol. 6, 175 (2004)

[3] N. Iizuka, K. Kaneko and N. Suzuki, "Sub-picosecond all-optical gate utilizing an intersubband transition," Optics Express, Vol. 13, pp. 3835~3840 (2005)

[4] P. K. Basu, "Theory of optical processes in semiconductors – Bulk and microstructures," Oxford University Press (1997)

[5] N. El Dahdah, G. Aubin, J.-C. Harmand, A. Ramdane, A. Shen, F. Devaux, A. Garreau and B.-E. Benkelfat, "Ultrafast InGaAs/InGaAlAs multiple-quantum-well electro-absorption modulator for wavelength conversion at high bit rates," Appl. Phys. Lett., Vol. 84, pp. 4268~4270 (2004)

[6] A. M. Fox, D. A. B. Miller, G. Livescu, J. E. Cunningham and W. Y. Jan, "Quantum well carrier sweep out: relation to electroabsorption andexciton saturation," IEEE J. Quantum Electron., Vol. 27, pp. 2281~2295 (1991)

[7] S. Tsujino, C. Metzner, T. Noda and H. Sakaki, "Saturation of intersubband absorption by real-space transfer in modulation doped single GaAs-AlAs quantum well," Phys. Stat. Sol. (B), Vol. 204, pp. 162~165 (1997)

[8] B. K. Ridley, "The electron-phonon interaction in quasi-two-dimensional semiconductor quantum-well structures," J. Phys. C, Vol. 15, pp. 5899~5917 (1982)

[9] R. Ferreira and G. Bastard, "Evaluation of some scattering times for electrons in unbiased and biased single- and multiple-quantum-well structures," Phys. Rev. B, Vol. 40, pp. 1074~1086 (1989)

[10] T. Asano, S. Noda and K. Tomoda, "Pump and probe measurement of intersubband relaxation time in short-wavelength intersubband transition," Appl. Phys. Lett., Vol. 74, pp. 1418~1420 (1999)

[11] T. Akiyama, N. Georgiev, T. Mozume, H. Yoshida, A. Venu Gopal and O. Wada, "Nonlinearity and recovery time of 1.55 μm intersubband absorption in InGaAs-AlAs-AlAsSb coupled quantum wells," Electron. Lett., Vol. 37, pp. 129~130 (2001)

[12] N. Suzuki and N. Iizuka, "Feasibility study on ultrafast nonlinear optical properties of 1.55-μm intersubband transition in AlGaN/GaN quantum wells," Jpn. J. Appl. Phys., Vol. 36, pp. L1006~L1008 (1997)

[13] J. D. Heber, C. Gmachl, H. M. Ng and A. Y. Cho, "Comparative study of ultrafast intersubband electron scattering times at ~1.55 μm wavelength in GaN/AlGaN heterostructures," Appl. Phys. Lett., Vol. 81, pp. 1237~1239 (2002)

[14] P. Bhattacharya, "Properties of lattice-matched and strained indium gallium arsenide," INSPEC, the Institution of Electrical Engineers (1993)

[15] O. Gauthier-Lafaye, F. H. Julien, S. Cabaret, J.-M. Lourtioz, G. Strasser, E. Gornik, M. Helm and P. Bois, "High-power GaAs/AlGaAs quantum fountain unipolar laser emitting at 14.5 μm with 2.5% tunability," Appl. Phys. Lett., Vol. 74, pp. 1537~1539 (1999)

[16] L. C. West and S. J. Eglash, "First observation of an extremely large-dipole infrared transition within the conduction band of a GaAs quantum well," Appl. Phys. Lett., Vol. 46, pp. 1156~1158 (1985)

[17] T. Akiyama, N. Georgiev, T. Mozume, H. Yoshida, A. V. Gopal and O. Wada, "1.55-μm picosecond all-optical switching by using intersubband absorption in InGaAs-AlAs-AlAsSb coupled quantum wells," IEEE Photon. Technol. Lett., Vol. 14, pp. 495~497 (2002)

[18] J. Faist, F. Capasso, D. L. Sivco, C. Sirtori, A. L. Hutchinson and A. Y. Cho, "Quantum cascade laser," Science, Vol. 264, pp. 553~556 (1994)

[19] S. Y. Yuen, "Fast relaxing absorptive nonlinear refraction in superlattices," Appl. Phys. Lett., Vol. 43, pp. 813~815 (1983)

[20] D. Ahn and S. L. Chuang, "Nonlinear intersubband optical absorption in a semiconductor quantum well," J. Appl. Phys., Vol. 62, pp. 3052~3055 (1987)

[21] D. Ahn and S.-L. Chuang, "Calculation of linear and nonlinear intersubband optical absorptions in a quantum well model with an applied electric field," IEEE J. Quantum Electron., Vol. 23, pp. 2196~2204 (1987)

[22] P. F. Yuh and K. L. Wang, "Large Stark effects for transitions from local states to global states in quantum well structures," IEEE J. Quantum Electron., Vol. 25, pp. 1671~1676 (1989)

[23] G. E. W. Bauer and T. Ando, "Electronic structure of free carriers in quantum wells calculated by density-functional theory," Phys. Rev. B, Vol. 34, pp. 1300~1303 (1986)

[24] A. V. Gopal, H. Yoshida, A. Neogi, N. Georgiev, T. Mozume, T. Simoyama, O. Wada and H. Ishikawa, "Intersubband absorption saturation in InGaAs-AlAsSb quantum wells," IEEE J. Quantum Electron., Vol. 38, pp. 1515~1520 (2002)

[25] T. Mozume, H. Yoshida, A. Neogi and M. Kudo, "1.45μm intersubband absorption in InGaAs/AlAsSb grown by melecular beam epitaxy," Jpn. J. Appl. Phys., Vol. 38, pp. 1286~1289 (1999)

[26] A. K. Ghatak, K. Thyagarajan and M. R. Shenoy, "A novel numerical technique for solving the one-dimensional Schrodinger equation using matrix approach – Application to quantum well structures," IEEE J. Quantum Electron., Vol. 24, pp. 1524~1531 (1988)

[27] G. H. Wannier, "The structure of electronic excitation levels in insulating crystals," Phys. Rev., Vol. 52, pp. 191~197 (1937)

[28] J. C. Slater, "Electrons in perturbed periodic lattices," Phys. Rev., Vol. 76, pp. 1592~1601 (1949)

[29] J. M. Luttinger and W. Kohn, "Motion of electrons and holes in perturbed periodic fields," Phys. Rev., Vol. 97, pp. 869~883 (1955)

[30] A. Y. Cho, "Growth of periodic structures by the molecular-beam method," Appl. Phys. Lett., Vol. 19, pp. 467~468 (1971)

[31] A. Y. Cho and M. B. Panish, "Magnesium-doped GaAs and $Al_xGa_{1-x}As$ by molecular beam epitaxy," J. Appl. Phys., Vol. 43, pp. 5118~5123 (1972)

[32] L. L. Chang, L. Esaki, W. E. Howard, R. Ludeke and G. Schul, "Structures grown by molecular beam epitaxy," J. Vac. Sci. Technol., Vol. 10, pp. 655~662 (1973)

[33] L. Esaki and L. L. Chang, "New transport phenomenon in a semiconductor "Superlattice" ," Phys. Rev. Lett., Vol. 33, pp. 495~498 (1974)

[34] H. M. Manasevit and W. I. Simpson, "The use of metal-organics in the preparation of semiconductor materials: I. epitaxial Gallium-V compounds," J. Electrochem. Soc., Vol. 116, pp. 1725~1732 (1969)

[35] R. D. Dupuis and P. D. Dapkus, "Room-temperature operation of $Ga_{(1-x)}Al_xAs$/GaAs double-heterostructure lasers grown by metalorganic chemical vapor deposition," Appl. Phys. Lett., Vol. 31, pp. 466~468 (1977)

[36] R. D. Dupuis, P. D. Dapkus, N. Holonyak, Jr., and R. M. Kolbas, "Continuous room-temperature multiple-quantum-well $Al_xGa_{1-x}As$-GaAs injection lasers grown by metalorganic chemical vapor deposition," Appl. Phys. Lett., Vol. 35, pp. 487~489 (1979)

[37] J. E. A. Whiteaway and E. J. Thrush, "Performance and characterization of GaAs-(GaAl)As double heterojunction lasers grown by metalorganic chemical vapor deposition," J. Appl. Phys., Vol. 52, pp. 1528~1536 (1981)

[38] L. Esaki, "A bird's-eye view on the evolution of semiconductor superlattices and quantum wells," IEEE J. Quantum Electron., Vol. 22, pp. 1611~1624 (1986)

[39] D. F. Welch, G. M. Wicks, D. W. Woodard and L. F. Eastman, "GaInAs-AlInAs heterostructures for optical devices grown by MBE," J. Vac. Sci. Technol. B, Vol. 1, pp. 202~204 (1983)

[40] L. Esaki and R. Tsu, "Superlattice and negative differential conductivity in semiconductors," IBM J. Res. Dev., Vol. 14, pp. 61~65 (1970)

[41] R. Dingle, W. Wiegmann and C. Henry, "Quantum states of confined carriers in very thin $Al_xGa_{1-x}As$-GaAs-$Al_xGa_{1-x}As$ heterostructures," Phys. Rev. Lett., Vol. 33, pp. 827~830 (1974)

[42] J. H. Davies, "The physics of low-dimensional semicondictors – an introduction," Cambridge University Press (1998)

[43] S. Datta, "Quantum phenomena," Addison-Wesley Publishing Company (1989)

[44] V. V. Mitin, V. A. Kochelap, M. A. Stroscio, "Quantum heterostructures – microelectronics and optoelectronics," Cambridge University Press (1999)

[45] D. Xu, J. Osaka, Y. Umeda, T. Suemitsu, Y. Yamane and Y. Ishii, "Modulation-doped field-effect transistors with an 8-nm InGaAs/InAs/InGaAs quantum well," IEEE Electron Device Lett., Vol. 20, pp. 109~112 (1999)

[46] D. M. Gill, B. C. Kane, S. P. Svensson, D.-W. Tu, P. N. Uppal and N. E. Byer, "High-performance, 0.1 μm InAlAs/InGaAs high electron mobility transistors on GaAs," IEEE Electron Device Lett., Vol. 17, pp. 328~330 (1996)

[47] S. Luryi and F. Capasso, "Resonant tunneling of two-dimensional electrons through a

quantum wire: A negative transconductance device," Appl. Phys. Lett., Vol. 47, pp. 1347~1349 (1985)

[48] K. Hess, H. Morkoç, H. Shichijo and G. B, Streetman, "Negative differential resistance through real-space electron transfer," Appl. Phys. Lett., Vol. 35, pp. 469~471 (1979)

[49] S. Luryi, "Light-emitting devices based on the real-space transfer of hot electrons," Appl. Phys. Lett., Vol. 58, pp. 1727~1729 (1991)

[50] T. K. Higman, M. S. Hagedorn, J. Chen and K. Y. Cheng, "Observation of light emission from real-space transfer devices," Appl. Phys. Lett., Vol. 60, pp. 1342~1344 (1992)

[51] J. Feldmann, K. Leo, J. Shah, D. A. B. Miller, J. E. Cunningham, T. Meier, G. von Plessen, A. Schulze, P. Thomas and S. Schmitt-Rink, "Optical investigation of Bloch oscillations in a semiconductor superlattice," Phys. Rev. B, Vol. 46, pp. 7252~7255 (1992)

[52] T. Dekorsy, P. Leisching, C. Waschke, K. Köhler, K. Leo, H. G. Roskos and H. Kurz, "Terahertz Bloch oscillations in semiconductor superlattices," Semicond. Sci. Technol., Vol. 9, pp. 1959~1964 (1994)

[53] E. E. Mendez, G. Bastard, L. L. Chang, L. Esaki, H. Morkoc and R. Fischer, "Effect of an electric field on the luminescence of GaAs quantum wells," Phys. Rev. B, Vol. 26, pp. 7101~7104 (1982)

[54] D. A. B. Miller, D. S. Chemla, T. C. Damen, A. C. Gossard, W. Wiegmann, T. H. Wood and C. A. Burrus, "Band-edge electroabsorption in quantum well structures: The quantum-confined stark effect," Phys. Rev. Lett., Vol. 53, pp. 2173~2176 (1984)

[55] D. A. B. Miller, D. S. Chemla, T. C. Damen, A. C. Gossard, W. Wiegmann, T. H. Wood and C. A. Burrus, "Electric field dependence of optical absorption near the band gap of quantum-well structures," Phys. Rev. B, Vol. 32, pp. 1043~1060 (1985)

[56] T. H. Wood, C. A. Burrus, D. A. B. Miller, D. S. Chemla, T. C. Damen, A. C. Gossard and W. Weigmann, "High-speed optical modulation with GaAs/GaAlAs quantum wells in a p-i-n diode structure," Appl. Phys. Lett., Vol. 44, pp. 16~18 (1984)

[57] D. A. B. Miller, D. S. Chemla, T. C. Damen, A. C. Gossard, W. Wiegmann, T. H. Wood and C. A. Burrus, "Novel hybrid optically bistable switch: The quantum well self-electro-optic effect device," Appl. Phys. Lett., Vol. 45, pp. 13~15 (1984)

[58] D. A. B. Miller, M. D. Feuer, T. Y. Chang, S. C. Shunk, J. E. Henry, D. J. Burrow and D.

S. Chemla, "Field-effect transistor self-electrooptic effects device: Integrated photodiode, quantum well modulator and transistor," IEEE Photon. Technol. Lett., Vol. 1, pp. 62~64 (1989)

[59] J. Bleuse, G. Bastard and P. Voisin, "Electric-field-induced localization and oscillatory electro-optical properties of semiconductor superlattices," Phys. Rev. Lett., Vol. 60, pp. 220~223 (1988)

[60] E. E. Mendez, F. Agulló-Rueda and J. M. Hong, "Stark localization in GaAs-GaAlAs superlattices under an electric field," Phys. Rev. Lett., Vol. 60, pp. 2426~2429 (1988)

[61] R. Dingle, H. L. Störmer, A. C. Gossard and W. Wiegmann, "Electron mobilities in modulation-doped semiconductor heterojunction superlattices," Appl. Phys. Lett., Vol. 33, pp. 665~667 (1978)

[62] C. Weisbuch and B. Vinter, "Quantum semiconductor structure: Fundamentals and applications," Academic Press (1991)

[63] T. Ando, "Self-consistent results for a GaAs/$Al_xGa_{1-x}As$ heterojunction. I. Subband structure and light-scattering spectra," J. Phys. Soc. Jpn., Vol. 51, pp. 3893~3899 (1982)

[64] Y. Ando and T. Itoh, "Analysis of charge control in pseudomorphic two-dimensional electron-gas field-effect transistors," IEEE Trans. Electron Devices, Vol. 35, pp. 2295~2301 (1988)

[65] G.-I. Ng, D. Pavlidis, M. Jaffe, J. Singh and H.-F. Chau, "Design and experimental characteristics of strained $In_{0.52}Al_{0.48}As/In_xGa_{1-x}As$ (x>0.53) HEMT's," IEEE Trans. Electron Devices, Vol. 36, pp. 2249~2259 (1989)

[66] J. E. Manzoli, M. A. Romero and O. Hipólito, "On the capacitance - voltage modeling of strained quantum-well MODFET's," IEEE J. Quantum Electron., Vol. 34, pp. 2314~2320 (1998)

[67] R. D. Dupuis and P. D. Dapkus, "$Ga_{(1-x)}Al_xAs/Ga_{(1-y)}Al_yAs$ double-heterostructure room-temperature lasers grown by metalorganic chemical vapor deposition," Appl. Phys. Lett., Vol. 31, pp. 839~841 (1977)

[68] R. D. Dupuis, P. D. Dapkus, N. Holonyak, Jr., E. A. Rezek and R. Chin, "Room-temperature laser operation of quantum-well $Ga_{(1-x)}Al_xAs$-GaAs laser diodes grown by metal organic chemical vapour deposition," Appl. Phys. Lett., Vol. 32, pp. 295~297 (1978)

[69] A. R. Adams, "Band-structure engineering for low-threshold high-efficiency semiconductor lasers," Electron. Lett., Vol. 22, pp. 249~250 (1986)

[70] H. K. Choi and C. A. Wang, "InGaAs/AlGaAs strained quantum well diode lasers with extremely low threshold current density and high efficiency," Appl. Phys. Lett., Vol. 57, pp. 321~323 (1990)

[71] K. Iga, F. Koyama and S. Kinoshita, "Surface emitting semiconductor lasers," IEEE J. Quantum Electron., Vol. 24, pp. 1845~1855 (1988)

[72] S. W. Corzine, R. S. Geels, R. H. Yan, J. W. Scott, L. A. Coldren and P. L. Gourley, "Efficient, narrow-linewidth distributed-Bragg-reflector surface-emitting laser with periodic gain," IEEE Photon. Technol. Lett., Vol. 1, pp. 52~54 (1989)

[73] S. L. McCall, A. F. J. Levi, R. E. Slusher, S. J. Pearton and R. A. Logan, "Whispering-gallery mode microdisk lasers," Appl. Phys. Lett., Vol. 60, pp. 289~291 (1992)

[74] T. Mimura, S. Hiyamizu, T. Fujii and K. Nanbu, "A new field-effect transistor with selectively doped GaAs/n-$Al_xGa_{1-x}As$ heterojunctions," Jpn. J. Appl. Phys., Vol. 19, pp. L225~L227 (1980)

[75] P. M. Solomon and H. Morkoç, "Modulation-doped GaAs/AlGaAs heterojunction field-effect transistors (MODFET's), ultrahigh-speed device for supercomputers," IEEE Trans. Electron Devices, Vol. 31, pp. 1015~1027 (1984)

[76] D. C. Streit, K. L. Tan, R. M. Dia, J. K. Liu, A. C. Han, J. R. Velebir, S. K. Wang, T. Q. Trinh, P.-M. D. Chow, P. H. Liu and H. C. Yen, "High-gain W-band pseudomorphic InGaAs power HEMTs," IEEE Electron Device Lett., Vol. 12, pp. 149~150 (1991)

[77] D. A. B. Miller, J. S. Weiner and D. S. Chemla, "Electric-field dependence of linear optical properties in quantum well structures: Waveguide electroabsorption and sum rules," IEEE J. Quantum Electron., Vol. 22, pp. 1816~1830 (1986)

[78] F. Dorgeuille and F. Devaux, "On the transmission performances and the chirp parameter of a multiple-quantum-well electroabsorption modulator," IEEE J. Quantum Electron., Vol. 30, pp. 2565~2572 (1994)

[79] Y.-J. Chiu, V. Kaman, S. Z. Zhang and J. E. Bowers, "Distributed effects model for cascaded traveling-wave electroabsorption modulator," IEEE Photon. Technol. Lett., Vol. 13, pp. 791~793 (2001)

[80] D. Walrod, S. Y. Auyang, P. A. Wolff and M. Sugimoto, "Observation of third order optical nonlinearity due to intersubband transitions in AlGaAs/GaAs superlattices," Appl. Phys. Lett., Vol. 59, pp. 2932~2934 (1991)

[81] S. Banerjee and K. A. Shore, "MIR and NIR nonlinear optical processing using intersubband $\chi^{(3)}$ in triple quantum well structures," Semicond. Sci. Technol., Vol. 18, pp. 655~660 (2003)

[82] N. Mustafa, L. Pesquera, C. Y. L. Cheung and K. A. Shore, "Terahertz bandwidth prediction for amplitude modulation response of unipolar intersubband semiconductor lasers," IEEE Photon. Technol. Lett., Vol. 11, pp. 527~529 (1999)

[83] R. Q. Yang, J. M. Xu and M. Sweeny, "Selection rules of intersubband transitions in conduction-band quantum wells," Phys. Rev. B, Vol. 50, pp. 7474~7482 (1994)

[84] D. Ahn and S. L. Chuang, "Intersubband optical absorption in a quantum well with an applied electric field," Phys. Rev. B, Vol. 35, pp. 4149~4151 (1987)

[85] B. Sung, H. C. Chui, M. M. Fejer and J. S. Harris, Jr., "Near-infrared wavelength intersubband transition in high indium content InGaAs/AlAs quantum wells grown on GaAs," Electron. Lett., Vol. 33, pp. 818~820 (1997)

[86] C.-L. Yang, D.-S. Pan and R. Somoano, "Advantages of an indirect semiconductor quantum well system for infrared detection," J. Appl. Phys., Vol. 65, pp. 3253~3258 (1989)

[87] J. S. Park, R. P. G. Karunasiri and K. L. Wang, "Normal incidence infrared detector using p-type SiGe/Si multiple quantum wells," Appl. Phys. Lett., Vol. 60, pp. 103~105 (1992)

[88] E. R. Brown and S. J. Eglash, "Calculation of the intersubband absorption strength in ellipsoidal-valley quantum wells," Phys. Rev. B, Vol. 41, pp. 7559~7568 (1990)

[89] A. Seilmeier, H.-J. Hübner, G. Abstreiter, G. Weimann and W. Schlapp, "Intersubband relaxation in GaAs-$Al_xGa_{1-x}As$ quantum well structures observed directly by an infrared bleaching technique," Phys. Rev. Lett., Vol. 59, pp. 1345~1348 (1987)

[90] D. Y. Oberle, D. R. Wake, M. V. Klein , J. Klem, T. Henderson and H. Morkoç, "Time-resolved Raman scattering in GaAs quantum wells," Phys. Rev. Lett., Vol. 59, pp. 696~699 (1987)

[91] J. H. Smet, C. G. Fonstad and Q. Hu, "Intrawell and interwell intersubband transitions in multiple quantum wells for far-infrared sources," J. Appl. Phys., Vol. 79, pp. 9305~9320

(1996)

[92] H. Rücker, E. Molinari and P. Lugli, "Microscopic calculation of the electron-phonon interaction in quantum wells," Phys. Rev. B, Vol. 45, pp. 6747~6756 (1992)

[93] B. K. Ridley, "Electron scattering by confined LO polar phonons in a quantum well," Phys. Rev. B, Vol. 39, pp. 5282~5286 (1989)

[94] Y. Hirayama, J. H. Smet, L.-H. Peng, C. G. Fonstad and E. P. Ippen, "Feasibility of 1.55 μm intersubband photonic devices using InGaAs/AlAs pseudomorphic quantum well structures," Jpn. J. Appl. Phys., Vol. 33, pp. 890~895 (1994)

[95] S. Lutgen, R. A. Kaindl, M. Woerner, T. Elsaesser, A. Hase and H. Künzel, "Nonlinear intersubband absorption of a hot quasi-two-dimensional electron plasma studied by femtosecond infrared spectroscopy," Phys. Rev. B, Vol. 54, pp. R17343~R17346 (1996)

[96] G. Ghislotti, E. Riedo, D. Ielmini and M. Martinelli, "Intersubband relaxation time for $In_xGa_{1-x}As$/AlAs quantum wells with large transition energy," Appl. Phys. Lett., Vol. 75, pp. 3626~3628 (1999)

[97] T. Müller, W. Parz, F. F. Schrey, G. Strasser and K. Unterrainer, "Intraband relaxation of photoexcited electrons in GaAs/AlGaAs quantum wells and InAs/GaAs self-assembled quantum dots," Semicond. Sci. Technol., Vol. 19, pp. S287~S289 (2004)

[98] C. D. Bezant, J. M. Chamberlain, H. P. M. Pellemans, B. N. Murdin, W. Batty and M. Henini, "Intersubband relaxation lifetimes in p-GaAs/AlGaAs quantum wells below the LO-phonon energy measured in a free electron laser experiment," Semicond. Sci. Technol., Vol. 14, pp. L25~L28 (1999)

[99] H. A. Tan, Z.-J. Xin, H. N. Rutt, J.-P. R. Wells and I. V. Bradley, "Intersubband lifetimes and free carrier effects in optically pumped far infrared quantum wells laser structures," Semicond. Sci. Technol., Vol. 17, pp. 645~650 (2002)

[100] N. Iizuka, K. Kaneko, N. Suzuki, T. Asano, S. Noda and O. Wada, "Ultrashort (≤150 fs) carrier relaxation time of intersubband transition in AlGaN/GaN multiple quantum wells," Conference on Lasers and Electro-Optics (CLEO 2000), pp. 358~359 (2000)

[101] N. Iizuka, K. Kaneko and N. Suzuki, "Near-infrared intersubband absorption in GaN/AlN quantum wells grown by molecular beam epitaxy," Appl. Phys. Lett., Vol. 81, pp. 1803~1805 (2002)

[102] T. Asano, S. Yoshizawa, S. Noda, N. Iizuka, K. Kaneko, N. Suzuki and O. Wada,

"Ultrafast all optical modulation based on intersubband transition in semiconductor quantum wells," Optical and Quantum Electronics, Vol. 33, pp. 963~973 (2001)

[103] K. G. Gan, C. K. Sun, S. P. DenBaars and J. E. Bowers, "Ultrafast valence intersubband hole relaxation in InGaN multiple-quantum-well laser diodes," Appl. Phys. Lett., Vol. 84, pp. 4675~4677 (2004)

[104] V. Jovanovi, D. Indjin, Z. Ikoni, V. Milanovi and J. Radovanovi, "Design of GaN/AlGaN quantum wells for maximal intersubband absorption in $1.3<\lambda<2$ μm wavelength range," Solid State Comm., Vol. 121, pp. 619~624 (2002)

[105] B. F. Levine, "Quantum-well infrared photodetectors," J. Appl. Phys., Vol. 74, pp. R1~R81 (1993)

[106] M. O. Mannasreh, "Semiconductor quantum wells and superlattices for long-wavelength infrared detectors," Artech House (1993)

[107] C. J. Chen, K. K. Choi, L. Rokhinson, W. H. Chang and D. C. Tsui, "Corrugated quantum well infrared photodetectors for polarization detection," Appl. Phys. Lett., Vol. 74, pp. 862~864 (1999)

[108] J. Kolodzey, T. N. Adam, R. T. Troeger, P.-C. Lv, S. K. Ray, G. Looney, A. Rosen, M. S. Kagan and I. N. Yassievich, "The design and operation of TeraHertz sources based on silicon germanium alloys," Topical Meeting on Silicon Monolithic Integrated Circuits in RF Systems, pp. 1~5 (2003)

[109] Z.-J. Xin and H. N. Rutt, "Design of intersubband quantum well far-infrared lasers," Semicond. Sci. Technol., Vol. 12, pp. 1129~1134 (1997)

[110] R. Colombelli, F. Capasso, C. Gmachl, A. L. Hutchinson, D. L. Sivco, A. Tredicucci, M. C. Wanke, A. M. Sergent and A. Y. Cho, "Far-infrared surface-plasmon quantum-cascade lasers at 21.5 μm and 24 μm wavelengths," Appl. Phys. Lett., Vol. 78, pp. 2620-2622 (2001)

[111] I. Lyubomirsky, Q. Hu and M. R. Melloch, "Measurement of far-infrared intersubband spontaneous emission from optically pumped quantum wells," Appl. Phys. Lett., Vol. 73, pp. 3043~3045 (1998)

[112] M. Rochat, J. Faist, M. Beck, U. Oesterle and M. Ilegems, "Far-infrared (λ=88 μm) electroluminescence in a quantum cascade structure," Appl. Phys. Lett., Vol. 73, 3724~3726 (1998)

[113] R. Colombelli, C. Ciuti, Y. Chassagneux and C. Sirtori, "Quantum cascade intersubband polariton light emitters," Semicond. Sci. Technol., Vol. 20, pp. 985~990 (2005)

[114] G. Scalari, L. Ajili, J. Faist, H. Beere, E. Linfield, D. Ritchie and G. Davies, "Far-infrared (λ≈87 μm) bound-to-continuum quantum-cascade lasers operating up to 90 K," Appl. Phys. Lett., Vol. 82, pp. 3165~3167 (2003)

[115] R. F. Kazarinov and R. A. Suris, "Possibility of the amplification of electromagnetic waves in a semiconductor with a superlattice," Sov. Phys. Semicond., Vol. 5, pp. 707~709 (1971)

[116] R. F. Kazarinov and R. A. Suris, "Electric and electromagnetic properties of semiconductors with a superlattice," Sov. Phys. Semicond., Vol. 6, pp. 120~131 (1972)

[117] M. Beck, A. Muller, J. Faist, C. Sirtori, U. Oesterle and M. Ilegems, "InP- and GaAs-based quantum cascade lasers," Indium Phosphide and Related Materials, pp. 199~202 (1999)

[118] M. Razeghi, A. Evans, A. Qubain, J. David, S. Slivken, J. Yu, K. Mi and S. Darvish, "High power quantum cascade lasers in the 3-12 micron wavelength range," The 17th Annual Meeting of the IEEE Lasers and Electro-Optics Society (LEOS 2004), Vol. 2, pp. 547~548 (2004)

[119] M. Beck, D. Hofstetter, T. Aellen, J. Faist, U. Oesterle, M. Ilegems, E. Gini and H. Melchior, "Continuous wave operation of a mid-infrared semicon-ductor laser at room temperature," Science, Vol. 295, pp. 301~305 (2002)

[120] A. Friedrich, G. Scarpa, G. Boehm and M.-C. Amann, "High-temperature (T=490K) operation of 5.8 μm quantum cascade lasers with InP/GaInAs waveguides," Electron. Lett., Vol. 40, pp. 1416~1417 (2004)

[121] M. Rochat, L. Ajili, H. Willenberg, J. Faist, H. E. Beere, A. G. Davies, E. H. Linfield and D. Ritchie, "Low-threshold terahertz quantum-cascade lasers," Appl. Phys. Lett., Vol. 81, pp. 1381~1383 (2002)

[122] B. F. Levine, K. K. Choi, C. G. Bether, J. Walker and R. J. Malik, "New 10 μm infrared detector wing intersubband absorption in resonant tunneling GaAlAs superlattices," Appl. Phys. Lett., Vol. 50, pp. 1092~1094 (1987)

[123] W. Zhang, H. Lim, M. Taguchi, S. Tsao, B. Movaghar and M. Razeghi, "High-detectivity InAs quantum-dot infrared photodetectors grown on InP by metal–organic

chemical–vapor deposition," Appl. Phys. Lett., Vol. 86, 191103 (2005)

[124] A. Köck, E. Gornik, G. Abstreiter, G. Böhm, M. Walther and G. Weimann, "Double wavelength selective GaAs/AlGaAs infrared detector device," Appl. Phys. Lett., Vol. 60, 2011~2013 (1992)

[125] X. Jiang, S. S. Li and M. Z. Tidrow, "Investigation of a multistack voltage-tunable four-color quantum-well infrared photodetector for mid- and long-wavelength infrared detection," IEEE J. Quantum Electron., Vol. 35, pp. 1685~1692 (1999)

[126] A. Sa'ar and R. Kapon, "Quantum Interference, Stark and Carrier Density Infrared Electrooptical Modulation Based on Intersubband Transitions in Asymmetrical Quantum Wells," IEEE J. Quantum Electron., Vol. 33, pp. 1517~1526 (1997)

[127] R. Kapon , A. Segev and A. Sa'ar, "Intersubband electro-optic modulators for near and mid infrared applications," Superlattices and Microstructures, Vol. 23, pp. 1083~1091 (1998)

[128] H. C. Liu, C. Y. Song, A. J. SpringThorpe and G. C. Aers, "Infrared quantum well intersuband modulator," Electron. Lett., Vol. 29, pp. 1149~1150 (2003)

[129] P. Holmström, "High-Speed Mid-IR Modulator Using Stark Shift in Step Quantum Wells," IEEE J. Quantum Electron., Vol. 37, pp. 1273~1282 (2001)

[130] H. Yoshida, T. Mozume, A. Neogi and O. Wada, "Ultrafast all-optical switching at 1.3 μm/1.55 μm using novel InGaAs-AlAsSb-InP coupled double quantum well structure for intersubband transitions," Electron. Lett., Vol. 35, pp. 1103~1105 (1999)

[131] H. K. Choi and S. J. Eglash, "High-power multiple-quantum-well GaInAsSb/AlGaAsSb diode lasers emitting at 2.1 μm with low threshold current density," Appl. Phys. Lett., Vol. 61, pp. 1154~1156 (1992)

[132] R. Hui, Y. Wan, J. Li, S.X. Jin, J.Y. Lin and H.X. Jiang, "Birefringence of GaN/AlGaN optical waveguides," Appl. Phys. Lett., Vol. 83, pp. 1698~1700 (2003)

[133] C. Gmachl, H. M. Ng and A. Y. Cho, "Intersubband absorption in GaN/AlGaN multiple quantum wells in the wavelength range of λ~1.75–4.2 μm," Appl. Phys. Lett., Vol. 77, pp. 334~336 (2000)

[134] C. Gmachl, H. M. Ng, S.-N. G. Chu and A. Y. Cho, "Intersubband absorption at λ~1.55 μm in well- and modulation-doped GaN/AlGaN multiple quantum wells with superlattice barriers," Appl. Phys. Lett., Vol. 77, pp. 3722~3724 (2000)

[135] N. Iizuka, K. Kaneko, N. Suzuki, T. Asano, S. Noda and O. Wada, "Ultrafast intersubband relaxation (≤150 fs) in AlGaN/GaN multiple quantum wells," Appl. Phys. Lett., Vol. 77, pp. 648 (2000)

[136] A. Waag, F. Fischer, H. J. Lugauer, Th. Litz, J. Laubender, U. Lunz, U. Zehnder, W. Ossau, T. Gerhardt, M. Möller and G. Landwehr, "Molecular-beam epitaxy of beryllium-chalcogenide-based thin films and quantum-well structures," J. Appl. Phys., Vol. 80, pp. 792~796 (1996)

[137] R. Akimoto, B. S. Li, F. Sasaki and T. Hasama, "Intersubband transition based on a novel II-VI quantum well structure for ultrafast all-optical switching," Jpn. J. Appl. Phys., Vol. 43, pp. 1973~1977 (2004)

[138] R. Akimoto, K. Akita, F. Sasaki and T. Hasama, "Sub-picosecond electron relaxation of near-infrared intersubband transitions in n-doped (CdS/ZnSe)/BeTe quantum wells," Appl. Phys. Lett., Vol. 81, pp. 2998~3000 (2002)

[139] J. H. Smet, L. H. Peng, Y. Hirayama and C. G. Fonstad, "Electron intersubband transitions to 0.8eV (1.55μm) in InGaAs/AlAs single quantum wells," Appl. Phys. Lett., Vol. 64, pp. 986~987 (1994)

[140] J. W. Matthews and A. E. Blakeslee,

a) "Defects in epitaxial multilayers: I. Misfit dislocations," J. Crys. Grow., Vol. 27, pp. 118~125 (1974)

b) "Defects in epitaxial multilayers: II. Dislocation pile-ups, threading dislo-cations, slip lines and cracks," J. Crys. Grow., Vol. 29, pp. 273~280 (1975)

c) "Defects in epitaxial multilayers: III. Preparation of almost perfect multilayers," J. Crys. Grow., Vol. 32, pp. 265~273 (1976)

[141] T. Asano, S. Noda, T. Abe and A. Sasaki, "Investigation of short wavelength intersubband transitions in InGaAs/AlAs quantum wells on GaAs substrate," J. Appl. Phys., Vol. 82, pp. 3385~3391 (1997)

[142] B. Jusserand, J. A. Brum, D. Gardin, H. W. Liu, G. Weimann and W. Schlapp, "Density dependence of intersubband transitions in a modulation-doped quantum well," Phys. Rev. B, Vol. 40, pp. 4220~4223 (1989)

[143] E. F. Schubert, J. B. Stark, B. Ullrich and J. E. Cunningham, "Spatial localisation of impurities in δ-doped GaAs," Appl. Phys. Lett., Vol. 52, pp. 1508~1510 (1988)

[144] H. Asai and Y. Kawamura, "Doping effects on intersubband absorption in InGaAS/InAlAs multiquantum wells," Appl. Phys, Lett., Vol. 56, pp. 1427~1429 (1990)

[145] S. Højfeldt and J. Mørk, "Modeling of carrier dynamics in quantum-well electroabsorption modulators," IEEE J. Select. Topics Quantum Electron., Vol. 8, pp. 1265~1276 (2002)

[146] F. Stern, "Iteration methods for calculating self-consistent fields in semiconductor inversion layers," J. Comput. Phys., Vol. 6, pp. 56~67 (1970)

[147] P. A. Chen, C. Juang and C. Y. Chang, "Carrier-induced energy shift in GaAs/AlGaAs multiple quantum well laser diodes," IEEE J. Quantum Electron., Vol. 29, pp. 2607~2618 (1993)

[148] E. Ozturk, Y. Ergun, H. Sari and I. Sokmen, "Si δ-doped GaAs structure with different dopant distribution models," J. Appl. Phys., Vol. 91, pp. 2118~2122 (2002)

[149] R. T. Carline and D. W. E. Allsopp, "A simplified self-consistent model of charge control in quasi-square quantum well HFETs," Semicond. Sci. Technol., Vol. 6, pp. 1151~1157 (1991)

[150] G. Liu, S.-L. Chuang and S.-H. Park, "Optical gain of strained GaAsSb/GaAs quantum-well lasers: A self-consistent approach," J. Appl. Phys., Vol. 88, pp. 5554~5561 (2000)

[151] M. Ramsteiner, J. D. Ralston, P. Koidl, B. Dischler, H. Biebl, J. Wagner and H. Ennen, "Doping density dependence of intersubband transitions in GaAs/$Al_xGa_{1-x}As$ quantum-well structures," J. Appl. Phys., Vol. 67, pp. 3900~3903 (1990)

[152] E. Ozturk, Y. Ergun H. Sari and I. Sokmen, "Electronic subband of single Si δ-doped GaAs structures," Superlattices Microstruct., Vol. 28, pp. 35~45 (2000)

[153] F. Bloch, "Quantum mechanics of electrons in crystal lattices" ("Uber die Quantenmechanik der Elektronen in Kristallgittern"), Zeits. f. Physik, Vol. 52, pp. 555~600 (1928)

[154] L. I. Schiff, "Quantum Mechanics," 3rd ed., McGraw-Hill (1968)

[155] R. F. Pierret, "Advanced Semiconductor Fundamentals," Addison-Wesley Publishing Company (1987)

[156] G. Bastard, "Hydrogenic impurity states in a quantum well: A simple model," Phys. Rev. B, Vol. 24, pp. 4714~4722 (1981)

[157] G. Bastard, "Superlattice band structure in the envelope-function approxima-tion," Phys. Rev. B, Vol. 24, pp. 5693~5697 (1981)

[158] G. Bastard, "Theoretical investigations of superlattice band structure in the envelope-function approximation," Phys. Rev. B, Vol. 25, pp. 7584~7597 (1982)

[159] V. Fock, "Näherungsmethode sur Lösung des quantenmechanischen Mehrkörper problems," Zeits. f. Physik, Vol. 61, pp. 126~148 (1930)

[160] J. C. Slater, "A simplification of the Hartree-Fock method," Phys. Rev., Vol. 81, pp. 385~390 (1951)

[161] K. M. S. V. Bandara, D. D. Coon, Byungsung O, Y. F. Lin and M. H. Francombe, "Exchange interactions in quantum well subbands," Appl. Phys. Lett., Vol. 53, pp. 1931~1933 (1988)

[162] M. H. Degani, "Electron energy level in a δ-doped layer in GaAs," Phys. Rev. B, Vol. 44, pp. 5580~5584 (1991)

[163] T. Asano, S. Noda, T. Abe and A. Sasaki, "Near-infrared intersubband transitions in InGaAs/AlAs quantum wells on GaAs substrate," Jpn. J. Appl. Phys., Vol. 35, pp. 1285~1291 (1996)

[164] D. V. Lang, M. B. Panish, F. Capasso, J. Allam, R. A. Hamm, A. M. Sergent and W. T. Tsang, "Measurement of heterojunction band offsets by admittance spectroscopy: InP/$Ga_{0.47}In_{0.53}As$," Appl. Phys. Lett., Vol. 50, pp. 736~738 (1987)

[165] P. F. Yuh and K. L. Wang, "Formalism of the Kronig-Penney model for superlattices of variable basis," Phys. Rev. B, Vol. 38, pp. 13307~13315 (1988)

[166] M. O. Vassell, J. Lee and H. F. Lockwood, "Multibarrier tunneling in $Ga_{1-x}Al_xAs$/GaAs heterostructures," J. Appl. Plys., Vol. 54, pp. 5206~5213 (1983)

[167] R. M. Kolbas and N. Holonyak, Jr., "Man-made quantum wells: A new perspective on the finite square-well problem," Am. J. Phys., Vol. 52, pp. 431~437 (1984)

[168] D. C. Hutchings, "Transfer matrix approach to the analysis of an arbitrary quantum well structure in an electric field," Appl. Phys. Lett., Vol. 55, pp. 1082~1084 (1989)

[169] W. H. Press, B. P. Flannery, S. A. Teukolsky and W. T. Vetterling, "Numerical recipes: the art of scientific computing," Cambridge University Press (1986),

[170] S. P. Wilson and D. W. E. Allsopp, "Efficient algorithm for the determination of the one

electron eigen spectrum of a double quantum well semiconductor heterostructure," Superlattices Microstruct., Vol. 11, pp. 363~374 (1992)

[171] J. Kundrotas, A Dargys and A. Čėsna, "Shallow donor impact ionization in n-InP and n-GaAs: influence of doping and compensation," Semicond. Sci. Technol., Vol. 11, pp. 692~696 (1996)

[172] K. J. Bachmann, E. Buehler, F. A. Thiel, B. I. Miller and J. H. McFee, "The current status of the preparation of single crystals, bicrystals, and epitaxial layers of p-InP and of polycrystalline p-InP films for photovoltaic applications," J. Cryst. Growth, Vol. 39, pp. 137~150 (1977)

[173] N. L. Rowell, H. K. Shin, D. J. Lockwood and P. J. Poole, "Polarized infrared spectroscopy at oblique incidence of optical phonons in $In_{1-x}Ga_xAs$ epilayers on InP," J. Appl. Phys., Vol. 92, pp. 629~631 (2002)

[174] R. E. Fern and A. Onton, "Refractive Index of AlAs," J. Appl. Phys., Vol. 42, pp. 3499~3500 (1971)

[175] L. Collatz, "Numerical treatment of differential equations," 3rd ed., Springer-Verlag (1960)

[176] S. P. Wilson, D. W. E. Allsopp and C. G. Morton, "Application of an efficient algorithm for solving the one-band effective mass equation self-consistently in the modelling of some low dimensional structure devices," International Journal of Numerical Modelling: Electronic Networks, Devices and Fields, Vol. 5, pp. 23~39 (1992)

[177] D. D. Coon and R. P. G. Karunasiri, "New mode of IR detection using quantum wells," Appl. Phys. Lett., Vol. 45, pp. 649~651 (1984)

[178] G. Bastard, "Wave Mechanic Applied to Semiconductor Heterostructures," Halsted, New York (1988)

[179] W. Heitler, "The quantum theory of radiation," 3rd ed., Oxford University Press (1954)

[180] S. Nojima, "Intraband optical absorption in semiconductor superlattices," Phys. Rev. B, Vol. 41, pp. 10214~10217 (1990)

[181] I. Vurgaftman, J. R. Meyer and L. R. Ram-Mohan, "Band parameters for III–V compound semiconductors and their alloys," J. Appl. Phys., Vol. 89, pp. 5815-5875 (2001)

[182] J. O. Sofo and G. D. Mahan, "Optimum band gap of a thermoelectric material," Phys.

Rev. B, Vol. 49, pp. 4565~4570 (1994)

[183] B. R. Nag, "Theory of electrical transport in semiconductors," Pergamen Press (1972)

[184] E. O. Kane, "Band structure of indium antimonide," J. Phys. Chem. Solids, Vol. 1, pp. 249~261 (1957)

[185] U. Ekenberg, "Nonparabolicity effects in a quantum well: Sublevel shift, parallel mass, and Landau levels," Phys. Rev. B, Vol. 40, pp. 7714~7726 (1989)

[186] D. F. Nelson, R. C. Miller and D. A. Kleinman, "Band nonparabolicity effects in semiconductor quantum wells," Phys. Rev. B, Vol. 35, pp. 7770~7773 (1987)

[187] E. M. Conwell and M. O. Vassell, "High-field transport in n-type GaAs," Phys. Rev., Vol. 166, pp. 797~821 (1968)

[188] M. Sugawara, N. Okazaki, T. Fujii and S. Yamazaki, "Conduction-band and valence-band structures in strained $In_{1-x}Ga_xAs/InP$ quantum wells on (001) InP substrates," Phys. Rev. B, Vol. 48, pp. 8102~8118 (1993)

[189] T. Kunikiyo, M. Takenaka, Y. Kamakura, M. Yamaji, H. Mizuno, M. Morifuji, K. Taniguchi and C. Hamaguchi, "A Monte Carlo simulation of anisotropic electron transport in silicon including full band structure and anisotropic impact-ionization model," J. Appl. Phys., Vol. 75, pp. 297~312 (1994)

[190] M. P. C. M. Krijn, "Heterojunction band offsets and effective masses in III-V quaternary alloys," Semicond. Sci. Technol., Vol. 6, pp. 27~31 (1991)

[191] T. Ishikawa, "Band lineup and in-plane effective mass of InGaAsP or InGaAlAs on InP strained-layer quantum well," IEEE J. Quantum Electron., Vol. 30, pp. 562~570 (1994)

[192] H. Asai and Y. Kawamura, "Intersubband absorption in $In_{0.53}Ga_{0.47}As/In_{0.52}Al_{0.48}As$ multiple quantum wells," Phys. Rev. B, Vol. 43, pp. 4748~4759 (1991)

[193] L. C. West and S. J. Eglash, "First observation of an extremely large-dipole infrared transition within the conduction band of a GaAs quantum well," Appl. Phys. Lett., Vol. 46, pp. 1156~1158 (1985)

[194] Y. Hirayama, J. H. Smet, L. H. Peng C. G. Fonstad and E. P. Ippen, "Observation of 1.798 μm intersubband transition in InGaAs/AlAs pseudomorphic quantum well heterostructures," Appl. Phys. Lett., Vol. 63, pp. 1663~1665 (1993)

[195] N. Georgiev, T. Dekorsy, F. Eichhorn, M. Helm, M. P. Semtsiv and W. T. Masselink,

"Short-wavelength intersubband absorption in strain compensated InGaAs/AlAs quantum well structures grown on InP," Appl. Phys. Lett., Vol. 83, pp. 210~212 (2003)

[196] T. Asano, S. Noda and A. Sasaki, "Enhancement of Absorption Magnitude of Short-Wavelength Intersubband Transition in InGaAs/AlAs Quantum Wells," Jpn. Appl. Phys., Vol. 37, pp. 2510~2515 (1998)

[197] T. Mozume and N. Georgiev, "Optical and structural characterization of InGaAs/AlAsSb quantum wells grown by molecular beam epitaxy," Jpn. J. Appl. Phys., Vol. 41, pp. 1008~1011 (2002)

[198] B. L. Smith, "Au (n-type) InP Schottky barriers and their use in determining majority Carrier concentrations in n-type InP," J. Phys. D: Appl. Phys., Vol. 6, pp. 1358~1362 (1973)

[199] R. H. Williams, V. Montgomery, R. R. Varma and A. McKinley, "The influence of interfacial layers on the nature of gold contacts to silicon and indium phosphide," J. Phys. D: Appl. Phys., Vol. 10, pp. L253~L256 (1977)

[200] G. G. Roberts and K. P. Pande, "Electrical characteristics of Au-Ti-(n-type) InP Schottky diodes," J. Phys. D: Appl. Phys., Vol. 10, pp. 1323~1328 (1977)

[201] S. C. Jain, J. M. McGregor and D. J. Roulston, "Band-gap narrowing in novel III-V semiconductors," J. Appl. Phys., Vol. 68, pp. 3747~3749 (1990)

[202] L. E. Vorobjev, V. Yu Panevin, N. K. Fedosov, D. A. Firsov, V. A. Shalygin, A. Seilmeier, S. R. Schmidt, E. A. Zibik, E. Towe and V. V. Kapaev, "Carrier transfer in coupled asymmetric GaAs/AlGaAs double quantum wells after ultrafast intersubband excitation," Semicond. Sci. Technol., Vol. 21, pp. 1267~1273 (2006)

[203] M. P. Semtsiv, M. Ziegler, W. T. Masselink, N. Georgiev, T. Dekorsy and M. Helm, "Near-infrared intersubband transitions in InGaAs-AlAs-InAlAs double quantum wells," J. Appl. Phys., Vol. 97, pp. 113538 (2005)

[204] T. Simoyama, H. Yoshida, J. Kasai, T. Mozume, A. V. Gopal and H. Ishikawa, "InGaAs–AlAs–AlAsSb Coupled Quantum Well Intersubband Transition All-Optical Switch with Low Switching Energy for OTDM Systems," IEEE Photon. Technol. Lett., Vol. 15, pp. 1363~1365 (2003)

[205] A. Neogi, T. Mozume, H. Yoshida and O. Wada, "Intersubband transitions at 1.3 and 1.55 μm in a novel coupled InGaAs-AlAsSb double-quantum-well structure," IEEE

Photon. Technol. Lett., Vol. 11, pp. 632~634 (1999)

[206] N. K. Patel, I. S. Millard, E. H. Linfield, P. D. Rose, M. P. Grimshaw, D. A. Ritchie, G. A. C. Jones and M. Pepper, "Exchange- and correlation-induced charge transfer observed in independently contacted triple-quantum-well structures," Phys. Rev. B, Vol. 53, pp. 15443~15446 (1996)

[207] N. Susa, "Design of double and triple quantum wells for InGaAs-AlAsSb intersubband unipolar semiconductor lasers," IEEE J. Quantum Electron., Vol. 32, pp. 20~28 (1996)

[208] H. Yoshida, T. Mozume, A. Neogi and O. Wada, "All-optical switching using ultrafast intersubband transitions in InGaAs/AlAsSb coupled triple quantum well structures," The Pacific Rim Conference on Lasers and Electro-Optics, Vol. 3, pp. 734~735 (1999)

[209] E. B. Dupont, D. Delacourt and M. Papuchon, "Mid-infrared phase modulation via Stark effect on intersubbandtransitions in GaAs/GaAlAs quantum wells," IEEE J. Quantum Electron., Vol. 29, pp. 2313~2318 (1993)

[210] F. Koyama and K. Iga, "Frequency chirping in external modulators," J. Lightwave Techno., Vol. 6, pp. 87~92 (1988),

[211] Y. Kim, H. Lee, J. Lee, J. Han, T. W. Oh and J. Jeong, "Chirp characteristics of 10-Gb/s electroabsorption modulator integrated DFB lasers," IEEE J. Quantum Electron., Vol. 36, pp. 900~908 (2000)

[212] T. Ando, A. B. Fowler and F. Stern, "Electronic-properties of two-dimensional systems," Rev. Mod. Phys., Vol. 54, pp. 437~672 (1982)

[213] D. Gammon, B. V. Shanabrook, J. C. Ryan, D. S. Katzer and M. J. Yang, "Exchange and correlation in the nonhomogeneous electron gas in semiconductor heterojunctions," Phys. Rev. Lett., Vol. 68, pp. 1884~1887 (1992)

[214] W. L. Bloss, "Effects of Hartree, exchange, and correlation energy on intersubband transitions," J. Appl. Phys., Vol. 66, pp. 3639~3642 (1989)

[215] M. Załużny, "Intersubband absorption line broadening in semiconductor quantum wells: Nonparabolicity contribution," Phys. Rev. B, Vol. 43, pp. 4511~4514 (1991)

[216] M. Załużny, "Intersubband absorption line shape in tunneling superlattices," Appl. Phys. Lett., Vol. 60, pp. 1486~1488 (1992)

[217] F. Szmulowicz, M. O. Manasreh, C. E. Stutz and T. Vaughan, "Temperature and many-body effects on the intersubband transition in a GaAs/$Al_{0.3}Ga_{0.7}As$ multiple

quantum well," Phys. Rev. B, Vol. 50, 11618~11623 (1994)

[218] F. Ponse, W. T. Masselink and H. Morkoc, "Quasi-Fermi Level Bending in MODFET's and Its Effects on FET Transfer Characteristics," IEEE Trans. Electron Devices, Vol. ED-32, pp. 1017~1023 (1985)

[219] M. J. Robertson, P. C. Kendall, S. Ritchie, P. W. A. McIlroy and M. J. Adams, "The weighted index method: a new technique for analyzing planar optical waveguides," J. Lightwave Technol., Vol. 7, pp. 2105~2111 (1989)

[220] P. C. Kendall, M. J. Robertson, P. W. A. McIlroy, S. Ritchie and M. J. Adams, "Advances in rib waveguide analysis using the weighted index method or the method of moments," IEE Proceedings-Optoelectronics, Vol. 137, pp. 27~29 (1990)

[221] P. Holmstrom, "High-confinement waveguides for mid-IR devices," Physica E, Vol. 7, pp. 40~43 (2000)

[222] H. C. Liu, R. Dudek, A. Shen, E. Dupont, C. Y. Song, Z. R. Wasilewski and M. Buchanan, "High absorption (90%) quantum-well infrared photodetectors," Appl. Phys. Lett., Vol. 79, pp. 4237~4239 (2001)

[223] J. S. Blakemore, "Semiconductor Statistics," Pergammon Press Inc., 1962

[224] J. S. Blakemore, "Solid state physics," Cambridge University Press, 1985

[225] S. P. Wilson, "One-dimensional modelling of pseudomorphic semiconductor heterostructure with applications to capacitance-voltage profiling and delta-doping," D.Phil Thesis, University of York, UK, 1991